UNIVERSITÀ DEGLI STUDI DI PADOVA

Dipartimento di Fisica e Astronomia “Galileo Galilei”

Physics of the Universe

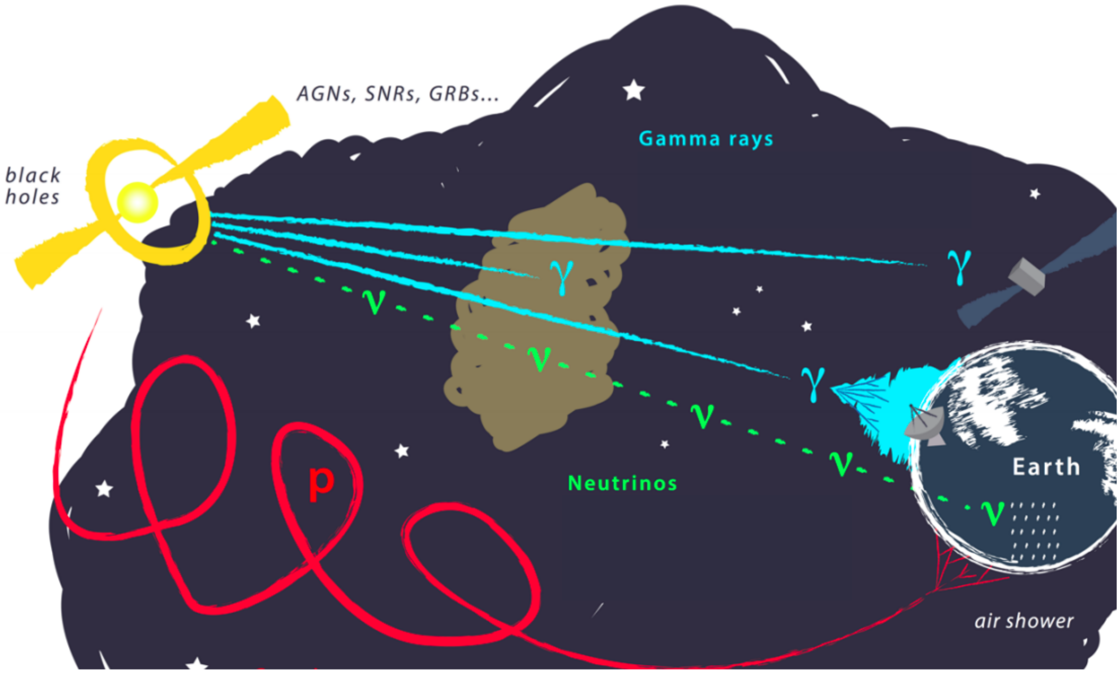

Multimessenger Astrophysics

Lectures held by

Elisa Bernardini

Academic year 2019/2020

Contents

List of Exercises

Introduction

These lecture notes are based on the Multimessenger Astroparticle Physics course, held by Professor Elisa Bernardini, `elisa.bernardini@unipd.it`, in the academic year of 2019-2020. The course was intended for the master degrees in Astrophysics and Cosmology and Physics at the University of Padova.

> *The word "multi-messenger" is quite new and increasingly used in astronomy and astroparticle physics. It refers to the combination of various techniques (both observational and theoretical) at different photon wavelengths and with different 'messengers', to get a deeper understanding of the astrophysical objects we observe in the sky with respect to what learnt from a single messenger alone.*
>
> *Visible light, in fact, reveals a small portion of the mysteries of the Universe. Astronomical observations are nowadays performed with different telescopes across the electromagnetic spectrum, from radio waves to* ***gamma-rays****, the highest observable energies. Whatever produces high energy gamma-rays, is expected to accelerate particles to energies that exceed the capabilities of man-made accelerators a billion times. Such particles can reach the Earth as* ***cosmic rays****. First discovered more than 100 years ago, cosmic rays are still nowadays one of the most misterious "messages" from our Universe.*
>
> *Cosmic rays may interact in the vicinity of their sources or even along their way to Earth, to produce elusive particles called* ***neutrinos****. Neutrinos are extremely difficult to detect, but the year 2013 has seen the first clear observation of neutrinos from distant astrophysical objects by the IceCube detector at the South Pole.*
>
> *Finally, the most known sources of gamma-rays (and likely cosmic-rays and neutrinos) are associated with black holes or neutron stars. Whenever two such compact objects orbit around each other they are expected to produce* ***gravitational waves****. Most recently, in 2015, gravitational waves were first observed by the LIGO detectors in the USA from the merger of two black holes. The Nobel-prize winning direct detection of gravitational waves opened another window through which astronomers can observe the violent Universe.*

Last compilation: July 5, 2020

* * *

1

Relativistic kinematics in a nutshell

1.1 Lorentz transformations

The special theory of relativity, proposed by Einstein in 1905, involves transformations between inertial frames (IFs) of reference. The famous Lorentz transformations come from these two assumptions:

i) The transformations should be linear, agreeing with the Galilean transformations in the non-relativistic limit. This is to ensure that the laws describing the evolution of the physical systems shall be independent on the chosen reference frame;

ii) The light propagates (in vacuum) at the same velocity in each inertial frame, regardless of the state of motion of the emitting source with respect to the chosen frame, as observed in numerous experiments.

These directly implies that the form and value of the *line element*

$$\mathrm{ds}^2 = -\mathrm{cdt}^2 + \mathrm{dx}^2 + \mathrm{dy}^2 + \mathrm{dz}^2$$

is a Lorentz invariant.

Let us consider two reference frames in rectilinear uniform relative motion $\mathrm{S}(t, x, y, z)$ and $\mathrm{S}'(t', x', y', z')$: we choose the axes as represented in Fig.(1.1). The frame S' moves relative to S with speed v, in the direction of the x-axis, and event is described by the four-vector of the coordinates $(c, \mathbf{r})$. Its components in the two frames are linked by the Lorentz transformations:

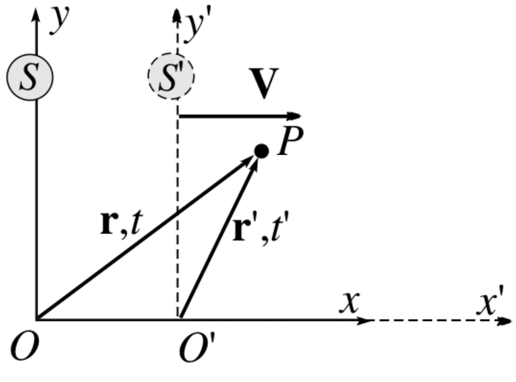

Figure 1.1: Two reference frames in rectilinear relative motion.

$$t' = \gamma(t - vx/c^2) \qquad x' = \gamma(x - vt) \qquad y' = y \qquad z' = z$$

where $\gamma = (1 - v^2/c^2)^{-1/2}$ is the so called Lorentz factor. The above transformation also makes the velocity of light invariant:

$$x'^2 + y'^2 + z'^2 - c^2t'^2 = x^2 + y^2 + z^2 - c^2t^2 = 0$$

It can be easily seen that when $v \to 0$ the Lorentz transformations tend to the Galileian ones of Newtonian physics: $\gamma \to 1$, $x' = x - vt$, $t' = t$.

According to these transformations, distances in the x-direction as measured in the frame S$'$ appear contracted with respect to a measure from S, while time intervals appear dilated. Let us suppose that an event happens at a fixed location in S$'$: then the Lorentz transformations for a finite time interval Δt is

$$\Delta t = \gamma \Delta t' \qquad \text{with} \quad \Delta x' = 0,$$

i.e. the time interval of the event in S$'$, as measured by an observer in S, will result larger than $Deltat'$ (and the non inertial measurer will have a dilated time). For an object in motion, then, a finite lenght L measured by the rest observer will be contracted too:

$$L = L'/\gamma \qquad \text{with} \quad \Delta t' = 0.$$

These are the well known phenomena of the *Lenghts contraction* and *Time dilation.*

Exercise 1.1. Can we observe muons at Earth?

We will largely cover the issue of the cosmic rays showers of secondary particle products, but let's investigate on a simple (not quite obvious) relativistic kinematics problem. Nowadays there is a direct experimental confirmation of the observation of muons produced by cosmic rays from interaction with the Earth's atmosphere.

Let us take as a fact that muons are produced around 10-15 km up by the decay of pions, with a lifetime of $\tau_\pi \simeq 2.6 \times 10^{-8}$ s. The muons themselves are unstable and they decay after $\tau_\mu \simeq 2.2 \times 10^{-6}$ s. The situation is pictorially shown in Fig.(1.2).

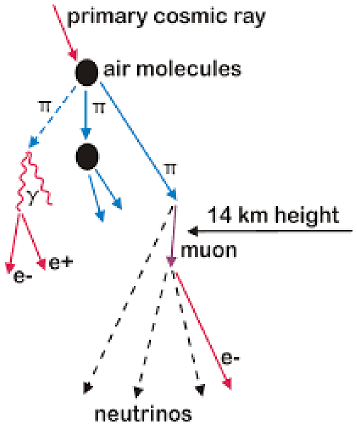

Figure 1.2: Pictorial representation of the cosmic rays shower.

We shall also assume these particles to be relativistic, with $v \simeq c$. A Newtonian thinker might then be tempted to say that the distance the muons cover in their lifetime is given by

$$l_\mu = c\tau_\mu \simeq 600\,\text{m},$$

with the same holding for the pions

$$l_\pi = c\tau_\pi \simeq 6\,\mathrm{m}.$$

Obviously something is wrong: we did not account for time dilation. Taking a typical energy value (out of an entire spectrum) of a μ particle, i.e. $E_\mu \simeq 10\,\mathrm{GeV}$, we can easily get the Lorentz factor and a correct relativistic estimate for the lifetime of a muon, as measured by us (Earth is approximately inertial in this example):

$$\gamma = \frac{E_\mu}{m_\mu c^2} \simeq 100 \qquad \Rightarrow \qquad t = \gamma\tau_\mu = 100 \times 2.2 \times 10^{-6}\ s$$

where we shall remember that $m_\mu \simeq 105\ \mathrm{MeV/c^2} \simeq 207\, m_e$. The time appears now clearly enough for them to reach the ground, given their production height, since $l_\mu = ct \simeq 60$ km. Alternatively we can say that, for a comoving (with the muons) observer, the distance that needs to be covered by them becomes smaller:

$$L = \frac{L'}{\gamma} \simeq \frac{10\ \mathrm{km}}{100} = 100\,\mathrm{m}.$$

For the pions, on the other hand, we will have $l_\pi = \gamma\tau_\pi c \simeq 800\,\mathrm{m}$, with $t = \gamma\tau_\pi = 100 \times 2.6 \times 10^{-8}\ s$. Indeed, pions are very rare at ground.

1.2 Invariant Mass

Let us consider a system of N particles, each with energy E_k and tridimensional momentum $\vec{p}_k$. Their 4-momenta shall be $p_k = (E_k/c, \vec{p}_k)$, and so the total 4-momentum of the system is given by

$$p_{\mathrm{tot}} = \sum_{k=1}^{N} p_k = \left(\frac{E_{\mathrm{tot}}}{c}\,,\, \vec{p}_{\mathrm{tot}}\right) = \left(\sum_k \frac{E_k}{c}\,,\, \sum_k \vec{p}_k\right)$$

The Minkowskian scalar product between a pair of momenta is immediately given by

$$p_1 \cdot p_2 = \frac{E_1 E_2}{c^2} - \vec{p}_1 \cdot \vec{p}_2$$

where we are using the mostly minus signature, and by definition this quantity is a Lorentz invariant. The mass m of the system can be written considering the on-shell condition connecting the total energy E_{tot} and the total momentum p_{tot}, i.e.

$$E_{\mathrm{tot}}^2 = |\vec{p}_{\mathrm{tot}}|^2 c^2 + m^2 c^4 \qquad \Rightarrow \qquad mc^2 = \sqrt{E_{\mathrm{tot}}^2 - |\vec{p}_{\mathrm{tot}}|^2 c^2},$$

which is clearly another Lorentz invariant. The *invariant mass* s is then defined by the following relation

$$\sqrt{s} \equiv \sqrt{p_{\mathrm{tot}}^2 c^2} = \sqrt{\left(\sum_k E_k\right)^2 - \left|\sum_k \vec{p}_k\right|^2 c^2}\,, \tag{1.1}$$

and, in natural units, s is nothing but the square of the mass. Notice that the invariant mass has the dimensions of a energy, and also that it cannot be negative: $s \geqslant 0$.
Considering the center of mass frame (COM), that is the one in which the total 3-momentum $\vec{p}_{\mathrm{tot}}$ is zero, we have

$$\sum_k \vec{p}_k^{\,*} = 0 \qquad \Rightarrow \qquad \sqrt{s} = \sum_k E_k^* = E_{\mathrm{tot}}^*,$$

where the starred quantities are evaluated in the COM. The result is that the invariant mass of a system of particles is also its energy in the COM frame.

Example: Fixed target experiment A particle of mass m_1, energy E_1 and 3-momentum $\vec{p_1}$ is moving against a fixed macroscopic target of mass m_2, which shall be at rest in our choice of coordinates. The momenta are $p_1 = (E_1/c,\, \vec{p_1})$ and $p_2 = (m_2 c,\, \vec{0})$, and so the total momentum is then

$$p_{\text{tot}} = \left(\frac{E_1}{c} + m_2 c \,,\, \vec{p_1} \right) ,$$

leading to an invariant mass of the system of

$$\sqrt{s} = \sqrt{(E_1 + m_2 c^2)^2 - |\vec{p_1}|^2 c^2} = \sqrt{m_1^2 c^4 + |\vec{p_1}|^2 c^2 + m_2 c^4 + 2 m_2 c^2 E_1 - |\vec{p_1}|^2 c^2} = \qquad (1.2)$$

$$= \sqrt{m_1^2 c^4 + m_2^2 c^4 + 2 E_1 m_2 c^2} \,.$$

Example: Two colliding particles Considering two particles of masses m_1, m_2, energies E_1, E_2 and 3-momenta $\vec{p_1}, \vec{p_2}$ moving against each other with an arbitrary direction univoquely defined by the scattering angle θ (see Fig.(1.3)), the four momenta are $p_1 = (E_1/c,\, \vec{p_1})$ and $p_2 = (E_2/c,\, \vec{p_2})$ and these trivially lead to the invariant mass

$$\sqrt{s} = \sqrt{(E_1 + E_2)^2 - |\vec{p_1} + \vec{p_2}|^2 c^2} =$$

$$= \sqrt{m_1^2 c^4 + m_2^2 c^4 + 2 \left(E_1 E_2 - |\vec{p_1}||\vec{p_2}| c^2 \cos\theta \right)} \,, \qquad (1.3)$$

where in the second equality we have used the on-shell condition for each particle $E_i^2 = m_i^2 c^4 + |\vec{p_i}|^2 c^2$. For a head-on collision, in which $\theta = \pi$ and consequently $\cos\theta = -1$, we obtain

$$\sqrt{s} = \sqrt{m_1^2 c^4 + m_2^2 c^4 + 2 \left(E_1 E_2 + |\vec{p_1}||\vec{p_2}| c^2 \right)} \,,$$

and if particles are relativistic, $E_i \simeq \vec{p_i} c$, an approximate form reads

$$\sqrt{s} \simeq 2 \sqrt{E_1 E_2} \,. \qquad (1.4)$$

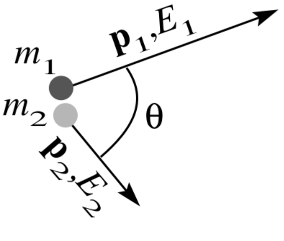

Figure 1.3: System of two non-interacting particles.

Exercise 1.2. LHC and cosmic rays energies

We know that the flux of cosmic rays decreases approximately as a powerlaw with the energy, with a sort of knee (tendency change) around $E \sim 10^{15}$ eV and an ankle at energies of $E \sim 10^{19}$ eV, the latter maybe due to extragalactic sources dominating the galactic ones. The actual state of art is depicted in Fig.(1.4): the small arrow labelled as "LHC" is obviously refering to the Large Hadron Collider and separates the lower, directly measurable, energies from the higher yet to be explored ones. We can actually confirm this with this simple exercise, knowing that the LHC is able to accelerate protons up to $E_{\text{LHC}} = 7$ TeV in the accelerator's rest frame.

i) *Find the center of mass energy* E^*_{tot} *of two protons colliding head-on.*

Since LHC accelerates the particles to energies of $E_{\text{LHC}} \simeq 7$ TeV, they can be safely considered fully relativistic ($m_p c^2 \ll E_{\text{LHC}}$), so E^*_{tot}, or equivalently $\sqrt{s}$, is obtained by

$$E_1 \sim E_2 \sim E_{\text{LHC}} \qquad \Rightarrow \qquad \sqrt{s} = 2E_{\text{LHC}} = 14 \text{ TeV},$$

where we have used Eq.(1.4).

ii) *What energy, in the Earth rest frame, of a cosmic ray proton is required to result into the same center of mass energy, when hitting a stationary proton* m_p *in the atmosphere?*

The 4-momenta are $p_1 = (E_1/c, \vec{p}_1)$ and $p_p = (m_p c, \vec{0})$, so using Eq.(1.2) the invariant mass reads

$$\sqrt{s} = \sqrt{2m_p^2 c^4 + 2E_1 m_p c^2},$$

which can be easily solved for the proton energy E_1 giving:

$$E_1 = \frac{s - 2m_p^2 c^4}{2m_p c^2} \simeq \frac{s}{2m_p c^2} \simeq 10^{17} \text{ eV},$$

where the approximation holds for the clearly ultrarelativistic incident particle. Indeed the most powerful accelerator at ground can achieve these kind of energies, probing with experiments up to 10^{17} eV, but still higher energies can be achieved only by cosmic rays.

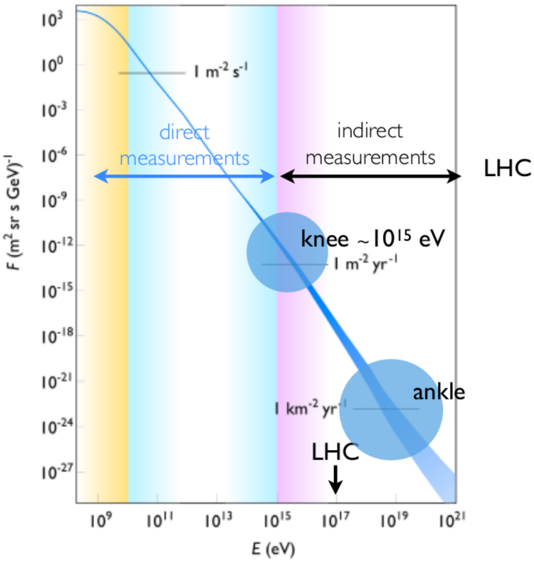

Figure 1.4: Cosmic rays flux as a function of energy.

2

Interactions of astroparticles

Astroparticles can be both charged and neutral, and different interaction mechanisms shall be involved for the various kinds of messengers. In this chapter we will then introduce the interactions of astroparticles, but first an overlook on basic tools to describe the interactions of particles in general is needed. In particular, we need to characterize the cross section, the interaction probability and the mean free path of a particle for a given process, as well as the range, since the understanding of these will play a fundamental role when we will discuss detectors and techniques.

2.1 Interactions of particles

2.1.1 The cross section

The cross section is a quantity which provides a measure of the probability for a reaction to occur; it is referred to as *partial* if we are considering a specific process, *total* when taking into account any possible reaction.
Let's consider a beam of particles incident against a single target of unit area dA, as depicted in Fig.(2.1).

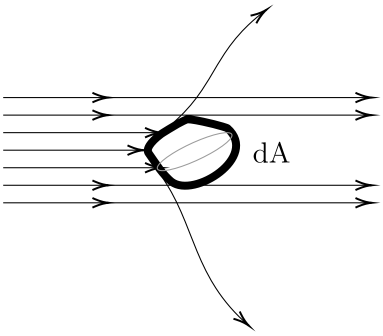

Figure 2.1: Interaction of a particle beam with a single object target. Lines represent different particles in the beam.

We assume that the beam is much broader than the target and that the particles in the beam are uniform in space and time. Let F be the flux of incident particles, i.e. the number of particles per unit time and per unit area dA, and dΩ shall be the infinitesimal solid angle of scatter (in any process, not a particular one).
We want to compute the number dN_s of particles scattered into the solid angle dΩ per unit time: being this process intrinsically stochastic, this number will fluctuate between different

measurements. However, if we average this number over many different observing periods, we can define an averaged quantity

$$\left\langle \frac{\mathrm{dN}_s}{\mathrm{d}\Omega} \right\rangle \qquad \text{with} \quad [N_s] = \mathrm{s}^{-1} \, .$$

For simplicity we will omit further on the average symbol, but it shall be clear that the cross section is an averaged physical quantity, calculated upon a large statistics of experimental results. The **differential cross section** is then defined as

$$\frac{\mathrm{d}\sigma}{\mathrm{d}\Omega}\left(E,\Omega\right) = \frac{1}{F}\frac{\mathrm{dN}_s}{\mathrm{d}\Omega} \, , \tag{2.1}$$

that is the average number of particles scattered per unit solid angle, normalized with the flux. It is in general a function of energy E and of the outgoing particle's direction Ω. This quantity is important since, in practice, detectors often cover only a given angular region. The total cross section for any scattering at a given fixed energy is

$$\sigma\left(E\right) = \int_{4\pi} \frac{\mathrm{d}\sigma}{\mathrm{d}\Omega} \mathrm{d}\Omega = \int_0^{2\pi} \int_{-1}^{1} \frac{\mathrm{d}\sigma\left(\theta,\phi\right)}{\mathrm{d}\Omega} \, \mathrm{d}(\cos\theta) \, \mathrm{d}\phi \, . \tag{2.2}$$

2.1.2 The scattering probability

In all experiments we typically have to deal with a given *slab* of material containing many scattering centers, see Fig.(2.2) for a visualization, and we are interested in estimating the number of scatters that happen on average. First we characterize the number of scattering centers that our beam of particles will encounter, supposing that these centers are uniformly distributed and that the slab of material is not too thick. The latter assumption is equal to suppose that the probability for any scattering center to shadow its neighbour is negligible. Calling δx the thickness of the material along the direction of the beam, the number of scattering centers per unit orthogonal area dA is

$$\mathrm{N}\delta x \qquad \text{with} \quad \mathrm{N} = \text{number density}, \ [\mathrm{N}] = \mathrm{cm}^{-3}.$$

Let's assume now a broad beam with a total target area A orthogonal to the beam: the number of particles that can interact, per unit time, with it is given by FA, and the average number of particles scattered per unit time and in the solid angle dΩ is

$$\frac{\mathrm{dN}_s}{\mathrm{d}\Omega}\left(E,\Omega\right) = F\mathrm{A}\cdot\mathrm{N}\delta x\cdot\frac{\mathrm{d}\sigma}{\mathrm{d}\Omega}\left(E,\Omega\right).$$

Thus the total number N_s of scattered particles in *any* direction per unit time is

$$\mathrm{N}_s\left(E\right) = F\mathrm{A}\cdot\mathrm{N}\delta x\cdot\sigma\left(E\right).$$

If we divide this number for FA we get the probability for the scattering of a single particle in thickness δx, $\mathrm{P}_{\text{int}}\left(\delta x\right)$:

$$\mathrm{P}_{\text{int}}\left(\delta x\right) = \frac{\mathrm{N}_s}{F\mathrm{A}} = \mathrm{N}\delta x \, \sigma\left(E\right).$$

In this simplified model we are neglecting the interactions between the scattered particles as well as the interactions between beam particles, the binding energies of the target components, the absorption, and the possible multiple scatterings of the beam within the target.

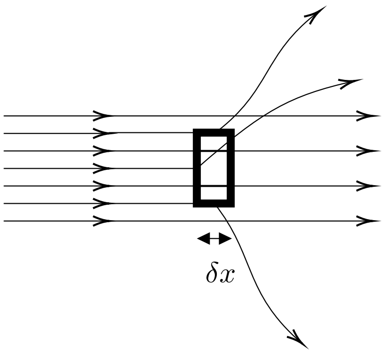

Figure 2.2: Interaction of a particle beam with a target composed of many sub-targets.

2.1.3 The mean free path

The mean free path is namely the mean distance particles can travel without having an interaction or suffering a collision.
Let's start from the probability $\mathrm{P}\left(x\right)$ of not to interact with the target, i.e. the probability of having survived over the distance x. It is reasonable to expect that the probability of not to interact within the infinitesimal thickness $(x, x + \mathrm{d}x)$ shall be given by the product of $\mathrm{P}\left(x\right)$ and the probability to survive further on a thickness δx:

$$\mathrm{P}\left(x, x+\mathrm{d}x\right) = \mathrm{P}\left(x\right)\mathrm{P}\left(\delta x\right) = \mathrm{P}\left(x\right)\left(1-\omega \mathrm{d}x\right) \qquad \Leftrightarrow$$

$$\mathrm{P}\left(x\right) + \frac{\partial \mathrm{P}}{\partial x}\mathrm{d}x = \mathrm{P}\left(x\right) - \omega \mathrm{P}\left(x\right)\mathrm{d}x \;,$$

where ω is a constant which quantifies the probability of an interaction in δx, that is $\mathrm{P}_{\text{int}}\left(\delta x\right) = \omega\delta x$, and in the second line we have made an expansion justified by the smallness of the infinitesimal thickness $(x, x + \mathrm{d}x)$. This allows us to obtain a differential equation for P

$$\mathrm{dP} = -\omega \mathrm{P}\left(x\right)\mathrm{d}x \;,$$

which easily integrates to give

$$\mathrm{P}\left(x\right) = e^{-\int_0^x \omega\, \mathrm{d}x} \qquad\qquad \text{with} \quad \mathrm{P}\left(0\right) = 1 \;,$$

an exponentially decreasing solution with increasing distance. The probability $\mathrm{P}_{\text{int}}\left(x\right)$ of having an interaction within the distance x shall be then given by

$$\mathrm{P}_{\text{int}}\left(x\right) = 1 - e^{-\int_0^x \omega\, \mathrm{d}x} \;. \tag{2.3}$$

The mean free path shall be given by definition by

$$\lambda \equiv \frac{\int_0^{+\infty} x\mathrm{P}\left(x\right)\, \mathrm{d}x}{\int_0^{+\infty} \mathrm{P}\left(x\right)\, \mathrm{d}x} \;,$$

and it is clear that this quantity must be related to the cross section and also to the density of the scattering centers, because it must depend upon the nature of the interaction we are considering, but also on the property of the material in which the particle is propagating. Noticing that we have supposed ω to be a constant and expanding the integral, one can also easily find:

$$\frac{\int_0^{+\infty} x\mathrm{P}\left(x\right)\, \mathrm{d}x}{\int_0^{+\infty} \mathrm{P}\left(x\right)\, \mathrm{d}x} = \frac{1}{\omega}\frac{\int_0^{+\infty} e^{-\omega x}\, \mathrm{d}x}{\int_0^{+\infty} e^{-\omega x}\, \mathrm{d}x} = \frac{1}{\omega} \qquad \Rightarrow \qquad \lambda = \frac{1}{\omega} \;,$$

where in the second equality we have simply exploited the integration by parts rule.
Recalling that in the previous section we were able to write

$$\mathrm{P_{int}}\left(\delta x\right) = \mathrm{N}\sigma\,\delta x\ ,$$

we are in the position to better characterize λ making use of the just found probability expression (Eq.(2.3))

$$\mathrm{P_{int}}\left(\delta x\right) = 1 - e^{-\omega\delta x} \approx 1 - \left(1 - \frac{\delta x}{\lambda}\right) = \frac{\delta x}{\lambda}\ , \tag{2.4}$$

so comparing the two expressions for $\mathrm{P_{int}}$ we can obtain

$$\mathrm{N}\sigma\,\delta x = \frac{\delta x}{\lambda} \qquad \Rightarrow \qquad \lambda = \frac{1}{\mathrm{N}\sigma} = \frac{\omega_a}{\rho\mathcal{N}_a\sigma}\ ,$$

where we have noted that the number density of our scattering centers N can be written in terms of the Avogadro number $\mathcal{N}_a = 1/m_{\mathrm{H}}$ and the mean atomic (or molecular) weight for our material ω_a as follows

$$\mathrm{N} = \frac{\mathcal{N}_a\rho}{\omega_a} \qquad \text{with} \quad \mathcal{N}_a = 6.022\times 10^{-27}\ \mathrm{mol^{-1}}\ . \tag{2.5}$$

This expression of λ can be also called **interaction lenght**, which has the meaning of the average distance required to be traversed in the material by a projectile particle for a given interaction to happen, and has obviously the dimension of a lenght, $[\lambda] = \mathrm{cm}$.
If you are dealing with a beam of particles crossing matter, the number of interactions happening will affect the beam itself with a reduction of its intensity. The relative attenuation in the number of particles $\mathcal{N}$ when crossing a thickness Δx shall be given by

$$\frac{\Delta\mathcal{N}}{\mathcal{N}} = \mathrm{P_{int}}\left(\Delta x\right) = \left(\mathcal{N}_a\frac{\rho}{\omega_a}\Delta x\right)\sigma\ ,$$

and since we can express the factor in round brackets in terms of the interaction lenght you immediately find that the variation of the particles density in the beam along their path is related to λ with

$$\frac{\mathrm{d}\mathcal{N}}{\mathrm{d}x} = -\frac{1}{\lambda}\mathcal{N}\ ,$$

where we have subsituted the macroscopic thickness Δx with an infinitesimal distance δx.
Thus, as particles propagate, their number density is attenuated exponentially with the distance:

$$\mathcal{N} = \mathcal{N}_0 \exp\left\{-\frac{x}{\lambda}\right\} \qquad \text{with} \quad \mathcal{N}(0) = \mathcal{N}_0\ .$$

In cosmic rays physics we shall use very often another quantity instead of the interaction lenght λ, that is its product with the density ρ of the target matter:

$$\lambda' \equiv \rho\lambda = \frac{\omega_a}{\sigma\mathcal{N}_a} \qquad \text{with} \quad \left[\lambda'\right] = \mathrm{g\,cm^{-2}}\ . \tag{2.6}$$

The reason why we do that is, when we will encounter cosmic rays propagating e.g. in the atmosphere, the density of the target often changes as the beam propagates, since we are usually not dealing with uniform materials. So the relevant quantity can't depend on it, as we want it to be constant. The total amount of matter which has been traversed is in fact better expressed using this newly defined interaction lenght, which has the dimensions of a surface density.

NB Indeed all the quantities can be defined specifying a particular interaction or simply generalizing to all of the possible reactions, since this choice results in a definition of σ as the total or the partial cross section.

Obviously λ' will depend on the particular interaction, and we will encounter many of them. A fundamental distinction is between *elastic* and *inelastic* processes. The first term holds for processes in which the total kinetic energy is preserved and, as a matter of fact, the particles remains the same and exchange energy and momentum, which will happen usually when the energies are not enough for a production of new particles; the second could often be the case for interactions of astroparticles, with production of new particles.

2.1.4 The range

The range $\langle R(E)\rangle$ of a particle is defined as the average distance traversed in a medium (namely, a detector) by a particle before being absorbed or, equivalently, before decaying. Obviously it shall be a function of the energy of the particle, $R = R(E)$, and it is a stochastic quantity, even though for simplicity we shall frequently drop the average symbol. With a brute-force approximation, the range shall be calculated as

$$R(E) \simeq \int_{E}^{mc^2} \frac{1}{\langle \mathrm{d}E/\mathrm{d}x\rangle}\,\mathrm{d}E\,, \tag{2.7}$$

where $\langle \mathrm{d}E/\mathrm{d}x\rangle$ is the mean specific energy loss of the particle, which will be characterized in detail later by specifying the various mechanism of losses for charged and neutral particles. R is a very important quantity which is measured for lots of different materials and for several incident particles, being a carrier of informations about:

i) Detector design: a certain range might imply a minimum size for the detection of the particle of interest;

ii) Particle identity (PID): different particles show very peculiar behavior and ranges.

Let us stress that Eq.(2.7) is an approximation: the fact that charged particles are actually deflected (see Sec.(2.3)) in their trajectory during their travel through a medium leads to an underestimate of the range as given simply by that expression.

2.2 Interactions of Astroparticles

In astroparticle physics we can distinguish the physical effects of the interactions into three main cathegories, based on their action's enviroment:

i) **Astrophysical enviroments**: we have to investigate processes that influence primary particles in astrophysical enviroments, e.g. on very large scales we are concerned with sources emitting astroparticles (photons, neutrinos or cosmic rays). Charged particles will be definitely deflected by the permeating magnetic fields in the (intra)galaxy medium, which is also made of matter and photons interacting and modifying cosmic rays before they arrive at Earth;

ii) **Earth's atmosphere**: definitely a lot of different phenomena will happen when these particles arrive at the Earth's atmosphere. The atmosphere is indeed opaque in some range of wavelenght, as depicted in Fig.(2.3) and Fig.(2.4).

iii) **Particle detectors**: we need the astroparticles to interact in some way such that they can be observed, hence we need to characterize the physics of particle detectors.

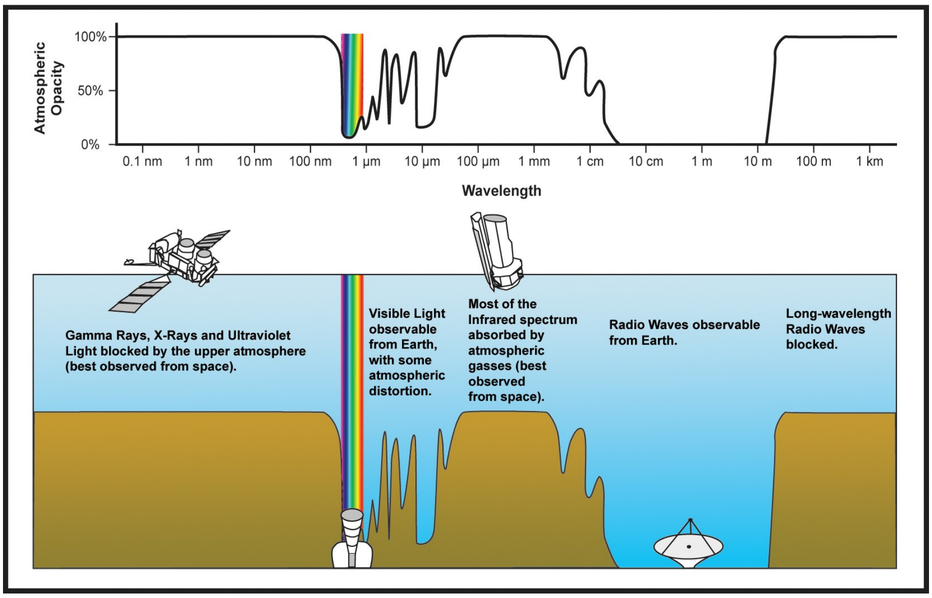

Figure 2.3: Atmospheric transparency (or opacity) to photons as a function of photon wavelenght: the rainbow depicts the range of the visible light, 400 nm – 700 nm. At very high energy, X-rays or gamma, the atmosphere is very opaque, while in the optical the opacity drops. Indeed astronomy has been performed in the optical over all the mankind the history! On the other hand, near the IR regime, the opacity is rising again, and the IR astronomy has to be performed with satellites, namely instruments beyond the Earth's atmosphere and collect the signal. Radio waves finally can traverse the atmosphere, making radio-astronomy again easier and natural.

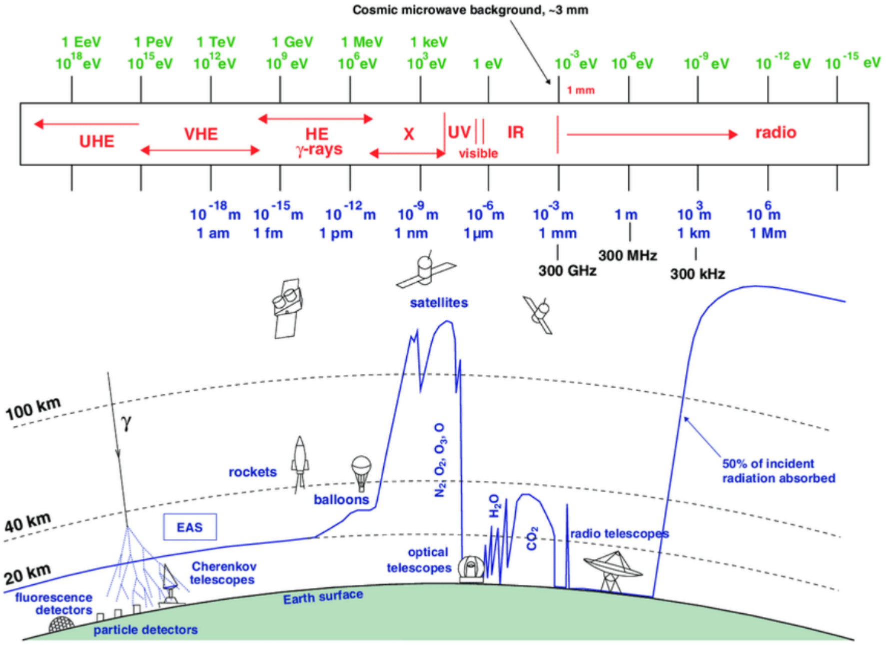

Figure 2.4: Typical atmospheric depht from the top of the atmosphere towards ground on which different photons will be absorbed: e.g., gamma rays typically will interact at a height of 20 km by orders of magnitude estimates

The astroparticle messengers that we will have to deal with can be essentially divided into three cathegories, neglecting for the moment the gravitational waves which are indeed another source of informations:

1) Nuclei, i.e. protons or heavier nuclei, they are the cosmic rays;
2) Photons;
3) Neutrinos.

For all of these classes we can safely neglect the gravitational interaction, since indeed all the other interactions are much stronger for our application. Clearly the interactions which will be involved are quite different: the nuclei are involved in strong, electromagnetic and weak interactions too, photon just have to deal with electromagnetic ones and neutrinos only with the weak ones.

2.2.1 Hadronic interactions

Let us start with nuclei, protons in particular, for which the strong interaction is the dominant process. The typical cross section σ_{pp} for the inelastic proton proton interaction is approximately given by

$$\sigma_{pp} = \pi r_0^2 = 45\,\mathrm{mb} \qquad \text{with} \quad 1\,\mathrm{mb} = 10^{-27}\,\mathrm{cm}^2\,,$$

for a typical value for $E_p = 100\,\mathrm{GeV}$, but of course this cross section is a function of energy. Also r_0 is a fundamental constant close to the charge radius of the proton $\mathrm{r}_p = 0.85\times10^{-13}\mathrm{cm}$. In cosmic rays physics we are usually interested in another kind of quantity, the proton-air cross section $\sigma_{p,\mathrm{air}}$, which quantifies the probability for a cosmic ray proton to interact with an air molecule as it reaches the atmosphere. The Pierre Auger observatory has successfully measured this cross section[1], and Fig.(2.5) shows the result.

We can calculate the interaction lenght, considering the air as made by nitrogen with mass number $\mathrm{A}_{\mathrm{atm}} = 14.5$, taking as $\sigma_{p,\mathrm{air}} \simeq 260\,\mathrm{mb}$ for $E_p = 100\,\mathrm{GeV}$:

$$\lambda' = \frac{\mathrm{A}_{\mathrm{atm}}}{\mathcal{N}_a \sigma_{p,\mathrm{air}}} \approx 93\,\mathrm{g\,cm}^{-2},$$

which shall be compared with the typical integrated density that cosmic rays protons will encounter in the Earth atmosphere. The so called atmospheric depht changes with height, and it is typically an order of magnitude higher than λ'. The effective interaction lenght then is much smaller than the density-normalized depht that cosmic rays will encounter in their propagation through the entire atmosphere: cosmic rays have no decent probability to arrive at ground, they will surely interact with the atmosphere, and we definitely shall have to describe these interactions.

NB At colliding experiments we measure a cross section which is considerably different from $\sigma_{p,\mathrm{air}}$, much more similar to σ_{pp}. So in many works on cosmic rays, like the one already mentioned, you will find an estimate of the proton-proton cross section derived from $\sigma_{p,\mathrm{air}}$ with a sort of conversion model, to some degree quite complex and involving nuclear physics. We can however make an order of magnitude estimate to have an idea, with a very simple model.
We will assume an independent on energy cross section (good approximation if one takes

---

[1] `https://arxiv.org/abs/1208.1520v2`. The Pierre Auger observatory is an international experiment located in Argentina and covering an area of $\approx 3000\ \mathrm{km}^2$. It is designed and operated to detect the so called Ultra High Energy (UHE) cosmic rays at $E > 10^{18}$ eV.

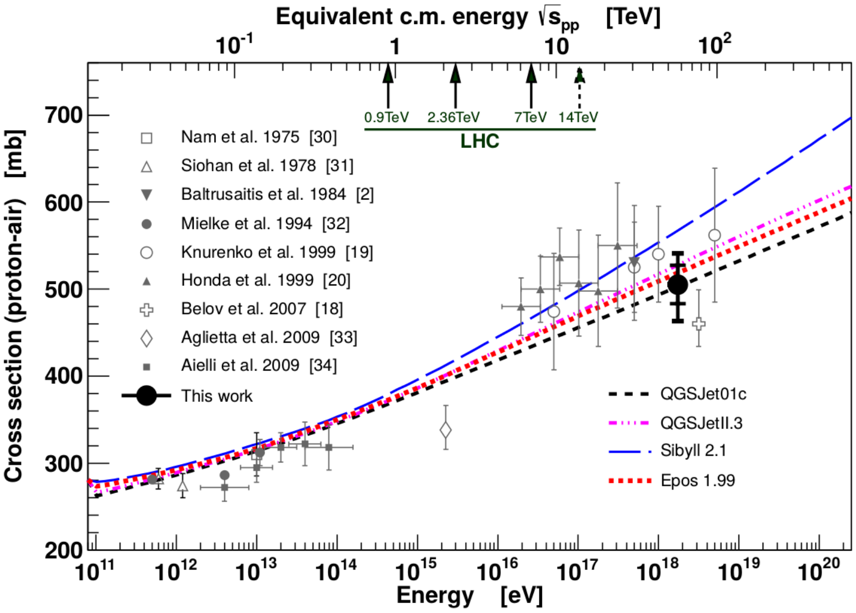

Figure 2.5: Measurement of the proton-air cross section $\sigma_{p,\mathrm{air}}$ at $\sqrt{s} = 57$ TeV equivalent energy with the Pierre Auger Observatory. The cross section is expressed in mb as a function of energy, and there is a compilation of different models applied on colliders data. The big black bullet referred as "this work" is a measurement performed using results from cosmic rays. The cross section changes appreciably with energy, and ranges from about 250 mb to a factor of two higher, reaching center of mass energies well beyond the LHC typical ones.

into account that the range of energies is huge and the increasing is quite slow), i.e. the geometrical cross section:

$$\sigma = \pi \mathrm{R}^2 \qquad \text{with} \qquad \mathrm{R} = \mathrm{R}_p + \mathrm{R}_t \,,$$

in which R_p is the radius of the projectile and R_t is the one of the target, which is a particle in the atmosphere, with a dependence on the atomic mass number given by the Fermi nuclear model

$$\mathrm{R}_t = \mathrm{r}_0 \mathrm{A}^{1/3} \qquad \text{with} \qquad \mathrm{r}_0 = 1.2 \times 10^{-13}\,\mathrm{cm}\,.$$

This simple model allows us to convert the proton-air cross section into the proton-proton cross section, to compare it with the colliders experiments, by means of the following:

$$\sigma \simeq \pi \left(\mathrm{r}_0 \mathrm{A}^{1/3}\right)^2 = \sigma_{pp} \mathrm{A}^{2/3} \,, \tag{2.8}$$

that is the cross section for a proton in a medium with mass number A can be written in terms of σ_{pp}. This kind of conversion is performed in the Pierre Auger work above mentioned, where the estimates of σ_{pp} of colliders and models are compared too, and the value of $\sigma_{pp} = 45$ mb for typical energies of $E_p = 100$ GeV can be confirmed.

2.2.2 Photons interactions

The interactions we are dealing with in this case are the electromagnetic ones, and the dominant mechanism at high energies above $E > 1022\,\mathrm{MeV}$ is the pair production. The pair production process is represented by

$$\gamma + N \rightarrow e^+ + e^- + N \,,$$

where N stands for a generic nucleus. The typical interaction lenght for pair production λ_γ, clearly defined as the length that attenuates the intensity of a photon beam to $1/e$ of its initial value, is related to the radiation lenght x_0 of electrons in air by the following

$$\lambda_\gamma = \frac{9}{7}\,\mathrm{x}_0 \approx\; 47\;\mathrm{g\,cm^{-2}}\,, \tag{2.9}$$

where we have substituted the typical value of the radiation lenght of electrons in air, $\mathrm{x}_0 \approx 36.6\,\mathrm{g\,cm^{-2}}$, for characteristic values of energy $E_\gamma \approx 10\,\mathrm{GeV}$.
The two quantities are intrinsically related because high energy photons and high energy electrons interact with matter with correlated processes, pair production and Bremsstrahlung correspondently, as we shall see in the following. The value of the radiation lenght for electrons is actually defined for Bremsstrahlung in matter. The Feynman diagrams of the two processes are represented in Fig.(2.6). The value shall be compared with the one obtained for λ' for hadronic interactions: the order of magnitude is the same, being again much smaller than the integrated density encountered when crossing the entire Earth's atmosphere, so, very similarly for cosmic rays, the Earth is opaque and the high energy photons are absorbed.

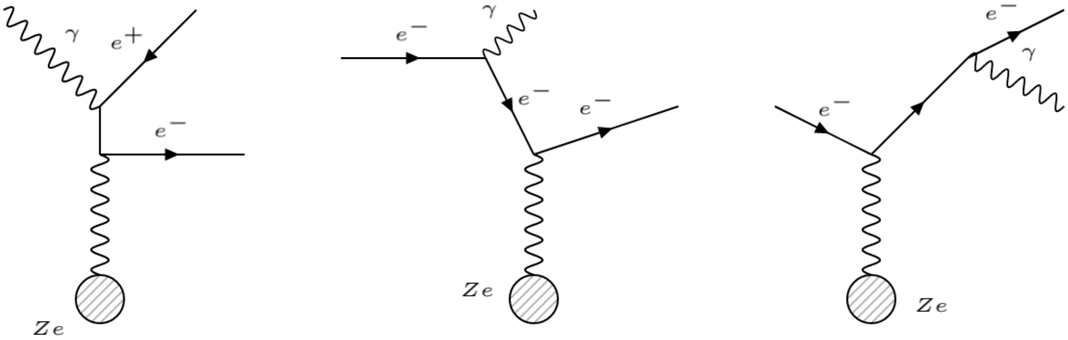

Figure 2.6: Feynman diagrams of Bremsstrahlung processes (i.e. the first two diagram starting from the right) and pair production. Ze is the nucleus whose presence is necessary, as we will see in Sec.(2.2).

A useful tool Suppose that we need to find some (continuously updated) informations about the fundamental quantities introduced by far, e.g. the interaction lenght for a process, or the cross sections. A very useful tool is the Particle Data Group (PDG) site[2]: a lot of different resources are available, but maybe the most interesting regard atomic and nuclear properties, where you can find the radiation lenght for every different material (x_0), as well as the nuclear interaction lenght (λ'). Also mixtures are characterized, not only fundamental materials. To conclude, the site provides also reviews on different topics, mainly cross sections measurements. A useful review can be the one about the passage of particles through matter [3].

2.2.3 Neutrinos

Neutrinos are neutral particles affected by weak interactions only (gravitational effects are negligible). High-energy neutrinos mainly interact with nucleons, being the neutrino-lepton cross section smaller. The cross section σ_ν for interaction with nuclei is approximately a

---

[2] `http://pdg.lbl.gov/`

[3] `http://pdg.lbl.gov/2019/reviews/rpp2019-rev-passage-particles-matter.pdf`

linear function of neutrinos energy E_ν, with a fitting formula such as the following

$$\sigma_\nu \simeq \left(0.67 \times 10^{-38} \, \frac{E_\nu}{\text{GeV}}\right) \, \text{cm}^2/\text{nucleon}$$

within the quite large range of 1 MeV $< E_\nu < \mathcal{O}\,(10\ \text{TeV})$[4]. At energies between 10 TeV $< E_\nu < 10^7$ TeV, a parametrization is

$$\sigma_\nu \simeq \left(0.67 \times 10^{-34} \sqrt{\frac{E_\nu}{10\ \text{TeV}}}\right) \, \text{cm}^2/\text{nucleon}\,.$$

Indeed this number is very small, leading to a tremendously large interaction lenght at 100 GeV, which in the atmosphere can be found to be

$$\lambda' \simeq 2.4 \times 10^{12} \text{ g cm}^{-2}.$$

So the probability for high energy neutrinos to interact with the atmosphere, and actually with the Earth too, is negligible[5], contrary to cosmic rays and photons. A measurement of σ_ν at $E_\nu > 10$ TeV, i.e. multi-TeV energies, is shown in Fig.(2.7). For this reason neutrinos are the ideal cosmic messengers, being able to go through very dense enviroments (e.g. gas clouds) and to carry informations about the most remote astrophysical situations.
Experimentally, the cross section σ_ν has so far been measured up to $E_\nu \sim 400$ GeV, so what is usually done is an extrapolation for the higher energies, since of course astrophysical neutrinos can easily reach and go beyond this limit. Essentially the extrapolations can be the ones written above. So what was known by far at the end of the '90s is depicted in the Fig.(2.8): it is clearly proportional to E_ν at low energies $E_\nu < 1$ TeV and to $E_\nu^{0.4}$ at high energies $E_\nu > 10^6$ GeV. By models, then, it is expected that at some point the σ_ν will saturate or even decrease, however the region in which this drastic change in the behavior starts is still unexplored experimentally.

NB Notice that σ_ν refers to the total cross section, to which both the "charged current" (CC) channel and the "neutral current" (NC) channel contribute. The first are mediated by the weak interactions charged bosons $W^\pm$, the latter by the neutral boson Z^0. The respective processes are the following semileptonic scattering from nucleons:

$$\begin{aligned} &\text{CC} \qquad && \nu_\mu + n \to \mu^- + p \\ &\text{NC} \qquad && \nu_\mu + p \to \nu_\mu + p \end{aligned} \tag{2.10}$$

A brief reminder on conserved quantities:
- Baryonic number B: $B = N(\text{baryons}) - N(\text{antibaryons})$
- Lepton number L: $L = N(\text{leptons}) - N(\text{antileptons})$
- Electric charge Q: $Q(\text{initial state}) = Q(\text{final state})$

The question to answer is how can we detect them? The fundamental requirement is a collimated beam of neutrinos with a known energy to interact with a target and, in particular, we need them to produce charged particles as product of their interaction. Large target areas are then usually necessary. There are three fundamental sources of usable, high energy ($E_\nu > 100$ GeV), neutrinos:

---

[4] Note that the cross section is measured in cm^2: this is because usually it shall be regarded as the approximate geometrical one the beam of neutrinos sees as its target.

[5] Solar neutrinos, which have MeV energies, typically cross the Earth undisturbed.

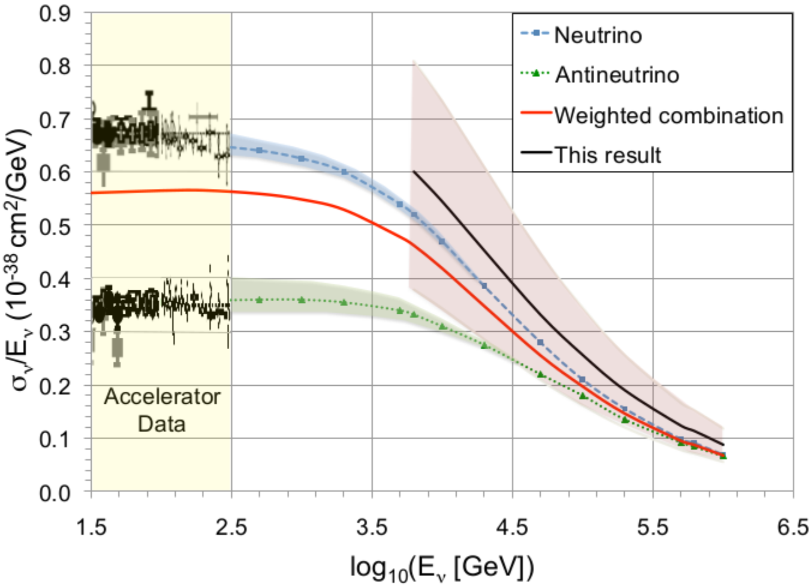

Figure 2.7: Figure lifted from `https://arxiv.org/pdf/1711.08119.pdf`, describing an IceCube work. Compilation of muon neutrino charged current cross section measurements, divided by neutrino energy. The blue and green lines are the Standard Model predictions for ν_μ and $\bar{\nu}_\mu$ respectively, with the uncertainties on the deep inelastic cross sections shown by the shaded bands. The red line is for the expected mixture of ν_μ and $\bar{\nu}_\mu$ in the IceCube sample. The black line shows the article's result, assuming that the charged and neutral current cross sections vary in proportion, and that the ratio between the actual cross section and the Standard Model prediction does not depend on energy. The pink band shows the total 1σ (statistical plus systematic) uncertainty. The cross section rises linearly with energy up to about 3 TeV, but then the increase moderates to roughly as $E_\nu^{0.3}$.

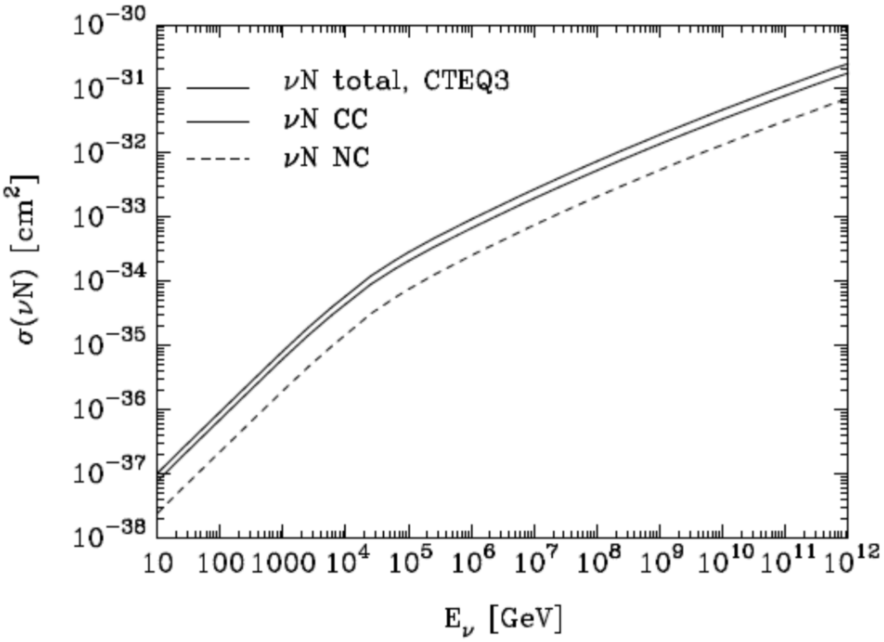

Figure 2.8: Figure lifted from `https://arxiv.org/pdf/1010.2647.pdf`, showing the neutrino–nucleon cross-section as a function of the neutrino energy. Charge-current and neutral-current contributions to the cross-section are shown with thin solid and dashed lines. The total cross-section is presented by a thick solid line.

i) **Nuclear reactors**, i.e. devices used to initiate and control a self-sustained nuclear chain reaction. In particular they can be arranged to produce a well controlled power spectrum of neutrinos;

ii) **Colliders**, which make use of the beam dump[6], producing neutrinos with energies limited by the energy of the primary accelerated beam;

iii) **Atmospheric neutrinos**, produced by the interaction of cosmic rays in the Earth atmosphere.

The latter mechanism is the more important one, and it is pictorially shown in Fig.(2.9). We shall recall that the most important processes of secondary production of neutrinos in atmosphere are the pions' and muons' decays:

$$\begin{aligned} &\pi^- \to \mu^- + \bar{\nu}_\mu \qquad &&\pi^+ \to \mu^+ + \nu_\mu \\ &\mu^- \to e^- + \bar{\nu}_e + \nu_\mu \qquad &&\mu^+ \to e^+ + \nu_e + \bar{\nu}_\mu \, , \end{aligned} \tag{2.11}$$

where the fundamental quantities are explicitly conserved, i.e. leptonic number and electric charge, and the second row are purely leptonic processes. The Feynman diagrams for these processes are shown in Fig.(2.10). Neutrinos are not expected to decay while they travel through the atmosphere, simply because, as what is by now known, they are stable: only lower bounds on their lifetimes are measured [7], and can be very large, such as the following:

$$\tau_\nu > 7 \times 10^9 \, \mathrm{s \, eV^{-1}} \, .$$

However nowadays it is also known that neutrinos are actually massive (at least two of them are NR matter as regards cosmological Ω_{0m} parameter, so at most one is UR), an upper bound on their total mass being

$$\sum_{\mathrm{i}} m_{\nu,\mathrm{i}} < 0.12 \, \mathrm{eV} \, ,$$

according to the PDG review. Being massive, then, they undergo the so called *neutrino oscillation* mechanism, through which they continuously change flavour eigenstates.

In IceCube, we shall expect that neutrinos could come from downwards (from the northern sky till the Earth's south pole) together with muons, while only neutrinos could arrive from upwards (from the southern sky to the underground detector), and a pictorial view is shown in Fig(2.11). It is possible to measure and isolate those atmospheric neutrinos essentially by looking at the tracks of particles which reach the detector from below. In order to exploit this source of neutrinos to measure the cross section, we need to recall that this σ_ν is expected to grow with E_ν, so at a certain point it will become quite likely that also neutrinos propagating through the Earth ("up-going") will be absorbed. So the study of the angular distribution of a large number of neutrinos as a function of energy allows us to make an estimate on the cross section on nuclei, because the up-going beam of neutrinos will be suppressed in comparison with the down-going sample. This is actually the technique described by the work in Fig.(2.7).

---

[6] A charged-particle beam dump consists essentially in a very dense (copper, aluminium, carbon, beryllium, or tungsten) target whose purpose is to safely absorb a beam of charged particles such as electrons, protons, nuclei, or ions. This allows, in high energy limit, the production of secondary particles such as neutrinos.

[7] See `http://pdg.lbl.gov/2019/listings/rpp2019-list-neutrino-prop.pdf` for details on neutrinos properties. Several different results from lots of works are present.

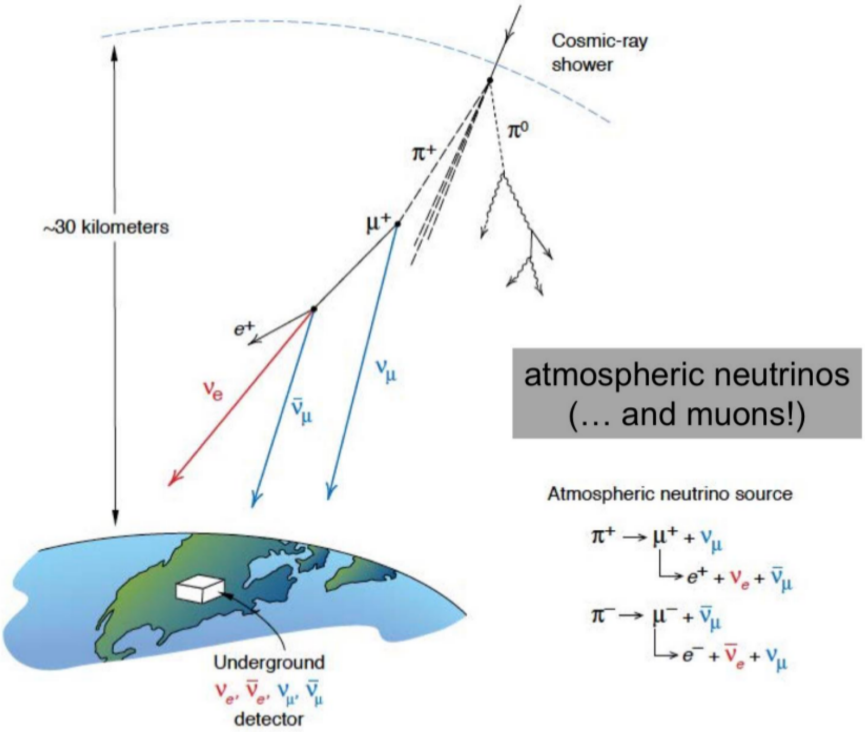

Figure 2.9: Pictorial representation of primary cosmic ray interacting with the Earth atmosphere. The first interactions produce a shower of secondary particles, which can either interact further, contributing to the increase in the number of secondary particles, or decay, if the energy per particle available becomes too low to give rise to further productions. The secondary particle flux is namely a *hadronic shower*, made very abundantly by charged mesons (π^+, π^-) as well as neutral pions π^0. The neutral pions can produce two photons, giving rise to pairs of e^+, e^-, in a generation called *electromagnetic shower*. The charged mesons either further interact or they decay, and their decays are shown in the bottom right corner. Remember that also muons and differently flavoured neutrinos, e.g. ν_μ, ν_e, are produced and will possibly reach the ground. The tau neutrinos, ν_τ and $\bar{\nu}_\tau$, have a negligible probability of being produced by atmosphere, instead. The pions usually don't reach the Earth, while sufficiently energetic muons usually do (see Exercise (1.1)).

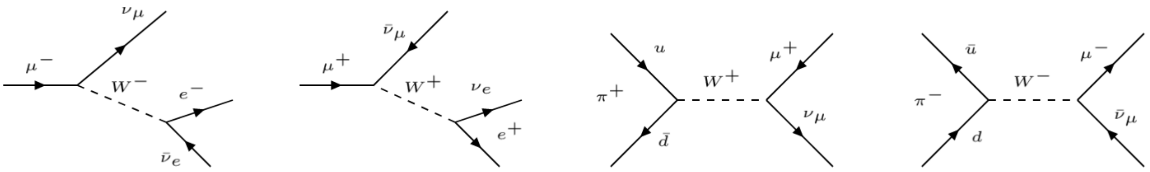

Figure 2.10: Feynman diagrams for the leptonic muon decay and the semileptonic pion decay. Remember that the pions are mesons, that is they are formed by two quarks. In particular $\pi^+ = u\bar{d}$, $\pi^- = \bar{u}d$ and $\pi^0 = u\bar{u}$ or $d\bar{d}$. The charged pions have a lifetime of only 26 ns, while the muon lifetime is 2 μs, much larger than that of the pions. Therefore, the composition of the shower becomes richer and richer in muons while travelling through the atmosphere.

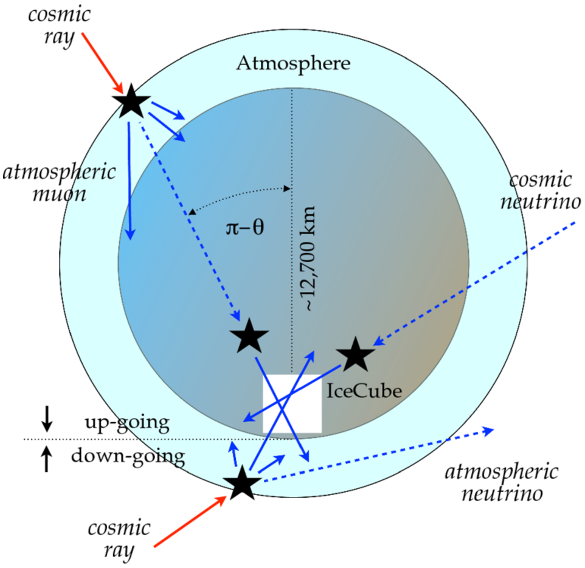

Figure 2.11: Pictorial representation of IceCube detection of neutrinos from all over the sky. Remember that the detector is located at a depht of 1.5 km.

2.3 Particles detection

Let us point out some basic concepts on the passage of radiation (here radiation refers to any ionizing agent) through matter. In fact, when a high energy charged or neutral particle passes through matter, it loses energy that excites and ionizes the molecules of the material, and it is through experimental observation of these alterations of the medium that elementary particles are detected. Let us distinguish between charged and neutral agents.

2.3.1 Charged particles

Charged particles interact basically with atoms, the interaction being mostly electro-magnetic, and they can be affected by two main effects:

1) *Energy loss* due to inelastic collisions with atomic electrons, which translates in an ionization or an excitation of the molecular (atomic) state of the material in the case of the so called "soft" collisions, or even in a powerful energy transfer which promotes the electron to ionizing radiation itself, i.e. δ-rays in "hard" collisions, see Sec(2.3.1.4);

2) *Deflection of trajectory* due to elastic collisions with nuclei, and becomes important with light particles like electrons and positrons.

Also the emission of Cherenkov radiation, nuclear reactions and Bremsstrahlung radiation could possibly happen, being much rarer processes but sometimes useful. Bremsstrahlung in particular affects electrons moving in the Coulomb fields of nuclei.

2.3.1.1 Ionization energy loss

The average energy loss to ionization per unit lenght of charged particles other than electrons is given by the famous **Bethe-Bloch** formula, which has known a lot of (non)relativistic derivations in the history and it is also referred to as "stopping power". The final result is given by

$$\left\langle -\frac{\mathrm{d}E}{\mathrm{d}x} \right\rangle = K\rho \left(\frac{\mathrm{Z}}{\mathrm{A}}\right) \frac{z^2}{\beta^2} \left[\log\left(\frac{2m_e\gamma^2v^2W_{\max}}{\mathrm{I}}\right) - 2\beta^2 - \delta - 2\frac{C}{\mathrm{Z}}\right] , \tag{2.12}$$

where $K \simeq 0.307\,\mathrm{MeV\,cm^2\,g^{-1}}$ is a constant, ρ is the density of the material, z the charge of the incident particle in units of the electron charge, m_e is the electron mass (which is the mass of the hit particle), $W_{\max}$ is the maximum energy which can be transfered to an electron with a single collision, I is an average ionization potential[8]. The latter and the second last of course depend on the material. Lastly, the term proportional to δ is called *density correction*, which becomes important at high energies[9], and the one proportional to C is the *shell correction*, crucial at low energies. Some important values and scales are summarized in Appendix (A).

The behavior is shown in Fig(2.12): the average energy loss per unit density of the medium and unit track lenght is an universal function of $\beta\gamma$ in a very rough approximation, since at high energies the flattenings are quite different for the materials. The choice of the abscissa is very convenient, since by means of this the profile does not depend on the incoming particle. We can underline the fundamental properties of the Bethe-Bloch stopping power:

- All the curves decrease rapidly at small momenta, roughly as $1/\beta^2$ for $\beta\gamma \leq 3-4$, and obviously the stopping power is higher at low energies;
- At $\beta\gamma \sim 3-4$ the curves reach a shallow minimum, and the particles entering the materials at these values of energies are called Minimum Ionizing Particles (MIP);
- From $\beta \geqslant 0.96$ then they increase very slowly with a relativistic rise $\sim \log\left(\beta^2\gamma^2\right)$, so at high energies we can say that they are essentially constant;
- The curves are proportional to Z/A, and for different mixtures or compounds you shall need to account for different molecular weights too.

In practice, most relativistic particles (such as cosmic-ray muons) have mean energy loss rates close to the minimum; they can be considered with good approximation as minimum ionizing particles. The loss from a minimum ionizing particle is well approximated by

$$\left.\left(\frac{1}{\rho}\frac{\mathrm{d}E}{\mathrm{d}x}\right)\right|_{\min} \approx -3.5\left(\frac{\mathrm{Z}}{\mathrm{A}}\right)\ \mathrm{MeV\,cm^2\,g^{-1}}\,. \tag{2.13}$$

Notice also that the Bethe-Bloch formula gives the average energy loss, while the measured quantity is the energy loss for a given lenght, which is a random variable.

The Landau distribution In the approximation of a thin absorber, the fluctuations for $\langle \mathrm{d}E/\mathrm{d}x\rangle$ are very large. The distribution of the stopping power around the most probable value agrees to an asymmetric distribution named from Landau, the theoretician who exploited it firstly. A typical profile is shown in Fig(2.13): the average energy loss per lenght $\langle\Delta E\rangle$, represented by the Bethe formula, is larger than the most probable energy loss, since the Landau distribution has a long tail and the collisions with small energy transfer are usually more probable. The Landau distribution expression is indeed quite complicated and holds only for thin absorbers, from which $\delta-$rays can escape easily, see Sec.(2.3.1.4).
For thick absorbers, instead, the fluctuations are not that dramatic, allowing for a quasi Gaussian distribution $f\left(E\right)$ for the probability to observe a certain energy loss, i.e.

$$f\left(x,\ \Delta E\right) \propto \exp\left(-\frac{\left(\Delta E - \langle\Delta E\rangle\right)^2}{2\sigma^2}\right)\,,$$

---

[8] This mean excitation energy in the material has a useful parametrization: for Z > 1 we can safely use $\mathrm{I} \simeq 16\,\mathrm{eV\,Z^{0.9}}$.

[9] The density correction accounts at high energies for the reduction in energy loss due to the so called *density effect*: as the incident particle velocity increases, media become polarized and their atoms can no longer be considered as isolated.

with width dependent on the material and, of course, on the particle. Whenever we deal with energy measurements of a particle, we often have to deal with individual measurements of energy deposition. So, in our instruments, we will sample the energy deposition of the particle in several places in the detector. At each segment, then, a measurement of ΔE in a thin absorber is obtained and, based on several such measurements, the energy of the incident particle can be inferred. Typically a statistical technique needs to be applied, so also samplings of each segment are needed. Often a "truncated mean" technique is employed, namely a fraction (e.g. 30 %) of the high energy tail, and possibly a fraction of the low tail too, is thrown away, and an average of the residual measurements is extracted. This average is then inserted in the known parametrization (e.g. the Bethe-Bloch) to find the incident energy.

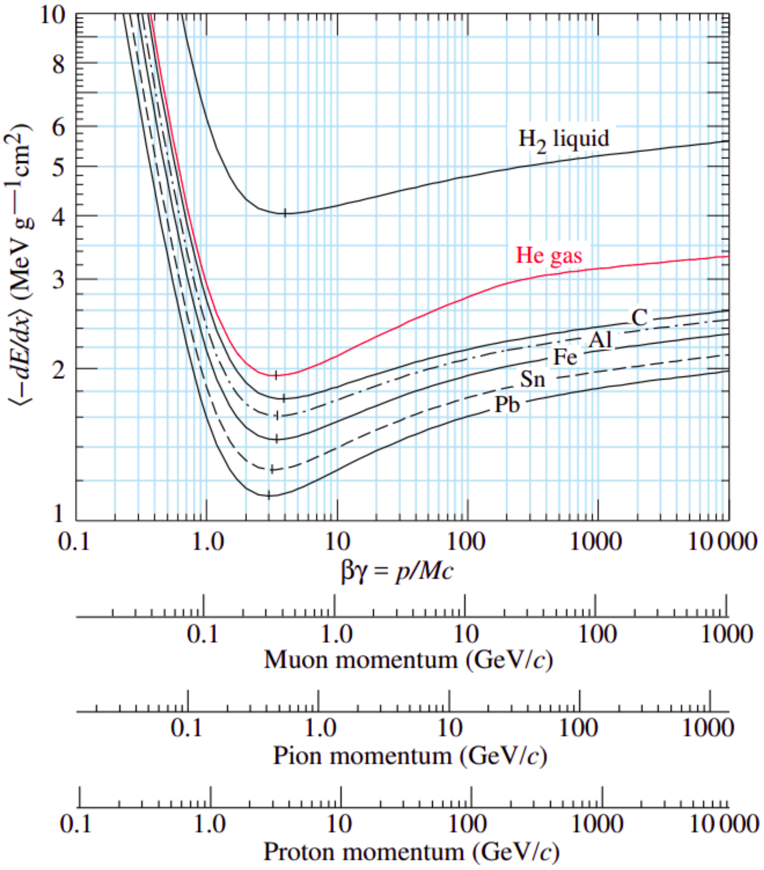

Figure 2.12: Mean energy loss per unit density (in g cm^{-2}) and unit lenght (in cm) in liquid (bubble chamber) hydrogen, gaseous helium, carbon, aluminum, iron, tin, and lead. Radiative effects, relevant for muons and pions, are not included. Figure lifted from `http://pdg.lbl.gov/2019/reviews/rpp2019-rev-passage-particles-matter.pdf`.

Validity limits for the Bethe-Bloch equation The Bethe-Bloch formula is valid only in the energy interval corresponding to approximately $0.05 < \beta\gamma < 1000$, (see Fig.(2.12) for reference values on energies of muons, pions and protons), since:

1) *At lower momenta* the particle speed is comparable to the speed of the atomic electrons, and in these conditions a large fraction of the energy loss is due to the excitation of atomic and molecular levels rather than to ionization. However this fraction is detectable too: it is measured as light coming from de-excitation of those levels or, in a crystal, as phonons;

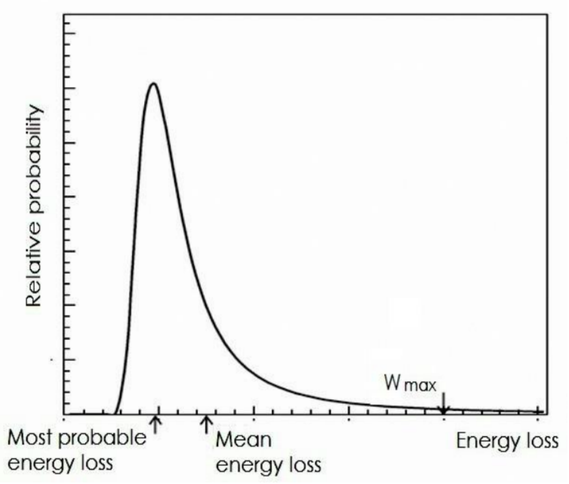

Figure 2.13: Landau distribution as a function of energy loss, namely ΔE in text.

2) *At energies larger* than a few hundred GeV for pions and muons, much larger (1 TeV) for protons, Bremsstrahlung losses in the nuclear fields become possibly more important than ionization. Consequently, the stopping power is expected to grow dramatically.

A beautiful application of the detectable de-excitation photons from unstable molecular (atomic) states are the *auroras*: they are produced by photoluminescence, i.e. de-excitation with emission into the visible or near-visible regime in transparent media, mainly due to cosmic rays concentrating in the geomagnetic poles. Every color is the marker of a chemical specie in the atmosphere. Often photoluminescence results into a fast ($t < 100\,\mu$s) excitation or de-excitation: in this last case we talk of fluorescence, or scintillation.

Exercise 2.1. The discovery of the positron

In 1932 C. D. Anderson discovered the positrons as a part of cosmic secondary radiation. Fig.(2.14) shows the famous photograph that led to this discovery: a large cloud chamber[10] was employed, whose magnets were designed to provide a uniform field up to about 1.5 T. Cosmic rays come from above, but the particles that appeared to be positive if moving downwards, could have been negative going upwards, perhaps originating from an interaction in the material under the chamber. The issue had to be settled by determining the direction of motion without ambiguity. To accomplish this, a plate of lead, 6 mm thick, was inserted across a horizontal diameter of the chamber. The direction of motion of the particles could then be ascertained due to the lower energy, and consequently larger curvature, after they had traversed the plate and suffered energy loss.

In the picture, the magnetic field point into the sheet plane with $|\vec{\mathrm{B}}|= 1.5$ T. The radius of the curvature of the trajectory in the lower part is $r_{\text{in}} = 14\,\text{cm}$, while the radius of the curvature in the upper part is $r_{\text{out}} = 7\,\text{cm}$. We assume that both trajectories are produced by the same particle, which crosses the lead plate. By analysing the ionization density, i.e. the condensation density of the cloud in the chamber, it can be concluded that the particle has a charge $|\mathrm{Q}|= e$[11].

---

[10] Cloud chambers were largely used in the last century, and they were typically cylinders filled with gas kept in saturated state, e.g. water vapors or alcohol. A charged particle entering the chamber would collide with molecules and strip off their electrons, creating a trail of ionized gas particles along the incident projectile. These ionized gas particles work as condensation centers around which droplets form, keeping memory of the trail for several seconds, allowing to take pictures of them.

[11] The density of the droplets in the cloud is proportional to the ionization density, i.e. $\mathrm{d}E/\mathrm{d}x$.

i) *What are the energies of the particle below and above the plate in case of a proton and in case of an electron/positron?*
The Lorentz force on the particle of mass m, charge Q, velocity $\vec{v}$ is given by

$$\vec{\mathrm{F}} = \mathrm{Q}\vec{v} \times \vec{\mathrm{B}}\,,$$

so the equation of motion for the particle under the electromagnetic field shall be

$$\gamma m \frac{\mathrm{d}\vec{v}}{\mathrm{dt}} = \mathrm{Q}\left(\vec{E} + \vec{v} \times \vec{\mathrm{B}}\right) \qquad \Rightarrow \qquad \vec{v} = \vec{r} \times \frac{\mathrm{Q}\vec{\mathrm{B}}}{\gamma m c}\,,$$

where we have performed an integration for a static and uniform magnetic field, and neglected the electic field counterpart. The Larmor radius (or gyroradius) for a relativistic particle of charge $\mathrm{Q} = \mathrm{Z}e$ will then be

$$r_{\mathrm{L}} = \frac{pc}{\mathrm{Z}e|\vec{\mathrm{B}}|} \simeq \frac{E}{\mathrm{Z}e|\vec{\mathrm{B}}|}\,, \tag{2.14}$$

so the radius is proportional to the energy, and the particle must then be going from below to above the plate. By comparison with the measured values r_{in} and r_{out} one easily finds

$$p_{\mathrm{in}}c = 63\,\mathrm{MeV} \qquad \text{and} \qquad p_{\mathrm{out}}c = 32\,\mathrm{MeV}\,.$$

ii) *Demonstrate that the particle is positively charged and that it cannot be a proton.*
Let us first hypothesize that the particle is a proton and estimate the expected energy loss as it crosses the lead plate. We need the following parametrization of the Bethe-Bloch formula (which neglects the logarithmic rise at $E \approx pc \gg mc^2$):

$$-\frac{1}{\rho}\frac{\mathrm{d}E}{\mathrm{d}x} = \frac{1}{\beta^2}\left(-\frac{1}{\rho}\frac{\mathrm{d}E}{\mathrm{d}x}\right)\bigg|_{\mathrm{min}}\,,$$

with the minimum value being well represented by Eq.(2.13)

$$\left(-\frac{1}{\rho}\frac{\mathrm{d}E}{\mathrm{d}x}\right)\bigg|_{\mathrm{min}} \approx 3.5\left(\frac{\mathrm{Z}}{\mathrm{A}}\right)\,\mathrm{MeV\,cm^2\,g^{-1}} \simeq 1.4\,\mathrm{MeV\,cm^2\,g^{-1}}\,.$$

The last estimate is appropriate for lead of course, and it is extracted from PDG[12], from which an average value of A over the possible observable isotopes is found, and in particular $\rho_{\mathrm{lead}} \simeq 11.35\,\mathrm{g\,cm^{-3}}$. So, for the entering proton,

$$\beta\gamma = \frac{p_{\mathrm{in}}c}{mc^2} = \frac{63\,\mathrm{MeV}}{938\,\mathrm{MeV}} \simeq 0.07\,.$$

Approximating $\beta\gamma \sim \beta$ we can easily find

$$-\frac{\mathrm{d}E}{\mathrm{d}x} = \rho\frac{1.4}{(0.07)^2}\,\mathrm{MeV\,cm^{-1}} \simeq 3\times10^3\,\mathrm{MeV\,cm^{-1}} \sim 3\,\mathrm{GeV\,cm^{-1}}\,,$$

which, for $\Delta x = 6\,\mathrm{mm}$, leads to $\Delta E \simeq 1.8\,\mathrm{GeV}$. This is indeed far too much, given the values found before! In fact one can find the energies

$$E_{\mathrm{in}} = \sqrt{(mc^2)^2 + (p_{\mathrm{in}}c)^2} = 940\,\mathrm{MeV}\,,$$

$$E_{\mathrm{out}} = \sqrt{(mc^2)^2 + (p_{\mathrm{out}}c)^2} = 938.5\,\mathrm{MeV}\,,$$

---

[12] See `http://pdg.lbl.gov/2019/AtomicNuclearProperties/index.html` for lead.

leading to $\Delta E = 1.5\,\mathrm{MeV}$, an energy loss about three orders of magnitude lower. The hypothesis of a proton can definitely be discarded: notice that the proton was the only positively charged particle known.
From the radius of curvature we infer that this unknown particle traverses the plate from below to above so, knowing the direction (and versus) of $\vec{\mathrm{B}}$ we infer that it is positively charged.

From more precise characterizations of its $\mathrm{d}E/\mathrm{d}x$ one is finally allowed also to infer that it should have the same mass of an electron. In such a way the positron was discovered.

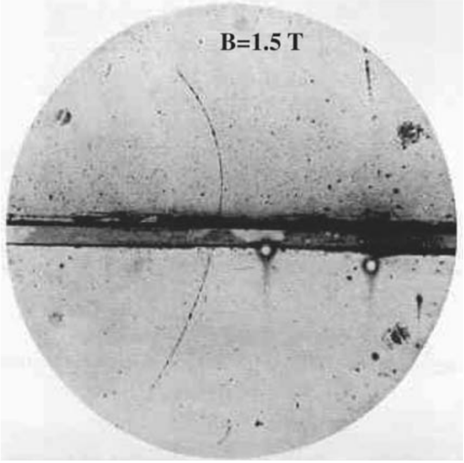

Figure 2.14: A positron track (from Anderson, 1933).

2.3.1.2 Electrons and positrons

With an accurate analysis one shall discover that the collisional energy loss given by Eq.(2.12) yields, for lighter particle such as electrons and positrons, an underestimate of the stopping power for collisional interaction (which henceforth will be called $\langle \mathrm{d}E/\mathrm{d}x\rangle|_{\mathrm{coll}}$). The fundamental reason is that the Bethe-Bloch is based on the idea that the incident particle shall not be dramatically affected by the inelastic collision with the much lighter nuclear electron. This hypothesis has in fact to be dropped if the incident particle becomes, e.g., an electron: it is reasonable to think that its trajectory will be very influenced by the collision, being the target mass comparable with its own one. Moreover a quantistic phenomenon occurs: the collision now is between identical particles, which can't be recognized anymore after the interaction, and this effect has to be taken into account in a (no more classical) calculation of the $\langle \mathrm{d}E/\mathrm{d}x\rangle|_{\mathrm{coll}}$. The energy loss per unit lenght by collisions of such lighter particles has a rather unfriendly expression, which we shall not derive:

$$\left\langle \frac{\mathrm{d}E}{\mathrm{d}x} \right\rangle \bigg|_{\mathrm{coll}} = \frac{2\pi \mathcal{N}_a r_e^2 m_e c^2 \rho \mathrm{Z}}{\mathrm{A}\beta^2} \left[\log\left(\frac{\tau^2(\tau+2)}{2\,(\mathrm{I}/m_e c^2)^2} \right) + F^{\pm}(\tau) - \delta - 2\frac{\mathrm{C}}{\mathrm{Z}} \right] ,$$

where $\tau = T_e/m_e c^2$ and $F^{\pm}(\tau)$ is a function which corresponds to positron (apex $+$) or electrons (apex -):

$$F^{-}(\tau) = 1 - 2\beta + \frac{\tau^2/8 - (2r_e+1)\log 2}{(\tau+1)^2} ,$$

$$F^{+}(\tau) = 2\log 2 - \frac{\beta^2}{12}\left(23 + \frac{14}{\tau+2} + \frac{10}{(\tau+2)^2} + \frac{4}{(\tau+2)^3} \right) .$$

Let us recall that r_e is the classical electron radius, i.e. the size the electron would need to have for its mass to be completely due to its electrostatic potential energy, under the assumption that charge has a uniform volume density and that the electron is a sphere. In particular: $r_e = (e^2/4\pi\epsilon_0)/(m_e c^2) \simeq 0.003\,\mathrm{pm}$.

2.3.1.3 High-Energy Radiation Effects

As already said, the Bethe-Bloch formula Eq.(2.12) at high energies $\beta\gamma \gtrsim 1000$ is inadequate to describe the stopping power of heavy particles such as protons, even more so if one considers lighter particles, e^- and e^+, for which the radiative energy losses become important at relatively low energies too. The radiative energy losses are described by Bremsstrahlung or, alternatively, braking radiation, that is the emission of electromagnetic waves by an accelerating (decelerating) charged particle in the Coulomb field of a nucleus:

$$e^- + N \to e^- + N + \gamma \qquad\qquad e^+ + N \to e^+ + N + \gamma\,.$$

Notice that this process is not possible in vacuum to assure the simultaneous conservation of energy and momentum. From classical electromagnetism it is known that the intensity of the emitted radiation from a dipole is proportional to the square of the acceleration (Larmor formula). Due to the much lower inertial mass of electron and positrons, Bremsstrahlung is thus a non negligible effect which reduces the kinetic energy of such particles in favor of electromagnetic emission. In general this effect's importance depends upon the energy E and the mass m of the incident particle, and we can summarize this argument with

$$\left\langle \frac{\mathrm{d}E}{\mathrm{d}x} \right\rangle\bigg|_{\mathrm{tot}} = \left\langle \frac{\mathrm{d}E}{\mathrm{d}x} \right\rangle\bigg|_{\mathrm{coll}} + \left\langle \frac{\mathrm{d}E}{\mathrm{d}x} \right\rangle\bigg|_{\mathrm{rad}}\,,$$

which is valid for any charged particle.
The average fractional energy loss by radiation for an electron of high energy $E \gg m_e c^2$ is approximately independent on the energy itself, and can be described by

$$\frac{1}{E}\left(\frac{\mathrm{d}E}{\mathrm{d}x}\right)\bigg|_{\mathrm{rad}} \simeq -\frac{1}{\mathrm{x}_0} \qquad \text{with} \quad [\mathrm{x}_0] = \mathrm{cm}\,,$$

where we have dropped the average symbol for simplicity. The quantity x_0 is the one already encountered in the previous section Sec.(2.2.2), i.e. it is called the *radiation length*, and is a characteristic of the material. A few typical values are: air, $\mathrm{x}_0 = 300$ m at NTP[13]; water, $\mathrm{x}_0 = 36$ cm; lead, $\mathrm{x}_0 = 0.5$ cm, but it is tabulated for a lot of different materials in PDG. It has the obvious interpretation of the distance after which the electron's (positron's) energy is reduced by a factor $1/e$ due to the Bremsstrahlung mechanism alone:

$$-\frac{\mathrm{d}E}{E} = \frac{\mathrm{d}x}{\mathrm{x}_0} \qquad \Rightarrow \qquad E = E_0 \exp\left\{-\frac{x}{\mathrm{x}_0}\right\}\,. \tag{2.15}$$

For a given, relatively large, range of atomic numbers a suitable parametrization is given by the following relation:

$$\frac{1}{\rho}\mathrm{x}_0 \simeq 180\,\frac{\mathrm{A}}{\mathrm{Z}^2} \qquad \text{with} \quad \frac{\Delta\mathrm{x}_0}{\mathrm{x}_0} < 20\,\%\,, \quad 12 < \mathrm{Z} < 93\,.$$

We show in Fig.(2.15) the electron energy loss in lead; in other materials the behavior is similar. At low energies the ionisation loss dominates, at high energies the radiation loss becomes more important, since the average energy loss by collision is practically constant. The crossover, when the two losses are equal, is called the *critical energy.* With a good approximation it is given by

$$E_{\mathrm{c}} \simeq \frac{550\,\mathrm{MeV}}{\mathrm{Z}} \qquad \text{with} \quad \frac{\Delta E}{E_{\mathrm{c}}} < 10\,\%\,, \quad 12 < \mathrm{Z} < 93\,,$$

and we can easily recognize that the expression is a decreasing function of the atomic number. For example, the critical energy of lead, which has Z = 82, is $E_{\mathrm{c}} = 7\,\mathrm{MeV}$; air, $E_{\mathrm{c}} = 84\,\mathrm{MeV}$;

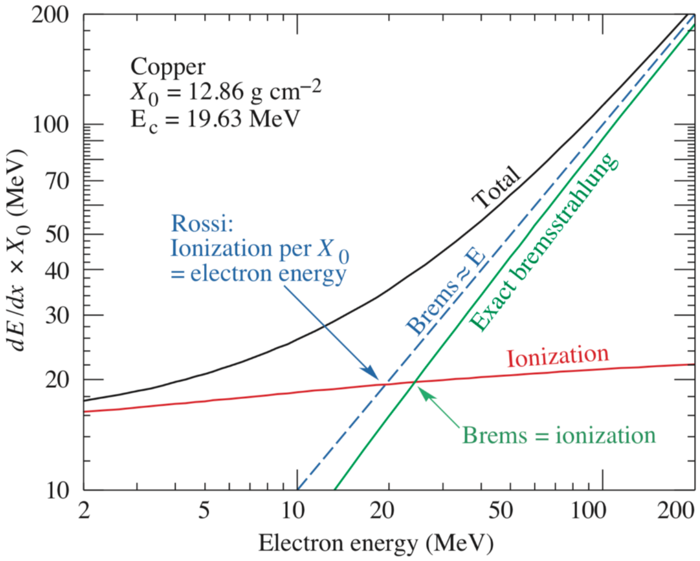

Figure 2.15: Fractional energy loss per radiation length in lead as a function of the electron or positron energy. From K.A. Olive et al. (Particle Data Group), Chin. Phys. C 38 (2014) 090001. In light blue a different parametrization is employed for Bremsstrahlung radiation: the difference in the resulting E_c between this model and the green one is very small and negligible to our scope.

water, $E_c = 74$MeV. A critical energy can be defined also for heavier particles, but in general it is not possible to have a satisfying parametrization for them; we shall limit ourselves to say that it is generally about one order of magnitude higher, with respect to the encountered numbers, for particles as muons.

2.3.1.4 δ-rays

We have already stated that hard collisions could free electrons from nuclei, promoting them to ionizing agents too. This is a very rare event, since it implies a large energy transfer in one single collision, but the correspondent effects of the electrons are indeed observable and measurable, since they are often producers of scintillation light. Delta rays can make also additional secondary ionization trails that may escape the active volume, so their energy can not be collected. The δ-rays indeed represent the high energy tail of the Landau distribution. In Fig.(2.16) a recent example is shown.

2.3.1.5 Cherenkov radiation

It is known that if a charged particle moves in a transparent material with a speed v larger than the phase velocity of light it generates a wave similar to the shock wave made by a supersonic jet in the atmosphere, namely if

$$v > \frac{c}{n} \qquad \text{with} \qquad n = \text{refractive index}\,.$$

The shock comes from an asymmetric polarization of the medium in the front with respect to the rear of the particle, giving rise to a varying dipole moment, which is indeed the fundamental responsible for the radiation. The wave front is the envelope of the elementary spherical waves emitted by the moving source at subsequent moments, and has a typical form of a triangle. Fig.(2.17) shows a scheme of the geometry for Cherenkov radiation. The angle θ_c of Cherenkov radiation relative to the particle's direction, for a particle with velocity

---

[13] NTP stands for Normal Temperature and Pressure, i.e. at P =1 atm and T = 293 K.

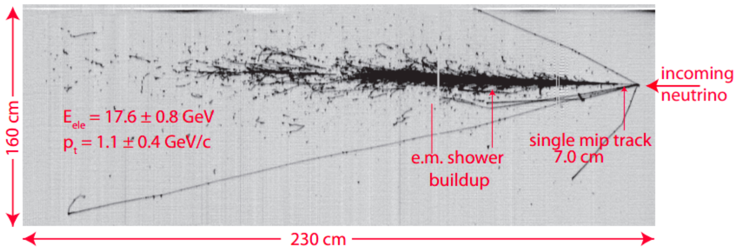

Figure 2.16: A recent result by ICARUS (Imaging Cosmic And Rare Underground Signals) collaboration, located originally at the Laboratori Nazionali del Gran Sasso (LNGS) and then reassembled at Fermilab. The ICARUS program was initiated by Carlo Rubbia in 1977, who proposed a new type of neutrino detector. These are called Liquid Argon Time Projection Chambers (LAr-TPC), which make use of the reaction ${}^{40}Ar + \nu \rightarrow^{40} K + e^-$ in order to study neutrino oscillations, measuring neutrinos of astronomic or solar sources, and CERN Neutrinos to Gran Sasso (CNGS) beam produced 730 km away by the Super Proton Synchrotron from CERN.
In figure you can clearly see a lot of scattered arms departing from the principal ionizing particle track, which knocks on several electrons, the so called δ-rays. Figure taken from `https://aip.scitation.org/doi/pdf/10.1063/1.4915574`

βc is given by

$$\cos\theta_c = \frac{1}{\beta n\left(\lambda\right)} \qquad \Rightarrow \qquad \theta_c = \arccos\left(\frac{1}{\beta n\left(\lambda\right)}\right) = \theta_c\left(\lambda\right) \ , \tag{2.16}$$

where we have highlighted the dependence on the wavelenght, which arises from the expression of the refractive index. The above relation can also be interpreted as a threshold condition for Cherenkov radiation to be emitted: in fact, Cherenkov angle is zero at the threshold velocity for the emission of this type of radiation, and the angle takes on a maximum as the particle speed approaches the speed of light.
This process is actually not important for energy loss, but is deeply used in high energy and cosmic ray physics detectors. In that context, we are particularly interested in characterising the number of photons produced per unit path length of a particle with charge ze and per unit energy interval of the photons, namely

$$\frac{\mathrm{d}^2N}{\mathrm{d}E\,\mathrm{d}x} = \frac{\alpha z^2}{\hbar c}\sin^2\theta_c = \frac{\alpha z^2}{r_e\, m_e c^2}\left(1 - \frac{1}{\beta^2 n^2(E)}\right) \approx 370\ \sin^2\theta_c(E)\ \mathrm{eV}^{-1}\,\mathrm{cm}^{-1} \ ,$$

where in the last estimate we have used $z = 1$, and E is obviously the photon energy. Equivalently,

$$\frac{\mathrm{d}^2N}{\mathrm{d}\lambda\,\mathrm{d}x} = \frac{2\pi\alpha z^2}{\lambda^2}\left(1 - \frac{1}{\beta^2 n^2(\lambda)}\right) \ .$$

This last expression shows an important feature, which is an inverse dependence of $\mathrm{d}N/\mathrm{d}x\mathrm{d}\lambda$ on the square of the wavelenght, approximately. This leads to a wavelenght spectrum which is characteristically *bluish*, i.e. the short wavelenghts will dominate the spectrum. The spectrum of the Cherenkov light is then continuous with important fractions in the visible and in the ultraviolet. E.g., in water, Cherenkov radiation will have a very charateristic blue glowing[14]! Let us give some numerical examples: a high energy electron (with sufficient energy to fulfill the threshold for emitting Cherenkov radiation) in water, where the refractive index is $n \simeq 1.33$, will emit ≈ 220 photons cm^{-1}; in air, instead, ≈ 30 photons m^{-1}, with $n \simeq 1$. Those are decent numbers of photons, and they can be well detected by counters, since this yield of photons is pretty good usually.

---

[14] You can see this looking at pictures of the basements of nuclear reactors, where the moderating material is water: `https://www.technobyte.org/cherenkov-radiation-blue-light/`.

Typically, one has to integrate the differential spectrum since detectors usually have a limited sensitivity range, being able to collect wavelenghts in the interval of [λ_1, λ_2], which for a typical PMT is of the order of [350 nm, 500 nm], even though these numbers may consistently vary with the building material of the photocatode and the window of the vacuum vessel. With these representative values, we can find

$$\frac{\mathrm{d}N}{\mathrm{d}x} = 2\pi r^2\,\alpha\,\sin^2\theta \int_{\lambda_1}^{\lambda_2} \frac{\mathrm{d}\lambda}{\lambda^2} = K\,\sin^2\theta\left(\frac{1}{\lambda_2} - \frac{1}{\lambda_1}\right) \simeq 400\,\sin^2\theta\ \text{ph}\,cm^{-1}\,,$$

where we have defined a constant K too. The number can appear to be small, but it is still detectable, and indeed we will see several instruments which exploit Cherenkov radiation from charged particles passing through them.
Additionally, the surface limiting the material in which the particle travels intersect the emitted light cone in circle or, more generally, an ellipse, called the *Cherenkov ring.* This can be detected by covering the surface with PMTs, and if the particle travels, say, towards that surface, the PMTs see a ring gradually shrinking in time. From this information the trajectory of the particle can be understood.

Is there any analogous effect for neutral particles? Neutral particles can be detected only after scatterings actually. Neutrons, for example, can be detected after they undergo a collision with protons, and the recoil of the latter can be consequently observed. Neutrons usually go through elastic scatterings in matter, and the efficiency in the energy transfer shall depend upon the relative masses for simple kinematic reasons, so a $n + p$ scattering will be very efficient in energy transfer terms[15]. In general, the only way to detect neutral particles is essentially via an energy transfer to charged species. Photons, for example, can be detected by the effects we shall discuss in the following, namely photoelectric effect, compton scattering and pair production, and in all these cases an energy transfer to charged particles is unavoidably present. The same is also true for neutrinos.

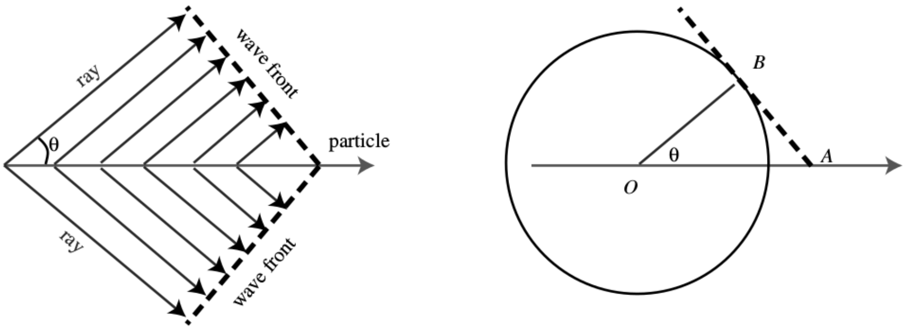

Figure 2.17: Pictorial view of Cherenkov radiation geometry. Left: typical V-form of the wavefront; Right: elementary spherical wave emitted at an istant t by the charged particle. At t, its radius is given by $\bar{\text{OB}} = ct/n$, and in the meantime the particle has moved by $\bar{\text{OA}} = vt$.

Muons We shall discuss a bit more about muons, which can be regarded as the most penetrating agents beyond neutrinos. For this type of particle there are three processes that can be regarded as radiative losses, namely to be incorporated into $\langle \mathrm{d}E/\mathrm{d}x\rangle|_{\text{rad}}$:

1) *Bremsstrahlung*, which we have already described for electrons and positrons: the mechanism is the same, and the by product is the emission of photons:

$$\mu^+ + N \to \mu^+ + N + \gamma \qquad\qquad \mu^- + N \to \mu^- + N + \gamma\,;$$

---

[15] This is actually a highly used mechanism to obtain thermalized neutrons, for example in nuclear reactors, where a proton rich enviroment, such as water, is used for these purpose.

2) *Photonuclear interactions*: this refers to an electromagnetic interaction with nuclei in which the target nucleus is fragmented in hadrons (H), giving rise to a hadronic cascade in the traversed matter:

$$\mu^+ + N \rightarrow \mu^+ + H \qquad\qquad \mu^- + N \rightarrow \mu^- + H \; ;$$

2) *Direct pair production*: the process is analogous to the pair production by photons, it happens in vicinity of a nucleus since in vacuum it is plainly forbidden, and it gives rise to a e^-, e^+ cascade:

$$\mu^+ + N \rightarrow \mu^+ + N + e^+ + e^- \qquad\qquad \mu^- + N \rightarrow \mu^- + N + e^+ + e^- \; .$$

The Feynman diagrams of the three processes are shown in Fig.(2.18). Each of these three kinds of products can eventually trigger also secondary particles cascades, which are very important in the context of measurements, since they are the means to rebuild the original incident muons signal. The processes become more and more important as the energies increase, and we shall remind that those are indeed stochastic mechanisms, in which large fluctuations are expected to occur and large energy transfers between particles become possible and probable to some degree. A general parametrization for the muons is given by

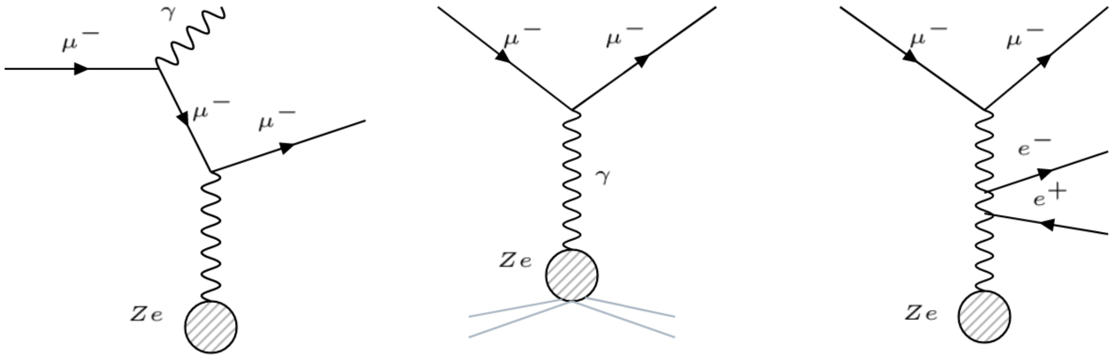

Figure 2.18: Feynman diagram of Bremsstrahlung, photonuclear interactions and direct pair production by high energy muons, in order from the left.

$$-\frac{1}{\rho}\frac{\mathrm{d}E}{\mathrm{d}x}\bigg|_{\mathrm{tot}} = a(E) + b(E)\cdot E \qquad \text{with} \qquad a(E) \simeq 0.002\ \mathrm{GeV\,g^{-1}\,cm^2} \; ,$$

where $a(E)$ is a mild function of energy and shall be considered as the loss due to collisions, while the second term represents the radiative losses and the dependence of $b(E)$ on E is much stronger. This latter term obviously describe each of the three processes mentioned above. A detailed representation of the coefficient b is given in Fig.(2.19): notice that, at increasing energies, a constant behavior is shown. Let us mention for completeness that the typical average range $\langle R(E)\rangle$ for muons is parametrized by

$$\langle R(E)\rangle \simeq \frac{1}{b}\log\left(1+\frac{E_0}{E_\mathrm{c}^\mu}\right) \qquad \text{with} \qquad E_\mathrm{c}^\mu(E) \simeq \frac{a(E)}{b(E)} \; ,$$

where E_0 is obviously the initial energy of the incident muon.

Muons lastly have some very nice and alive applications in nowadays researches: it is indeed easy to find something interesting in the net about the so called **muon tomography**. The

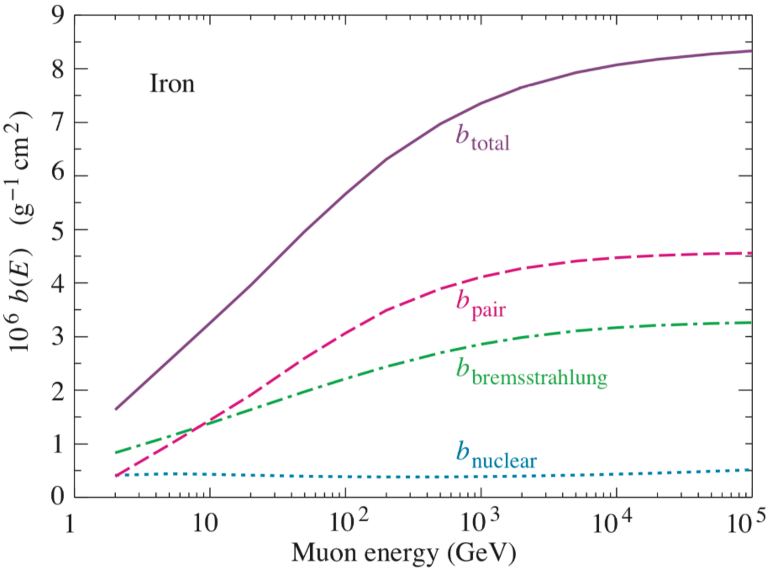

Figure 2.19: Contributions to the fractional energy loss by muons in iron due to e^+, e^- pair production, Bremsstrahlung and photonuclear interactions.

ability of muons to survive well beyond the penetration of the atmospheric layers down till undeground levels is of fundamental importance for several underground laboratories (in Italy, e.g., the National Laboratories of Gran Sasso LNGS)[16]. Muons will usually lose energy by collisions and, at higher energies, via the three listed processes: observations in underground laboratories will regard those lowered energy particles, the energy loss being itself a flag for the density profiles of the traversed materials. The idea to probe these profiles traces its roots back to the '50, when the question of finding hidden treasure chambers below the Egyptian pyramids was raised. Indeed this kind of analysis allowed to avoid (or to schedule!) archaeological excavations[17]. Also geological studies are actually involved, the monitoring of the movements of incandescent material below (in)active volcanoes being just a reductive example. Finally, the imaging of the Fukushima nuclear reactor, which still remains an ecological problem and to which no man can get close anymore, is nowadays a very promising technique which implies muons[18].

A general picture of the muons interactions is given in Fig.(2.20), in which Landau, Bethe-Bloch and radiation regimes are clearly depicted, together with a sensitive correction for the δ density parameter.

2.3.2 Neutral particles

Neutrinos were indeed treated in the previous section, so we are now focusing on the interaction of **photons** with matter. There are three main mechanisms of interaction, one of which is the already mentioned pair production, and each one will dominate at a certain range of energies. The cross sections for these processes is usually much lower than the one σ_{coll} involved in collisional mechanisms of charged particles to atoms, and indeed the interaction is very different. We shall expect, in this case, an attenuation in the *number* of photons N. Photons are actually absorbed or scattered, and the attenuation law is in fact

---

[16] Typically the penetration capability through the Earth levels is measured in unity of "meter water equivalent", m.w.e., namely the meters they would travel if their propagation medium was pure water all the way through. In LNGS the m.w.e. for muons is about 3.7×10^3 m!

[17] `https://asia.nikkei.com/Business/Biotechnology/Using-elementary-particles-to-peer-inside-the-pyramids`

[18] `https://www.world-nuclear-news.org/RS-Muons-suggest-location-of-fuel-in-unit-3-0210174.html`

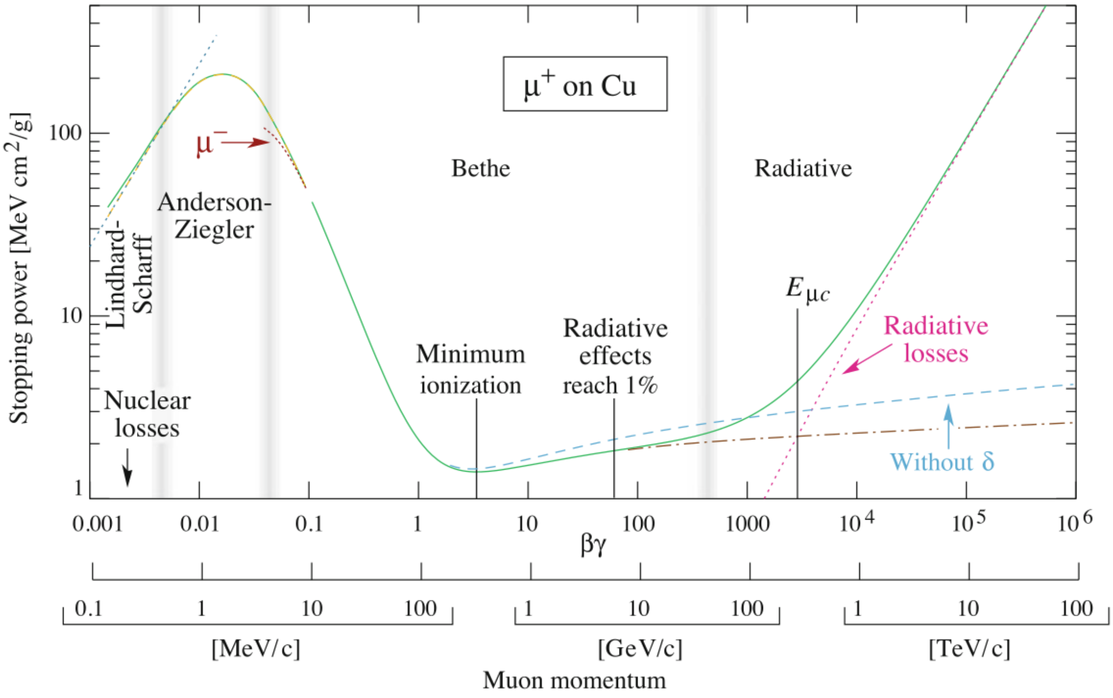

Figure 2.20: The stopping power for positive muons in copper as a function of $\beta\gamma$ is shown over nine orders of magnitude in momentum (corresponding to 12 orders of magnitude in kinetic energy). From K.A. Olive et al. (Particle Data Group), Chin. Phys. C 38 (2014) 090001

an exponential:

$$N = N_0 \exp\{-\mu x\} \qquad \text{with} \qquad \mu = \frac{\rho \mathcal{N}_a}{\text{A}}\,\sigma\,,$$

with σ being the total cross section for the different mechanisms of interaction of radiation with matter; μ is plainly the (inverse of the) average interaction lenght of photons in matter, as we have defined in the previous section Sec(2.1.3). A view of the total cross section behavior as a function of the photon energy is shown in Fig.(2.21): the different contributions from the mechanisms we are about to describe are evident.

2.3.2.1 Photoelectric effect

At energies of the order of dozens of electronvolts, i.e. of the order of the binding energy of atoms in a medium, the photons lose energy mainly by the photoelectric effect on atomic electrons. The effect is described by the release of an electron by an atom traversed by an incident photon, which grant to it its energy. In this case the photon is *absorbed*:

$$\gamma + N \to N^* + e^-\,,$$

where N^* denotes an excited state of the target nucleus. Notice that actually this process can't happen in vacuum, so the presence of the nucleus is fundamental. The energy of the emitted electron shall be given by

$$E_e = E_\gamma - B = h\nu - B \qquad \text{with} \qquad B \simeq eV\,,$$

and it results that the more bound is e^- the higher is the cross section $\sigma_{\text{p.e.}}$. The spikes are due to the K-shell and L-shell of atomic models. The non relativistic expression is given by

$$\sigma_{\text{p.e.}} = \sqrt{\frac{32}{(E_\gamma/m_e c^2)^7}}\,\alpha^4\,\mathrm{Z}^5\,\sigma_{\text{th}}^2 \qquad \text{with} \qquad \sigma_{\text{th}} = \frac{8}{3}\pi r_e^2 = 6.65\times 10^{-25}\,\text{cm}^2\,,$$

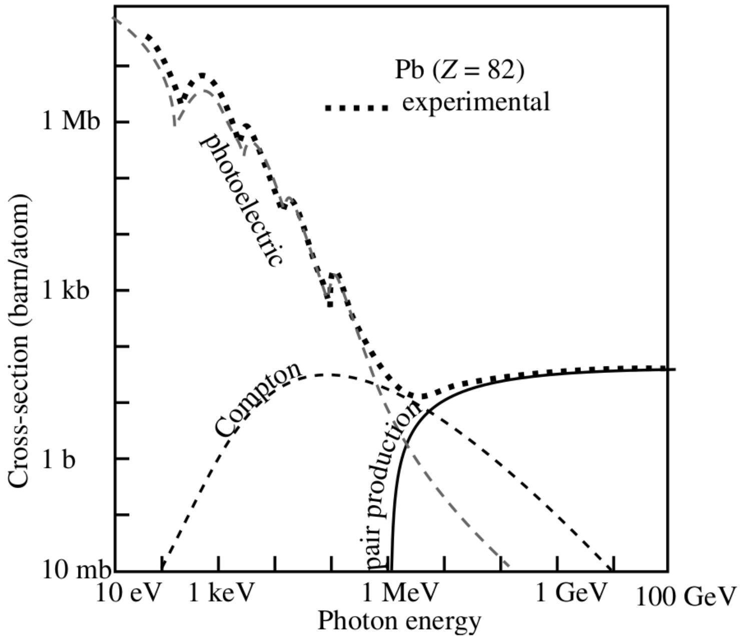

Figure 2.21: Photon cross sections in Pb versus energy; total and calculated contributions of the three principal processes (from Yao et al. 2006).

where $\alpha = 1/137$ is the usual fine structure constant, $\sigma_{\rm th}$ is the classical Thomson cross section. Notice the strong dependence on the atomic number and E_γ.
The photoelectric effect is predominant at low energies $E_\gamma < 100\,{\rm keV}$.

Photomultipliers (PMT) Photomultipliers are relatively simple detectors which make use of the photoelectric effect to detect the intensity of an incident radiation beam, coming from a direct source or conveyed to it with e.g. a scintillator. It consists in a glass vessel with a high level of vacuum (fundamental feature to enhance its performances). A window, which works as a photocatode, allows primary photons to enter from a collimated opening: the photoelectric effect is expected to happen in that exact point. A high number of photoelectrons is built up and accelerated with a series of electrodes (semiconductors, in practice) positioned along the vessel, each of them at higher voltage to create an electric field gradient. More precisely, when the electron hits the first electrode it causes the secondary emission of several electrons of less energy. The system structure is designed so that each emitted electron is accelerated and causes the emission of several others from the next electrode, and so on. There is thus a cascade phenomenon whereby a single photon that hits the tube causes the passage of many photoelectrons. At the final dinode, i.e. the anode, a significant gain in number of electrons can be easily computed, and shall be converted into an electric signal whose intensity is proportional to that of the incident photon beam's one. A schematic view of a PMT is shown in Fig.(2.22).

Reminder on scintillators A scintillator is a very common kind of detector which exploits the property of matter to convert ionizing radiation into detectable photons. They can be divided into inorganic and organic scintillators, which differ by the constructive material and the physical process:

a) *Inorganic scintillators* are crystalline compounds, usually doped semiconductors, in which ionizing radiation leads electrons from the valence band to the conduction band (or just below it) to form a system of charge-positive hole pair called exciton. The doping is employed to create additional levels in the energy gap into which excitons

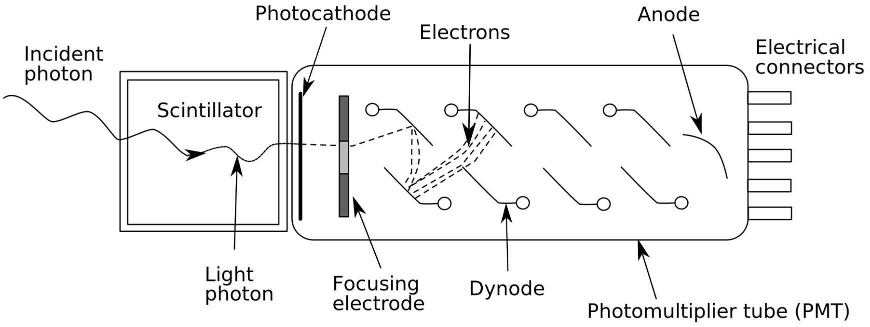

Figure 2.22: Scheme of a linear photomultiplier combined with a scintillator.

can move. The excitons can then undergo recombination with a consequent energy emission via photons (fluorescence) or phonons (quenching), or also being trapped in an energy level for some time, with a delayed emission (phosphorescence). As an example of inorganic doped semiconductors: NaI(Tl) and the modern $Bi_4Ge_3O_{12}$.

b) *Organic scintillators* can be composed by liquid, solid or gas phases, and the light emission is associated with transitions between different energy levels in the molecular or multi-electrons atoms state. The main difference with the inorganic ones is due to their usual much faster response, and also their considerably higher capability of absorbing neutrons due to their hydrogen content. This latter property is very decisive when choosing moderating materials for nuclear reactors.

2.3.2.2 Compton scattering

Above a few keV, namely $100\,\text{keV} < E_\gamma < 5\,\text{MeV}$, the Compton effect becomes important. The process is described by an incoming wave being scattered to an electron, with a cross section which reduces to the classical Thomson σ_{th} in the non relativistic limit, approaching the Klein-Nishina one at higher energies. In this case, conversely, the photon is *scattered*:

$$\gamma + e^- \to \gamma + e^- \ ,$$

where, being the E_γ much higher than the binding energy, the electron can be considered as free. In astrophysics the Inverse Compton process is of particular interest, being probably deeply involved in the cosmic rays acceleration mechanism and also protagonist of production of γ-rays and X-rays coming towards us from extreme enviroments. Even though the kinematical description of these processes is the same, in the Inverse Compton a transfer of energy from electrons to the radiation field is involved rather than the contrary, happening in the simple Compton. The behavior of the cross section, depicted in Fig.(2.21), is approximately described by $\propto E_\gamma^2$ in the decreasing branch.

2.3.2.3 Pair production

When the production threshold of the electron–positron pairs is crossed, at 1.022 MeV, this channel rapidly becomes dominant, and in this case the photon is again *absorbed*. We have already described this kind of mechanism in Sec.(2.2.2):

$$\gamma + N \to e^+ + e^- + N \ ,$$

which can only happen in the presence of a nucleus. The cross section for pair production logarithmically increases with energy E_γ and tends to saturate, with an asymptotic expression given by

$$\sigma_{e^\pm} \simeq \frac{28}{9} \mathrm{Z}^2 \alpha^3 \left(\frac{\hbar c}{m_e c^2} \right)^2 \log \left(\frac{E'_\gamma}{m_e c^2} \right) \overset{E_\gamma \to +\infty}{\simeq} \frac{28}{9} \mathrm{Z}^2 \alpha^3 \left(\frac{\hbar c}{m_e c^2} \right)^2 \log \left(\frac{183}{\mathrm{Z}^{1/3}} \right)$$

$$\Rightarrow \qquad \sigma_{e^\pm} = \frac{7}{9} \frac{\mathrm{A}}{\rho \mathcal{N}_a} \frac{1}{\mathrm{x}_0} \, ,$$

with x_0 being the radiation lenght and E_γ the photon energy assuming the nucleus to be at rest (usually a good assumption). From this expression and Eq.(2.6) one can easily obtain that the mean free path for a photon in matter for pair production is given by

$$\lambda_\gamma = \frac{\mathrm{A}}{\mathcal{N}_a \, \sigma_{e^\pm}} = \frac{9}{7} \, \mathrm{x}_0 \, .$$

Indeed we notice the tight connection between the radiation lenght x_0 and the mean free path λ_γ. The Feynman diagrams, with the usual temporal convention from the left to the right, of each of these processes are reported in Fig.(2.23). As a summary on the different interaction mechanisms for photons with matter, one can plot the atomic number Z as a function of the photon energy E_γ, finding the three different regimes in which each effect is predominant: Fig.(2.24).

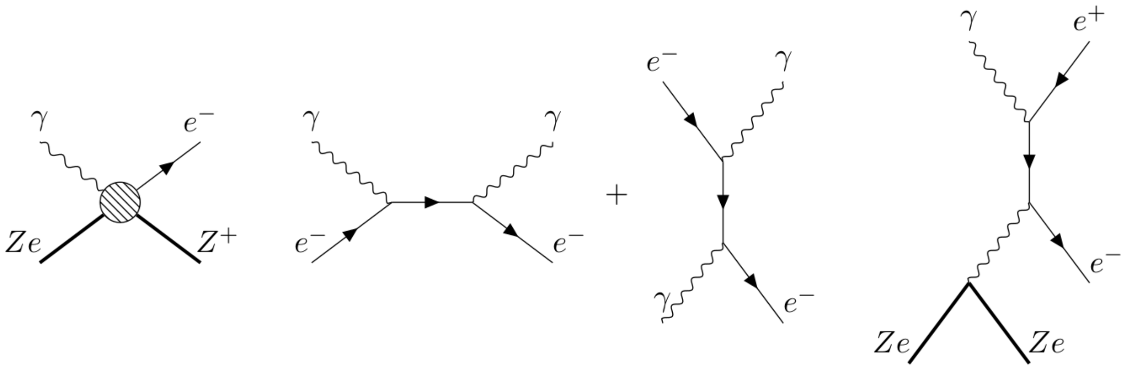

Figure 2.23: Feynman diagrams for photoelectric effect, Compton scattering+Inverse Compton, pair production, correspondently from the left to the right. The nucleus in the photoelectric effect is regarded as an absence of proper interaction description, in QFT sense; Z^+ is the excited nucleus after the electron ejection; Ze are the spectator nuclei.

Exercise 2.2. Impossible in vacuum!

Let us demonstrate that the pair production and photoelectric processes can't actually happen in vacuum, i.e. on free target particles. The proof shall be the same as for muons pair production, since it will involve the same physical condition: conservation of four-momentum. Remember that these are inelastic processes, so the conservation of kinetic energy can't be imposed.

1) *Pair production* Let's consider $\gamma \to e^- + e^+$. $E_\pm$ will be the energy of the electron and positron, $p_\pm$ correspondingly the momentum and $m_\pm = m_e$ the masses. In the initial state the photon momentum is given by $p_\gamma = (|\vec{p_\gamma}| \, , \, \vec{p_\gamma})$ so

$$\sqrt{s} = \sqrt{E_\gamma^2 - |\vec{p_\gamma}|^2 \, c^2} = 0 \, .$$

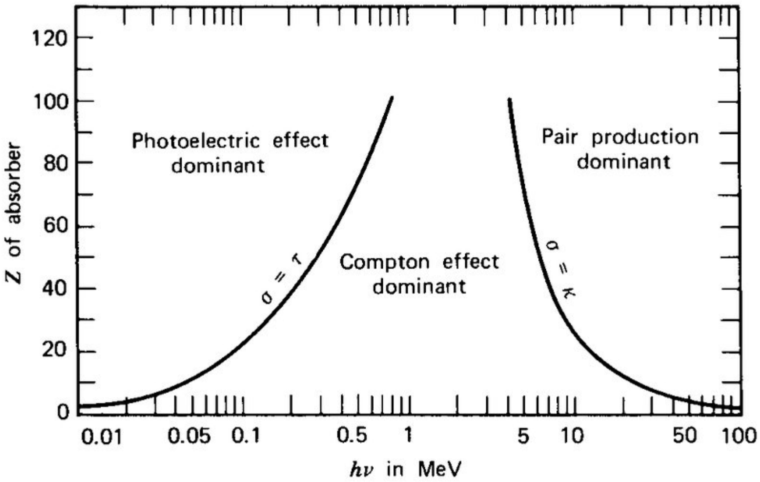

Figure 2.24: Summary of regimes for the three mechanisms for photons interactions with matter.

In the final state the momenta of e^+ and e^- are $p_\pm = \left(\sqrt{m_\pm^2 c^4 + |\vec{p_\pm}|^2 c^2}/c,\ \vec{p_\pm}\right) = (E_\pm/c,\ \vec{p_\pm})$, so

$$\sqrt{s} = \sqrt{(E_+ + E_-)^2 - |\vec{p_+} + \vec{p_-}|^2 c^2} =$$

$$= \sqrt{2m_e^2 c^4 + 2\left(E_+ E_- - |\vec{p_+}|\,|\vec{p_-}|\, c^2 \cos\theta\right)} > \sqrt{2} m_e c^2 > 0\,,$$

which concludes the proofs.

2) *Photoelectric effect* Let's consider $\gamma + e^- \to e^-$. E_- will be the energy of the electron, p_{in} correspondingly the initial momentum and $m_- = m_e$ the mass. In the initial state the photon momentum is given by $p_\gamma = (|\vec{p_\gamma}|\,,\ \vec{p_\gamma})$ and $p_{\text{in}} = \left(\sqrt{m_e^2 c^4 + |\vec{p_{\text{in}}}|^2 c^2}/c,\ \vec{p_{\text{in}}}\right) = (m_e c,\ \vec{0})$ if we take the target to be initially at rest. The invariant mass then is

$$\sqrt{s} = \sqrt{(m_e c^2 + |\vec{p_\gamma} c|)^2 - |\vec{p_\gamma}|^2 c^2} = \sqrt{m_e^2 c^4 + 2 m_e c^3 |\vec{p_\gamma}|}\,.$$

In the final state the momentum of e^- is $p_{\text{fin}} = (m_e c + |\vec{p_{\text{fin}}}|\,,\ \vec{p_{\text{fin}}})$, and

$$\sqrt{s} = \sqrt{\left(m_e^2 c^4 + |\vec{p_{\text{fin}}}|^2 c^2\right) - |\vec{p_{\text{fin}}}|^2 c^2} = \sqrt{m_e^2 c^4}\,,$$

so a comparison of the two expressions leads to $2 m_e c^2 E_\gamma = 0$, which is definitely false. This concludes the proof, and it is also valid for the inverse process $e^- \to e^- + \gamma$, which is indeed Bremsstrahlung in presence of a nucleus.

To conclude this chapter, Fig.(2.25) and Fig.(2.26) describe a summary on charged particles and photons detection techniques.

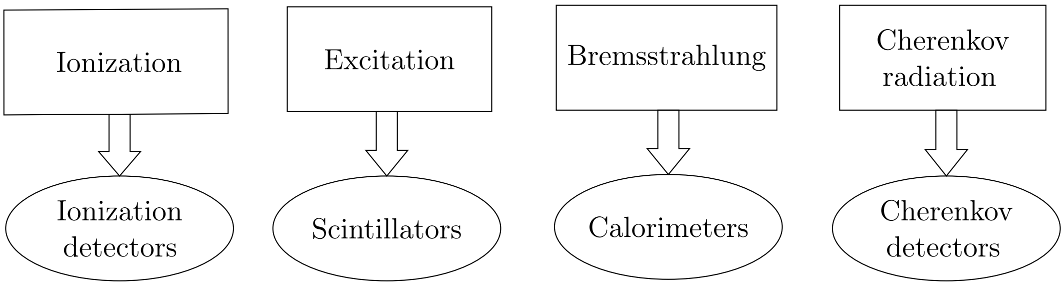

Figure 2.25: Summary on charged particles detection techniques.

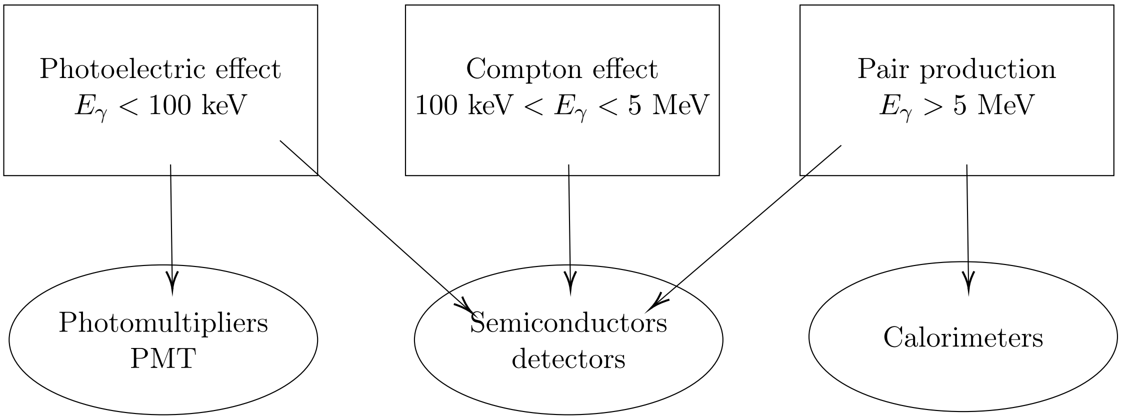

Figure 2.26: Summary of detectors for photons interaction with matter.

3

Cosmic Rays showers in the atmosphere

Usually one refers to indirect cosmic rays detection as the measurements and experiments performed at Earth ground after the CRs have interacted with the atmosphere, by looking at the secondary products of these interactions and collecting all of the informations from them. The *showers* are the fundamental consequences of this process, and in this chapter we address the question of their description and modeling, while in the following chapter the astrophysical fundamentals of CRs will be depicted instead.
This is a very important topic both per se, since CRs provide the occasion to study a very rich astrophysics and phenomenology, and also for the characterization of the interactions of gamma rays and neutrinos. It is indeed very complex: it will concern hadronic as well as all the other kind of interactions.

3.1 The exponential atmosphere

In this preliminary section a simple model called "the exponential atmosphere" is presented, through which the dependence of pressure and density on height is derived. This will obviously influence the probability of cosmic rays particle to interact, in particular density changes are important to understand the development of secondary particles. More precisely, we want to write the *atmospheric depht* x, which is the amount of matter traversed by a cosmic ray particle before interacting.
Let's start, for simplicity, by assuming a vertical propagation of particles towards the Earth, and let h be the height from ground. The vertical atmospheric depht x_v is given by

$$x_v \equiv \int_h^{+\infty} \rho\left(h'\right) \mathrm{d}h' \qquad \text{with} \qquad [x_v] = \mathrm{g\,cm^{-2}}\,. \tag{3.1}$$

This quantity clearly determines the competition between interaction and decay of secondary (primary) particles, since the interaction probability $\mathrm{P_{int}}$ is related to the density (Eq.(2.4)), and the probability of decaying $\mathrm{P_d}$ to the travelled path.
The exponential atmosphere model is described by the relation

$$\rho\left(h\right) = \rho_0 \exp\left\{-\frac{h}{h_0}\right\} \qquad \text{with} \qquad h_0 = 6.5\ \mathrm{km}\,, \tag{3.2}$$

and ρ_0 is the normalization value for atmospheric density. This relation can be easily derived from thermodynamics. Let's consider a small slice of the atmosphere as in Fig.(3.1): the downwards superficial force due to pressure $P_{\text{top}} = P\left(h + \mathrm{d}h\right)$ and the gravity on the unitary volume $F_\text{g} = \rho g A$ balance the upwards superficial force of pressure $P_\text{bottom} = P(h)$. Letting A be the cross sectional infinitesimal area, the hydrostatic equilibrium reads:

$$[P(h) - P(h + \mathrm{d}h)]\ A = \left[P(h) - P(h) - \frac{\mathrm{d}P(h)}{\mathrm{d}h}\mathrm{d}h\right]\ A = \rho(h)\, g\mathrm{d}h\ A$$

$$\Leftrightarrow \qquad -\frac{\mathrm{d}P(h)}{\mathrm{d}h} = \rho(h)\, g\,. \tag{3.3}$$

The hydrostatic equilibrium equation considers a constant $g = 9.81\ \mathrm{m\,s^{-2}}$, and in principle a density which varies with height h. We can exploit the ideal gas equation of state

$$P = \mathrm{N}kT = \frac{\mathcal{N}_a \rho}{\omega_a}\, kT\,, \tag{3.4}$$

where we have used Eq.(2.5) and $k = 1.38 \times 10^{-23}\,\mathrm{m^2\,kg\,s^{-2}\,K^{-1}}$ is the Boltzmann constant, to write the density as a function of the pressure such that

$$\rho = \frac{\omega_a}{\mathcal{N}_a}\frac{P}{kT} = \frac{MP}{kT} \qquad \Rightarrow \qquad \frac{\mathrm{d}P(h)}{\mathrm{d}h} = -\frac{M}{kT}\,P(h)\, g\,.$$

We shall precise that $M \equiv \omega_a/\mathcal{N}_a$ typically depends on height, but we will consider the average value already employed in Sec.(2.2.1) that is $\langle \mathrm{A} \rangle \simeq \mathrm{A}_\text{atm} = 14.5$. In particular, considering that most molecules are biatomic,

$$M = 2m_p \cdot 14.5 = 4.8 \times 10^{-23}\ \mathrm{g}\,,$$

with a composition of 78% nitrogen, 21% oxygen and a percent of other light materials. What about the temperature profile $T = T(h)$? The temperature is obviously tightly related to the atmospheric height. In particular the atmosphere is modeled in a set of different layers, as pictorially shown in Fig.(3.2). For practical purposes we shall consider the layer called *stratosphere*, where the temperature is appoximately constant $T(h) \simeq$ cost from 10 km to 50 km above the sea level, see the figure with the temperature profile, but things are quite different e.g. in the troposphere, where $T(h)$ decreases with h with a rate of $\Delta T/T \approx -6.5\ \mathrm{K\,km^{-1}}$. We can now easily integrate by parts the differential equation of hydrostatic equilibrium, finding for both pressure and density the following exponential profiles

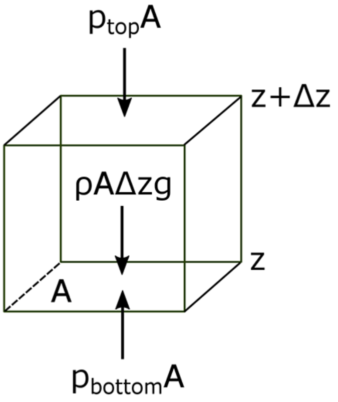

Figure 3.1: Hydrostatic equilibrium of forces on the volume element in the atmosphere.

$$P = P_0 \exp\left\{-\frac{h}{h_0}\right\} \qquad \text{and} \qquad \rho = \rho_0 \exp\left\{\frac{h}{h_0}\right\}\,,$$

where the latter is obtained by substituting the ideal gas law Eq.(3.4) in Eq.(3.3), and $h_0 = kT/Mg$. A typical value of h_0 is found for the sea level, $T \simeq 290\,\mathrm{K}$, to be $h_0 \simeq 8.4\,\mathrm{km}$;

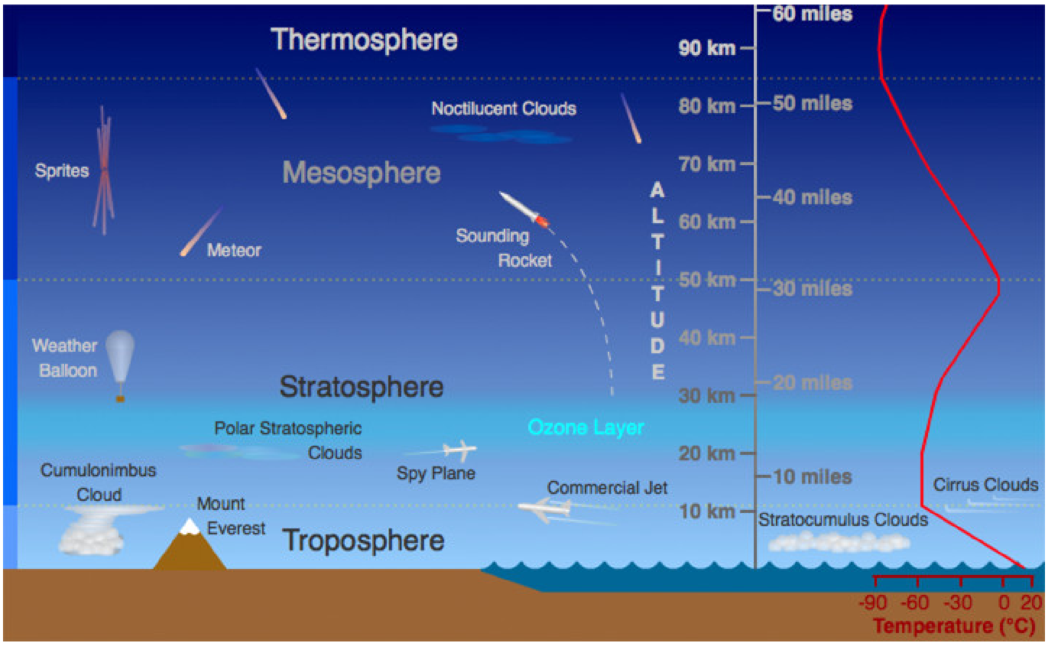

Figure 3.2: Atmospheric layers: troposphere, stratosphere, mesosphere and thermosphere.

i) *Troposphere*: this is the lowest layer of our atmosphere. Starting at ground level, it extends upwards to about 10 km above sea level. We humans live in the troposphere, and nearly all weather occurs in this lowest layer;

ii) *Stratosphere:* this is the next layer up. The stratosphere extends from the top of the troposphere to about 50 km above the ground. The infamous ozone layer is found within the stratosphere. Ozone molecules in this layer absorb high-energy ultraviolet (UV) light from the Sun, converting the UV energy into heat;

ii) *Mesosphere*: it lays above the stratosphere. It extends upwards to a height of about 85 km above our planet. Most meteors burn up in the mesosphere. Unlike the stratosphere, temperatures once again grow colder as you rise up through the mesosphere;

iv) *Thermosphere*: The layer of very rare air above the mesosphere is called the thermosphere. High-energy X-rays and UV radiation from the Sun are absorbed in the thermosphere, raising its temperature to hundreds or even thousands of degrees. The auroras, the Northern Lights and Southern Lights, occur in this layer;

v) *Exosphere*: although some experts consider the thermosphere to be the uppermost layer of our atmosphere, others consider the exosphere to be the actual "final frontier" of Earth's gaseous envelope. There is no clear-cut upper boundary where the exosphere finally fades away into space;

vi) *Ionosphere*: this is not a distinct layer like the others mentioned above. Instead, the ionosphere is a series of regions in parts of the mesosphere and thermosphere where high-energy radiation from the Sun has knocked electrons loose from their parent atoms and molecules. The electrically charged atoms and molecules that are formed in this way are called ions, giving the ionosphere its name and endowing this region with some special properties.

Credits to `https://scied.ucar.edu/atmosphere-layers`.

for the height at which usually cosmic rays interact, with $T \simeq 210$ - $240\,\mathrm{K}$, it corresponds to $h_0 \simeq 6$ - $7\,\mathrm{km}$, which is what we stated at the start in Eq.(3.2). In fact $h_0 = h_0\,(g, T)$, and this quantity is called *atmospheric scale height.*
With this simple model of atmosphere we can now exploit the ideal gas law Eq.(3.4) to find an expression for the vertical atmospheric depht:

$$x_v = \int_h^{+\infty} \rho\left(h'\right)\, \mathrm{d}h' = x_v^{\mathrm{atm}} \exp\left\{-\frac{h}{h_0}\right\} \tag{3.5}$$

with $$x_v^{\mathrm{atm}} = \int_0^{+\infty} \rho\left(h'\right)\, \mathrm{d}h' = \rho_0 h_0 = 1030\,\mathrm{g\,cm^{-2}}\,,$$

and plainly x_v^{atm} is the total vertical thickness of the atmosphere. If we consider that the temperature decreases with increasing altitude h, some analytical parameterizations are obtained [1]], which can be useful as inputs for Monte Carlo simulations of the CR cascades. Fig.(3.3) shows the dependence of x_v (here along the x-axis) upon h as derived with one of these detailed parametrizations.

Let us now drop the hypothesis of simple vertical directions of propagation, and consider the curvature of the Earth and a generic non-vertical direction (zenith angle θ). The effective path lenght l shall be related to the height h by the following

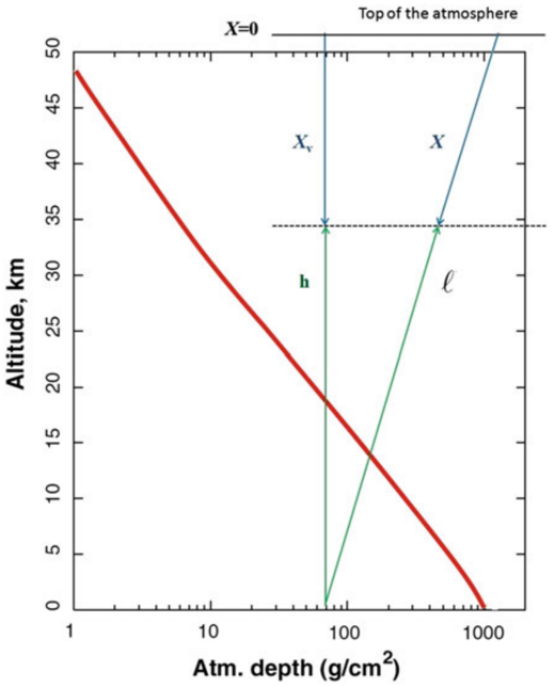

Figure 3.3: The red curve represents the altitude in km, which corresponds to a given residual atmospheric depth x_v. The atmospheric depth x for non-vertical directions is usually denoted as slant atmospheric depth. The total depth of the atmosphere is $x_v^{\mathrm{atm}} = 1030\mathrm{gcm}^{-2}$, which corresponds to ~ 10 m of a material with the density of water (m.w.e)[2].

$$h = l\cos\theta + \frac{1}{2}\frac{l^2}{R_\oplus}\sin^2\theta\,,$$

where $R_\oplus$ is the Earth radius, being the second term of this expression indeed a correction for the ground curvature, which becomes increasingly important when a very large height is considered (translating into considering long living particles), or conversely a very big region

---

[1] See for example T. Stanev, High Energy Cosmic Rays, (Springer, 2010), ISBN 9783540851486

of interest. The atmospheric depth for such an inclined direction is called the **slant depth** and corresponds to:

$$x \equiv \int_{l}^{+\infty} \rho\left(l'\right)\,\mathrm{d}l' \qquad \text{with} \qquad l' = l'\left(h\right)\ .$$

For small zenith angles, i.e. $\theta < 60°$, one can scale the slant depth as

$$x \simeq \frac{x_v}{\cos\theta} \qquad \text{and} \qquad \rho \simeq \frac{x_v}{h_0} = \frac{x\cos\theta}{h_0}\ ,$$

and this scaling is called *flat Earth approximation.*

Exercise 3.1. Interaction versus decay probability of secondary cosmic rays

Primary cosmic ray protons interact in the atmosphere with a mean free path $\lambda_I \simeq 100\mathrm{g\ cm}^{-2}$. They produce relativistic charged pions, i.e. secondary cosmic rays, travelling downwards. Such pions may subsequently decay in flight or they may undergo further interactions, which will be nuclear interactions and with a mean path that we approximate as equal to λ_I.

i) Assuming that secondary pions only undergo nuclear interactions, what is the probability $\mathrm{d}P_I^\pi/\mathrm{d}x$ for a pion to interact at the atmospheric depth $[x,\ x+\mathrm{d}x]$?

ii) Pions have indeed a finite lifetime $\tau_\pi = 26\,\mathrm{ns}$. Show that the overall probability for a pion with energy E_π to decay rather than interacting is

$$P_d^\pi = \frac{E_0}{(E_0 + \beta E_\pi)} \qquad \text{with} \qquad E_0 = \frac{m_\pi c^2 h_0}{c\tau}\ ,$$

being β the pion velocity in units of c and $h_0 = 6.5\,\mathrm{km}$;

iii) At which depth $x = x_{\mathrm{max}}$ as a function of E_π most likely does the interacting/decaying pion disappear, i.e. at which value of x the probability distribution $\mathrm{d}P^\pi/\mathrm{d}x$ has its maximum?

iv) At the energies respectively of $E_\pi = m_\pi c^2$, $E_\pi = E_0$ and $E_\pi \to +\infty$, calculate the depth $x = x_{-1}$ at which a fraction $1/e$ of all pions are surviving. To which heights above sea level h_{max} and h_{-1} do such depths correspond?

Let us consider from now on both primary and secondary particles to propagate vertically downwards, i.e. $x = x_v$. The interaction probability P_I in the infinitesimal atmospheric depht interval $[x,\ x+\mathrm{d}x]$ is given by

$$\frac{\mathrm{d}P_I}{\mathrm{d}x} = \frac{1}{\lambda_I'}\,e^{-x/\lambda_I'} \qquad \text{with} \quad \lambda_I = \frac{1}{\mathrm{N}\sigma} = \frac{\omega_a}{\rho\,\mathcal{N}_a\,\sigma}\ , \qquad [\lambda] = \mathrm{cm}\ , \tag{3.6}$$

that is the product of the probability for a particle to have survived till x above the ground and the probability to interact within $\mathrm{d}x$, see Eq.(2.4). Recall that in Sec.(2.1.3) we have seen that the quantity of interest for cosmic rays is $\lambda_I' = \rho\lambda_I$, with $[\lambda_I'] = \mathrm{g\,cm}^{-2}$, which happens to be the same dimensions of $x = x_v$: indeed they are to be compared and, as we have already stated (without proof) in Sec.(2.2.1), $x_{\mathrm{atm}} \gg \lambda_I'$, that is the entire atmospheric height is much larger than the average nuclear interaction lenght, and also than the interaction lenght for pair production λ_γ' (Eq.(2.9)).We can see that the probability to survive for a path lenght x is exponentially decreasing with x, as expected.

---

[2] The density of water is $\rho_{\mathrm{H_2O}} = 997\,\mathrm{kg\,m}^{-3}$ so $\frac{x_v^{\mathrm{atm}}}{\rho_{\mathrm{H_2O}}} \simeq 10.4\,\mathrm{m}$.

Finally, an expression for the finite probability of interaction between $x = 0$ to any value of x is given by integration of the infinitesimal expression Eq.(3.6)

$$P_I\,(x) = \int_0^x \frac{1}{\lambda'_I}\, e^{-x/\lambda'_I}\,\mathrm{d}x = 1 - e^{-x_0/\lambda'_I}\,. \tag{3.7}$$

Having said this, we can now answer to the questions of the problem.

i) To find the probability $\mathrm{d}P_I^\pi/\mathrm{d}x$ for a pion to interact in the infinitesimal interval $[x,\, x + \mathrm{d}x]$, we need to consider three fundamental steps.

1. A proton must survive in the atmosphere till a column density x_0 and then must interact within $[x_0,\, x_0 + \mathrm{d}x_0]$ to produce a pion, and this infinitesimal probability is given by:
$$\frac{\mathrm{d}P_{\text{prod}}}{\mathrm{d}x_0} = e^{-x_0/\lambda'_I}\,\frac{1}{\lambda'_I}\;;$$
2. The pion must not interact up to a depht $x_1 > x_0$, and the finite probability of surviving such a path is
$$P_{\text{surv}}\,(x_1 > x_0) = 1 - \int_0^{\Delta x} \frac{\mathrm{d}P_I}{\mathrm{d}x'}\,\mathrm{d}x' = e^{-(x_1 - x_0)/\lambda'_I}\;, \tag{3.8}$$
where clearly we have called $\Delta x = x_1 - x_0$;
3. The pion, lastly, must interact within the infinitesimal depht $[x_1,\, x_1 + \mathrm{d}x_1]$. This probability is
$$\frac{\mathrm{d}P_I}{\mathrm{d}x_1} = \frac{1}{\lambda'_I}\;,$$
where we stress that λ'_I is the same as for the proton by assumption.

Putting all these factors together, the probability for a pion to be produced at $[x_0,\, x_0 + \mathrm{d}x_0]$, to survive till $x_1 > x_0$ and finally to interact within $[x_1,\, x_1 + \mathrm{d}x_1]$ is the following product:

$$\frac{\mathrm{d}^2 P_I^\pi}{\mathrm{d}x_0\,\mathrm{d}x_1} = \frac{\mathrm{d}P_{\text{prod}}^\pi}{\mathrm{d}x_0}\,(x_0)\;P_{\text{surv}}^\pi\,(x_1 > x_0)\;\frac{\mathrm{d}P_I^\pi}{\mathrm{d}x_1}\,(x_1) = \frac{1}{\lambda'^2_I}\,e^{-x_1/\lambda'_I}\;,$$

and we shall note that we have chosen x_1 and x_0 quite generically, so the probability for a pion to interact at a generic $[x,\, \mathrm{d}x]$ is obtained by replacing x_1 with a generic x and integrating for any $y < x_1 = x$, with y replacing x_0:

$$\frac{\mathrm{d}P_I^\pi}{\mathrm{d}x} = \int_0^x \frac{\mathrm{d}^2 P_I^\pi}{\mathrm{d}y\,\mathrm{d}x}\,\mathrm{d}y = \frac{x}{\lambda'^2_I}\,e^{-x/\lambda'_I}\;,$$

which has also the right normalization since

$$\int_0^{x_{\text{atm}}} \frac{\mathrm{d}P_I^\pi}{\mathrm{d}x}\,\mathrm{d}x = \int_0^{x_{\text{atm}}} \frac{x}{\lambda'^2_I}\,e^{-x/\lambda'_I}\,\mathrm{d}x = \int_0^{x_{\text{atm}}/\lambda'_I} u e^{-u}\,\mathrm{d}u =$$

$$= 1 - \left(\frac{x_{\text{atm}}}{\lambda'_I} + 1\right) e^{-x_{\text{atm}}/\lambda'_I} \simeq 1\;,$$

with the change of variable $u = x/\lambda'_I$. We have used the fact that $x_{\text{atm}} = 1030\,\mathrm{g\,cm^{-2}}$ and $\lambda'_I = 100\mathrm{g cm^{-2}}$, so the deviaton from one is represented by a completely negligible factor. Indeed the profile of the function is extended towards infinity, and by integrating from 0 to $+\infty$ would have given exactly 1, but to be consistent with our definition of

$x_{\rm atm}$ this integration does not make sense: the Earth atmospheric depht is a finite, though big, value. Furthermore the approximations we are working with are definitely introducing bigger errors than this one: we are neglecting energy losses by collisions and radiation which are indeed affecting charged particles such as our meson. In Fig.(3.4) we show the behavior of $\mathrm{d}P_I^\pi/\mathrm{d}x$: the profile has a maximum at $x = \lambda_I'$, which is coherent with the fact that in this treatment we have considered only nuclear interactions, neglecting the probability of decay and other kind of reactions.

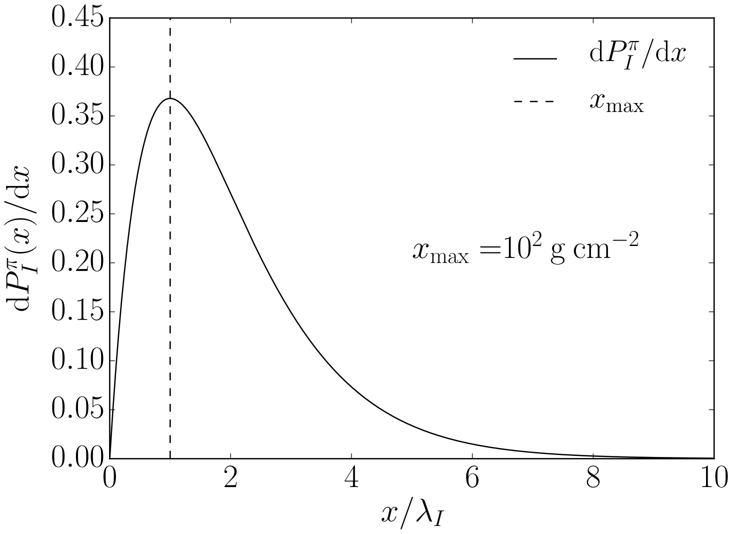

Figure 3.4: Differential probability $\mathrm{d}P_I^\pi/\mathrm{d}x$ as a function of the ratio between x and λ_I'. The maximum is also calculated and shown.

To address the second request we need to calculate the probability P_d^π for a pion to decay within the time interval $[t_\pi, t_\pi + \mathrm{d}t_\pi]$, where t_π is measured in the pion rest frame. Calling τ_π the mean lifetime of a pion, the differential probability law of decay is given by

$$\frac{\mathrm{d}P_d}{\mathrm{d}t_\pi} = \frac{1}{\tau_\pi}\, e^{-t_\pi/\tau_\pi} \ ,$$

which intuitively corresponds to the combined probability of decay in a fraction of τ_π, that is the first factor, and the probability to have survived for a lifetime of τ_π, that is the exponential law of the second factor. Let's express this probability as a function of the atmospheric depht x:

$$\frac{\mathrm{d}P_d}{\mathrm{d}x} = \frac{\mathrm{d}P_d}{\mathrm{d}t_\pi}\,\frac{\mathrm{d}t_\pi}{\mathrm{d}h}\,\frac{\mathrm{d}h}{\mathrm{d}x} \ ,$$

where h is the vertical height travelled by the particle. The first factor is actually what we have just written above; the second factor can be simply obtained by writing

$$\mathrm{d}t = \mathrm{d}t_\pi \gamma \ , \qquad\qquad \mathrm{d}h = -v\mathrm{d}t \ ,$$

with which we found the time in the observer reference frame via a Lorentz transformation and the differential law for the accelerated motion of the meson with a velocity v in $\mathrm{d}t$. Combining the two expressions we obtain

$$\mathrm{d}h = -\beta c \gamma\, \mathrm{d}t_\pi \qquad \Rightarrow \qquad \frac{\mathrm{d}t_\pi}{\mathrm{d}h} = -\frac{1}{c\beta\gamma} \ . \tag{3.9}$$

The third factor is again straightforward, once one differentiates Eq.(3.5):

$$\mathrm{d}x = \frac{-x_{\rm atm}}{h_0}\, e^{-h/h_0}\, \mathrm{d}h \qquad \Rightarrow \qquad \frac{\mathrm{d}h}{\mathrm{d}x} = -\frac{h_0}{x_{\rm atm}}\, e^{h/h_0} = -\frac{h_0}{x} \ , \tag{3.10}$$

and we shall stress that clearly the atmosphere is not homogeneous. By integration of the previous expression one easily finds also the dependence of h with x:

$$h = \int_{x}^{x_{\mathrm{atm}}} \frac{h}{x'}\,\mathrm{d}x' = h_0 \log\left(\frac{x_{\mathrm{atm}}}{x}\right) \tag{3.11}$$

So the differential probability of a pion decay within a given atmospheric depht interval $[x,\, x + \mathrm{d}x]$ is completely known. In practice however we need to consider a sequence of processes as the one we hypothesized before: this is what we are doing addressing the second request.

ii) To find the probability $\mathrm{d}P_d^{\pi}/\mathrm{d}x$ for a pion to decay in the infinitesimal interval $[x,\, x + \mathrm{d}x]$, we need to consider three fundamental steps.

1. A proton must survive in the atmosphere till a column density x_0 and than must interact within $[x_0,\, x_0 + \mathrm{d}x_0]$ to produce a pion, and this infinitesimal probability is given by:

$$\frac{\mathrm{d}P_{\mathrm{prod}}}{\mathrm{d}x_0} = e^{-x_0/\lambda_I'}\,\frac{1}{\lambda_I'}\ ;$$

2. The pion must not interact neither decay up to a depht $x_1 > x_0$, and the finite probability of surviving such a path is

$$P_{\mathrm{surv}}\,(x_1 > x_0) = 1 - \int_0^{\Delta x} \frac{\mathrm{d}P_I}{\mathrm{d}x'}\,\mathrm{d}x' = e^{-(x_1 - x_0)/\lambda_I'}\ ,$$

where clearly we have called $\Delta x = x_1 - x_0$. In particular, here we have accounted for the probability of not having an interaction, while the third factor will account also for the probability for a pion to not undergo a decay in $[x_0,\, x_1]$;

3. The pion, lastly, must decay within the infinitesimal depht $[x_1,\, x_1 + \mathrm{d}x_1]$. This probability is

$$\frac{\mathrm{d}P_d}{\mathrm{d}x_1}\,(x_1\,, x_0) = \frac{\mathrm{d}P_d}{\mathrm{d}t_\pi}\,\frac{\mathrm{d}t_\pi}{\mathrm{d}h}\,\frac{\mathrm{d}h}{\mathrm{d}x_1} = \left(\frac{1}{\beta\gamma c}\right)\left(\frac{h_0}{x_1}\right)\frac{1}{\tau_\pi}\,e^{-t_\pi/\tau_\pi}\ ,$$

where we stress that λ_I' is the same as for the proton by assumption. Integrating Eq.(3.9) from $h(x_1)$ to $h(x_0)$ and substituting for Eq.(3.11), the time t_π in the pion rest frame can be rewritten in these terms

$$t_\pi = -\frac{1}{\beta\gamma c}\,[h\,(x_1) - h\,(x_0)] = -\frac{h_0}{\beta\gamma c}\log\left(\frac{x_{\mathrm{atm}}}{x_1}\,\frac{x_0}{x_{\mathrm{atm}}}\right) = -\frac{h_0}{\beta\gamma c}\log\left(\frac{x_0}{x_1}\right)\ ,$$

so the probability for a pion not to decay within $[x_0,\, x_1]$ and then decay in the infinitesimal interval $[x_1,\, x_1 + \mathrm{d}x]$ becomes

$$\frac{\mathrm{d}P_d}{\mathrm{d}x_1}\,(x_1\,, x_0) = \frac{\alpha}{x_1}\exp\left\{\alpha\log\left(\frac{x_0}{x_1}\right)\right\} = \frac{\alpha}{x_1}\left(\frac{x_0}{x_1}\right)^{\alpha}\ ,$$

with α being a factor dependent on energy which shall be defined in few rows.

Putting all these factors together, the probability for a pion to be produced at $[x_0,\, x_0 + \mathrm{d}x_0]$, to survive till $x_1 > x_0$ and finally to decay within $[x_1,\, x_1 + \mathrm{d}x_1]$ is the following product:

$$\frac{\mathrm{d}^2 P_d^{\pi}}{\mathrm{d}x_0\,\mathrm{d}x_1} = \frac{\mathrm{d}P_{\mathrm{prod}}}{\mathrm{d}x_0}\,(x_0)\ P_{\mathrm{surv}}\,(x_1 > x_0)\ \frac{\mathrm{d}P_d}{\mathrm{d}x_1}\,(x_1,\, x_0)\ ,$$

where we notice that the last factor depends on both the production point and the decay point. The resulting expression is

$$\frac{\mathrm{d}^2 P_d^\pi}{\mathrm{d}x_0\,\mathrm{d}x_1} = \frac{1}{\lambda_I' x_1}\exp\left\{-\frac{x_1}{\lambda_I'}\right\}\alpha\left(\frac{x_0}{x_1}\right)^\alpha \qquad \text{with} \quad \alpha \equiv \frac{h_0}{c\tau_\pi\beta\gamma} ,$$

so, analogously to the first request, the probability for a pion to decay at a generic $[x,\, \mathrm{d}x]$ is obtained by replacing x_1 with a variable x and integrating for any $y < x_1 = x$, with y replacing x_0:

$$\frac{\mathrm{d}P_d^\pi(x)}{\mathrm{d}x} = \int_0^x \frac{\mathrm{d}^2 P_d^\pi}{\mathrm{d}x\,\mathrm{d}y}\,\mathrm{d}y = \frac{\alpha}{\alpha+1}\frac{1}{\lambda_I'}\exp\left\{-\frac{x}{\lambda_I'}\right\} . \tag{3.12}$$

This expression decreases exponentially with x, so the shape is very different from the previous Fig.(3.4): in fact, the decay probability depends mainly on the time of flight of the pion, while the interaction probability depends on the amount of matter encountered. Anyway it is important to realize that this is not a simple decay law: it keeps in memory the production point and deeply depends on it via α, which measures the energy of the produced pion since $\alpha = \alpha(\gamma,\, \beta)$. The profile of $\mathrm{d}P_d(x)/\mathrm{d}x$ is shown in Fig.(3.5), with different values of α which will be interesting in the following. The overall probability P_d^π for a pion to decay anywhere is given by integration

$$P_d^\pi = \int_0^{x_\mathrm{atm}} \frac{\mathrm{d}P_d^\pi(x)}{\mathrm{d}x}\,\mathrm{d}x = \frac{\alpha}{\alpha+1}\left(1 - e^{-x_\mathrm{atm}/\lambda_I'}\right) \simeq \frac{\alpha}{\alpha+1} ,$$

where the approximation holds for the large value of $x_\mathrm{atm} \gg \lambda_I'$. The energy of the pion in the Earth rest frame is given by $E_\pi = m_\pi c^2\gamma$, and introducing a critical energy E_0 such that

$$E_0 \equiv \alpha\beta\, E_\pi = \frac{m_\pi c^2 h_0}{c\tau_\pi} ,$$

we can write P_d^π in the requested form

$$P_d^\pi = \frac{E_0}{(E_0 + \beta E_\pi)} .$$

We shall note that $\alpha > 0$ by definition, meaning that no pions will have a zero probability of decay before reaching the ground, which is in agreement with our previous calculation in Sec.(1.1). Also $P_d^\pi \neq 1$, since it accounts for the probability of pions to be produced.

iii) This request involves comparing the two factors, decay and interaction, for the pion. Let's then study the probability for a pion to interact and *not* decay $\mathrm{d}P_{I,\,\bar d}^\pi/\mathrm{d}x$ whithin an infinitesimal interval $[x,\, x + \mathrm{d}x]$: the usual multiplication rule of probability gives

$$\frac{\mathrm{d}P_{I,\,\bar d}^\pi(x)}{\mathrm{d}x} = \frac{\mathrm{d}P_I^\pi}{\mathrm{d}x}\,P_{\bar d}^\pi = \frac{\mathrm{d}P_I^\pi}{\mathrm{d}x}\,(1 - P_d^\pi) = \frac{1}{\alpha+1}\,\frac{x}{(\lambda_I')^2}\,e^{-x/\lambda_I'} . \tag{3.13}$$

Finally, the probability for a pion to disappear at atmospheric depht $[x,\, x + \mathrm{d}x]$ by means of decay *or* nuclear interaction is given by

$$\frac{\mathrm{d}P^\pi}{\mathrm{d}x} = \frac{\mathrm{d}P_{I,\,\bar d}^\pi(x)}{\mathrm{d}x} + \frac{\mathrm{d}P_d^\pi(x)}{\mathrm{d}x} = \left[\frac{1}{\alpha+1}\,\frac{x}{\lambda_I'} + \frac{\alpha}{1+\alpha}\right]\frac{1}{\lambda_I'}\,e^{-x/\lambda_I'} ,$$

which is nothing else than the sum of the probabilities of two mutually exclusive events. This expression is a function of the energy of the pion through α, and we can

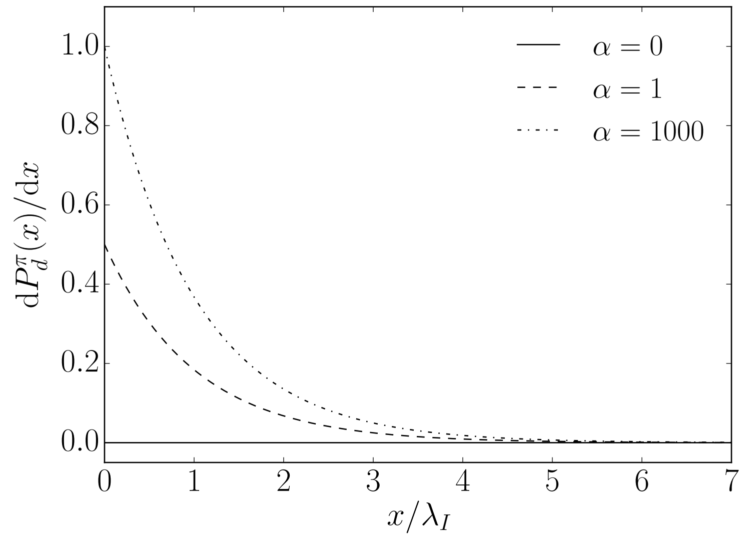

Figure 3.5: Differential probability $\mathrm{d}P_d^\pi/\mathrm{d}x$ for a pion to disappear by decaying within $[x,\, \mathrm{d}x]$.

consider it for some fixed values of this parameter: Fig.(3.6) shows the behavior for $\alpha = 0, 1, 1000$. In particular we can see that for large values of α, namely for $\alpha \to +\infty$, the profile reduces to a pure decay law, since this case corresponds to a meson produced at rest with energy $E = m_\pi c^2$ and an immediate decay right at the production point is expected; for $\alpha \to 0$ the pion is produced with very high energy, and the decay probability is completely negligible with respect to interaction processes, namely the case of request i) is recovered; lastly for $\alpha = 1$ the two processes are competing. These observations translate into the fact that

- if $E_\pi < E_0$ ($\alpha > 1$) the decay is more likely, P_d^π is large;
- if $E_\pi > E_0$ ($\alpha < 1$) the interactions are more likely and P_d^π becomes very low.

So what will be the maximizing value $x_{\max}$ of the atmospheric depht for this probability density distribution? A functional analysis leads to

$$\frac{\mathrm{d}}{\mathrm{d}x}\left(\frac{\mathrm{d}P^\pi}{\mathrm{d}x}\right) = \frac{1}{\alpha+1}\,\frac{1}{\left(\lambda_I'\right)^2}\left[1 - \frac{x}{\lambda_I'} - \alpha\right] e^{-x/\lambda_I'} \overset{!}{=} 0 \qquad \Leftrightarrow$$

$$x_{\max} = \lambda_I'\,(1-\alpha) = \lambda_I'\left(1 - \frac{E_0}{\beta E_\pi}\right) ,$$

and for $x_{\max} > 0$ we need $\alpha < 1$, which is indeed the case in which the curve really shows a maximum as we can see in Fig.(3.6).

iv) We need to find the depht $x = x_{-1}$ at which a fraction $1/e$ of all pions are surviving for different energies. We can find it integrating the probability profile with the substitution $u = x_{-1}/\lambda_I'$:

$$\int_{x=0}^{x=x_{-1}} \frac{\mathrm{d}P^\pi}{\mathrm{d}x}\,\mathrm{d}x = \frac{1}{\alpha+1}\left[-ue^{-u}\Big|_0^{x_{-1}/\lambda_I'} - e^{-u}\Big|_0^{x_{-1}/\lambda_I'} - \alpha\, e^{-u}\Big|_0^{x_{-1}/\lambda_I'}\right] =$$

$$= 1 - \frac{e^{-x_{-1}/\lambda_I'}\left(1+\alpha+x_{-1}/\lambda_I'\right)}{1+\alpha} \overset{!}{=} 1 - \frac{1}{e}\,, \tag{3.14}$$

which can't be solved analytically for an expression of x_{-1}. Some numerical values can be given for some interesting values of α, and can be visualize also in Fig.(3.7):

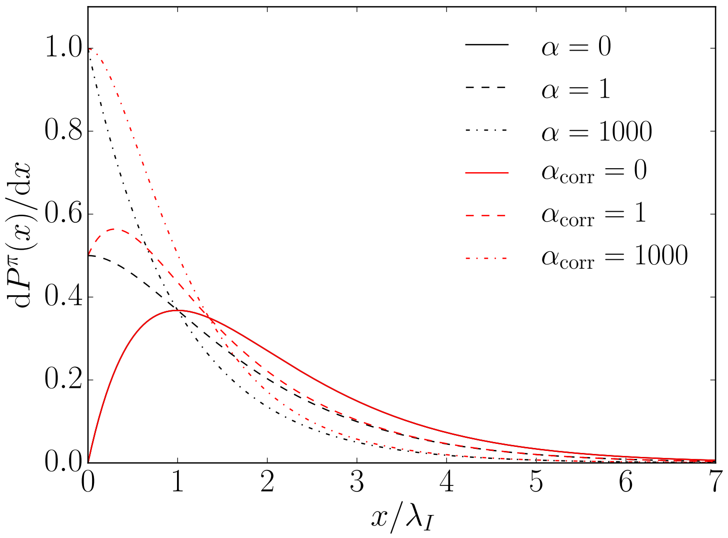

Figure 3.6: Differential probability $\mathrm{d}P^\pi/\mathrm{d}x$ for a pion to disappear by either decaying or interacting with atmospheric nuclei within $[x,\,\mathrm{d}x]$. See text for explanations for the red curves and $\alpha_{\rm corr}$.

- For $\alpha = 0$ ($E_\pi \to +\infty$) one finds $x_{-1} \simeq 2.14\;\lambda'_I$;
- For $\alpha = 1$ ($E_\pi \simeq E_0$) one finds $x_{-1} \simeq 1.58\;\lambda'_I$;
- For $\alpha \to +\infty$ ($E_\pi = m_\pi c^2$) one finds $x_{-1} \simeq \lambda'_I$.

An integration of Eq.(3.10) gives the height corresponding to such atmospheric depht $h_{-1} = h(x_{-1})$ and also for the maximum depth of the probability density $h_{\rm max} = h(x_{\rm max})$:

$$h = \int_x^{x_{\rm atm}} \frac{h}{x'}\,\mathrm{d}x' = h_0 \log\left(\frac{x_{\rm atm}}{x}\right) = 6.5\;\mathrm{km}\left(2.3 - \log\frac{x}{\lambda'_I}\right) \qquad (3.15)$$

$$\Rightarrow \qquad h_{\rm max} = 6.5\;\mathrm{km}\,(2.3 - \log\,(1-\alpha)) = 14.95\;\mathrm{km}\,,$$

where the last estimate is obviously taken for $\alpha = 0$, and then

$$\Rightarrow \qquad h_{-1} \overset{\alpha=0}{=} 10\;\mathrm{km}\,, \qquad h_{-1} \overset{\alpha=1}{=} 11.98\;\mathrm{km}\,, \qquad h_{-1} \overset{\alpha\to+\infty}{=} 14.95\;\mathrm{km}\,.$$

Actually, now that we have computed the integral of $\mathrm{d}P^\pi/\mathrm{d}x$ till the depht x_{-1}, we can also check the normalization of the total probability:

$$\int_{x=0}^{x=x_{\rm atm}} \frac{\mathrm{d}P^\pi}{\mathrm{d}x}\,\mathrm{d}x = 1 - \frac{e^{-x_{\rm atm}/\lambda'_I}\,(1+\alpha+x_{\rm atm}/\lambda'_I)}{1+\alpha} \simeq 1\,,$$

since again $x_{\rm atm}/\lambda'_I \gg 1$ and the exponential function of this argument always wins over the argument itself.

A puntualization on request i) In the first request the decay possibility is essentially neglected. This approximation enters in the estimate of $P_{\rm surv}\,(x_1 > x_0)$, Eq.(3.8): in this term only the probability of surviving an interaction till a depht x_1 was accounted for, and one can wonder what actually changes in the total profile of $\mathrm{d}P^\pi_I/\mathrm{d}x$, namely the probability for a pion to interact at a generic $[x,\,\mathrm{d}x]$, if the decays are introduced. The possibility of decays can be introduced as follows:

$$P_{\rm surv}\,(x_1 > x_0) = \left[1 - \int_0^{\Delta x} \frac{\mathrm{d}P_I}{\mathrm{d}x'}\,\mathrm{d}x'\right]\,e^{-t_\pi/\tau_\pi} = e^{-(x_1-x_0)/\lambda'_I}\,e^{-t_\pi/\tau_\pi}\,,$$

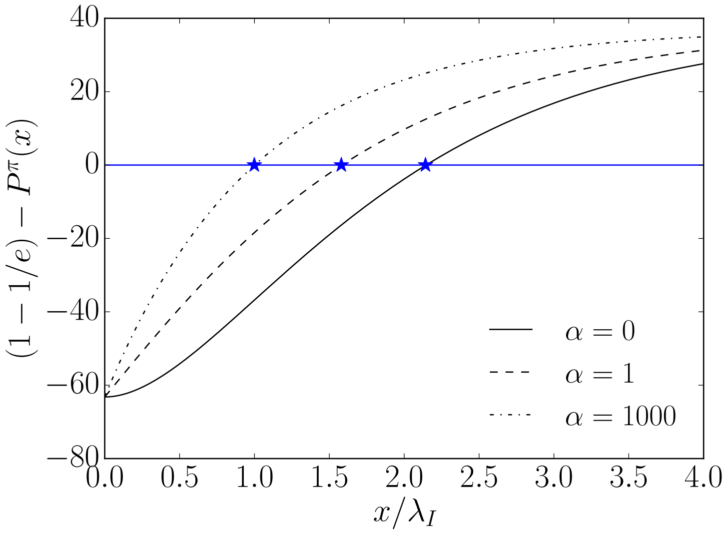

Figure 3.7: Graphical resolution with $\epsilon = 10^{-6}$ tolerance of the equation Eq.(3.14). The solutions in text are highlighted in blu with starred points.

where we have essentially multiplied our previous result by the additional factor which accounts for the probability of surviving a decay within a fraction t_π of the pion lifetime. The dependence on the traveled column density in the new exponential term can be made explicit by the same arguments as in request ii):

$$\frac{\mathrm{d}t_\pi}{\mathrm{d}h} = -\frac{1}{c\beta\gamma} \qquad \Rightarrow \qquad t_\pi = -\frac{1}{c\beta\gamma}\left[h(x_1) - h(x_0)\right] = -\frac{1}{c\beta\gamma}\log\left(\frac{x_0}{x_1}\right) .$$

Now that we have modified $P_{\mathrm{surv}}(x_1 > x_0)$, let us put all the factors together and write the final expression for the probability for a pion to be produced at $[x_0,\, x_0 + \mathrm{d}x_0]$, to survive till $x_1 > x_0$ and finally to interact within $[x_1,\, x_1 + \mathrm{d}x_1]$:

$$\frac{\mathrm{d}^2 P_I^{\pi}}{\mathrm{d}x_0\, \mathrm{d}x_1} = \frac{\mathrm{d}P^{\pi}_{\mathrm{prod}}}{\mathrm{d}x_0}(x_0)\; P^{\pi}_{\mathrm{surv}}(x_1 > x_0)\; \frac{\mathrm{d}P_I^{\pi}}{\mathrm{d}x_1}(x_1) = \frac{1}{\lambda_I'^2}\, e^{-x_1/\lambda_I'}\left(\frac{x_0}{x_1}\right)^{\alpha} ,$$

in which, with respect to the previous case, a new factor, dependent on the energy of the pion, appears. The probability for a pion to interact at a generic $[x,\, \mathrm{d}x]$ is obtained by replacing x_1 with a generic x and integrating for any $y < x_1 = x$, with y replacing the generic x_0:

$$\frac{\mathrm{d}P_I^{\pi}}{\mathrm{d}x} = \int_0^x \frac{\mathrm{d}^2 P_I^{\pi}}{\mathrm{d}y\, \mathrm{d}x}\, \mathrm{d}y = \frac{1}{\lambda_I'^2}\, \frac{1}{x^{\alpha}}\, e^{-x/\lambda_I'} \int_0^x y^{\alpha}\, \mathrm{d}y = \frac{1}{1+\alpha}\, \frac{x}{\lambda_I'^2}\, e^{-x/\lambda_I'} ,$$

and again a new factor $1/(\alpha+1)$ is gained. This factor is not expected to introduce new features in the profile of the probability, anyway it is explicative of the fact that, for increasing α, the interaction probability is suppressed at *any* atmospheric depht, that is for lower production energies the decay is much more likely to happen anywhere. This is shown in Fig.(3.8), where for $\alpha = 1000$ the profile is flattened to zero, and for $\alpha = 0$ the correspondence with the previous result is perfect, as expected.
Furthermore, what we have just found is indeed the very same expression we got in request iii) for the probability for a pion to interact and *not* decay within $[x,\, x + \mathrm{d}x]$, namely $\mathrm{d}P^{\pi}_{I,\bar{d}}/\mathrm{d}x$ from Eq.(3.13). This is quite reasonable: the intrinsic meaning of accounting for decay possibility is encoded in the new factors, and they shall be recovered in both approaches.

Let us check the normalization of this probability $\mathrm{d}P_I^\pi/\mathrm{d}x$:

$$\int_0^{x_{\mathrm{atm}}} \frac{\mathrm{d}P_I^\pi}{\mathrm{d}x}\,\mathrm{d}x = \frac{1}{1+\alpha}\int_0^{x_{\mathrm{atm}}} \frac{x}{\lambda_I'^2}\,e^{-x/\lambda_I'}\,\mathrm{d}x = \frac{1}{1+\alpha}\int_0^{x_{\mathrm{atm}}/\lambda_I'} u e^{-u}\,\mathrm{d}u =$$

$$= \frac{1}{1+\alpha}\left[1-\left(\frac{x_{\mathrm{atm}}}{\lambda_I'}+1\right)e^{-x_{\mathrm{atm}}/\lambda_I'}\right] \simeq \frac{1}{1+\alpha}\,,$$

and again $u = x_{\mathrm{atm}}/\lambda_I'$, with $x_{\mathrm{atm}}/\lambda_I' \gg 1$. This probability is unavoidably less than one, since $\alpha > 0$: this can be explained by the fact that now the decays are taken into account.

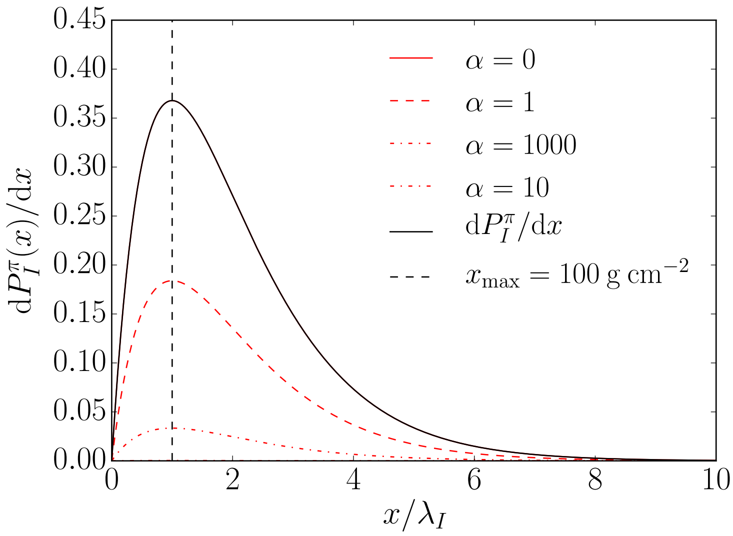

Figure 3.8: Differential probability of interactions at $[x,\ x+\mathrm{d}x]$ for a pion, taking into account the decay possibility with the red profiles. Also the maximum x_{max}, unchanged in both cases, is highlighted.

A puntualization on request iii) In the computation of $\mathrm{d}P_{I,\bar{d}}^\pi/\mathrm{d}x$, Eq.(3.13), one can object that, instead of taking into account the total probability for a pion not to decay $P_{\bar{d}}^\pi$, the correct expression shall account just for an interval of the column density, till a generic value x. Let's see what actually changes if one follows this way. Firstly, $\mathrm{d}P_{I,\bar{d}}^\pi/\mathrm{d}x$ becomes

$$\frac{\mathrm{d}P_{I,\bar{d}}^\pi(x)}{\mathrm{d}x} = \frac{\mathrm{d}P_I^\pi}{\mathrm{d}x}\left[\int_0^x \frac{\mathrm{d}P_{\bar{d}}^\pi}{\mathrm{d}x}\,\mathrm{d}x\right] = \frac{\mathrm{d}P_I^\pi}{\mathrm{d}x}\left[1-\int_0^x \frac{\mathrm{d}P_d^\pi}{\mathrm{d}x}\,\mathrm{d}x\right]\,,$$

where the fundamental difference is that the upper limit of the integral is x, not anymore x_{atm}. The factor in square brackets contains an elementary integral. Recalling the expression of the differential probability to decay $\mathrm{d}P_d^\pi/\mathrm{d}x$ Eq.(3.12), we obtain:

$$\int_0^x \frac{\mathrm{d}P_d^\pi}{\mathrm{d}x}\,\mathrm{d}x = \int_0^x \frac{\alpha}{\alpha+1}\,\frac{1}{\lambda_I'}\,e^{-x/\lambda_I'}\,\mathrm{d}x = \frac{\alpha}{\alpha+1}\int_0^{x/\lambda_I'} e^{-u}\,\mathrm{d}u = \frac{\alpha}{\alpha+1}\left(1-e^{-x/\lambda_I'}\right)\,,$$

where we have performed the substitution $u = x/\lambda_I'$. So the resulting expression for $\mathrm{d}P_{I,\bar{d}}^\pi/\mathrm{d}x$ becomes:

$$\frac{\mathrm{d}P_{I,\bar{d}}^\pi(x)}{\mathrm{d}x} = \frac{\mathrm{d}P_I^\pi}{\mathrm{d}x}\left(\frac{1}{\alpha+1}+\frac{\alpha}{\alpha+1}\,e^{-x/\lambda_I'}\right) = \frac{x}{(\lambda_I')^2}\,\frac{1}{\alpha+1}\,e^{-x/\lambda_I'}\left(1+\alpha\,e^{-x/\lambda_I'}\right)\,.$$

Finally, the total probability for a pion to disappear at atmospheric depht $[x,\, x+\mathrm{d}x]$ by means of a decay *or* nuclear interaction is given by

$$\frac{\mathrm{d}P^\pi}{\mathrm{d}x} = \frac{\mathrm{d}P^\pi_{I,\bar{d}}(x)}{\mathrm{d}x} + \frac{\mathrm{d}P^\pi_{d}(x)}{\mathrm{d}x} = \frac{1}{\lambda_I'}\, e^{-x/\lambda_I'} \left[\frac{x}{\lambda_I'}\,\frac{1}{\alpha+1} + \frac{\alpha}{\alpha+1}\right] + \frac{x}{(\lambda_I')^2}\,\frac{\alpha}{\alpha+1}\, e^{-2x/\lambda_I'} =$$

$$= \left.\frac{\mathrm{d}P^\pi}{\mathrm{d}x}\right|_{\text{before}} + \frac{x}{(\lambda_I')^2}\,\frac{\alpha}{\alpha+1}\, e^{-2x/\lambda_I'}\,,$$

where the first term is exactly the result we haave obtained before, without the correction. The new term is expected to introduce some mild new features in the profile of $\mathrm{d}P^\pi/\mathrm{d}x$, and this is shown in Fig.(3.6) in red. The lines corresponding to $\alpha_{\text{corr}} = 0$ are perfectly superimposed in the two cases, as expected: in this case the curve is simply the interaction probability, which does not depend on our new correction. For $\alpha_{\text{corr}} = 1$ a new maximum appears too, showing a non trivial addition of the processes of decay and interaction, which are indeed competing. The case of $\alpha_{\text{corr}} = 1000$ is interesting: for the red curve the profile is not yet a perfect exponential law, differently from the black line.
Let us now inspect on the consequences on the estimate of the maximazing value $x_{\max}$ of the atmospheric depht for this probability density distribution. A functional analysis leads to

$$\frac{\mathrm{d}}{\mathrm{d}x}\left(\frac{\mathrm{d}P^\pi}{\mathrm{d}x}\right) = \frac{1}{\alpha+1}\,\frac{1}{\left(\lambda_I'\right)^2}\left[1 - \frac{x}{\lambda_I'} - \alpha\right] e^{-x/\lambda_I'} + \frac{1}{(\lambda_I')^2}\,\frac{\alpha}{\alpha+1}\, e^{-2x/\lambda_I'}\left[1 - \frac{2x}{\lambda_I'}\right] \stackrel{!}{=} 0$$

$$\Leftrightarrow \qquad 1 - \frac{x}{\lambda_I'} - \alpha + \alpha\left(1 - \frac{2x}{\lambda_I'}\right) e^{-x/\lambda_I'} \stackrel{!}{=} 0$$

$$\Leftrightarrow \qquad x \stackrel{!}{=} \lambda_I' \left[\frac{1 + \alpha\, e^{-x/\lambda_I'} - \alpha}{1 + 2\alpha\, e^{-x/\lambda_I'}}\right],$$

which can't be solved for an analytical expression of $x_{\max}$, but some numerical values can be given through the relaxation method with $\epsilon = 10^{-6}$ tolerance for some interesting values of α:

- For $\alpha_{\text{corr}} = 0$ ($E_\pi \to +\infty$) one finds the exact value $x_{\max} = \lambda_I'$, which is exactly what is expected for a pure interaction probability;
- For $\alpha_{\text{corr}} = 1$ ($E_\pi \simeq E_0$) one finds the approximate value $x_{\max} \simeq 0.3\,\lambda_I'$ after 5 iterations, and this is indeed the "new" maximum which we can see in the plot, in between $0 < x_{\max}/\lambda_I' < 1$ because the effects are competing;
- For $\alpha_{\text{corr}} \to +\infty$ ($E_\pi = m_\pi c^2$) one finds simply $x_{\max} \to 0$, as expected for a pure decay law, in which simply the maximum search makes no sense.

What we need to investigate now are the effects of the corrections in the determination of the depht x_{-1} at which a fraction $1/e$ of all pions are surviving for different energies. Let us then integrate the probability profile:

$$\int_0^{x=x_{-1}} \frac{\mathrm{d}P^\pi}{\mathrm{d}x}\,\mathrm{d}x = \int_0^{x=x_{-1}} \left.\frac{\mathrm{d}P^\pi}{\mathrm{d}x}\right|_{\text{before}} \mathrm{d}x + \int_0^{x=x_{-1}} \frac{x}{(\lambda_I')^2}\,\frac{\alpha}{\alpha+1}\, e^{-2x/\lambda_I'}\,\mathrm{d}x\,,$$

and the second integral is elementary with the substitution $u = 2x/\lambda_I'$:

$$\int_0^{x=x_{-1}} \frac{x}{(\lambda_I')^2}\,\frac{\alpha}{\alpha+1}\, e^{-2x/\lambda_I'}\,\mathrm{d}x = \frac{\alpha}{\alpha+1}\,\frac{1}{4}\int_0^{2x_{-1}/\lambda_I'} u\, e^{-u}\,\mathrm{d}u =$$

$$= \frac{\alpha}{\alpha+1}\,\frac{1}{4}\left[-u\,e^{-u}\Big|_0^{2x_{-1}/\lambda'_I} + \int_0^{2x_{-1}/\lambda'_i} e^{-u}\,\mathrm{d}u\right]$$

$$= \frac{\alpha}{\alpha+1}\,\frac{1}{4}\left[\frac{-2x_{-1}}{\lambda'_I}\,e^{-2x_{-1}/\lambda'_I} - e^{-2x_{-1}/\lambda'_I} + 1\right] .$$

Eventually, recalling also Eq.(3.14) for the first term, the condition to determine x_{-1} is then given by

$$\int_0^{x=x_{-1}} \frac{\mathrm{d}P^\pi}{\mathrm{d}x}\,\mathrm{d}x \overset{!}{=} 1 - \frac{1}{e} \qquad \Leftrightarrow \tag{3.16}$$

$$1 - \frac{e^{-x_{-1}/\lambda'_I}\,(1+\alpha+x_{-1}/\lambda'_I)}{1+\alpha} + \frac{\alpha}{\alpha+1}\,\frac{1}{4}\left[\frac{-2x_{-1}}{\lambda'_I}\,e^{-2x_{-1}/\lambda'_I} - e^{-2x_{-1}/\lambda'_I} + 1\right] \overset{!}{=} 1 - \frac{1}{e} ,$$

which is of course not possible to be rewritten in a friendly form for x_{-1}. Numerical values can be found with a graphical method with $\epsilon = 10^{-6}$ tolerance such the one used before in Fig.(3.7), and it is shown in Fig.(3.9). Some interesting values for $\alpha_{\text{corr}} = 0,\ 1,\ 1000$ are given by:

- For $\alpha_{\text{corr}} = 0$ ($E_\pi \to +\infty$) one finds $x_{-1} \simeq 2.14\,\lambda'_I$, which is exactly what is found in our previous analysis, as expected;
- For $\alpha_{\text{corr}} = 1$ ($E_\pi \simeq E_0$) one finds the approximate value $x_{-1} \simeq 1.27\,\lambda'_I$ which is a bit lower than the correspondent value without correction;
- For $\alpha_{\text{corr}} \to +\infty$ ($E_\pi = m_\pi c^2$) one finds $x_{-1} \simeq 0.74\,\lambda'_I$, sensibly lower too.

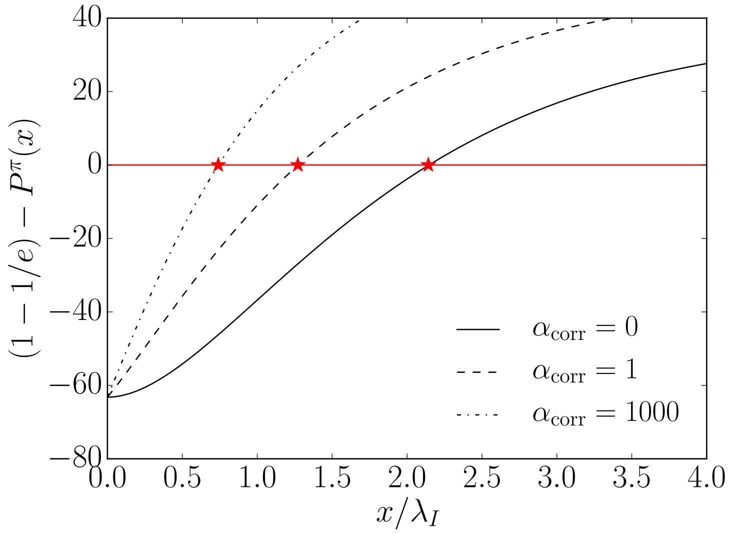

Figure 3.9: Graphical resolution with $\epsilon = 10^{-6}$ tolerance of the equation Eq.(3.16). The solutions in text are highlighted in red with starred points.

Finally, we can perform the calculations of the heights $h_{-1} = h(x_{-1})$ at which $1/e$ of pions have survived and $h_{\max} = h(x_{\max})$ at which the total probability is at its maximum. From Eq.(3.15):

$$h_{-1} \overset{\alpha=0}{=} 10\,\text{km} , \quad h_{-1} \overset{\alpha=1}{=} 13.4\,\text{km} , \quad h_{-1} \overset{\alpha\to+\infty}{=} 16.9\,\text{km} ,$$

$$h_{\max} \overset{\alpha=0}{=} 14.95\,\text{km} , \quad h_{\max} \overset{\alpha=1}{=} 22.78\,\text{km} .$$

These estimates increase for increasing values of α, which means that for lower energies the heights at which only a fraction $1/e$ have survived and at which the probability of disappearence is at maximum are higher, and this is quite reasonable. Actually, now that we have computed the integral of $\mathrm{d}P^{\pi}/\mathrm{d}x$ till the depht x_{-1}, we can also check the normalization of the total probability:

$$\int_0^{x_{\mathrm{atm}}} \frac{\mathrm{d}P^{\pi}}{\mathrm{d}x}\,\mathrm{d}x =$$

$$= 1 - \frac{e^{-x_{\mathrm{atm}}/\lambda_I'}\left(1+\alpha+x_{\mathrm{atm}}/\lambda_I'\right)}{1+\alpha} + \frac{\alpha}{\alpha+1}\,\frac{1}{4}\left[\frac{-2x_{\mathrm{atm}}}{\lambda_I'}\,e^{-2x_{\mathrm{atm}}/\lambda_I'} - e^{-2x_{\mathrm{atm}}/\lambda_I'} + 1\right] \simeq$$

$$\simeq 1 + \frac{1}{4}\,\frac{\alpha}{\alpha+1} = \frac{3\alpha+4}{4\,(\alpha+1)} > 1\,,$$

and notably this expression is unavoidably larger than one, giving exactly one in the case of $\alpha = 0$, which is the case of negligible decay probability, since the interaction probability had indeed the right normalization, at least in the first calculation! In the case of the probability of interaction given in the first puntualization, the normalization is again not one, since decays are taken into account.

3.2 Electromagnetic showers

In this section we shall describe, with a very simple model, an electromagnetic cascade, which is a shower containing only e^+, e^- and γ. The general characteristics we will be able to derive will be very general, valid also in situations other than atmospheric cosmic rays interactions, e.g. in particle detectors. EM showers are governed mainly by Bremsstrahlung of electrons and positrons and pair production by photons. In addition to Bremsstrahlung, electrons and positrons are subject to excitation/ionization energy loss.

3.2.1 The Bethe-Heitler model

Let's describe the so called **Bethe-Heitler** model. In this model, the evolution of electromagnetic cascades is described as a perfect binary tree (Fig.(3.10)). An incoming $e^{\pm}$ interacts in the atmosphere after traveling a certain "step" and produces two new particles by Bremsstrahlung, a photon and its antiparticle, each with half the energy of the initial particle. Similarly, a photon converts into an electron-positron pair if its energy $E_\gamma > 2m_ec^2$: in this way, a sort of equipartition of the primary particle energy is performed. The following simplifying assumptions are adopted:

a) We are treating the interactions of photons and $e^{\pm}$ as they were perfectly equal, which translates into considering the cross sections of the pair production and Bremsstrahlung as identical and independent on the energy. As a consequence, also the radiation length x_0 represents both photon's and electron's mean free paths in the matter, neglecting for the former the factor 7/9. The two processes are intimately related, as Fig.(2.6) shows;

b) Additional energy loss mechanisms, other than the two listed processes, are ignored, introducing a great degree of approximation in particular for the ignored excitation/ionization losses.

Let's recall that the radiation length, x_0, and the critical energy E_c (the energy at which radiation energy losses equal those deriving from excitation/ionization) depend on the material and for electrons in air we have

$$\mathrm{x}_0 \simeq 37\,\mathrm{g\,cm^{-2}}\,, \qquad\qquad E_c \simeq 86\,\mathrm{MeV}\,,$$

just to keep in mind the order of magnitude of our approximations.
Let $d = t\,\mathrm{x}_0$ be the path lenght, with $t \in \mathbb{N}$, x_0 as the fundamental step[3], and $t = d/\mathrm{x}_0$ the

---

[3] In some works it is often found a similar definition $d = t\,\mathrm{x}_0 \log 2$, with a fundamental step of $\mathrm{x}_0 \log 2$.

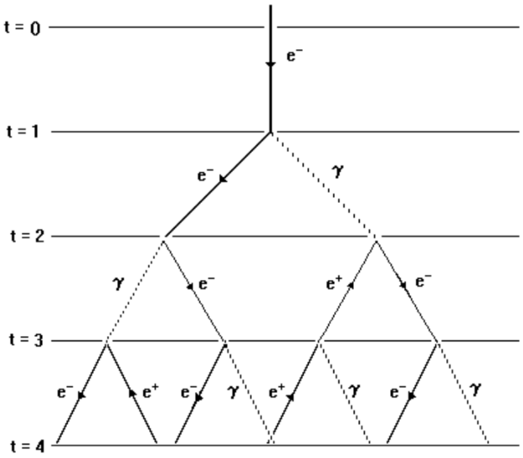

Figure 3.10: Toy model evolution of an electromagnetic cascade. At each step of the cascade the number of particles is multiplied by two, through either pair creation or single photon bremsstrahlung. Backward arrows indicate a positron, as in Feynman diagrams. The evolution stops when the individual particle energy falls below the critical energy E_c. The number N of particles at each step d and the average particle energy E in the Heitler's model are reduced by an exponential factor of two.

traveled path per unit of the fundamental step. Then, after t steps, the average number of particles in the shower is N_t, with an energy $E\,(t)$:

$$N_t = 2^t\,, \qquad\qquad E\,(t) = \frac{E_0}{2^t}\,.$$

This development continues until, at the step $t_{\max}$, the individual energy drops below the critical energy E_c, that is when $e^{\pm}$ start to lose energy by ionization, and the Bremsstrahlung production of new photons is abruptely decreased. At such an energy the multiplication process slows down and, soon after, stops altogether. At $t_{\max}$ the number of secondary particles reaches, therefore, a maximum (the so-called *shower maximum*) $N_{\max}$, which can be easily found from

$$E(t_{\max}) = \frac{E_0}{2^{t_{\max}}} \overset{!}{=} E_c \qquad \Leftrightarrow \qquad t_{\max} = \frac{\log\left(E_0/E_c\right)}{\log 2}\,, \tag{3.17}$$

$$\Rightarrow \qquad N_{\max} \simeq \frac{E_0}{E_c} = 2^{t_{\max}} \approx 10^4 \qquad\qquad \text{with} \qquad E_0 = 1\ \text{TeV}\,. \tag{3.18}$$

So, a 1 TeV photon reaching the top of the atmosphere produces in the Heitler's model $N_{\max} \approx 10^4$ secondary particles at the shower maximum: this number is indeed huge. Also the maximum atmospheric depht $x_{\max}$, that is where the maximum of the electromagnetic cascade occurs, can be obtained from Eq.(3.17):

$$x_{\max} = x_f + d = x_f + t_{\max}\,\mathrm{x}_0\,, \tag{3.19}$$

where x_f is the atmospheric depth where the cascade starts. More detailed computations, which consider the energy distribution of particles in the shower, agree with this estimate, with $x_f \simeq \mathrm{x}_0/2$ as an appropriate value.

The Heitler's model, although oversimplified, illustrates some important features of the electromagnetic component of the air showers. More accurate analytical modeling and Monte Carlo simulations confirm the properties of Heitler's model, although the particle number at maximum is overestimated by factors of 2-3: this is explained by the fact that during the Bremsstrahlung process, multiple photons are emitted and electrons lose energy through additional channels, as we shall see in the following. A useful comparison can be made with Fig.(3.11): longitudinal profiles from an EGS4[4] simulation of a 30 GeV electron-induced cascade in iron are shown. The electron number evidently falls off more quickly than energy deposition. This is because, with increasing depth, a larger fraction of the cascade energy is carried by photons. We shall remember that the critical energy E_c is highly dependent on the material, e.g. $E_c(\mathrm{Fe}) \simeq 27.4$ MeV while $E_c(\mathrm{H_2O}) = 92$ MeV, and the difference is due to the fact that ionization depends linearly on the atomic number Z while Bremsstrahlung depends quadratically $\propto \mathrm{Z}^2$.

If we compute t_{max} in our model, Eq.(3.17), for an incident electron of $E_0 = 30\,\mathrm{GeV}$ as the

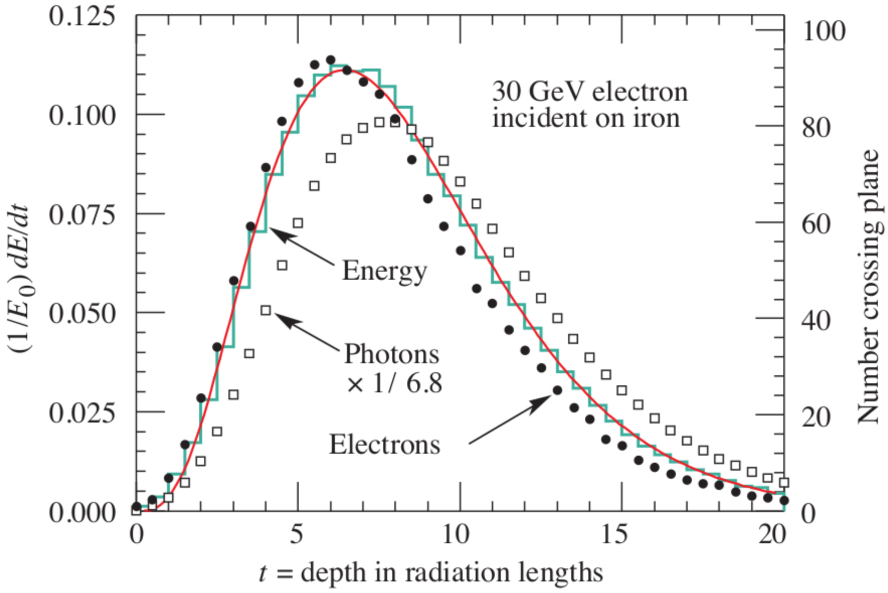

Figure 3.11: An EGS4 simulation of a 30 GeV electron-induced cascade in iron. The histogram shows fractional energy deposition per radiation length, and the curve is a gamma function fit to the distribution. Circles indicate the number of electrons with total energy greater than 1.5 MeV crossing planes at $x_0/2$ intervals (scale on right) and the squares the number of photons with $E > 1.5$ MeV crossing the planes (scaled down to have same area as the electron distribution). $E = 1.5\,\mathrm{MeV}$ is here chosen as the cut off energy.

one hypothesized in the simulation, we obtain

$$t_{\mathrm{max}} = \frac{1}{\log 2} \log\left(\frac{30\,\mathrm{GeV}}{27.4\,\mathrm{MeV}}\right) \simeq 10\,,$$

which is actually not so far from the maximum we observe in Fig.(3.11), that happens earlier due to the other loss mechanisms. Lastly, the drop of the energy deposition (and thus of the cascade) is very mild: these processes are intrinsically stochastic, so a sharp cut-off is definitely not expected, which is a fundamental difference with respect to the Bethe-Heitler's model.

The mean longitudinal profile, i.e. along the direction of the primary incoming particle, of the energy deposition in an electromagnetic cascade is reasonably well described by a *gamma distribution*, which is also used in Fig.(3.11) as a fitting function:

$$\frac{\mathrm{d}E}{\mathrm{d}t} = E_0\, b\, \frac{(bt)^{a-1}\, e^{-bt}}{\Gamma\,(a)}\,,$$

---

[4] See `https://www.slac.stanford.edu/pubs/slacpubs/5000/slac-pub-5193.pdf`.

where a, b are two constants dependent on the material, and the maximum occurs at

$$\frac{\mathrm{d}}{\mathrm{d}t}\left[\frac{\mathrm{d}E}{\mathrm{d}t}\right] = \frac{E_0\, b}{\Gamma(a)}\, e^{-bt}\left[(a-1)\frac{(bt)^{a-1}}{t} - b(bt)^{a-1}\right] \overset{!}{=} 0 \qquad \Leftrightarrow \qquad t_{\max} = \frac{a-1}{b}\,.$$

Usually one assumes $b \approx 0.5$ (or search for a more accurate value, e.g. see Fig.(3.12)) and measures $t_{\max}$ from Eq.(3.17); then a is immediately found, and the longitudinal profile $\mathrm{d}E/\mathrm{d}t$ is built.

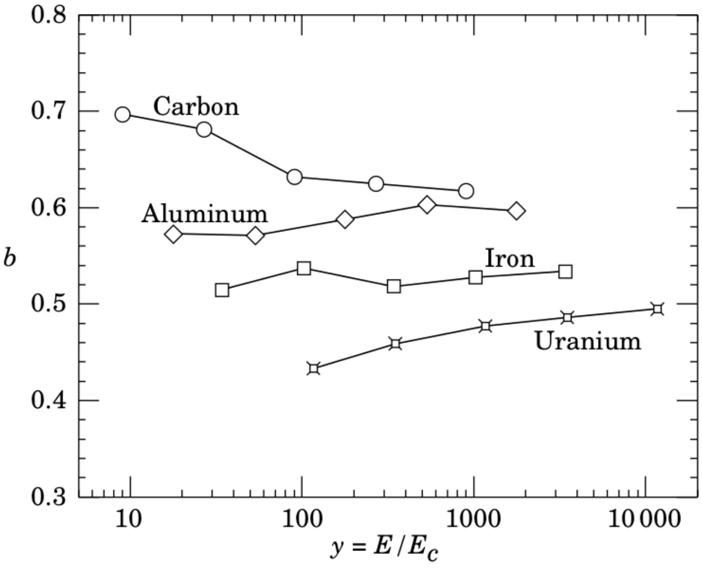

Figure 3.12: Fitted values of the scale factor b for energy deposition profiles, obtained with EGS4 for a variety of elements and for incident electrons with $1\,\mathrm{GeV} < E_0 < 100\,\mathrm{GeV}$. Values obtained for incident photons are essentially the same, around 0.5.

On the other hand, the transverse development of electromagnetic showers, namely the particle density as a function of the distance r to the shower core, as you look at it in the plane orthogonal to the incident particle, in different materials scales fairly accurately with the Molière radius R_M, given by

$$R_M = \frac{E_s}{E_0}\,\mathrm{x}_0 \qquad \text{with} \qquad E_s = m_e c^2\sqrt{4\pi/\alpha} \approx 21\,\mathrm{MeV}\,, \tag{3.20}$$

with $\alpha \simeq 137$ being the QED fine structure constant. The lateral particle distribution is mainly determined by multiple Coulomb scattering of electrons[5], which are very important for light particles such as $e^{\pm}$. Also other effects can enter in determining the transverse profile: the pair production of $e^{\pm}$ has a characteristic opening angle; there is also a sort of emission angle of Bremsstrahlung photons with respect to the direction of the emitting $e^{\pm}$. In general, on average, only 10% of the energy lies outside the cylinder with radius R_M, and about 99% is contained inside of $3.5R_M$.

NB on MonteCarlo simulations As we have already stressed, the Heitler toy model is highly simplified and x_0, which is taken essentially as a constant in the present, is indeed a function of atmospheric density through the different atmospheric layers. The model implicitly assumes a homogeneous medium, and yet provides an efficient method for order of

---

[5] A charged particle traversing a medium is deflected by many small-angle scatters. This deflection is due to the superposition of many Coulomb scatterings, i.e. elastic scatterings, from individual nuclei, and hence the effect is called multiple Coulomb scattering. The multiple Coulomb scattering distribution is well represented by a Gaussian distribution, while individual scatters in angle are described by the Rutherford formula.

magnitude estimates of the principal quantities of interest, namely $t_{\max}$ and $N_{\max}$. However, even if the $\rho \sim$ cost was a good assumption, a MC simulation is indeed needed to take into account the stochastic nature of the electromagnetic shower, the non-monochromatic production of Bremsstrahlung photons and finally the energy loss by collisions. We shall remember that such simulations for $N \approx 10^4$ particles are irredeemably GPU-consuming, so our toy model can be useful in some cases.

3.2.2 The Greisen model

We have already said that the Bethe-Heitler model is in particular characterized by a substantial overestimate of N_e, which is the *electron size* of the shower (number of electrons produced), since $N_{e,\,\max} \approx 2/3\, N_{\max}$ is a typical prediction at maximum development. With a quick look to the MC EGS4 simulation results in Fig.(3.11) one can see that this estimate is very far from the reality since the number of photons $N_{\gamma,\,\max}$ outnumbers consistently $N_{e,\,\max}$:

$$N_{\gamma,\,\max} \simeq 6.8\, N_{e,\,\max} \,,$$

as we can see from the rescaling factor in picture. The reasons why this happens are essentially two:

a) The light charged particles $e^{\pm}$ lose a lot of energy, namely they range out, disappearing much faster;

b) Bremsstrahlung process can, and usually does, emit multiple photons.

So, for the Heitler model to be more accurate in the prediction of the number of charged particles $N^{\gamma}_{e,\,\max}$ (where the apex γ indicates the electromagnetic nature of the shower), a numerical correction factor g needs to be introduced such that

$$N^{\gamma}_{e,\,\max} = \frac{1}{g} N_{\max} = \frac{1}{g}\left(\frac{E_0}{E_c}\right) \qquad \text{with} \quad g \equiv \frac{\sqrt{\log\left(E_0/E_c\right)}}{0.31} \,, \tag{3.21}$$

with the parametrization being valid in the range 10^{15} eV $< E_0 < 10^{18}$ eV. A useful rule of thumb can be to assume $g \sim 10$ for order of magnitude estimates: thus, the e.m. size at maximum is about 10 % of the total size obtained from the Heitler's model. This result comes from the so called **Greisen model**, a more refined version of the Bethe-Heitler model in which a useful parametrization for the mean number of charged particles N^{γ}_{e}, in an electromagnetic cascade produced by γ, is derived

$$N^{\gamma}_{e} = \frac{0.31}{\sqrt{\log\left(E_0/E_c\right)}} \exp\left\{\left(1 - \frac{3}{2}\log s\right)\frac{x}{\mathrm{x}_0}\right\} . \tag{3.22}$$

The new parameter s is called the "age parameter" of the shower, and is given as a function of the atmospheric depht x by

$$s \simeq \frac{3x}{x + 2x^{\gamma}_{\max}} \,, \tag{3.23}$$

and the profile of the electron size N^{γ}_{e} is shown in Fig. (3.13) as a function of $t = x/\mathrm{x}_0$ and for different energies E_0 of the incoming particle. The shapes of the curves, describing the electron size for showers initiated by primary photons with different energies E_0 as a function of t, look very similar. Showers have age $s = 1$ at maximum and age $s < 1$ before the maximum, they are "young" showers; "old" showers have $s > 1$. At shower maximum Eq.(3.22) corresponds by definition to $N^{\gamma}_{e,\,\max}$, and thus:

$$N^{\gamma}_{e,\,\max} = \frac{0.31}{\sqrt{\log\left(E_0/E_c\right)}} \exp\left(\frac{x^{\gamma}_{\max}}{\mathrm{x}_0}\right) \qquad \text{with} \quad x^{\gamma}_{\max} = x_f + \mathrm{x}_0 \log\left(\frac{E_0}{E_c}\right) ,$$

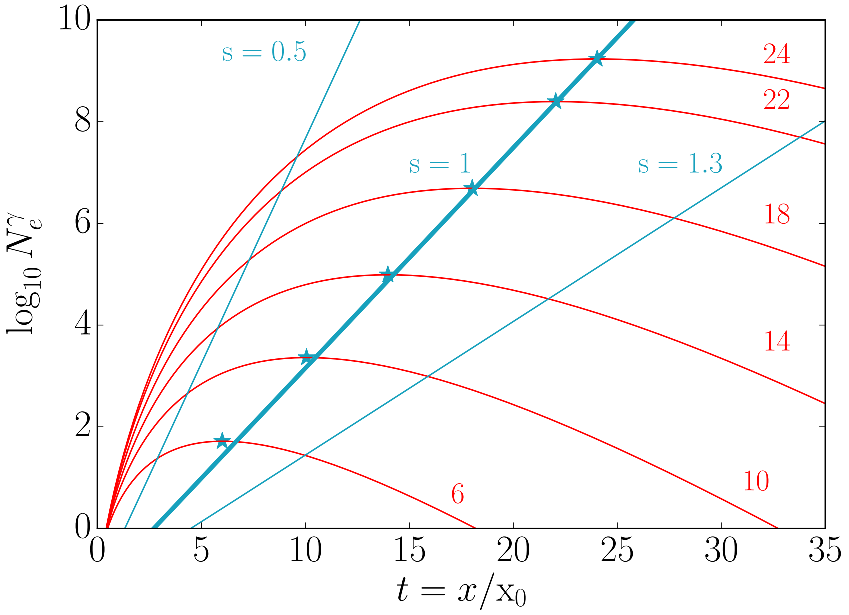

Figure 3.13: Shower size $N_e(t)$ as a function of the atmospheric depth $t = x/\mathrm{x}_0$ (the longitudinal variable in units of radiation lengths) for primary CR photons. The numbers in red are the values of $\log(E_0/E_c)$ where E_c is the critical energy. The corresponding six energies E_0 are in increasing order: 0.035, 2, 100 TeV; 5.7, 320, 2, 300 PeV. The diagonal line connecting the maxima of the different curves is labeled with $s = 1$. The different age values are shown by the light blue numbers. The light blue diagonal lines indicates the positions in the atmosphere with constant age s. The sea level corresponds to $t \simeq 27$.

and with the neglection of the starting atmospheric depht x_f we can easily obtain

$$N^\gamma_{e,\,\max} = \frac{1}{g}\left(\frac{E_0}{E_c}\right) \qquad \text{with} \qquad g = \frac{\sqrt{\log\left(E_0/E_c\right)}}{0.31}\,.$$

The Greisen profile describes accurately the average development of purely electromagnetic showers, and can be adapted for the description of proton and nuclei-induced showers, as presented in the following section. It cannot be easily adapted for the description of neutrino-induced showers. From the analytical solution, it also follows that, for $E > E_c$, the energy spectrum of secondary particles in a shower is approximately described by a power law:

$$\frac{\mathrm{d}N_e^\gamma}{\mathrm{d}E} \simeq E^{-(s+1)} \qquad \text{and} \qquad \left.\frac{\mathrm{d}N_e^\gamma}{\mathrm{d}E}\right|_{s=1} \simeq E^{-2}\,, \tag{3.24}$$

which is a quite surprising behavior, since the spectral index 2 will be common for some other situations. In general, however, the spectral index depend on the shower age s. As the shower becomes older, the energy spectrum of secondary electrons becomes *softer*: the fraction of high energy electrons decreases, namely young showers have a *harder* spectral index. This nomenclature of soft and hard spectral index is quite common in astrophysics: a harder spectrum has a larger component of high-energy particles.
Let us stress that the Greisen model is a description of electromagnetic showers with a primary incident particle given by a γ-ray photon. Cascades initiated by γ-rays are almost pure e.m. showers, that is composed by $e^\pm$ and γ, without other particles. For instance, muon production depends on mechanisms such as the Drell-Yan process[6], characterized by a small cross section: $N^\gamma_\mu \simeq 0$.

---

[6] This process is described by a quark from one hadron and an antiquark from another hadron which annihilate to create a pair of leptons through the exchange of a virtual photon: obviously this involves a highly energetic hadron-hadron scattering, and it is studied both in fixed-target and collider experiments.

NB on detectors and Greisen profile Greisen model is developed mainly for atmospheric showers, and the corrections applied to $N^{\gamma}_{e,\,\mathrm{max}}$ from the Greisen profile Eq.(3.22) are indeed fairly good. The same kind of corrections however can't hold for showers in detectors: indeed detectors are concerned with the measurement of the number of charged particles too, but the s parameter-dependent evolution does not make any sense in the context of such compact regions of detectors' active volumes.

Lastly we can conclude stating that Monte Carlo simulations of the cascades confirm that the e.m. component of the showers exhibits a number of universal features. In particular, e.m. cascades induced by primary photons and electrons have properties which are independent on the primary type and rather insensitive to the primary energy. These features are the following:

1) The longitudinal development of EM cascades depends on two parameters: the energy E_0 of the primary nucleus and the shower age s. They can also be described in terms of analytical formulas like that of Greisen, Eq.(3.22);
2) Near the shower core, the electron energy distribution is a universal function of the age parameter as in Eq.(3.24).

Exercise 3.2. Heitler model for an electromagnetic shower

An electron with energy $E_0 = 1$ TeV enters the atmosphere and triggers a shower. Assume for simplicity an isothermal atmosphere with a temperature $T_{\mathrm{atm}} = 273$ K and a radiation length $\mathrm{x}_0 = 40\ \mathrm{g\,cm^{-2}}$.

i) *Calculate the density of the atmosphere as a function of the altitude h;*
Since an isothermal atmosphere is assumed, the temperature dependent relation $h_0 = h_0\,(T)$ is readily simplified by the constant value $h_0 = kT_{\mathrm{atm}}/Mg$, and then one can simply use the definition of the vertical atmospheric depht $x_v = x$ Eq.(3.5):

$$x = x_{\mathrm{atm}}\, e^{-h/h_0} = 1030\ \mathrm{g\,cm^{-2}}\ e^{-h/7.99\ \mathrm{km}}\ ,$$

$$\text{with}\quad h_0 = \left.\frac{kT}{Mg}\right|_{T_{\mathrm{atm}}} = \frac{\left(1.38\times10^{-23}\ \mathrm{J\ K^{-1}}\right)(273\ \mathrm{K})}{(4.8\times10^{-26}\ \mathrm{kg})\,(9.81\ \mathrm{kg\,m\,s^{-2}})} \simeq 7.99\ \mathrm{km}\ .$$

ii) *Assume that the interaction of the primary electron takes places after it has traversed one radiation length in air. Calculate the height above ground where this first interaction takes place;*
If the first interaction happens at $x = \mathrm{x}_0$ the height can be found inverting the $x = x\,(h)$ relation, that is using Eq.(3.11):

$$h = h_0 \log\left(\frac{x_{\mathrm{atm}}}{x}\right) = 7.99\ \mathrm{km}\ \log\left(\frac{1030\ \mathrm{g\,cm^{-2}}}{40\ \mathrm{g\,cm^{-2}}}\right) \simeq 25.95\ \mathrm{km}\ .$$

iii) *Calculate the height h_{max}, the atmospheric depth x_{max} and the number of secondary particles N_{max} once the average energy per particle has reached $E_c = 100\ MeV$;*
Making use of the results of the Heitler model, in particular Eq.(3.17), we find

$$t_{\mathrm{max}} = \frac{\log\left(E_0/E_c\right)}{\log 2} = \frac{\log\left(1\ \mathrm{TeV}/100\ \mathrm{MeV}\right)}{\log 2} \simeq 13.29\ ,$$

$$\Rightarrow \qquad x_{\mathrm{max}} = t_{\mathrm{max}}\,\mathrm{x}_0 \simeq 531.5\ \mathrm{g\,cm^{-2}}\ ,$$

$$\text{and}\quad h_{\mathrm{max}} = 7.99\ \mathrm{km}\ \log\left(\frac{1030\ \mathrm{g\,cm^{-2}}}{531.5\ \mathrm{g\,cm^{-2}}}\right) \simeq 5.27\ \mathrm{km}\ .$$

iv) *After having reached E_c, assume that all particles are absorbed. Determine if the atmosphere is large enough to entirely absorb the shower.*
Actually we could have already answered to this question simply noticing that $x_{\rm max} \ll x_{\rm atm}$. Let us however assume that the shower traverses all the atmosphere without being stopped by going below the E_c threshold. The total number of required steps t and the average energy per particle E are given by the Heitler model:

$$t = \frac{1}{\log 2}\frac{d}{\mathrm{x}_0} = \frac{1}{\log 2}\frac{x_{\rm atm}}{\mathrm{x}_0} = \frac{1}{\log 2}\frac{1030\,\mathrm{g\,cm^{-2}}}{40\,\mathrm{g\,cm^{-2}}} \simeq 36$$

$$\Rightarrow \qquad E = \frac{E_0}{2^{t_{\rm max}}} = \frac{1\ \mathrm{TeV}}{2^{36}} \simeq 1.46\,\mathrm{eV}\ ,$$

where we have used the analogous definition for the fundamental step $\mathrm{x}_0 \log 2$. The energy per particle is extremely low compared to the initial energy, so we can safely say that the shower cannot traverse the entire atmosphere.

3.3 Hadronic showers

Cosmic rays are mainly protons and heavier nuclei, which initiate a hadronic shower by interacting with atmospheric nuclei after traversing on average one interaction length λ_I'. The number of charged particles produced in the interaction increases with the center of mass energy $\sqrt{s}$. Before starting modeling this new kind of showers, we need to better characterize the hadronic interaction lenght in the atmosphere and the correspondent cross section.

3.3.1 The hadronic interaction lenght

As we have already said in Sec.(2.2.1), some characteristic values for the interaction lenght of hadrons can be found for different propagation media in PDG and, in general, in the literature. We are anyway interested on what actually changes with different targets and incident particles. We were able to write the following relation between the cross section σ for a proton in a medium with mass number A, that is Eq.(2.8):

$$\sigma = \pi \left[\mathrm{r}_0\, \mathrm{A}^{1/3}\right]^2 = \sigma_{pp}\, \mathrm{A}^{2/3}\ ,$$

which is a scaling law in A with respect to the geometrical cross section given by the proton radial dimension $\mathrm{r}_0 = 1.2 \times 10^{-13}$ cm, and we are neglecting the radius of the projectile, namely $r_p = 0.85 \times 10^{-13}$ cm. In PDG site one can easily find the following key values for air:

$$\mathrm{x}_0 \simeq 36.6\,\mathrm{g\,cm^{-2}} \qquad \lambda_I^{p,\,\rm air} \simeq 90\,\mathrm{g\,cm^{-2}} \qquad E_c \simeq 86\,\mathrm{MeV}\ .$$

Knowing the value of the entire atmospheric depht $x_{\rm atm}$, we can notice that $x_{\rm atm} = 1030\mathrm{gcm^{-2}} \simeq 11\,\lambda_I^{p,\,\rm air}$ and $x_{\rm atm} \simeq 28\,\mathrm{x}_0$. Taking also $\langle A\rangle = \mathrm{A}_{\rm atm} = 14.5$, we were also able to write a typical value for the proton-air cross section $\sigma_{p,\,\rm air}$:

$$\sigma_{p,\,\rm air} = \sigma_{pp}\,\mathrm{A}_{\rm atm}^{2/3} \simeq 270\,\mathrm{mb} \qquad \text{for} \quad \mathrm{GeV} \leq E \leq\ \mathrm{TeV}\ ,$$

as we confirmed by looking at Pierre Auger Observatory results in Fig.(2.5), too. In that plot it was also evident that this cross section increases with energy, up till $\sigma_{p,\,\rm air} \simeq 600$ mb for energies $E \geq 10$ TeV. So the interaction lenght for these values is simply computed as

$$\lambda_I^{p,\,\rm air} = \frac{\mathrm{A}}{\mathcal{N}_a\,\sigma_{p,\,\rm air}} \simeq 89.7\,\mathrm{g\,cm^{-2}}\ , \tag{3.25}$$

and this value is really close to the one reported in PDG, so the simple model of Eq.(2.8) seems a pretty good parametrization.

What we want to do now is to describe the cross section $\sigma_{m,\,\mathrm{air}}$ and the interaction lenght $\lambda_I^{m,\,\mathrm{air}}$ of **mesons** m propagating through the atmosphere. In particular we will consider the most interesting ones for our scopes, i.e. the pions π. We would like to write a scaling relation with respect to the σ_{pp} for these hadrons too. To do so we will adopt a great simplification: we will assume that only one quark interacts with the target, neglecting completely the interactions of the color field not to enter in QCD details. In particular, the assumption will be

$$\sigma\,(uu) = \sigma\,(dd) = \sigma\,(ud) \qquad \text{and} \qquad \sigma\,(q\bar{q}) = \sigma\,(qq) \ ,$$

where in the last expression we have called q a generic quark. Hence we can predict the following ratio:

$$\frac{\sigma\,(\pi,\,N)}{\sigma\,(N,\,N)} \simeq \frac{2\cdot 3}{3\cdot 3} = \frac{2}{3} \,,$$

that is the number of possible quark-to-quark interaction between the pion and a baryon (or nucleus N) normalized to the total number of possible interactions is a factor $2/3$, which turns out to be actually in reasonable agreement with experimental results, for which we can usually find $\sigma_{\pi,\,p}/\sigma_{pp} \simeq 0.7$. So we can expect

$$\sigma_{\pi,\,p} = \frac{2}{3}\,\sigma_{pp} \simeq 30\,\mathrm{mb} \qquad \text{and} \qquad \lambda_I^{\pi,\,\mathrm{air}} \simeq 120\,\mathrm{g\,cm^{-2}} \ ,$$

where the expected mean interaction lenght for pions in the atmosphere can be found in PDG, and it is larger than the one of protons, while being compatible still.

Let's study lastly the case of an interacting **heavier nucleus**, e.g. iron, which has the atomic number $\mathrm{A}_{^{56}\mathrm{Fe}} = 56$. This is a rather interesting case because it represents the heaviest isotope that we could eventually expect to compose a cosmic ray from astrophysical sources. The cross section shall be

$$\frac{\sigma_{^{56}\mathrm{Fe,\,air}}}{\sigma_{\mathrm{p,\,air}}} \approx \frac{\left(\mathrm{A}_{^{56}\mathrm{Fe}}^{1/3} + \mathrm{A}_{\mathrm{atm}}^{1/3}\right)^2}{\mathrm{A}_{\mathrm{atm}}^{2/3}} = 6.5 \ ,$$

and the interaction lenght $\lambda_{^{56}\mathrm{Fe,\,air}}$ will be given by

$$\lambda_{^{56}\mathrm{Fe,\,air}} = \frac{\mathrm{A}}{\mathcal{N}_a\ \sigma_{^{56}\mathrm{Fe,\,air}}} \simeq 13.8\,\mathrm{g\,cm^{-2}} \ ,$$

which is again in good agreement with measurements. The reason why we have studied such extreme cases, i.e. the proton and the pion in air and ^{56}Fe, is that in principle we don't usually have precise measurements of A of the different components of CR particles, the identification is very challenging and it becomes easy only when distinguishing two such extreme cases.

3.3.2 The Heitler splitting approximation

The Heitler splitting approximation for hadronic showers assumes that the secondary particles produced are just mesons, the two charged pions $\pi^{\pm}$ and the neutral π^0 (less frequent products would be K mesons and, even more rarely, other hadrons). The hadrons produced in the first collision generally have enough energy to produce other hadrons in a further collision, and so on: the "hadronic cascade" is then built.
The mechanism is depicted in Fig.(3.14). A significant fraction of the initial energy E_0 is

carried away by a single leading particle, which has in general small transverse momentum with respect to the primary CR particle and, undergoing nuclear interactions, it will produce the three species of pions. The pions are unstable and have very different lifetimes. Let us summarize the most common channels ($> 99\%$) of these processes:

$$\begin{aligned} \pi^- &\to \mu^- + \bar{\nu}_\mu & \tau_{\pi^-} &\simeq 2.6 \times 10^{-8}\,\mathrm{s}\,, \\ \pi^+ &\to \mu^+ + \nu_\mu & \tau_{\pi^+} &\simeq 2.6 \times 10^{-8}\,\mathrm{s}\,, \\ \pi^0 &\to \gamma + \gamma & \tau_{\pi^0} &\simeq 8.4 \times 10^{-17}\,\mathrm{s}\,. \end{aligned} \tag{3.26}$$

The charged mesons decays' Feynman diagrams are depicted in Fig.(2.10). The electromagnetic decay is characterized by an extremely short lifetime: the neutral pions decay right at the production point, giving rise to an electromagnetic component of the shower, which works exactly as we have already described. The charged mesons, instead, will either decay or interact further with nuclei, producing again the triplet of pions, since the nuclear interaction lenght is $\lambda_I' = \lambda_I^{\pi,\,\mathrm{air}} \simeq 120\,\mathrm{g\,cm^{-2}}$. The path d traveled by the mesons before a decay occurs is easily computed in the Earth rest frame:

$$d_{\pi^\pm} = \gamma\, c\tau_{\pi^\pm} = 780\,\mathrm{cm}\,\gamma\,,$$

$$d_{\pi^0} = \gamma\, c\tau_{\pi^0} = 2.5 \times 10^{-6}\,\mathrm{cm}\,\gamma\,.$$

In the end the products which we would expect to find in the shower are mostly muons $\mu^\pm$ and neutrinos $\nu_{e,\,\mu}$, $\bar{\nu}_{e,\,\mu}$ from muon decay, see Eq.(2.11).

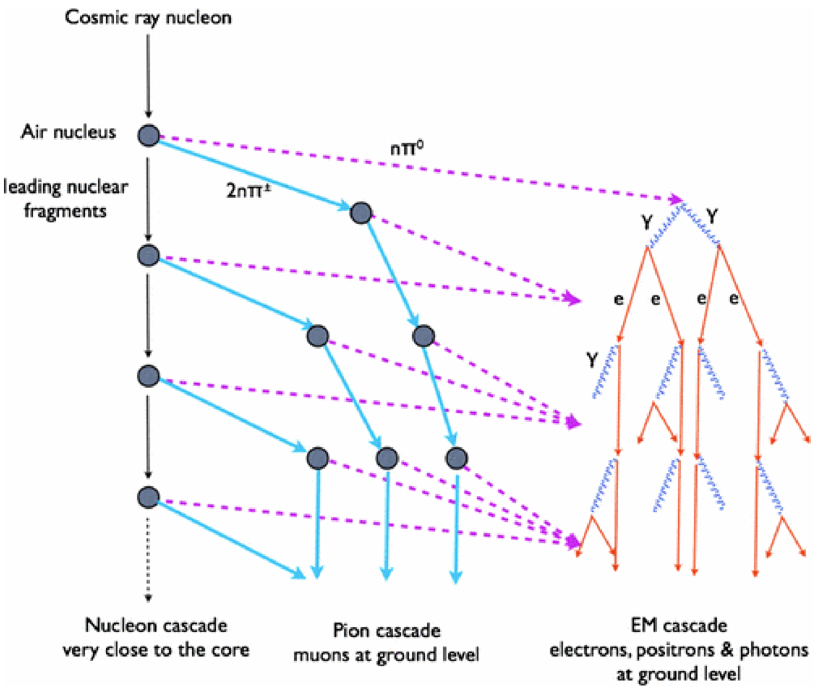

Figure 3.14: Schematic evolution of cascades initiated by hadrons. At each step roughly 1/3 of the energy is transferred from the hadronic cascade to the electromagnetic one. The long purple dashed trail depicted for the neutral pion π^0 is only symbolic: the meson will decay almost right at its production point. The large circles represent the nuclear interactions.

The Heitler splitting model again is useful to estimate the maximum depht $x_{\max}$ and the size $N_{\max}$ of the shower, and can be considered as approximately valid in the range $10^{14}\,\mathrm{eV} \leq E \leq 10^{17}\,\mathrm{eV}$. In analogy with the Heitler model for the e.m. cascade, we can identify the fundamental step x_0 with the nuclear interaction lenght λ'_I and consider the various splitting as the productions of mesons. In particular, the critical energy E_c below which the losses for collisions overcome the Bremsstrahlung radiation shall be identified with E_c^π, the critical energy below which the pions are more likely to decay, leaving the shower poorer and poorer. Ultimately the analogy proceeds this way:

$$x_0 \to \lambda'_I = \lambda_I^{\pi^\pm,\,\mathrm{air}} \simeq 120\,\mathrm{g\,cm^{-2}} \qquad\qquad E_c \to E_c^\pi\ .$$

This analogy is depicted in Fig.(3.15). We shall call the *multiplicities* of charged, neutral and total products as respectively n_{ch}, n_0, n_{h}, such that $n_{\mathrm{h}} = n_0 + n_{\mathrm{ch}}$ in the Heitler splitting approximation. In this first order model we assume that $\pi^\pm$ always interact if their energy is above the threshold energy E_c^π, and decay if the energy is below E_c^π. In the case of interaction, additional n_{h} particles of lower energy are produced, and we assume also that all n_{h} are pions. The assumption of only mesonic products is a great simplification since:

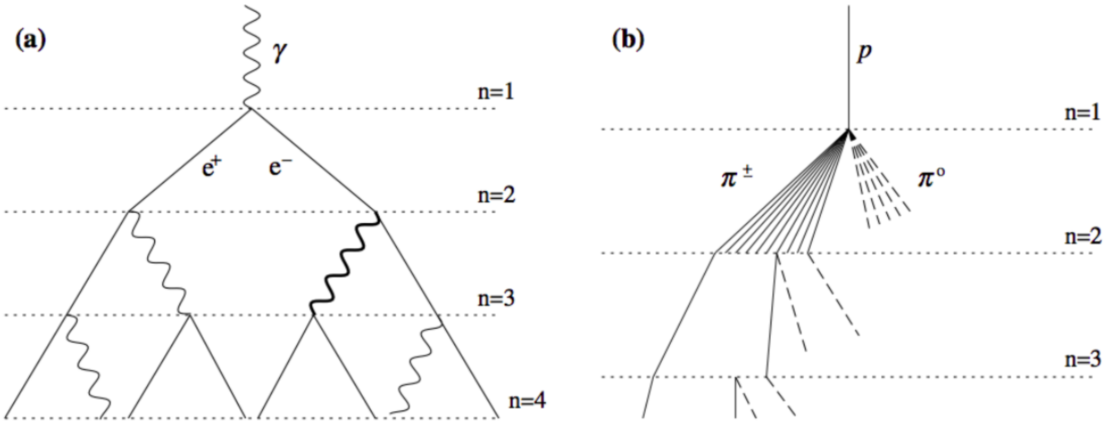

Figure 3.15: Schematic view of (a) electromagnetic and (b) hadronic cascades. In the latter, dashed lines represent neutral particles (π^0) and solid lines charged particles ($\pi^\pm$). Only one charged hadron interaction is shown for each generation.

a) the physics is essentially described by QCD, which per se is still subject of continuous researches and problem-solving theories. MonteCarlo simulations still have problems to explain all of the properties of showers;

b) hadronic cascades are very much more complex than e.m. ones in first place, so the above analogy is quite naive.

Let's compute the critical energy E_c^π, knowing that whether decay or interaction dominates depends upon which of the two, $d_{\pi^\pm}$ or $\lambda'_I = \lambda_I^{\pi^\pm}$, is smaller. Thus we can estimate the energy at which the decay length $d_{\pi^\pm}\,\rho$ of a charged pion equals its interaction length $\lambda_I^{\pi^\pm}$ by

$$\lambda_I^{\pi^\pm} \overset{!}{=} d_{\pi^\pm}\,\rho = \left(\frac{E_c^\pi}{m_{\pi^\pm}c^2}\right) c\tau_{\pi^\pm}\,\rho \qquad \Leftrightarrow \qquad E_c^\pi = \frac{m_{\pi^\pm}c^2\lambda_I^{\pi^\pm}}{c\tau_{\pi^\pm}\,\rho} \simeq 20\,\mathrm{GeV}\,,$$

where in the last estimate we have used the value of $\rho = 10^{-3}$ g cm^{-3} at sea level and $m_{\pi^\pm} = 139.57\,\mathrm{MeV}/c^2$. We have thus neglected the height dependence of density, that is $\rho = \rho(h)$: actually, the resulting critical energy is much lower in this computation than what we have seen with great detail in Ex.(3.1), mostly for this reason. The role of the two processes is in reality complicated by the fact that $\rho = \rho(h)$, but somehow this complexity factor is compensated by the physics of showers:

- at high altitudes the atmosphere is less dense, so the probability of decay is higher. Anyway at such heights one expects the harder component to be still present, with a quite negligible, in general, probability to decay;
- at lower altitudes the atmosphere is denser: the probability to interact is higher. But then again, at such height the softer component should be led to decay rather than interact.

So our approximation of constant density atmosphere is not that awful. We shall stress that indeed the stochastic interaction/decay competition, with all of its details, determines the development of hadronic showers.

We assume also that at each generation $2/3E_0$ is transferred to hadrons through n_{ch} and $1/3$ to an electromagnetic component through n_0. After k generations, the energies of the hadronic (E_{h}) and e.m. (E_{em}) components are given by:

$$E_{\mathrm{h}} = \left(\frac{2}{3}\right)^k E_0 \, , \qquad E_{\mathrm{em}} = E_0 - E_{\mathrm{h}} \, . \tag{3.27}$$

Hence, after k interactions, the energy per pion is $E = E_0/(n_{\mathrm{h}})^k$, with n_{h} being the average number of hadrons. At a certain value k^* the energy per particle E becomes smaller than E_c^π, and the number of interactions needed to reach $E(k^*) = E_c^\pi(k^*)$ is:

$$k^* = \frac{\log\left(E_0/E_c^\pi\right)}{\log\left(n_{\mathrm{h}}\right)} \simeq 3 - 6 \, , \tag{3.28}$$

which is a fairly good result comparing with MC simulations for 10^{14} eV $\leq E_0 \leq 10^{17}$ eV. This expression has a strong dependence on n_{h}, and with detailed discussions we shall expect a dependence on energy, too.

Let's try to characterize the total primary energy E_0 in terms of the observable quantities that we might want to measure. Our simple cascade model consists of two interrelated processes: the development of a hadronic shower, whose observables are mostly the muons, and an e.m. shower. We have already characterized the importance of these two contributions to the energy equipartition at every interaction k with Eq.(3.27). The immediate consequence is that the primary energy E_0 at the maximum of the shower is finally shared between N_μ^p muons and N_{max}^p electrons and photons. Here we emphasized with an apex "p" that the primary particle was a proton, to distinguish from N_{max}^γ used in the previous section Sec.(3.2.2). Indeed, the e.m. shower component E_{em} can be described in analogy with Eq.(3.18), and with the usual hypothesis of equipartition of energy between the products for our hadronic shower we get

$$E_0 = E_{\mathrm{em}} + E_{\mathrm{h}} = E_c \, N_{\mathrm{max}}^p + E_c^\pi \, N_\mu^p \, , \tag{3.29}$$

where we have assumed the main final products of the hadronic shower, namely the second term, to be just muons, and $E_c \simeq 86\,\mathrm{MeV}$ is the critical energy for Bremsstrahlung to become less important. Scaling to the electron size $N_{e,\,\mathrm{max}}^p = N_{\mathrm{max}}^p/g$ using the Greisen correction Eq.(3.21), we can find that:

$$E_0 = gE_c\left(N_{e,\,\mathrm{max}}^p + \frac{E_c^\pi}{gE_c}\,N_\mu^p\right) \simeq 0.85\left(N_{e,\,\mathrm{max}}^p + 24\,N_\mu^p\right)\ \mathrm{GeV} \, . \tag{3.30}$$

The last parametrization has been obtained by substituting the typical values for $g \approx 10$ and E_c, and it was also compared with MC simulations: actually the two parameters are "effective parameters", tuned by looking at more refined results. In the end, the relative magnitude of the contributions from N_μ^p and $N_{e,\,\mathrm{max}}^p$ depends on their respective critical energies, the energy scales at which electromagnetic and hadronic multiplication ceases.

3.3.3 The proton-initiated shower

The Heitler splitting model is an idea with which both showers initiated by protons and the ones originated by nuclei can be described. We want now to investigate on the two fundamental components appearing in Eq.(3.29), the muons N_μ^p and the electrons and photons N_{max}^p, for the most simple kind of hadronic shower: the one produced by a single proton striking the top of Earth atmosphere. We will make use of the general results obtained from Heitler splitting framework.

3.3.3.1 The muon component N_μ^p

Let us consider the dependence of the number of muons in a cascade initiated by a proton on E_0. Muons are produced in the decay of the k^* generation of charged pions, when $\pi^\pm$ reach an energy below the threshold E_c^π and each of them decays into a muon-neutrino pair via the processes in Eq.(3.26). Thus one should expect that for every pion a muon is produced:

$$N_\mu^p = N_\pi^p = (n_{\mathrm{ch}})^{k^*} \ ,$$

and without specifying the electric charge we are describing generically $\mu^\pm$ and $\pi^\pm$. We can make use of Eq.(3.28) to write a logarithmic form of this equality:

$$\log\left(N_\mu^p\right) = k^* \log\left(n_{\mathrm{ch}}\right) = \frac{\log\left(n_{\mathrm{ch}}\right)}{\log\left(n_{\mathrm{h}}\right)} \log\left(E_0/E_c^\pi\right) \ ,$$

being n_{h} the average number of hadrons at each generation. Defining a new quantity β and taking the exponential of both sides, we can write

$$\log\left(N_\mu^p\right) = \beta \log\left(E_0/E_c^\pi\right) \qquad \Rightarrow \qquad N_\mu^p = \left(\frac{E_0}{E_c^\pi}\right)^\beta \ , \tag{3.31}$$

and this result is fairly similar to the one obtained in the Heitler model for $N_{e,\,\mathrm{max}}^\gamma$, that is Eq.(3.21). In that case the dependence on energy was purely linear (neglecting the mild g factor), while in this expression an exponential dependence is found with $\beta \lesssim 1$: this parameter encodes the hadrons' multiplicities, and because of this fact it slowly depends on energy, with values ranging from $0.85 < \beta < 0.95$ from what we can infer from MC simulations. A consistent value can be found with $n_{\mathrm{ch}} = 10$ and $n_{\mathrm{h}} = 3/2\, n_{\mathrm{ch}} = 15$[7], which leads to $\beta = 0.85$, so our first approximation model looks not so bad.
The hadronic energy in Eq.(3.27) can then be completely accounted for in the muon component as:

$$E_{\mathrm{h}} = N_\mu^p\, E_c^\pi \ . \tag{3.32}$$

A question arises naturally at this point: can we measure N_μ^p placing detectors at ground level? The answer is encoded in the fact that muons, as we have shown in Ex.(1.1), are quite likely to reach ground. The average energy of each muon in our model is of the order of $E_c^\pi/2 \approx 10$ GeV, where the division by two is because of the neutrino production. Giving a look at the Bethe-Bloch equation for ionization losses, Eq.(2.12), one can immediately realize that muons with such energies are indeed MIPs, with an average specific energy loss given by

$$-\frac{\mathrm{d}E_\mu}{\mathrm{d}x} \simeq 2 \times 10^{-3}\ \mathrm{GeV\,g^{-1}\,cm^2} \ ,$$

thus most muons have enough energy to cross the entire atmospheric depth $x_{\mathrm{atm}} = 1030\mathrm{gcm}^{-2}$, even when the ionization losses are taken into account. Only muons with very low energy have a large decay probability. Let us in fact recall the purely leptonic decays of muons:

$$\mu^- \to e^- + \bar{\nu}_e + \nu_\mu \qquad \mu^+ \to e^+ + \nu_e + \bar{\nu}_\mu \ ,$$

---

[7] This comes from the fact that, at each generation, $n_0 = 1/2\, n_{\mathrm{ch}}$ and $n_{\mathrm{h}} = n_0 + n_{\mathrm{ch}}$.

for which the muon typical decay lenght $d_{\mu^\pm}$ is given by

$$d_{\mu^\pm} = \gamma\, c\tau_{\mu^\pm} = \gamma\, 0.66\,\mathrm{km} \qquad \text{with} \quad \tau_{\mu^\pm} \simeq 2.2 \times 10^{-6}\,\mathrm{s}\,.$$

As an example, one can consider a muon with $E_\mu = 1$ GeV, for which $\gamma \simeq 10$: such a particle will have approximately 20% probability of decaying before reaching the ground, if the production point is $h \sim 10\,\mathrm{km}$. Thus, the number of muons reaching the detection level is only very slightly depleted with respect to N_μ^p at the position of the maximum.

3.3.3.2 The electromagnetic component $N^p_{\mathbf{max}}$

The number of electrons is estimated using the relation $E_0 = E_{\mathrm{em}} + E_{\mathrm{h}}$, with E_{h} given by Eq.(3.32). The energy fraction carried by the electromagnetic component is given by:

$$\frac{E_{\mathrm{em}}}{E_0} = \frac{E_0 - N_\mu^p\, E_c^\pi}{E_0} = 1 - \left(\frac{E_0}{E_c^\pi}\right)^{\beta-1} .$$

The average number of electrons at maximum can be obtained by considering a single generation, in which the number of neutral pions is given by n_0, and each neutral pion carries the energy E_0/n_{h}. Summing up, there would be n_0 independent showers started by the e.m. decay of each neutral pion, each carrying this same fraction of the primary energy. We can then use the Heitler model with Greisen correction, Eq.(3.21), with this substitution

$$E_0 \to \frac{E_0}{n_{\mathrm{h}}} \qquad \text{with} \qquad \frac{n_0}{n_{\mathrm{h}}} = \frac{1}{3}\,,$$

$$\Rightarrow \qquad N^p_{e,\,\mathrm{max}} = \frac{n_0}{g}\left(\frac{E_0/n_{\mathrm{h}}}{E_c}\right) = \frac{1}{3g}\frac{E_0}{E_c} \approx 4 \times 10^5\, \frac{E_0}{\mathrm{PeV}}\,, \qquad (3.33)$$

where we have substituted the typical value for critical energy $E_c \approx 86$ MeV and $g \approx 10$. This value underestimates by $\sim 30\%$ the electron size due to the additional contribution of successive interactions of the leading particle and of charged pions, producing additional neutral particles. We stress that the number of electrons at maximum grows linearly as function of energy in our simple model, resembling the Heitler description.

We are now able to trace a summary on what we can expect from a hadronic shower, in terms of products and fractional energies carried by the components. In particular, table Tab.(3.1) shows these informations in the case of a 10^{19} eV proton striking vertically the top of the atmosphere. Such a proton will produce about 3×10^{10} particles with energies larger than 200 keV.

Specie	Abundance %	Energy	Energy $\%E_0$
$e^\pm$	99%	1-10 MeV	85%
$\mu^\pm$	$\lesssim 1\%$	~ 4 GeV	10%
$\pi^\pm$	$\ll 1\%$	$\sim$ GeV	4%
$\nu^\pm$ and baryons	$\ll 1\%$	/	$\lesssim 1\%$

Table 3.1: The table shows the principal components of a hadronic shower, with the typical energies and the percent abundances, for the case of a primary proton of about $E_0 = 10^{19}$ eV.

Such very high energies for the primary protons are indeed expected in the astroparticle physics contest: the most powerful and mysterious cosmic accelerators, as we shall see in

the following chapters, are able to provide these kinds of spectacular energies, and the most powerful cosmic rays are usually called UHECRs: Ultra High Energy Cosmic Rays. The footprint of the shower on ground extends over a few km^2, and these estimates are of course the product of MC detailed simulations. These showers are usually referred to as **Extensive Air Showers**, EAS.
We can conclude summarizing the main features of the e.m. and muonic components produced by a proton:

1) The number of muons N_μ^p, Eq.(3.31), produced in an air shower increases almost linearly with the proton energy, that is $N_\mu^p \propto E_0^\beta$, with $\beta \sim 0.9$;

2) The energy E_0 of a primary can be simply estimated if both $N_{e,\,\mathrm{max}}$ and N_μ^p are measured, Eq.(3.29). The relation is linear and almost insensitive to fluctuations on the EM and muonic size: if more primary energy than the average is on the muonic component, the EM one is depleted keeping constant their sum, and viceversa.

3.3.3.3 The depth of the shower maximum

The atmospheric depth at which the electromagnetic component of a proton-induced shower reaches its maximum is denoted as x^p_{max}. Considering only the first interaction, the $n_0 = 1/3\, n_\mathrm{h}$ neutral pions produced generate $2n_0$ γ-rays starting the e.m. cascade at the same position in the atmosphere, and summing up the cascade is provided by the superposition of many individual showers. For a primary proton the first interaction occurs on average at an atmospheric depth $\lambda_I^{p,\,\mathrm{air}} = \lambda_I^p$, and each γ-ray carries an energy of $E_0/2n_\mathrm{h}$ of the primary energy. A simple estimate of x^p_{max} can be obtained using the result from Eq.(3.19) for a shower initiated by a γ-ray with the substitutions

$$x_f \to \lambda_I^p \qquad\qquad E_0 \to E_0/2n_\mathrm{h}\ ,$$

obtaining the following relation

$$x^p_{\mathrm{max}} = \lambda_I^p + \mathrm{x}_0 \log\left(\frac{E_0}{2E_c\, n_\mathrm{h}}\right) = \lambda_I^p + \mathrm{x}_0 \left[\log\left(\frac{E_0}{E_c}\right) - \log\left(2n_\mathrm{h}\right)\right]\ .$$

We are interested in estimating the difference between the position of the maximum in the atmosphere for an electron or a γ-ray initiated shower of the same energy E_0. The first interaction point for the proton is deeper in the atmosphere, $\lambda_I^p \simeq 2.5\,\mathrm{x}_0$, having used the estimate from Eq.(3.25) and the typical radiation lenght for electrons, $\lambda_I^p \simeq 89$ g cm^{-2} and $\mathrm{x}_0 \simeq 36$ g cm^{-2}. So

$$x^p_{\mathrm{max}} \simeq \mathrm{x}_0 \left[2.5 + \log\left(\frac{E_0}{E_c}\right) - \log\left(2n_\mathrm{h}\right)\right] = 2.5\,\mathrm{x}_0 + x^\gamma_{\mathrm{max}} - \frac{\mathrm{x}_0}{2} - 3.4\,\mathrm{x}_0\ ,$$

where we have called the maximum depht for an e.m. shower as x^γ_{max} differently from the previous sections to better tell things apart, and the last numerical factor $\log(2n_\mathrm{ch}) \simeq 3.4\mathrm{x}_0$ comes from $n_\mathrm{h} = (3/2)\, n_\mathrm{ch} = 15$. Also we have used the fact that an appropriate value for x_f can be $x_f = \mathrm{x}_0/2$, as we have said for Eq.(3.19). Notice finally that in this case the convention for the fundamental step is $\mathrm{x}_0 \log 2$, which is equivalently good. Numerically we immediately get

$$x^\gamma_{\mathrm{max}} - x^p_{\mathrm{max}} \simeq 1.4\,\mathrm{x}_0\ ,$$

corresponding to about 50 g cm^{-2} in atmosphere. The maximum of the e.m. shower induced by a proton occurs higher in the atmosphere than that induced by a photon of the same energy E_0. Lastly, the difference $x^\gamma_{\mathrm{max}} - x^p_{\mathrm{max}}$ is dependent on energy, as a full MC simulation reveals, and a possible correction arises from the fact that only the first generation pions are accounted for, and the sub-showers generated in the following steps are neglected.

3.3.4 The nuclei-induced shower

To extend the simple approach from primary protons to nuclei, the *superposition model* is used. This assumes that a nucleus with atomic mass number A and energy E_0 is equivalent to A individual single nucleons, each having an energy E_0/A, and acting independently. The resulting EAS is treated as the sum of A individual proton-induced showers, all starting at the same point. Let's see how the corresponding shower features, namely the sizes $N^{\mathrm{A}}_{e,\,\mathrm{max}}$ and N^{A}_{μ}, change in this case, making use of the following substitutions

$$E_0 \to E_0/\mathrm{A} \qquad\qquad x_f \to \lambda_I^{\mathrm{A}} \,,$$

in the expressions derived for proton showers, and in the end summing A such showers. This is clearly a simplified approach, anyway the same spirit of the previous sections has to be adopted, and the results also for this model are fairly good.

The number of the $e^{\pm}$, γ (the electromagnetic component) at the maximum of the shower induced by a primary nucleus is

$$N^{\mathrm{A}}_{e,\,\mathrm{max}} = \mathrm{A}\left(\frac{E_0/\mathrm{A}}{3g\,E_c}\right) = N^{p}_{e,\,\mathrm{max}} \,,$$

where we have clearly used Eq.(3.21), and this is an important result, which has important implications for experiments: from the measurement of the electromagnetic size, it is hard to distinguish a proton with energy E_0 from a nucleus A of the same energy E_0. The corresponding number of muons in nucleus-induced showers is then

$$N^{\mathrm{A}}_{\mu} = A\left(\frac{E_0/\mathrm{A}}{E_c^{\pi}}\right)^{\beta} = \mathrm{A}^{1-\beta}\,N^{p}_{\mu} \,, \tag{3.34}$$

where we have used Eq.(3.31), and we can see that N^{A}_{μ} increases slowly as a function of mass A of the primary particle, $N^{\mathrm{A}}_{\mu} \propto \mathrm{A}^{0.1}$: the heavier the shower-initiating particle is, the more muons are expected for a given primary energy. In this case thus we have a mild dependence on the chemistry of the primary particle, and this is very important in experiments.

To evaluate the average depth of the shower maximum from a nucleus of mass A we must use again Eq.(3.19) for the maximum atmospheric depht in the Heitler model, assuming that the shower is originated from a nucleon in the nucleus with energy E_0/A. We get

$$x^{\mathrm{A}}_{\mathrm{max}} = \lambda_I^{\mathrm{A}} + \mathrm{x}_0 \log\left(\frac{E_0}{2\mathrm{A}\,E_c\,n_{\mathrm{ch}}}\right) = \lambda_I^{\mathrm{A}} + \mathrm{x}_0\left[\log\left(\frac{E_0}{2E_c\,n_{\mathrm{ch}}}\right) - \log\mathrm{A}\right] \,, \tag{3.35}$$

$$\Rightarrow \qquad x^{\mathrm{A}}_{\mathrm{max}} < x^{p}_{\mathrm{max}} \,,$$

which we have noted to be surely less than the maximum depht achieved by a proton-originated shower. In particular, if we neglect the difference between the first interaction point $\lambda_I^{\mathrm{A}} \sim \lambda_I^{p}$, we get

$$x^{\mathrm{A}}_{\mathrm{max}} \approx x^{p}_{\mathrm{max}} - \mathrm{x}_0 \log\mathrm{A} \,. \tag{3.36}$$

Using this relation, an air shower initiated by a He, O and Fe nucleus of the same total energy reaches its maximum $\sim$ 50, 100, 150 g cm^{-2} earlier than that initiated by a proton with the same energy. The depth of the maximum as a function of the primary energy for proton and iron showers is presented in Fig.(3.16). When a Monte Carlo simulation is performed, the differences $x^{\mathrm{A}}_{\mathrm{max}} - x^{p}_{\mathrm{max}}$ are smaller, and with a mild dependence on the CR energy, too. The main qualitative results and properties of our first order estimate for nucleus-induced showers are the following:

1) The electromagnetic size $N^{\mathrm{A}}_{e,\,\mathrm{max}}$ is equal for a cascade initiated by a proton with energy E_0 and by a nucleus A of the same energy, while the hadronic size is mildly dependent on the mass $N^{\mathrm{A}}_{\mu} \propto \mathrm{A}^{1-\beta}$;

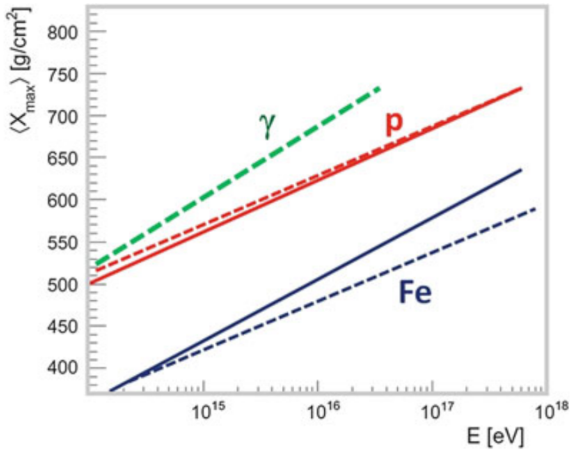

Figure 3.16: Depth of maximum versus primary energy for the e.m. component of air showers. The green dotted line represents showers induced by a photon primary; dashed lines are showers induced by proton (red) and iron (blue) primaries. They are uniformly shifted by 150 g cm^{-2} accordingly with the prediction reported in the text. Red and blue solid lines are from full MC simulations of p and Fe showers.

2) The energy of the primary CR can be measured from the number of secondaries, N_μ^{A} and $N_{e,\,\max}^{\mathrm{A}}$;
3) The chemical composition A of the primary particle can be inferred from the relative $N_\mu^{\mathrm{A}}/N_{e,\,\max}^{\mathrm{A}}$ and $x_{\max}$ measurements.

Exercise 3.3. CORSIKA simulations of EAS

EAS experiments cannot be exposed to test beams for calibration, which are instead used in LHC. The interpretations of their measurements rely on comparisons of the experimental data with model predictions of the shower development, obtained via MC simulations of particle interactions and transport in the atmosphere. In particular, in astroparticle physics, we are usually dealing with very high energies and correspondently huge numbers of particles, such that very strong simulation tools are needed. A lot of difficulties arise also from the very nature of these showers: the *hadronic interactions* are complicated, and a still quite incomplete understanding of QCD interactions is in fact the actual obstacle. In particular, the up to now hadronic interaction models are usually a mixture of basic theoretical ideas and empirical parameterizations tuned to describe the experimental data, where measurements exist.

CORSIKA is a Monte Carlo code which was initially developed for an airshower cosmic-ray experiment and later became widely used in the astroparticle physics community, involved in experiments focusing also on gamma-rays and neutrinos. EAS are simulated in great detail, and different primary particles can be treated: photons, nucleons, or nuclei. Secondary particles are propagated (tracked) along the atmosphere, including all Standard Model physics processes: energy losses, deflection due to multiple scattering and to the Earth's magnetic field, decay modes and electromagnetic and hadronic interactions. Hadronic interactions can be described using different modelings of nucleons and nuclei.
At the web site of the Karlsruhe Institute of Technology, `https://web.ikp.kit.edu/corsika/movies/Movies.htm`, we can find movies describing results for different primary particles of different energies. By viewing and comparing those movies, a good understanding of the physics of Extensive Air Showers can be gained.

Particles are represented as moving points (except the last set of movies, in which tracks are used, connecting the production and the end point of each particle). Distances are given in meters. Several views, looking at the shower sideview or upwards, either from the Earth's frame or from the shower comoving frame, are presented and different primaries and/or different energies were simulated. Secondary photons are not shown to avoid a too busy and confusing view.

i) *Give a general description of how the shower develops.*
The general trend of the showers is to assume a bell shape, starting from the first interaction, and enlarging with a faster trend than a linear with time one. In particular a γ-ray, proton p and Fe-nucleus shower are shown, with the same initial energy $E_0 = 100$ TeV, and also a proton-induced non vertical shower with $E_0 = 1$ PeV is shown.
In the γ-ray initiated shower the spreading is initially given by $e^{\pm}$, the lightest particles, especially by their elastic scatterings with themselves. The other light products which are expected, the muons $\mu^{\pm}$, are appearing with a consistent size N_μ^γ only at the very end of the movie. Notice that this is not a simple electromagnetic shower as the one we have modeled in class: not just photons and electrons are present, but also a quite small family of muons is pair-produced by photons, see the answer below. The most consistent spread is experienced by electrons. As seen from directly below it, the shower appears as a cirlce with increasing radius, till the critical energy E_c is reached and it starts to die out. The maximum radius is about $\simeq 200\,\mathrm{m}$.
In the proton initiated shower the bell shape is very much larger, escaping from lateral borders of the movie earlier than in the e.m. case. The spreading is again led by the light $e^{\pm}$, but this time also hadrons achieve very strong spatial enlargement from the leading nuclear fragment, due to their own scatterings which deflect the trajectories. Also neutrons are protagonists in the spread-leading. Obviously, hadrons spread remains consistently smaller than the lighter particle's one. As seen from below it, the shower appears to have a higher maximum radius than in the first case, that is about $\simeq 300\,\mathrm{m}$.
The Fe initiated shower is appearing longitudinally much similiar to a cylinder instead of a bell: the enlargement is huge from just about the first interaction point, even though the outer parts are consistently populated in a somewhat later stage of development. Also in this case the electrons are the first particles to experience the spreading, followed quite lately by hadrons and neutrons. As seen from below, the maximum radius achieved is very large, $\simeq 600\,\mathrm{m}$.

ii) *Which particles are produced?*
In the γ-ray initiated shower the main products are mostly electrons, since the processes of creation of muons from electromagnetic interactions are expected to be suppressed in importance with respect to radiation effects of Bremsstrahlung and $e^{\pm}$ pair production. Indeed this expectation is met.
In the proton initiated shower the main products are again electrons, with a consistent production of muons from pion decays. Following in importance are the hadrons and the neutrons.
In the Fe initiated shower the same kind of importance in product abundances is encountered, namely electrons and muons have the larger sizes. Everything seems however to be magnified: much more particles are in general produced in each family.

iii) *Do you expect muons to be produced in a shower initiated by a photon? Why?*
Indeed yes, as we have already said. In particular, muons are produced by photons through pair production. This process is similar to electron pair production, scaled by the mass of the muon, i.e. with a threshold energy of $E_\gamma = 2m_\mu c^2$. This is described

by the following

$$\gamma + N \to N + \mu^+ + \mu^- \ ,$$

with N being an atmospheric nucleus. This kind of production of muons becomes increasingly important also in hadronic showers at higher energies, when the production via decay of $\pi^\pm$ (and $K^\pm$) is less efficient due to the decay lenght of these mesons, which can become of the order of the interaction lenght at higher energies.
Actually there is another possibility for muon's production in electromagnetic showers: via the interaction of photons with nuclei in the atmosphere, namely photomeson productions of $\pi^\pm$ and $K^\pm$,

$$\gamma + N \to \pi(K) + H \ ,$$

where H are obviously hadrons, see App.(B). In an article cited below[8], this production channel seems to become very prior at energies $E_\gamma > 3$ TeV with respect to the decay of the mesons, whose muons become very negligible at $E_\gamma > 30$ TeV. Let's recall the main decay modes of the Kaon K^+:

$$K^+ \to \mu^+ + \nu_\mu \ \ (\mathrm{BR} = 63.6\%) \qquad K^+ \to \pi^+ + \pi^0 \ \ (\mathrm{BR} = 20.7\%) \ .$$

However these kinds of processes are, at the interest energies, highly suppressed with respect to the Bremsstrahlung radiation and the $e^\pm$ pair production. The products of the γ-ray initiated shower are in fact dominated by the presence of $e^\pm$.

iv) *Compare different primary particles at the same energies. Which difference do you notice?*
Beside from the differences I have already highlighted, a kind of eye-estimate of the altitude at which the showers die out can be made for the three primaries at same energy $E_0 = 100$ TeV. The altitude of the first interaction can also guessed with the same method and compared. The γ-ray initiated shower seems to start its decay at an altitude from ground of $\simeq$ 2000-3000 m, with very low precision since the evolution of this kind of shower seems very quick. The altitude of the first interaction seems to be about $\simeq$ 17 km.
The proton initiated shower starts to become increasingly smaller at an altitude of $\simeq$ 6000 m, which instead is a more precise estimate since this height can be clearly seen in the movies comparing the product abundances, and also the shower development appears slower. The altitude of the first interaction seems to be quite similar to the previous case but quite smaller, about $\simeq$ 16 km.
The Fe initiated shower is by far the slowest one, with height of first shadowing at about $\simeq$ 1000-2000 m from ground: indeed this shower is the most penetrating one, and we shall remember that its main products are electrons together with muons, the latter being the most penetrating astrophysical probe, second only to neutrinos. By the way the estimate is rough: the scale of the plot is prepared for the highly penetrating cascade, with a resolution of 2000 m and a much higher estension with respect to the previous cases. The altitude of the first interaction seems to be about $\simeq$ 42-44 km, a great difference.

v) *Compare different energies for the same primary particle. Which difference do you notice?*
The evolution of a shower initiated by a proton of energy $E_0 = 100$ TeV and $E_0 = 1$ PeV are showed, this time with a non zero angle of incidence with respect to the perpendicular direction to the ground. The principle difference is the height of the

---

[8] See the interesting articles `https://pos.sissa.it/358/961/pdf` and V. S. Berezinsky, G. Cini-Castagnoli, V. A. Kudryavtsev, O. G. Ryazhskaya and G. T. Zatsepin. Astron. Astrophys., 189 (1988) 306.

first interaction: for the lower energy it happens at $\simeq$ 21 km, while in the other case $\simeq$ 23 km: the precise estimates are red in the movies which show the tracks of hadrons, muons and electrons. These movies show another clear difference: the higher energy shower is more beamed, while the lower energy one experiences a higher spread. Furthermore in the lower energy case the main products seems to be electrons, as said for the vertical develop of a shower initiated by such a primary; the more energetic case is instead dominated, at very early stages (namely at high altitudes) by muons and neutrons. The height at which both die out is very difficult to guess from these movies.

4

Cosmic Rays astrophysics

> *The time has now arrived, it seems to me, when we can say that the so called cosmic rays definitely have their origin at such remote distances from the Earth that they may properly be called cosmic and that the use of the rays has by now led to results of such importance that they may be considered a discovery of the first magnitude.*
>
> – Compton, awarding Hess the Nobel Prize, 1936

In 1912, V. F. Hess, flying aerostatic balloons at high altitudes, discovered that charged particle radiation originated outside the atmosphere, in the cosmos; Fermi formulated a theory of the acceleration mechanism in 1949. Today we know that primary Cosmic Rays (CRs) are fully ionized atomic nuclei and other particles accelerated at astrophysical sources and reaching the Earth, and until the early 1950s, when the first high energy accelerators were built, cosmic rays were the only source of particles with energy larger than a GeV. Having then in mind the general definition of Cosmic Rays, namely that they are **high energy radiation**, we shall describe now their general features and their origin, which is still an open question.

4.1 Historical background

The roots of men's questioning about CRs are traced back to the end of the 18th century, when Coulomb found that electroscopes discharge spontaneously, due to the atmosphere ionization. In 1896 spontaneous radioactivity, that is the emission of particles from nuclei as a result of nuclear instability, was discovered by Becquerel and electroscopes were used again to probe the atmospheric radioactivity level: the problem then became the origin itself of this ionization. The hypothesis of an extraterrestrial origin popped out naturally and in 1909 father Theodor Wulf, a German scientist and a Jesuit priest, thought of checking the variation of ionization with height, with an improved electroscopic experiment on the top of the Eiffel Tower in Paris, about 300 m high. Anyway the results of the experiment seemed to suggest a terrestrial origin, since the ionization rate was a little smaller at such heights, the decrease being somehow not actually *very* dramatic.

Further investigations were indeed needed and a lot of other experiments were carried, till in the 1910s a series of balloon flights by the Austrian physicist Victor Hess settled the issue, firmly establishing the extraterrestrial origin of at least part of the radiation causing the atmospheric ionization. What was found by Hess was that ionization decreased to a minimum value, but then it *increased again.* Hess concluded that the increase in the ionization rate with altitude was due to radiation coming from above, and he thought that this radiation was of extraterrestrial origin. The first natural hypothesis was about our Sun

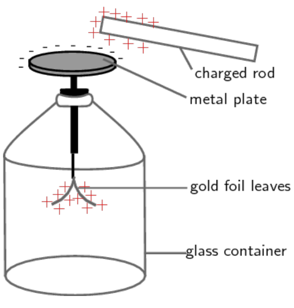

Figure 4.1: Schematic view of an electroscope. The electroscope is a device for detecting electric charge. A typical electroscope (the configuration in the figure was invented at the end of the eighteenth century) consists of a vertical metal rod from the end of which two gold leaves hang. A disk or ball is attached to the top of the rod. The leaves are enclosed in a glass vessel, for protection against air movements. The test charge is applied to the top, charging the rod, and the gold leaves repel and diverge.

as the possible source, but Hess observations during the day and during the night showed no variation and excluded this possibility.

This was the actual birth of the researches about what were promptly called Cosmic Rays, and a shared Nobel Prize in 1936 was finally awarded to Hess together with Anderson for the positron discovery. Those years marked actually also the first milestone of Particle Physics, which was originally born as Astro-Particle Physics properly through the subsequent Cosmic Rays experiments, in which pions by nuclear emulsions expositions, muons, ecc. along with the first antimatter building blocks, e.g. the positron itself, were discovered. High altitudes experiments were also established around the world, like Pierre Auger's one in the Alps, but also in the Andes, the Rocky Mountains, the Caucasus. This was the way to the first detections of EAS, with the awareness of event coincidences in very distant detectors.

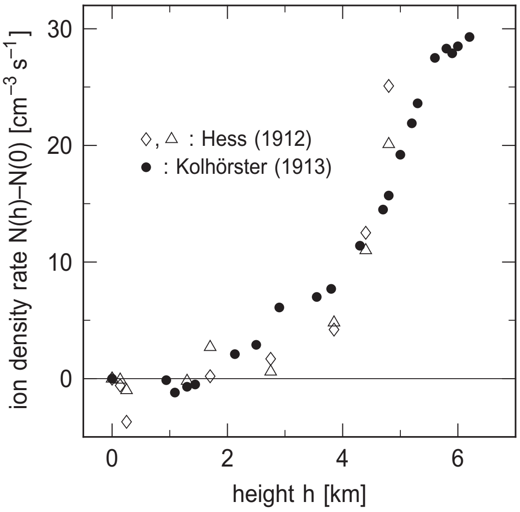

Figure 4.2: Ion density rate as function of balloon height as originally measured by Hess in 1912 and Kolhörster in 1913. Plotted are the data as obtained during the flights. The date plotted with open rhombuses and with triangels refer to results obtained by Hess with his electrometers labelled I and II, respectively.

A hundred years or more have indeed passed from these key events in the history of Cosmic Rays, but still a lot of open questions have to be addressed for this chapter of science history to be considered effectively closed.

4.2 General features

During the previous chapter we have called "primary" the particle which interacts with atmospheric nuclei and gives rise to EAS, their products being the "secondaries". Now we have to distinguish, instead, from primary and secondary with respect to the production and acceleration mechanisms: in particular, the primary cosmic rays will be the ones at their production point in the astrophysical enviroments, while the secondaries shall be the particles which, after being produced, underwent acceleration, deflection and interaction processes and arrive to Earth's atmosphere. The composition of CRs is usually the following:

- 99% protons and heavier nuclei;
- 1% electrons;
- other particles, maybe antimatter and such.

These numbers do not correspond to a charge-asymmetry in the CR sources. The very few electrons are due to the fact that such light particles lose energy very efficiently during their travel to Earth, and by no means $e^{\pm}$ produced by astrophysical sources can arrive as secondary cosmic rays. That 1% shall be than due to terrestrial productions.

4.2.1 Differential and integral flux

Let us define the concepts of differential and integral flux, which are fundamental to understand the energy spectrum of CRs. The flux, in general, is the number of particles per unit time dt hitting a surface of unit area dA at a given solid angle dΩ. The incident direction is defined by the usual two angles, the zenith θ and the azimuth ϕ:

$$\mathrm{d}\Omega = \sin\theta \, \mathrm{d}\theta \, \mathrm{d}\phi \, .$$

We define the *differential flux* $\Phi(E)$ as the number N of CRs particles in a given energy interval dE, time dt, unit area dA and solid angle dΩ, that represents the differential intensity of particles of a given energy in the given solid angle:

$$\Phi(E) \equiv \frac{\mathrm{d}^2\varphi}{\mathrm{d}E\,\mathrm{d}\Omega} = \frac{\mathrm{d}N}{\mathrm{dA}\,\mathrm{d}t\,\mathrm{d}\Omega\,\mathrm{d}E} \qquad \text{with} \qquad [\Phi(E)] = \frac{\#\,\text{particles}}{\text{m}^2\,\text{sr s GeV}} \, , \tag{4.1}$$

and φ is clearly the flux. Sometimes, particles can be measured only if their energy is larger than a given energy threshold E_0: the *integral flux* is defined as

$$\Phi(> E_0) \equiv \frac{\mathrm{d}\varphi}{\mathrm{d}\Omega}(E) = \int_{E_0}^{+\infty} \frac{\mathrm{d}^2\varphi}{\mathrm{d}E\,\mathrm{d}\Omega}\,\mathrm{d}E \qquad \text{with} \qquad [\Phi(> E_0)] = \frac{\#\,\text{particles}}{\text{m}^2\,\text{sr s}\,,} \tag{4.2}$$

and it clearly represents the measurement of the CRs intensity for particles with energy larger than the given threshold. The arrival direction of CRs is usually largely isotropic. The particles' flux through a spherical surface is then given by the integration over the solid angle of Eq.(4.1):

$$\frac{\mathrm{d}\varphi}{\mathrm{d}E} = \int_{4\pi} \frac{\mathrm{d}^2\varphi}{\mathrm{d}E\,\mathrm{d}\Omega}\,\mathrm{d}\Omega = 4\pi\Phi(E) \qquad \text{with} \qquad \left[\frac{\mathrm{d}\varphi}{\mathrm{d}E}\right] = \frac{\#\,\text{particles}}{\text{m}^2\,\text{s GeV}} \, .$$

A plot of the differential flux as a function of energy is called **energy spectrum**. In a large number of cases, particle spectra are simply power law of energy. They can thus usually be represented weighting the y-axis with a power of the energy, so that such a quantity shall be reproduced

$$E^{\alpha}\,\frac{\mathrm{d}N}{\mathrm{dA}\,\mathrm{d}t\,\mathrm{d}\Omega\,\mathrm{d}E} \, ,$$

and this is a useful parametrization to better visualize some structures in the spectrum. Many spectra are steep, and a typical value for α can be $\alpha = 2$. This exponent is often referred to as "spectral index".

4.2.2 The energy spectrum of primary CRs

The spectrum of primary cosmic rays is the main feature of this high energy radiation, and it is being continuously built up by collaborations and experiments, each with a compilation of data sets and with their different sensitivities, to give a broad variety of investigations in energy regimes. Fig.(4.3) shows the differential flux, weighted as just described with a spectral index $\alpha = 2$, as a function of the kinetic energy E_{kin} of the primary CR particle. We stress that the primary component arriving on the top of the atmosphere includes all stable charged particles and nuclei; also some unstable nuclei (with lifetimes larger than 10^6 years) are found.

The energy scale is huge: the extension is from MeV to 10^{20} eV. Above about 100 GeV the profile is a simple power law, despite ten orders of magnitude! Up till $E_{\text{kin}} \simeq 10^4$ GeV, **direct measurements** are possible and also charge and mass identifications of the single primaries: the data are labeled also with "electrons", "positrons" ecc. Indeed experiments mounted on balloons and satellites (and recently on the International Space Station) allow a direct study of the CRs impinging on the top of the atmosphere, before the first interaction with Earth occurs. At higher energies such an identification is not possible anymore. In fact, the energy spectrum falls steeply as a function of energy, and the integral flux corresponding to different energy thresholds roughly gives

$$\Phi \left(> 10^9 \text{ eV}\right) \sim 1000 \,\text{particles m}^{-2}\,\text{s}^{-1} \; ;$$

$$\Phi \left(> 1 \text{ PeV}\right) \sim 1 \,\text{particles m}^{-2}\,\text{yr}^{-1} \; ;$$

$$\Phi \left(> 10^{20} \text{ eV}\right) \sim 1 \,\text{particles km}^{-2}\,\text{century}^{-1} \; .$$

Thus, in the PeV region and beyond, the CRs intensity is too low for direct measurements; only **indirect measurements** of air showers from the ground are possible. Since the particles are not identified on an event-by-event basis, the energy spectrum derived from measurements of air showers is given as an "all particle" spectrum, in terms of *energy per particle* (or nucleus) rather than *energy per nucleon.* In practice, an identification is impossible, and we can only measure the secondary products and sum up their energies. While balloons and such are good means for collecting relatively low energy data, indirect measurements are a must since the areas we need to obtain a good statistic is huge and by now unachievable.

The most interesting energy range is possibly $E > 10^{18}$ eV: these are the already cited Ultra High Energy Cosmic Rays (UHECRs), which are probably of extragalactic origin, and the study of this energetic radiation is complicated by the serious drop of differential flux. There are nowadays some collaborations with the idea of observing the Earth's EAS by satellites, but still nothing has been realized.

The Solar Flares Below few GeV, namely $E < 4$ GeV, the main source of CRs are the so called *Solar Flares*, which are episodic solar activities consisting in sudden brightenings observed over the Sun's surface. They are interpreted as large energy releases, occuring in active regions around sunspots, where intense magnetic fields penetrate the photosphere to link the corona to the solar interior. They were first observed in 1940s and mainly produce protons, electrons, and heavy ions. From now on we will concentrate on other astrophysical sources, mainly extra solar ones, since higher energies CRs are produced by them.

An example of differential energy flux, weighted with a spectral index of $\alpha = 2.6$, is shown in Fig.(4.4), as a function of the energy per nucleus. Some structures in the plot are also fairly evident:

1) A first knee is at about $E \sim 10^{15}$ eV: it represents a change of slope of the power-law. Possibly lower energy CRs are dominated by particles of galactic origin. In

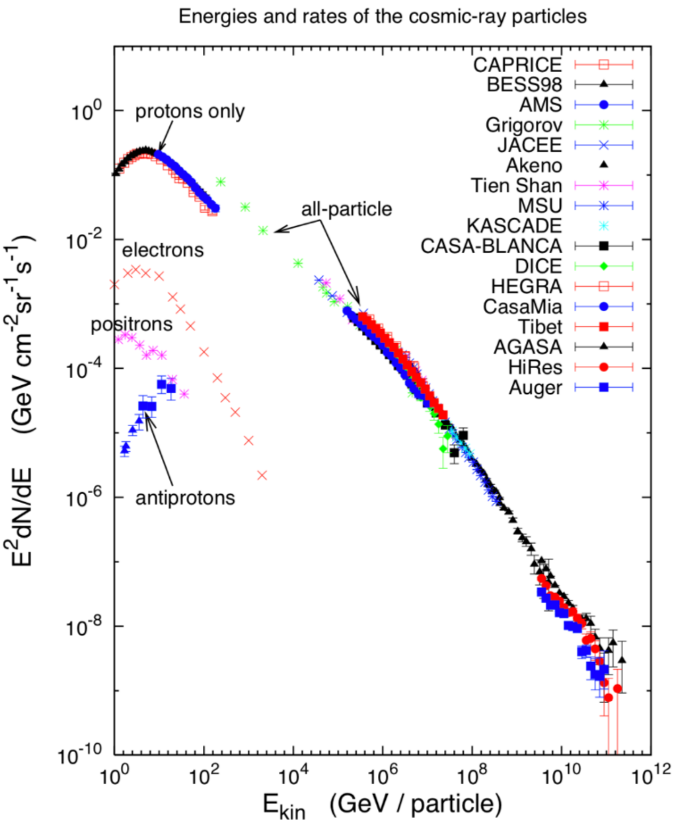

Figure 4.3: Cosmic rays differential flux as a function of energy. Lifted from `https://arxiv.org/pdf/astro-ph/0608553.pdf`.

particular it could indicate that most cosmic accelerators in the Galaxy have reached their maximum energy for acceleration of these particles;

2) Another steepening occurs around 10^{17} eV, known as the *second* knee. This second knee may have a similar origin to the first, but corresponding to steepening of the spectrum of heavy nuclei, particularly iron;

3) At the energy of $\sim 10^{18}$-10^{19} eV the spectrum becomes flatter again in correspondence of the second transition point, called the *ankle*. CRs above the ankle are thought to have an extragalactic origin, possibly a higher energy population of particles overtaking the lower energy galactic flux.

We don't actually know what is in reality happening in between 10^{15} eV and 10^{18} eV, and the explanations given above for the features of the spectrum are only attempted. As regards the region of the ankle, a very well known effect proposed for UHECRs is the **dip mechanism**, described by

$$p + \gamma_{\rm CMB} \to p + e^- + e^+ \,,$$

which accounts for energy losses of extragalactic protons on the cosmic microwave background radiation (CMB). The energy threshold is estimated from relativistic kinematics, see Ex.(4.1). Another mechanism can be an important source of losses: if the cosmic-ray flux at the highest energies is extragalactic in origin, there should be a rapid steepening of the spectrum (called the *GZK feature*, which is explained in details in App.B) around 5×10^{19} eV, resulting from the onset of inelastic interactions of UHE cosmic rays with the cosmic microwave background, namely photo-productions of pions:

$$\gamma_{\rm CMB} + p \to p + \pi^0 \qquad\qquad \gamma_{\rm CMB} + p \to n + \pi^+ \,,$$

$$\text{or, in general} \qquad \gamma_{\text{CMB}} + p \to p + n\pi^0 + m(\pi^+ + \pi^-) \ ,$$

with n, m integers to allow the charge conservation, and the multiple pion production dominates at high energies. Also photo-dissociation of heavy nuclei, instead of protons, would feel a similar effect, with the interactions dominated by fragmentations

$$N + \gamma \to H + ...$$

with hadrons labeled by H. Summarizing, this kind of explanations seems to suggest that

a) Galactic CRs do not contribute significantly to the flux at $E > 10^{18}$ eV: this is essentially due to the mean free path of the GZK mechanism, which will be computed in Ex.(4.4): the result is that $\lambda_{mfp} \simeq 3.15$ Mpc, indeed much larger than the radius of the Milky Way;

b) Cosmic rays at those energies are mostly protons, heavier nuclei being suppressed: this is because of the photodisintegrations, which are very probable especially in the EBL (Extragalactic Background Light) interactions.

We shall deepen the issue of the ankle possible explanations in Sec.(4.5.5). At energies larger than few GeV, where the contribution of particles coming from the Sun is negligible, the energy spectrum can be described by a power-law:

$$\Phi(E) = K \left(\frac{E}{1\text{ GeV}}\right)^{-\alpha} \qquad \text{for} \quad 1\text{ GeV} < E < 1\text{ TeV} \ , \tag{4.3}$$

$$\text{with} \quad K = 2,\, 3 \quad , \quad \alpha = 2.7 \ .$$

The parameter α is often referred to as the differential spectral index of the cosmic rays flux, and K is a normalization factor which changes if we are looking at the "all particle spectrum" or at the dependence on the energy per nucleon. The integral flux is

$$\Phi(> E) = \frac{K'}{\alpha - 1} \left(\frac{E}{1\text{ GeV}}\right)^{1-\alpha} \ , \tag{4.4}$$

with $K' = K(1\text{GeV})$ and different compilations of data exist which determine the parameters K and α using direct measurements of the CR flux. Notably, at energies above the knee, $E > 10^{15}$ eV, the spectral index of the CR spectrum becomes steeper, such that $\alpha \approx 3.1$, becoming flatter again approaching the second knee at $E \simeq 10^{17}$ eV.

Exercise 4.1. The dip mechanism model

This model is by Vieniamin Berezinsky[1], an active scientist at LNGC, and it is a well perceived explanation of the ankle in cosmic rays flux. The hypothesized process is

$$p + \gamma_{\text{CMB}} \to p + e^- + e^+ \ .$$

Assume that $E_\gamma = kT_{\text{CMB}}$ with $T_{\text{CMB}} = 2.73$ K, which is a rough estimate neglecting the full black body spectrum of the Cosmic Microwave Background.

i) *What is the energy threshold E_{min} for this process to happen?*
This is of course a relativistic kinematic problem and the resolution is essentially similar to the one presented in App.(B) for the pion production in $\gamma + p \to p + \pi^0$, so let's start with the four momenta of the particles in the initial state:

$$p_\gamma = (E_\gamma/c,\, \vec{p_\gamma}) = (|\vec{p_\gamma}|\,,\, \vec{p_\gamma}) \ ,$$

---

[1] See `https://arxiv.org/pdf/hep-ph/0204357.pdf`

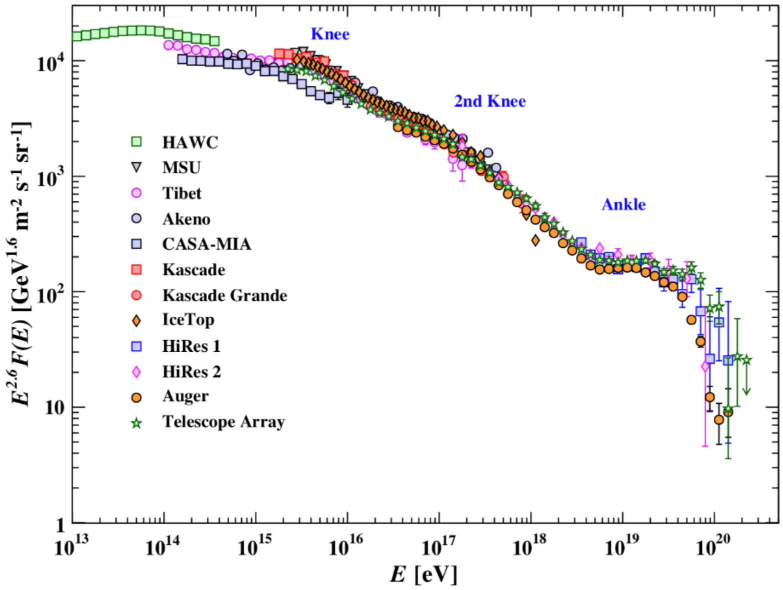

Figure 4.4: All particle spectrum as a function of the energy per nucleus, E, from air shower measurements. A lot of different data compilations are shown, and the structures described in the text are also highlighted. Picture from `http://pdg.lbl.gov/2019/reviews/rpp2019-rev-cosmic-rays.pdf`.

$$p_{p,\,\mathrm{in}} = (E_{p,\,\mathrm{in}}/c,\ \vec{p_{\mathrm{in}}}) = \left(\sqrt{m_p^2c^4 + |\vec{p_{\mathrm{in}}}|^2\,c^2}/c,\ \vec{p_{\mathrm{in}}}\right) .$$

The invariant mass in the initial state is immediately given by Eq.(1.3):

$$\sqrt{s} = \sqrt{m_p^2c^4 + 2E_{p,\,\mathrm{in}}E_\gamma - 2\,|\vec{p_{\mathrm{in}}}|\,|\vec{p_\gamma}|\,c^2\cos\theta} .$$

The threshold energy for the process is the total energy available in the COM frame, where the produced particles are at rest, i.e. $E_{\mathrm{thr}} = E^*$, and it is given by the invariant mass calculated in that frame $\sqrt{s}$ to the power of two, that is Eq.(1.1):

$$\sqrt{s} = \sum_k E_k^* = m_pc^2 + 2m_ec^2 ,$$

$$\Rightarrow \qquad E_{\mathrm{thr}} = \left(\sqrt{s}\right)^2 = m_p^2c^4 + 4m_e^2c^4 + 4m_pm_ec^4 ,$$

where we have labeled with k the product particles and their respective energy E_k^* in their COM frame. Let's impose that the energy of the initial state, $E_{\mathrm{in}} = s$, is equal to the threshold energy to find the minimum energy for this process to happen:

$$E_{\mathrm{in}} \overset{!}{=} E_{\mathrm{thr}} \qquad \Leftrightarrow \qquad E_{p,\,\mathrm{in}}E_\gamma - |\vec{p_{\mathrm{in}}}|\,|\vec{p_\gamma}|\,c^2\cos\theta \overset{!}{=} \left[2m_e^2c^4 + 2m_pm_ec^4\right] .$$

We can divide the RHS by m_pc^2, noticing that $E_\gamma = |\vec{p_\gamma}|\,c$, and introducing the γ_p Lorentz factor of the proton we find:

$$\gamma_p = \frac{E_{p,\,\mathrm{in}}}{m_pc^2} \qquad \text{and} \qquad \sqrt{\gamma_p^2 - 1} = \sqrt{\frac{E_{p,\,\mathrm{in}}}{m_p^2c^4} - 1} = \sqrt{\frac{E_{p,\,\mathrm{in}} - m_p^2c^4}{m_p^2c^4}} = \frac{|\vec{p_{\mathrm{in}}}|\,c}{m_pc^2} ;$$

$$\Rightarrow \qquad \gamma_p\,|\vec{p_\gamma}|\,c - \sqrt{\gamma_p^2 - 1}\,|\vec{p_\gamma}|\,c\cos\theta \overset{!}{=} 2m_ec^2\left[\frac{m_e}{m_p} + 1\right] .$$

Dividing by c^2 and taking into account a high γ_p, that is $\beta \sim 1$, and the most favorable case, namely a head on collision $\theta = \pi$, one eventually finds

$$\gamma_p^2 - 1 = \frac{1}{1-\beta^2} - 1 = \beta^2\gamma_p^2 \qquad \Rightarrow \qquad \gamma_p \simeq \frac{m_ec}{|\vec{p_\gamma}|}\left(\frac{m_e}{m_p} + 1\right) ,$$

and in particular the minimum energy $E_{\text{min}} = \gamma_p m_p c^2$ is given by:

$$E_{\text{min}} = m_p c^2 \, \frac{m_e c^2}{|\vec{p_\gamma}|\, c} \left(\frac{m_e}{m_p} + 1\right) \simeq 4.8 \times 10^{14} \left(\frac{E_\gamma}{1\ \text{eV}}\right)^{-1} \text{eV}\ , \tag{4.5}$$

for $m_e = 0.511\,\text{MeV}/c^2$ and $m_p = 938.27\,\text{MeV}/c^2$. Now we are able to assume a CMB photon with an average energy of $T_{\text{CMB}} = 2.73\ \text{K} = 2.4 \times 10^{-4}$ eV, and the resulting threshold is:

$$E_{\text{min}} \simeq 4.8 \times 10^{14} \left(\frac{2.4 \times 10^{-4}\ \text{eV}}{1\ \text{eV}}\right)^{-1} \text{eV} \simeq 2 \times 10^{18}\ \text{eV}\ ,$$

and this is very similar to the energies at which the ankle starts, i.e. $E \simeq 10^{18}$ eV. This model is actually in good agreement, at least from this simple calculation, with this structure of the CRs spectrum.

ii) *What is the mean free path?*
The estimate of the mean free path for the mechanism is actually quite delicate, since it envolves the knowledge of the so called Bethe-Heitler cross section, which can be very complicated when computed explicitly with the Feynmann rules. In practice, in the literature[2] one finds two parametrizations as a function of the photon energy $\mathcal{E}' = E'_\gamma$ in the rest reference frame of the proton:

$$\sigma_{\text{BH}}^{\text{thr}}(\epsilon') \simeq \frac{2\pi}{3}\alpha^3 \left(\frac{\hbar c}{m_e c^2}\right)^2 \left(\frac{\epsilon' - 2}{\epsilon'}\right)^2 \left(1 + \frac{1}{2}\eta + \frac{23}{40}\eta^2 + \frac{37}{120}\eta^3 + \frac{61}{192}\eta^4\right)\ ,$$

where $\epsilon' = \mathcal{E}'/(m_e c^2)$ is the photon energy in the proton rest frame normalized to $m_e c^2$ and $\eta = (\epsilon' - 2)/(\epsilon' + 2)$, and this is valid just for energies within $2 < \epsilon' < 4$, that is near the threshold, at which the photon energy in the rest frame of the proton is plainly given by $\epsilon' = 2$ since the following holds

$$\left(\mathcal{E}'_{\text{thr}} + m_p c^2\right)^2 \overset{!}{=} s^2 = \left(m_p c^2 + 2 m_e c^2\right)^2 \qquad \Leftrightarrow \qquad \mathcal{E}'_{\text{thr}} = 2 m_e c^2 \ \ (\epsilon' = 2)\ .$$

What can be easily noticed is that, for $\epsilon' \to 2$, the cross section σ_{BH} tends to zero. This is reasonable: we should expect a suppression of the process below the threshold, but yet a smooth function too. At higher energies than the threshold one the cross section is

$$\begin{aligned}\sigma_{\text{BH}}^{\text{HE}}(\epsilon') \simeq \alpha^3 \left(\frac{\hbar c}{m_e c^2}\right)^2 \Bigg\{ &\frac{28}{9}\delta - \frac{218}{27} + \left(\frac{2}{\epsilon'}\right)^2 \left[6\delta - \frac{7}{2} + \frac{2}{3}\delta^3 - \delta^2 - \frac{\pi^2}{3}\delta + 2\zeta(3) + \frac{\pi^2}{6}\right] - \\ &- \left(\frac{2}{\epsilon'}\right)^4 \left[\frac{3}{16}\delta + \frac{1}{8}\right] - \left(\frac{2}{\epsilon'}\right)^6 \left[\frac{29}{9 \times 256}\delta - \frac{77}{27 \times 512}\right]\Bigg\}\ ,\end{aligned}$$

with $\delta = \log(2\epsilon')$, and this parametrization is valid for $\epsilon' > 4$. This latter parametrization is logarithmically increasing at high energies, and at first order it reduces to the well known form

$$\sigma_{\text{BH}} = \frac{28}{9}\alpha^3 \left(\frac{\hbar c}{m_e c^2}\right)^2 \log\left(\frac{E'_\gamma}{m_e c^2}\right)\ , \tag{4.6}$$

which we have already encountered in Sec.(2.3.2.3) when dealing with photon energy losses in matter via pair production: the mechanism is essentially the same, but here in presence of a proton. Notice the right dimensionality of the cross section in each

---

[2] See the review article `https://arxiv.org/abs/1503.07749v1`.

of the above cases: $\alpha = e^2/(4\pi\epsilon_0\hbar c)$ (in SI units, while in natural units one has $\alpha = e^2/(4\pi\hbar c)$) is the fine structure constant, and here it appears with the third power since the Feynmann vertexes are three, each one proportional to $\sqrt{4\pi\alpha}$, see Fig.(4.5). In summary, one can write

$$\sigma_{\rm BH} \simeq \alpha^3 \left(\frac{\hbar c}{m_e c^2}\right)^2 f'(s) = \alpha\,\frac{8\pi}{3} r_e^2 \left[\frac{3}{8\pi} f'(s)\right] = \alpha\,\sigma_{\rm th}\, f(s)\,,$$

where we have called the square bracketed factor as $f(s)$, that is a function depending on the energy $s = E'_\gamma$ of the photon in the rest frame of the proton, which tends to zero at threshold. Also we have converted a factor of α^2 to the Thomson cross section since

$$\alpha^3 \left(\frac{\hbar c}{m_e c^2}\right)^2 = \alpha\, r_e^2 \quad \text{with} \quad r_e \equiv \frac{1}{4\pi\epsilon_0}\,\frac{e^2}{m_e c^2} = \alpha \left(\frac{\hbar c}{m_e c^2}\right)\,,$$

in SI units. In practice one can see that the cross section sensibly runs choosing different values of ϵ' and, consequently, different parametrizations from the ones above. Let's compute it for two values of ϵ', let's say $\epsilon' = 4$ and $\epsilon > 4$ at first order, just to use both parametrizations.

$$\sigma^{\rm thr}_{\rm BH}(\epsilon' = 4) \simeq \frac{2\pi}{3}\alpha^3 \left(\frac{\hbar c}{m_e c^2}\right)^2 \left(\frac{\epsilon' - 2}{\epsilon'}\right)^2\Bigg|_{\epsilon'=4} = \frac{2\pi}{12}\,\alpha\, r_e^2 = 2\left(\frac{\alpha}{32}\right)\sigma_{\rm th} =$$

$$= \frac{6.652 \times 10^{-25}\,{\rm cm}^2}{16 \times 137} = 3.03 \times 10^{-28}\,{\rm cm}^2 = 0.303\,{\rm mb}\,,$$

$$\sigma^{\rm HE}_{\rm BH}(\epsilon' > 4) \simeq \frac{28}{9}\,\alpha^3 \left(\frac{\hbar c}{m_e c^2}\right)^2 \log(2\epsilon')\big|_{\epsilon'>4} \simeq \frac{28}{9}\,\alpha\, r_e^2 = \frac{7}{6\pi}\,\alpha\,\sigma_{\rm th} =$$

$$= \frac{7}{6\pi}\,\frac{6.652 \times 10^{-25}\,{\rm cm}^2}{137} = 1.8 \times 10^{-27}\,{\rm cm}^2 = 1.8\,{\rm mb}\,,$$

and we can see that the results are different by an order of magnitude, and in the estimate for HE we have taken the factor $\log(2\epsilon')$ to be unity, while for higher $\epsilon' > 4$ it could be even larger. Let us finally compute the mean free path λ_{mfp} resulting from these two estimates:

$$\lambda^{\rm thr}_{mfp} = \frac{1}{n_\gamma\, \sigma^{\rm thr}_{\rm BH}} = 8 \times 10^{24}\,{\rm cm} = 2.60\,{\rm Mpc}\,,$$

$$\lambda^{\rm HE}_{mfp} = \frac{1}{n_\gamma\, \sigma^{\rm HE}_{\rm BH}} = 1.35 \times 10^{24}\,{\rm cm} = 438.1\,{\rm kpc}\,,$$

and we have used the fact that $n_\gamma = 411\,{\rm cm}^{-3}$ and also $1\,{\rm cm} = 3.24 \times 10^{-25}$ Mpc.

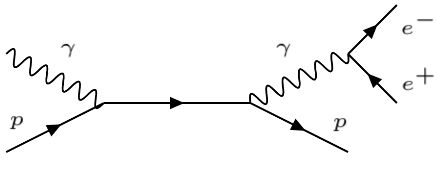

Figure 4.5: Feynmann diagram of the Bethe-Heitler process. The Feynmann vertexes are three, each one proportional to $\sqrt{\alpha}$, since the Feynmann vertex is given by $-ie\gamma^\mu$, and the amplitudes shall be simply $e^2 = 4\pi\alpha$ in natural units.

4.3 Overview on direct measurements of CRs

We would like to give a general overview on the state of art for the direct measurements of CRs and the open question marks about their results. As we have already stated, direct measurements encode both balloon and space missions experiments, measuring accurately the flux and the chemical composition of CRs up to ~ 100 TeV$= 10^{13}$ eV. Of course we need to stress that the rough estimates of the fluxes $\Phi\,(> E)$ refer to primary CRs, i.e. particles hitting the atmosphere, while for higher energies the measurements refer to the shower's products, namely the set of correlated particles hitting ground that we can attribute to the same interacting primary in the Earth atmosphere. We will discuss the most important results regarding the chemical composition, that is the relative percentage of protons and heavier nuclei in the cosmic radiation, and the energy spectrum of different particle species, but first a quick look on a simple model of primary CR detector is needed.

4.3.1 A toy detector for Primary Cosmic Rays

Actually we have already seen a sort of prototype for a primary cosmic rays detector, when we talked about the discovery of the positron Ex.(2.1). As we can deduce from that, any experimental apparatus for CRs detection should be able to do the following:

1) identify the particle, namely complete a PID;
2) measure its electric charge;
3) measure its energy and momentum.

It is clear then that every such detector shall be able to track particles' trajectories and measure energy losses in every segment of the travel. Tipically, the flux of particles can be measured with the simple experimental device shown in Fig.(4.6). Usually a series of different *layers* is employed, each one separated by a distance Δz, which can perform the counting on the basis of the excitation/ionization energy loss of traversing charged particles, namely they measure $\mathrm{d}E/\mathrm{d}x$. From the hit point of the incoming particle, the additional informations that can be extrapolated are the positions on the area A of the layer and the time of arrival (ToA) t. So the entire set of infos about the hits are given by $(x_i,\ y_i,\ z_i,\ t_i,\ \mathrm{d}E/\mathrm{d}x)$.

A major requirement of any experiment is the **trigger logic**, allowing to distinguish a real signal from a bunch of possible sources of noise, which are very probable and usually have much higher rates than the events we are interested in. Possible sources can be e.g. the presence of radioactive elements in the surrounding materials, or electronic noise. These spurious hits are not correlated with a crossing particle and constitute a background which can often be recognized by the most simple example of trigger logic, that is the coincidence between layers. This corresponds to have a correlated signal in the plates, within a tolerance window of time coherent with the propagation of relativistic, $\beta \sim 1$, particles in the separation Δz between counter layers. In vacuum, a relativistic particle has a time travel of

$$\Delta t = \frac{\Delta z}{c} \simeq 3.33\,\mathrm{ns} \qquad \text{with} \quad \Delta z = 1\,\mathrm{m}\,,$$

which is a simple estimate showing that usually such detectors have a very good time resolution[3], around 1 ns, and can also distinguish from upwards and downwards going particles, $\Delta t \gtrless 0$. A time-of-flight (ToF) measurement can thus be performed.

---

[3] This is a peculiar characteristic of scintillators, which can be suitably (and not too expensively) arranged to have sufficient spatial resolution to distinguish different directions. A similar experiment was carried in our High energy Laboratory! In addition, their response depends on the ionization energy loss, and thus on the particle Z^2.

For the charge measurements, a uniform **magnetic field** in the region between the counters performing a ToF measure has to be present too. The magnetic field allows the measurement of the particle momentum and energy, since one can make an estimate on the gyroradius and obtain the momentum in this way

$$r_{\mathrm{L}} = \frac{pc}{\mathrm{Z}e\,|\vec{B}|} \simeq \frac{E}{\mathrm{Z}e\,|\vec{B}|} \qquad \Rightarrow \qquad pc = \mathrm{Z}e\,|\vec{B}|\,r_{\mathrm{L}}\,,$$

which can be used if Ze is known. Also the sign of the charge can be inferred, as charged particles are deflected according to their *rigidity* R. The rigidity is defined as

$$R \equiv \frac{pc}{\mathrm{Z}e} \simeq \frac{E}{\mathrm{Z}e} = \frac{1.6\times10^{-12}\,\mathrm{eV/erg}\cdot E(\mathrm{erg})}{4.8\times10^{-10}\,\mathrm{statC}} = \frac{1}{300}\left(\frac{E}{\mathrm{eV}}\right)\,\mathrm{V}\,, \tag{4.7}$$

where we have converted the electric charge in statcoulomb (cgs sytem) and the rigidity is measured in Volts. This quantity is important since it is clear that it measures the effect of a magnetic field on the particle. Usually even a *tracking system* is implemented to accurately measure the curved particle trajectory, namely additional detectors are needed inside the magnetic field region, which depend also on the different charged particles: leptons and hadrons have very different interaction lenght. The combination of the magnetic field and tracking detectors is usually referred to as a "magnetic spectrometer".

Lastly, the major requirement for any detector is a **calorimeter**, an additional unit at the basement of our toy detector to study the end of the travel of the particle. Calorimeters have usually the task to measure a total energy deposition E_{tot}, since the particle is stopped and fragmented. The kinetic energy of the incident particle is thus converted inside the absorbing material into a cascade of many secondary particles, and at the end the primary energy of the incident particle is dissipated via excitation and ionization of the absorber. Obviously, even in this case, the mean free path of different particles can be a primary constructive parameter: muons, for example, are much more penetrating then hadrons, which are in turn more penetrating than electromagnetic products. For practical purposes, one adapts the dimensions to the need: hadronic calorimeters are usually bigger the EM ones.

Obviously this kind of device can work for the purpose of direct detection if it is carried to the top of the atmosphere by a balloon or outside the atmosphere by a satellite, and calorimeters' dimensions and absorber's thickness are thus limited due to weight restrictions.

The Interplanetary Monitoring Platform (IMP) The IMP was a series of 10 scientific satellites launched by NASA between 1963 and 1973. These experiments were sensible mainly in an energy region where the solar wind significantly affects CRs, and provided relevant informations concerning the solar activity. The structure of the IMP-7 and IMP-8 was very similar to our simple toy detector: particles pass through a series of three silicon layers, namely D1, D2, D3, which measure the differential energy loss $\mathrm{d}E/\mathrm{d}x$, and then the travel stops at D4, a CsI (Tl) scintillator, which is supposed to measure E_{tot}. Counters D5 and D6 act as *veto*, to confirm that the particle is stopped in D4 and eliminate other sources of disturbances. These detectors had a fundamental role in the particle identification side, especially in the estimate of isotopic fluxes, which will be treated in the following. The structure is schematically shown in Fig.(4.7—Left). The energy scale of effectiveness for these detectors was up to $\sim$ 100 MeV.

4.3.2 The modern satellite experiments

We have already talked about the IMP detector as a prototypical "toy telescope" of primary CRs, being also quite innovative and in fact a milestone for the new, modern space mission

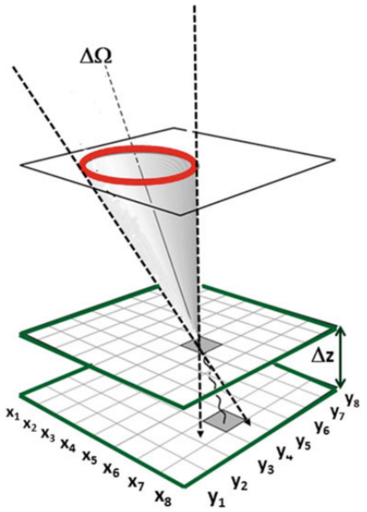

Figure 4.6: Layout of a simple telescope for the measurement of CRs. A CR arriving within the solid angle dΩ will produce a sequence of hits on the layers.

experiments. The main difference now from the early 1970s satellite detectors is the energy range explored by the new technologies: from 50 MeV to few TeVs, these direct measurements devices can cover largely the range of the lower energies CRs. The protagonists are PAMELA and AMS-02.

PAMELA

The PAMELA experiment is a powerful particle identifier using a permanent magnet spectrometer with a variety of specialized detectors that accurately measure the abundance and energy spectra of CR electrons, positrons, antiprotons and light nuclei. The name refers to Payload for Anti Matter Exploration and Light-nuclei Astrophysics, and was launched in 2006, remaining operative till 2016. A schematic view of the apparatus is shown in Fig.(4.8—Left). The ToF system has a very good resolution of ~ 0.3 ns, regarded as usual as the principal trigger logic.

AMS-02

The AMS-02, which stands for Alpha Magnetic Spectrometer, is the largest particle physics detector ever carried outside the atmosphere and it was designed to operate as an external module on the International Space Station (ISS): its lifetime is then expected to coincide with the lifetime of the ISS itself. The reason for the 02 is simply because the prototype was called AMS-01 and was very simplified with respect to the one operating now. The time of flight (ToF) system is able to measure with precision of ~ 0.15 ns the particle transit time through the detector and provides trigger for the other subdetectors. AMS-02 is also equipped with an Anti Coincidence Counter (ACC) which provides a way to distinguish *albedo particles* from the the interesting ones, namely upwards from downwards going particles. A side section view of AMS-02 is given in Fig.(4.8—Right).

4.3.3 The measured quantities

4.3.3.1 The chemical composition in our Galaxy

The particle identification is a very important topic for cosmic rays, since it is fundamentally related to the history of the CRs propagation through the galaxy. The first kind of differentiation between incident particles relies on the fact that ionization energy losses depend

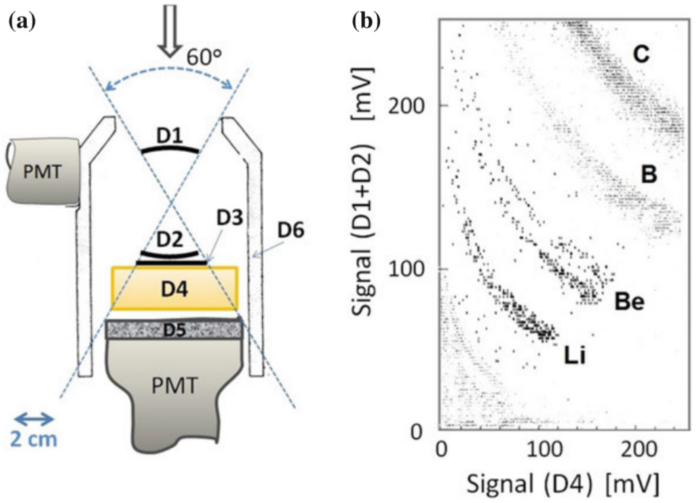

Figure 4.7: Left: Layout of the telescope on board IMP-7, IMP-8. Right: Result from IMP-8, data collected between 1974 and 1975. On the y-axis, the signal is proportional to the energy loss measured in (D1 + D2); on the x-axis, to the residual energy of the particle measured in D4.

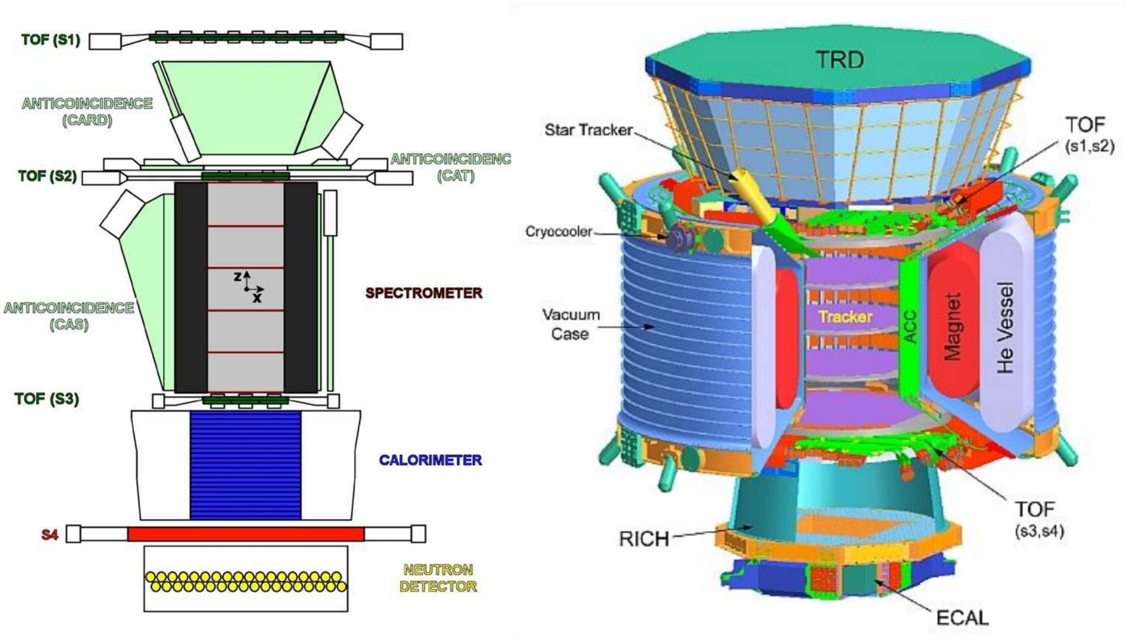

Figure 4.8: Left: A schematic overview of the PAMELA satellite experiment. The experiment stands ∼ 1.3 m high and, from top to bottom, consists of a time-of-flight (ToF) system (S1, S2, S3 scintillator planes), an anticoincidence shield system, a permanent magnet spectrometer (the magnetic field runs in the y-direction), a silicon-tungsten electromagnetic calorimeter, a shower tail scintillator (S4) and a neutron detector. The experiment has an overall mass of 470 kg. Credits to `https://arxiv.org/pdf/1001.3522.pdf`. Right: AMS-02 schematic view. Credits to the official site `https://ams02.space`.

on the atomic number Z. In particular, recalling the Bethe-Bloch equation[4] Eq.(2.12), the dependence is quadratic in both Z and the incident velocity β, $\mathrm{d}E/\mathrm{d}x \propto (\mathrm{Z}/\beta)^2$. The quite clear separation of specific energy losses from different nuclei is shown in Fig.(4.7—Right): at a given energy, the $\mathrm{d}E/\mathrm{d}x$ increases as Z^2. Most importantly, at a given energy and also for a fixed Z, nuclei with larger mass number A have smaller $\beta = v/c$ and undergo larger energy losses: in this way different isotopes can be identified too.

The Fig.(4.7) refers to results of IMP-8, and this experiment was peculiar since it was the first one to measure the isotopic Li, Be, and B flux, especially the flux of ^{10}Be isotope, which is unstable to β^- decay[5] and thus important for the CRs aging techniques. This experiment was highly reproduced in satellites, as we will presently see. In particular, the experiment measured the following flux ratios

$$^{7}\mathrm{Be} \ : \ ^{9}\mathrm{Be} \ : \ ^{10}\mathrm{Be} = 329 \ : \ 147 \ : \ 15 \, ;$$

and this turned out to be fairly in good agreement with the results obtained by predictions of productions of these elements by *spallation* effects (see below) with the effective cross section data from accelerators:

$$^{7}\mathrm{Be} \ : \ ^{9}\mathrm{Be} \ : \ ^{10}\mathrm{Be} = 9.7 \ : \ 4.3 \ : \ 2.3 \, .$$

The main difference between the predicted and the measured ratio is the quite lower flux of ^{10} Be isotope: the logic explanation is that a large fraction of this unstable isotope had time to decay before detection. This allows the measurement of the *CR escape time* τ_{esc} from our Galaxy.

The spallation process for lighter nuclei In general, one refers to C, N, O as primary particles, and to the slightly lighter nuclei Li, Be, B as secondaries. The reason is that stellar nucleosynthesis is the major responsible for the enrichment, via SN explosions, of the insterstellar medium with the first three species of metals, while the latter triplet is certainly not expected since these lighter nuclei are usually catalysts in thermonuclear reactions. The origin of the fluxes measured e.g. in IMP-8 is believed to reside in the CRs propagation as an effect of interactions of heavier nuclei with protons of the interstellar medium. The term "*spallation*" generally refers to inelastic nuclear reactions that occur when energetic particles interact with an atomic nucleus, and in the CRs context it is simply a fragmentation. However, the result of this interaction process is the ejection of some nucleons from the nucleus that has been hit. The interstellar medium (ISM) is deeply filled mostly with hydrogen, and the reaction we are interested in is then the following:

$$p + X \to Y + \text{anything} \qquad \text{with} \qquad X = \mathrm{C, N, O} \, ,$$

and the spallation is happening with a proton approximately at rest in the ISM. Y refers, for our purpose, to possible isotopes of Li, Be, B. Such reactions can be studied in accelerators, to obtain estimates in the cross sections and mean free path. We will study this process in Sec.(4.6.3.1), to obtain an estimate for τ_{esc}.

Let us investigate further on the chemical composition estimates from CRs direct measurements. In particular, Fig (4.9—Left) shows a comparison between the Solar System abundances[6] and the composition of CRs, as a function of the atomic number Z. Remarkably, the

---

[4] Here we call Z the atomic number of the incident particle, while on the Bethe-Bloch formula we have called like that the atomic number of the medium, and z took instead the other role: here no confusion can be made between the two.

[5] The lifetime of a ^{10}Be nucleus is about $\tau_{1/2} = 4.77 \times 10^{13}\ s \approx 1.5 \times 10^{6}$ yr.

[6] Clearly the informations we get for the Solar System come mostly from chemical analysis of meteorites and photospheric measurements of the light from the Sun.

two profiles show some analogies, mainly in the see-saw behavior typical of nuclear parity effect on binding energies of the various atomic species, see Fig.(4.9—Right). Medium mass nuclei are quite in agreement, and all the elements present in the Solar System have been found in cosmic rays as well. The immediate and striking conclusion is that the accelerated matter arriving on Earth consists of material plausibly originated by the same mechanism that originated the Solar System.
A peculiar difference can be noticed as regards the much higher abundances of Li, Be, B, as already explained, and also of heavier metals as Sc, V. The most rated explanation is that, again, all these differences must be due to the effect of the propagation in the Galaxy, C, N, O being the primary products from astrophysical sources and the other lighter isotopes being born from nuclear reaction in the ISM.

The Cosmic Abundances The chemical elements existing in nature reflect the materials produced and processed from the fundamental fuels of the early universe, namely the products of the Big Bang Nucleosynthesis (BBN). The BBN left the cosmo filled with these fractions:

$$75\%\,\text{protons} \qquad 25\%\,\text{He} \qquad < 1\%\,\text{other isotopes}\,,$$

where the protons were ready for the subsequent Hydrogen Recombination which gave rise to the CMB. After the first generation of stars was born (and quickly perished actually), the elemental abundances of the Universe started to be determined by the nuclear fusions in stellar cores, and today these abundances are inevitably continuing to be fed and regulated by stellar nucleosynthesis. This process naturally proceeds via fusion up to isotopes of the iron group, wih A< 60, and the heavier nuclei are produced in advanced stages of stellar evolution by neutronizations. The binding energy curve shows a maximum at ^{56}Fe, and then proceeds till the last stable isotope with A=220. Let us recall that the binding energy is defined as the difference between the mass of the nucleus and the sum of the masses of the constituent nucleons:

$$M_{\mathrm{A}} = \sum_{k=1}^{\mathrm{A}} m_k - BE = (\mathrm{Z}m_p + \mathrm{N}m_n) - BE\,,$$

which is called semi-empirical mass function, and the modeling of the binding energy contributions is very precise in the context of the "nuclear drop" model of nuclei. What is sufficient to recall for our purposes is that a contribution to the binding energy is given by the *parity term*, which cause higher relative binding energy of even atomic numbers with respect to odd atomic numbers, by virtue of the Pauli exclusion principle.

4.3.3.2 The energy spectrum of protons and nuclei

We have seen the typical example of an "all particle" spectrum, in which the energy per nucleus was represented. Through direct experiments, instead, the energy per nucleon, E/A, can be discerned, thanks to the identification of both Z and A, and Fig.(4.10) shows the differential energy spectra of primary protons and helium nuclei obtained by the BESS-Polar Collaboration. The differential flux is represented as

$$E^{2.7}\,\frac{\mathrm{d}N}{\mathrm{dA}\,\mathrm{d}t\,\mathrm{d}\Omega\;(\mathrm{d}E/\mathrm{A})} \qquad \text{in} \qquad \frac{\#\,\text{nucleons}}{\mathrm{m}^2\,\mathrm{s}\,\mathrm{sr}\,\mathrm{GeV}^{1.7}}\,.$$

This experiment measured the energy spectra of cosmic ray protons and helium during two balloon flights over Antarctica in December 2004 and December 2007, at different levels of *solar modulation*. Actually balloons experiments were, since the beginning of CRs studies, an important mean in alternative to the much more expensive satellite ones, even though balloons had the disadvantage of very short exposure, of course. Antarctica has the advantage

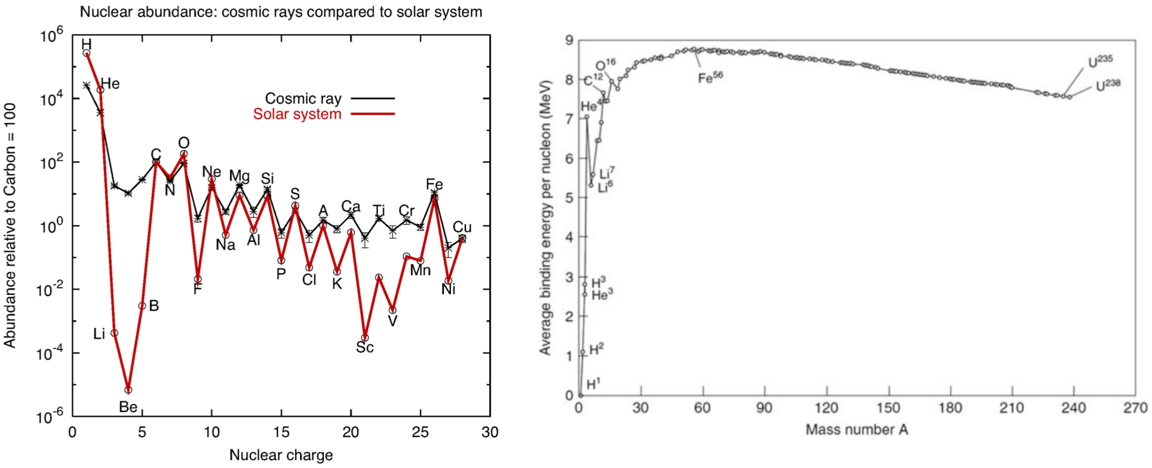

Figure 4.9: Left: Relative abundance of nuclei in cosmic rays as a function of their nuclear charge number Z, normalized to Carbon=100, with the Solar System abundances also superimposed. Right: the very well known binding energy per nucleon curve for different atomic number Z.

of quasi circular and well studied winds, which can be means of controlling the balloon flights. A part from the differences at low energies due to the solar activities, at higher energies the agreement with other experiment is quite good. However BESS-Polar spectra do not extend to high enough energy to test the spectral hardening reported by PAMELA and AMS-02.

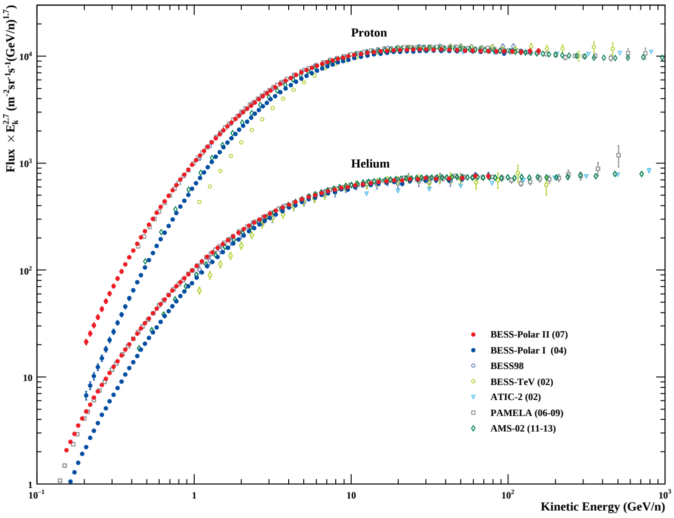

Figure 4.10: Differential energy spectra of primary protons and helium nuclei weighted by $E^{2.7}$ and measured by BESS-Polar I and BESS-Polar II. Spectra reported by other collaborations, such as PAMELA and AMS-02, are shown for comparison. Differences in the BESS-Polar I and BESS-Polar II spectra at low energies are essentially due to solar modulation, since the two flights happened at different times and the solar activities provide an unpredictable shielding effect.

The solar modulation at low energies While Solar Flares are a direct source of CRs at energies < 4 GeV, our star is the protagonist of important influences in the propagation of low energy charged particles due to the *solar wind*, which is a stream of plasma material continuously released from the upper atmosphere of the sun, the heliosphere. CRs at few GeV entering the heliosphere are scattered by irregularities in the heliospheric magnetic field. Such particles undergo convection and adiabatic deceleration in the expanding solar wind, being partially excluded from the inner solar system. This gives rise to a modification of the energy spectra known as “solar modulation”. The magnetic activity and the solar modulations are manifested through sunspots, which have a $\Pi \sim 10.9$ year cycle.

Also some results from AMS-02 are shown in Fig.(4.11), with a comparison with other compilations of data. In the Right panel also a comparative study of the proton flux is shown. AMS-02 reaches much higher energies than the BESS-Polar, and does not show the same inconsistences due to solar modulations in the low energy tail. AMS-02 studied mainly the Helium flux and the main results can be summarized as follows:

1) the spectral index progressively hardens at rigidities larger than 100 GV, as is shown in Fig.(4.11—Left) in the top panel;
2) correspondingly, a change in the slope above 100 GeV is also shown in the energy spectrum of He as a function of kinetic energy E_k, Fig.(4.11—Left) middle panel;
3) the rigidity dependence of the helium flux spectral index is similar to that of the proton spectral index, though the magnitudes are different as shown in Fig.(4.11—Right) in the top panel;
4) the spectral index $\gamma_{p/\mathrm{He}}$ of the proton to helium flux ratio p/He increases with rigidity up to 45 GV and then becomes constant, as shown in Fig.(4.11—Right) in the bottom panel. The spectral index $\gamma_{p/\mathrm{He}}$ is obtained by

$$\gamma_{p/\mathrm{He}} \equiv \frac{\mathrm{d}\log\left(\Phi_{p/\mathrm{He}}\right)}{\mathrm{d}\log\left(R\right)} \qquad \text{with} \qquad \Phi_{p/\mathrm{He}} = \frac{\Phi_p}{\Phi_{\mathrm{He}}}\ ;$$

5) the flux ratio p/He above 45 GV is well described by a single power law, Fig.(4.11—Right) middle panel.

Finally, Fig.(4.12) shows the major nuclear components in CRs as a function of the energy per nucleus. The separation of different nuclei is quite clear, being enhanced also by a multiplication by constant factors. Notably, the instruments devoted to indirect detection, e.g. VERITAS and HESS, can also perform some direct measurements. The exponent spectral index α_i is almost the same for all nuclear species shown, apart from protons, whose one seems to be harder. The insert of this figure shows the p/He ratio as a function of rigidity, and the comparison from PAMELA and AMS-02 is made as in Fig.(4.11—Right) in the middle panel. The differential spectra are then described globally by a power law such as Eq.(4.3):

$$\Phi\left(E\right) = K_i \left(\frac{E}{1\ \mathrm{GeV}}\right)^{-\alpha_i} \qquad \text{in} \qquad \frac{\#\ \text{particles}}{\mathrm{m}^2\ \mathrm{sr}\ \mathrm{s}\ \mathrm{GeV}}\ ,$$

where of course the different species are labeled with pedex i, and K_i, α_i are obtained by fits on the experimental data.

The summary of results obtained by AMS-02 is indeed a list of general features which are found in mostly all other experiments with good agreement. Therefore by now a lot of efforts are devoted into providing explanations about the explicit deviation from a simple power law highlighted by both PAMELA and AMS-02 for energies above 100 GeV. Several possible explanations are being explored, mainly different mechanisms of propagation at different energies are not to be excluded, as well as a hardening effect caused by the propagation process itself, or lastly a young/local source which takes over the extragalactic sources at a given energy.

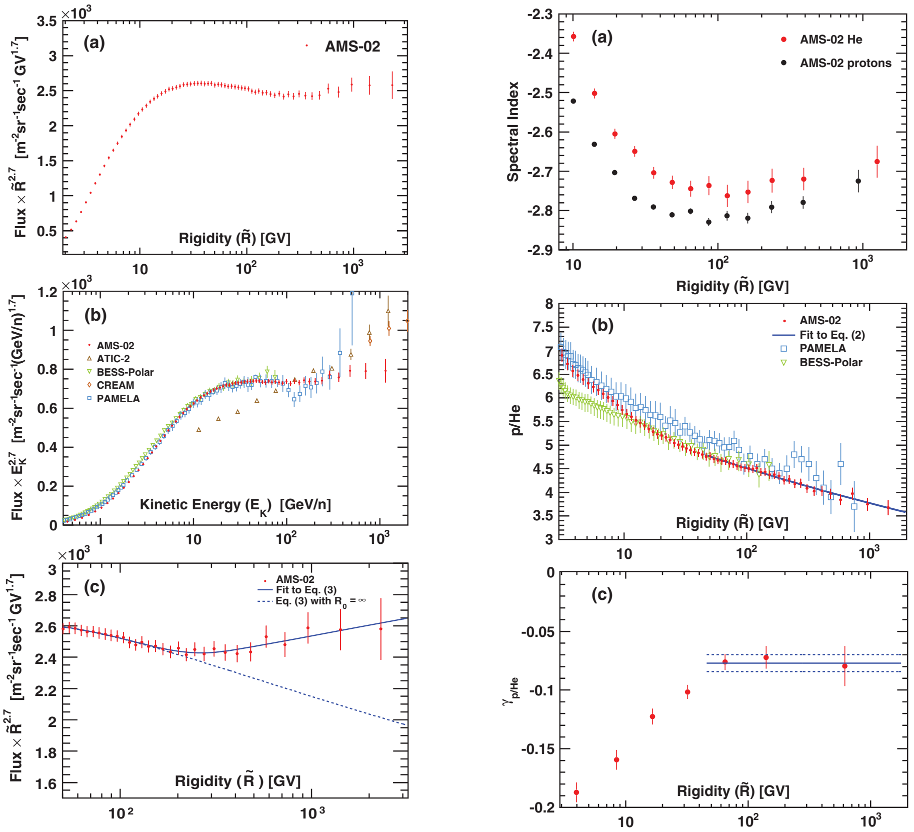

Figure 4.11: Left:(a) The AMS helium flux multiplied by $R^{2.7}$ as a function of rigidity R. The spectral index progressively hardens at rigidities larger than 100 GV. (b) The flux as a function of kinetic energy per nucleon E_k multiplied by $E_k^{2.7}$. (c) Fit with a double power law of rigidity to the AMS helium flux. For illustration, the dashed curve uses the same fit values but with R_0, initial rigidity, set to infinity. Right: (a) The dependence of the helium and proton spectral indices on rigidity. (b) The p/He ratio as a function of rigidity. The solid blue curve indicates the fit of a single power law to the AMS data. As seen, above 45 GV the ratio is well described by a single power law. (c) The rigidity dependence of the p/He spectral index $\gamma_{p/\mathrm{He}}$ as measured by AMS. As can be easily seen, it increases up to about 45 GV, and then becomes constant. The dashed blue lines are the total errors. Credits to `https://journals.aps.org/prl/pdf/10.1103/PhysRevLett.115.211101`.

4.3.3.3 The antimatter in our Galaxy

The Big Bang Theory predicts that equal amounts of matter and antimatter should have been produced at the beginning of the Universe, but as far as we observe there seems to be only matter in the cosmo. The most mysterious question mark of cosmology and particle physics is indeed the so called *Baryon Asymmetry*, a process which must have happened right after Inflation in the Standard Inflationary Model and which must have created the conditions for matter and antimatter annihilation, with the final prevail of the first. Anyway antimatter is observed: positrons and antiprotons were first discovered in the mid 1900s', and we know that they are a fundamental component of the CRs radiation. The most accredited explanation[7] is that the creation of those components happen in the context of CRs propagation, by interactions with the ISM. As an example, secondary antiprotons are mainly produced by CR protons interacting with ISM ones by the following

$$p + p \to p + p + p + \bar{p} \qquad \text{with} \quad E_{\mathrm{thr}} \simeq 7\,\mathrm{GeV}\,, \tag{4.8}$$

---

[7] Another explanation can be the Dark Matter decay processes, which are object of a lot of studies from the theoretical point of view.

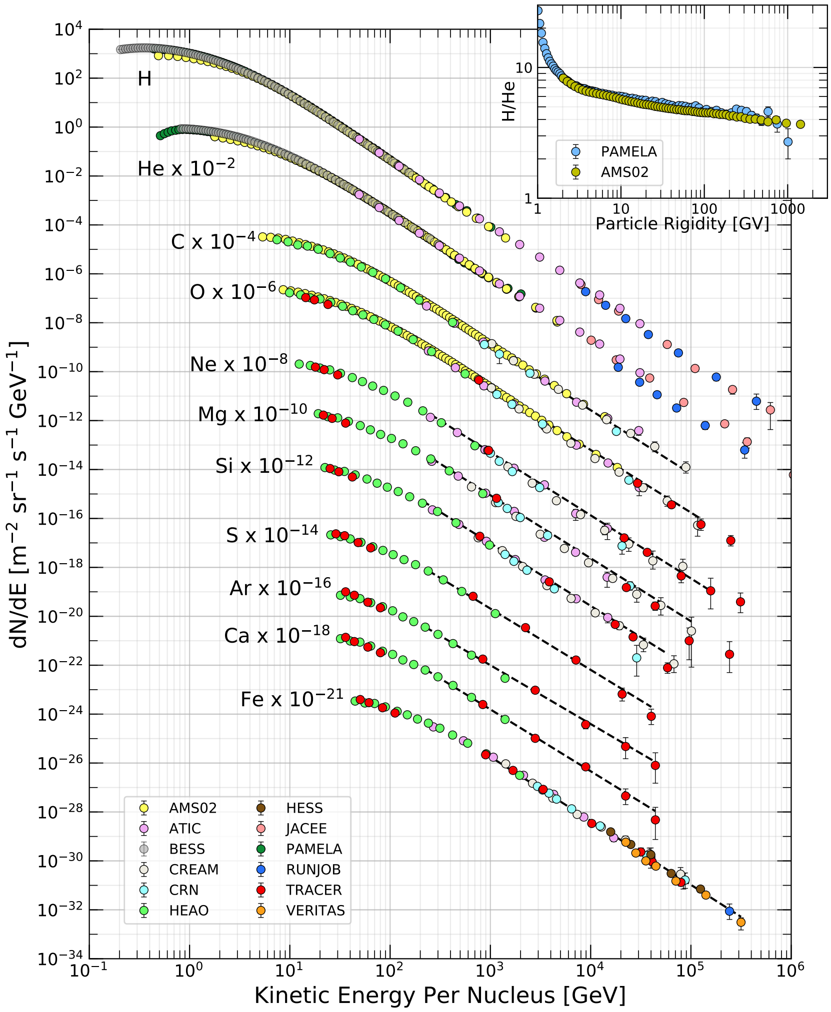

Figure 4.12: Fluxes Φ_i of CR nuclei of primary CRs as a function of energy per nucleus, as a summary of data obtained by direct experiments. For a better understanding of the figure, the flux of each nuclear species is multiplied by a scaling factor. The insert at the top right corner shows the p/He ratio as a function of rigidity. To be precise, not all the instruments cited in figure are measuring CRs directly, as we could have already guessed looking at the energy range, going well beyond the TeV. See `http://pdg.lbl.gov/2019/reviews/rpp2019-rev-cosmic-rays.pdf`, PDG review on Cosmic Rays.

which was actually a Nobel winning reaction. This reaction can give a first order rule of thumb to estimate the ratio of the fluxes of antiprotons and protons $\Phi_{\bar{p}}/\Phi_p$. In particular, if one considers the general behavior of the spectral index in Fig.(4.10), namely $\alpha \simeq 2.7$, and the fact that the maximum in Fig.(4.12) for the protons is at $E \sim 0.1$ GeV, we get

$$\frac{\Phi_{\bar{p}}}{\Phi_p} \simeq \left(\frac{0.1\,\text{GeV}}{7\,\text{GeV}}\right)^{2.7} \approx 10^{-5}\,,$$

where the value of E_{thr} is assumed to be the energy of the maximum flux for positrons. Despite being very naive, it happens to be in good agreement with the results from PAMELA, shown in Fig.(4.13), at the energy of E_{thr}. Obviously, in general this flux is a function of energy $\Phi_{\bar{p}}/\Phi_p(E)$. The most important result regarding this measure is that the measured spectrum is consistent with the hypothesis that the observed antiprotons are secondary particles produced by CR interactions with the interstellar medium. Remarkably, no heavier antinuclei have been detected so far. A very well known code, GALPROP, is highly used for MC simulations about CRs propagation mechanism, and it accounts for all the mapped magnetic fields and nebulae of our Galaxy.

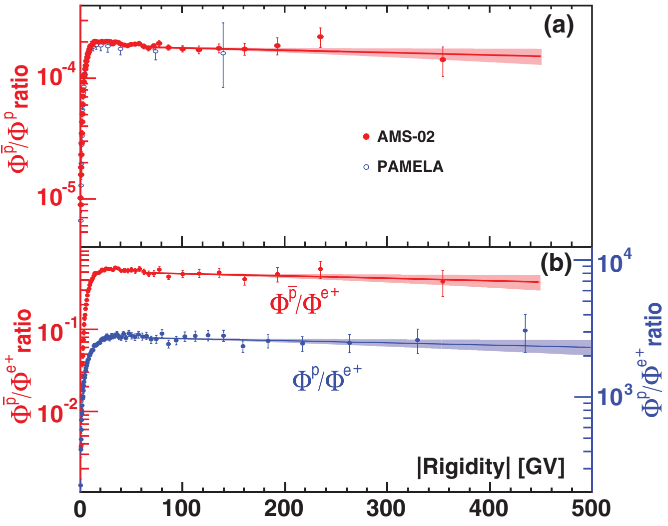

Figure 4.13: The top panel shows the measured $\bar{p}/p$ flux ratio as a function of the absolute value of the rigidity from 1 to 450 GeV. The bottom panel are the measured $\bar{p}/e^+$ (red, left axis) and p/e^+ (blue, right axis) flux ratios. The solid lines show the best fit of the data with the 68% C.L. range (shaded regions). From `https://journals.aps.org/prl/pdf/10.1103/PhysRevLett.117.091103`.

4.3.3.4 Electrons and Positrons fluxes

A question which naturally arises is about the energy spectrum of electrons and positrons. They constitute a very small fraction of the CRs flux, namely $< 1\%$. This is caused by just one fact: the leptons are promptly subject to large electromagnetic energy losses already in proximity of their sources. The mechanisms are mainly

- emission of synchrotron radiation in the galactic magnetic field $|\mathrm{B_{MW}}| \simeq \mu\mathrm{G}$;
- collision losses and Bremsstrahlung in the ISM gas clouds encounterings, but these are much less prominent.

Via these phenomena, the accelerated electrons are the source of most of the non thermal[8] electromagnetic radiation measured from radio to X-rays energy range. In particular these mechanisms are expected to distort the spectrum of these particles. Actually, a steepening of one power in E is theoretized from synchrotron dispersions, such that

$$\Phi^{e}\left(E\right) = K\left(\frac{E}{1\ \mathrm{GeV}}\right)^{-\alpha} \mathrm{m}^{-2}\,\mathrm{sr}^{-1}\,\mathrm{s}^{-1}\,\mathrm{GeV}^{-1} \qquad \Rightarrow \qquad \Phi^{e}_{\mathrm{source}}\left(E\right) \propto E^{-\alpha+1}\,,$$

where $\Phi^{e}_{\mathrm{source}}$ is the expected differential flux of electrons at the source production. From experimental results, the measured spectral index $\alpha \sim 3.1$ indicates a spectral index of CR sources of $\alpha \simeq 2$, which is a recurrent number in astroparticle physics. Fig.(4.14) shows the differential spectrum of both electrons and positrons, with weight on y-axis given by E^3, showing a good compatibility with spectral index 3 over a broad range of energies. We shall underline that the eventual presence of a structure in a smooth spectrum of the lepton component would represent an important signature for unexpected physics, particularly prominent for annihilation of dark matter candidates, but so far no structures have been confirmed.

---

[8] Non thermal emission is continuum emission that cannot be originated by blackbody radiation or thermal bremsstrahlung.

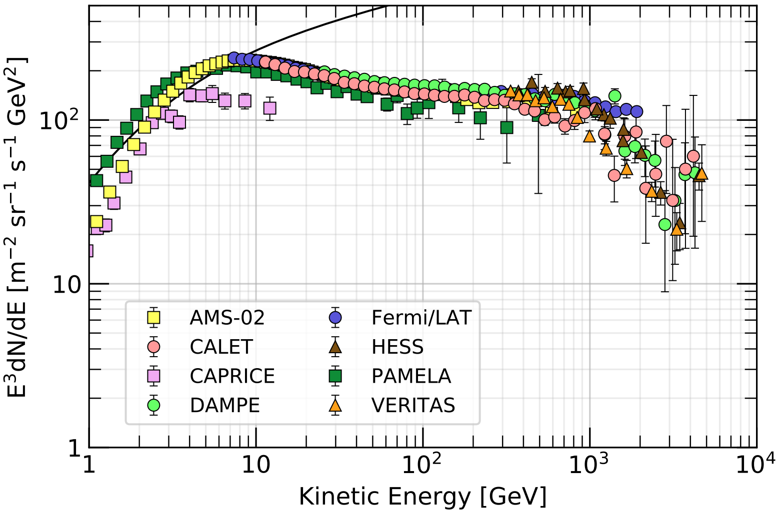

Figure 4.14: Differential spectrum of electrons plus positrons (except PAMELA data, which concern electrons only) multiplied by E^3. The line shows the proton spectrum multiplied by 0.01. Taken from `http://pdg.lbl.gov/2019/reviews/rpp2019-rev-cosmic-rays.pdf`.

Lastly few more words about the positron component are due. These leptons can be easily discerned from the electrons thanks to the magnetic spectrometers, and the vast majority of positrons arise as secondary products of CR interactions in our Galaxy. This is a fundamental difference with the electrons, which are instead a consistent portion of primary particles promptly produced at astrophysical sources. Fig.(4.15) shows the relative flux of positrons normalized to the total flux of the two leptons,

$$\frac{\Phi^{e^+}(E)}{\Phi^{e^+}(E)+\Phi^{e^-}(E)},$$

as a function of energy. A comparison with the model, namely the solid black line, for a pure secondary production such as the one of Eq.(4.8), gives immediately the taste of the so called **positron excess**, which is still an open question mark. A lot of hypothesis are being explored: dark matter effects are usually discarded, since it would otherwise fail to explain the behavior of $\bar{p}$ profiles; maybe local sources of positrons or effects of propagations are the most common possibilities. Surely, since this ratio is of the order of 10%, then about 90% of the observed electrons must be of primary origin, because of the fact that positrons are always created in pair with an electron.

4.4 Overview on indirect measurements of CRs

Let us now consider some results, techniques and issues concerning indirect measurements of CRs. Direct measurements essentially work for energies up to $\sim$ 100 TeV, and beyond this limit the flux of cosmic rays drops sharply. The statistic starts to be not enough to build up a real sample, and even to identify the primary particles. So, for energies higher than 10^{13} eV, we have to rely on observations of the extensive air showers, EAS, with ground-based instruments. Mostly they will be *arrays* of detectors, with these fundamental properties:

a) They usually cover up to several thousands of km^2 to enhance the statistics;

b) They are arranged to be long duration experiments, since the exposure to CRs showers has to last several years, to enhance the statistics again;

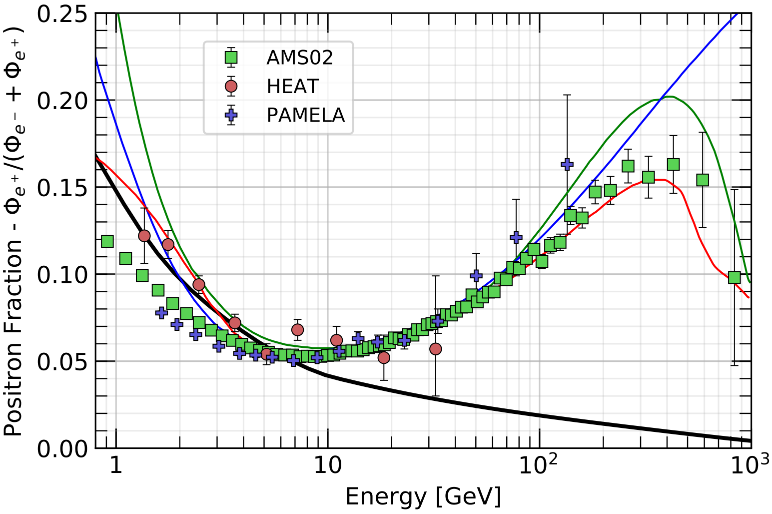

Figure 4.15: The positron fraction (ratio of the flux of e^+ to the total flux of e^+ and e^-). The heavy black line is a model of pure secondary production and the three thin lines show three representative attempts to model the positron excess with different phenomena, namely green: dark matter decay; blue: propagation physics; red: production in pulsars. The ratio below 10 GeV is dependent on the polarity of the solar magnetic field. Still taken from the PDG reviews `http://pdg.lbl.gov/2019/reviews/rpp2019-rev-cosmic-rays.pdf`.

c) They will aim to study the nature, flux, mass, and direction of primary CRs up to the highest energies.

In particular, these arrays are formed by a series of different sensors, namely scintillators, water Cherenkov tanks, muon detectors, and Cherenkov telescopes, spread over a large area. We shall discuss them with a short presentation of a toy model for an EAS array in the following, not before overviewing some common challenges of the indirect measurements analysis.

4.4.1 The challenge about MC simulations

With respect to direct experiments, some practical challenges arise naturally in the context of indirect measurements. As one can already have perceived from Sec.(3.2.2) and also Ex.(3.3), we have always to rely on MC simulations, and this kind of approach introduce a number of uncertainties.
Firstly the **calibration** of the full array can't be always performed, since EAS experiments cannot be exposed to a test beam. The interpretations of their measurements rely on comparison of the experimental data with model predictions of the shower development via MC.

Secondly, the fact that the **atmosphere** is part of the detector introduces a lot of issues, since it is indeed a time changing and complex enviroment. MC simulations are able to model in general all kinds of energy losses, deflections of trajectory due to scatterings and, for charged particles, due to Earth magnetic field, and most importantly the interactions between particles. As we have already stated, while the electromagnetic and the weak interactions are rather well understood, the major uncertainties in MC simulations of EAS arise from the hadronic interaction model, namely QCD theory, being, on one hand, very successful in reproducing some experimental results, is by now not completely settled in modeling the quite complex interactions such as that in hadronic showers. In particular, it can't be applied to compute the hadronic inelastic cross section σ_{inel} with air molecules, and the multiplicities N_i of secondary hadrons, which are actually very important parameters. A sort of combination of experimental data and modeling has to be performed, and goes under the name of *MC tuning*: this constists indeed on building some effective parametrizations as best fitting semi-theoretical results.

Last but not least, the **energies** which are to be studied are much larger than the actual energy range which is explored by colliders data, which allow for detailed tests of interaction models up to energies of $\sim 10^{17}$ eV (see Ex.(1.2)). So a certain amount of extrapolation of the properties of hadronic interactions is still needed to interpret the air shower data. This is certainly a non trivial task. A striking difference is that of the transverse momentum component p_t, which is usually very small in atmospheric showers (the reason being essentially in the momentum conservation for high energy quasi relativistic particles), making a great fraction of secondaries move in the primary direction, i.e. a *forward production*. These low p_t particles transport a large energy fraction deep into the atmosphere, and are of course of great importance. On the other hand, colliders barely even produce this kind of highly collimated particles due to beam pipes, i.e. the guidelines of the colliding beams, and so can help with the study of these phenomena with only a poor statistic. So by now σ_{inel}, N_i distributions and even transverse momenta p_t have to be extrapolated.

CORSIKA is one of the most used MC algorithm, containing different computer codes for the hadronic interaction modeling of nucleons and nuclei. Some famous names are VENUS, QGSJET, DPMJET, SIBYLL, and EPOS. The latter in particular was fundamentally developed for colliders, and then applied for EAS with great success. Detailed comparisons of the models available by now have been performed, revealing differences on the 25–40% level. As an example of this kind of comparisons, in Fig.(4.16) the average depth of maximum $< x_{\max} >$ of proton and iron-induced air showers is shown as function of the energy for various models and data. The name CONEX refers to a fast 1D code for showers profile simulations released in 2004[9], and it is compared to some CORSIKA submodels and experimental data too. Remarkably, the two most extreme sources are studied, namely assuming that the CRs are exclusively made by light nuclei like p or exclusively heavy particles like Fe. Notice that the energies are very extreme, even above the knee. Some differences can indeed be spotted, and these are the sources of systematic uncertainties, which are actually very challenging to be faced.

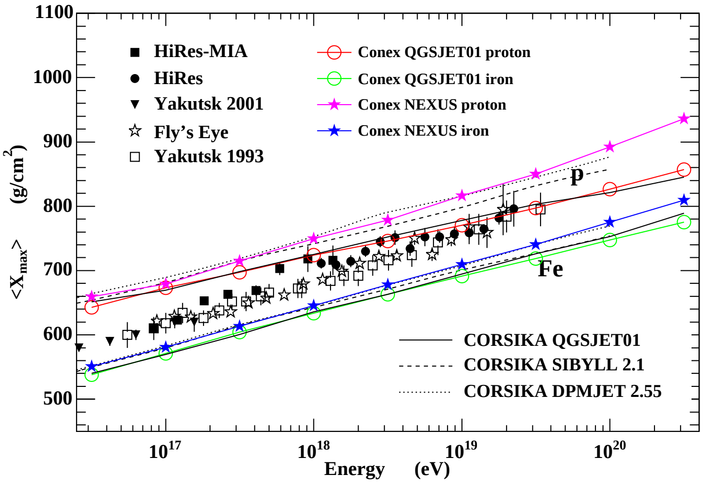

Figure 4.16: $< x_{\max} >$ of proton and iron-induced showers for different models together with data. CORSIKA shower simulations are based on 500 showers for each energy point.

---

[9] See `https://arxiv.org/pdf/astro-ph/0411260.pdf` for details.

4.4.2 A toy model for an EAS array

We have already described the fundamental characteristics that every array must share. In particular, they must be composed by different elements spread in a large area. The basic idea is that, when secondary particles from showers fall to the ground, the subset of detectors placed near enough to the shower core will be hit and perform a measurement. Let us then describe every kind of sensor which can be present in such an ideal, "toy" array, and their different functions. Fig.(4.17) pictorially shows the scheme we are going to describe. We shall see that these techniques are also appliable to γ-rays.

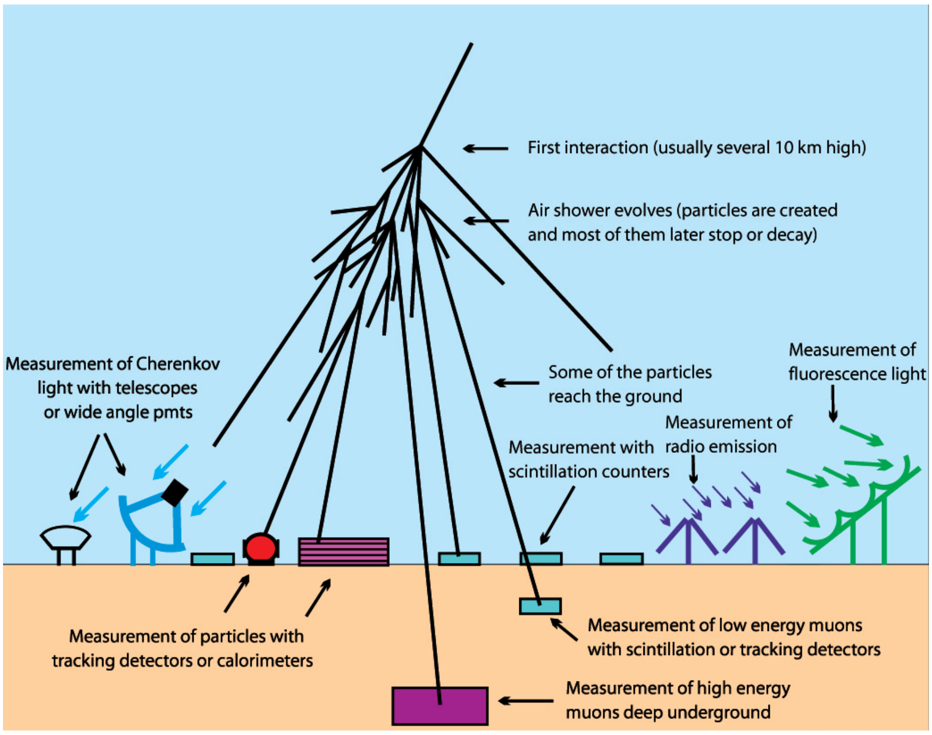

Figure 4.17: Pictorial representation of an EAS detector system, namely an array. All principal sensors are highlighted.

1) *Scintillators*, tracking detectors and calorimeters: at the ground level, these kinds of sensors perform measurements of the shower core particles, i.e surviving hadrons in forward productions. These have very low p_t in general, so most particles observed at ground level are close to the shower axis, within 2-3 Molière radii, this value depending however on energy. These are usually coupled with PMTs. One alternative to scintillator counters is the use of water Cherenkov tanks, which exploit the fact that in water charged particles emit Cherenkov radiation, whose intensity is proportional to the path length of the particle. Water tanks also offer a nonzero effective surface for horizontal showers too, because they are usually very big.

2) Not so deep underground, the same kind of detectors are operating to measure the lower energy muons. In particular they are usually *Cherenkov tanks*. Scintillators are able to measure the energy loss per collision $\mathrm{d}E/\mathrm{d}x$ via its conversion into de-excitation light of the material and then into an electric signal amplified by PMTs; in the case of Cherenkov tanks the mechanism is the same, but makes use of Cherenkov light by charged particles.

3) *Cherenkov telescopes* are also present at ground level to detect the Cherenkov light emitted by the large fraction of electrons and positrons, which are produced by the

shower too. This kind of radiation is usually very directional with a small typical angle θ_c, and therefore electrons will emit photons within a cone around its own trajectory. Thus we typically succeed to detect Cherenkov photons only if we are looking exactly towards the primary particle direction, and from this fact comes the need for telescopes with very large mirrors. Light reflected from these mirrors is focused into a camera and then collected by several PMTs, to be finally converted into an image of the Cherenkov light of the shower. Actually, this is an extremely successful and well developed technique for observing γ-rays, too!

4) Much deeper underground, the higher energy muons (E$\simeq$ 100 GeV) can reach other detectors, which are typically very large. Those are arranged to detect the most penetrating components of the byproducts of interactions of CRs, being often located as deep as km below ground level. The higher energy muons are the only components which are able to penetrate this far: by no means any $e^{\pm}$ could succeed in doing it too.

5) *The air* itself constitutes a medium with which a large fraction of the produced charged secondary particle can interact. Elastic together with inelastic scatterings with atomic or molecular electrons then can possibly happen, causing a mechanism of energy loss per collision very similar to the one we expect in detectors. In particular, air molecules can be excited and consequently emit light, in the same way as auroras are produced in the correspondence of geomagnetic poles. Anyway the advent of CRs showers is very rapid and much more isolated, so typically by eye the same effects of auroras are not usually seen.
In any case flourescence light is indeed expected, and these photons are very isotropic: a large system of mirrors could in principle detect pretty well this emission. The caveat is that the light yield of flourescence photons is typically lower than that of Cherenkov radiation, so a high energy is needed, $E \simeq 10^{18}$ eV, for this light to be easily collected. When this condition is fulfilled, the constructed image is usually very precise, with the feature of being able to trace the shower profile, which is a characteristic of Cherenkov telescopes too.

To summarize, the Cherenkov telescopes and fluorescence mirrors surely provide the most powerful imaging techniques to study the shower profile. A common critical point can however be highlighted: these kinds of imaging can be done only with extremely favorable conditions, namely very obscure nights, since the daylight and even the moonlight can be decent obstacles, and these are actually the typical problems of every astronomical instrument. On the other hand, all the other detectors that measure instead the charged particles can be operative 24h a day, with the only need of maintainance and calibration. Also, Cherenkov telescopes have the additional caveat that they need to have the right direction with respect to the light source, while all the other instruments would in principle collect anything that comes from the sky.

NB on the word Cherenkov Cherenkov telescopes and Cherenkov detectors are two dramatically different kind of detectors. Their common name refers just to the mechanism of light production. A Cherenkov tank will detect only charged particle's radiation within the own tank, while telescopes perform an imaging of the entire shower's Cherenkov light as it develops in the atmosphere. We have talked about an imaging instrument, since it is the most common configuration for EAS arrays, but in general we can list two types of Cherenkov telescopes:

a) *Integrating Cherenkov detectors*, which essentially perform an integrated count of all incoming photons, and typically consist of arrays of PMTs looking upwards into the sky and distributed over a large area at ground level;

b) *Imaging Cherenkov detectors*, composed of large area collection mirrors and a camera with segmented photomultiplier read-out. They perform a detection well resolved in time, namely a differential measurement of $\mathrm{d}E/\mathrm{d}t$ or $\mathrm{d}E/\mathrm{d}x$. In fact, the number of Cherenkov photons are indeed proportional to the number of charged particles (secondaries) available at a given depht in the shower: counting the number N_γ of photons as a function of time, they provide a count on the number of charged particles produced as a function of time, too. In this way a complete following of the profile of the shower is essentially traced.

Few words on filtering Cherenkov light Since Cherenkov light is in the optical range, the distinction between other light sources can often be very tricky, being sometimes relatively simple instead. Being towards bluish frequencies, Cherenkov light can be readily recognized with respect to some other sources just for the spectral differences, however a common Cherenkov telescope can be disturbed e.g. by starlights. The fundamental difference resides in the time evolution of the phenomenon: the development of the shower is an extremely fast mechanism, with timescale $\tau \ll$ ns. So extremely rapid snapshots are to be red by PMTs, with a hardware "trigger window" usually of $\sim \mu$s.
Another requirement can be a triggering condition such that a given wanted fraction of camera area is hit at the same time by flashes of Cherenkov light. In fact, the typical cone of Cherenkov radiation covers areas of 200-300 m, within the typical 2-3 R_M. The mirrors of these telescopes can be as large as 10-20 meters, so any of them which happens to be hit by a shower can have the hope to detect at least some fraction of Cherenkov light[10]. The cameras, which typically have diameters of few meters, are usually segmented and covered with several PMTs, namely pixels, of few cms size, and the projection of the Cherenkov light impinging on it will assume a characteristic elliptic shape, called *fish*. This projection will have of course a decreasing density profile towards its own borders, reflecting the fact that the majority of photons is expected to be concentrated around the shower axis. A typical starlight won't light up large portions of the cameras and activate many PMTs, being also an almost constantly active source, too. This is very different from a shower flash! Of course other sources of light are present in the atmosphere, such as the diffuse background created by starlight from all the sky together, and PMTs typically will record also them: a combination of both hardware and software conditions are then needed to effectively remove them.

4.4.3 The measured quantities

The common goal of all the detectors we have highlighted in the previous section is the measurements of the following quantities:

- energy of the secondary products and E_0;
- direction of the primary CRs;
- composition of the shower, when possible.

In particular, energy and composition are determined by combining the informations about the muonic and electronic sizes N_e and N_μ, as well as $x_{\max}$, while the direction is deeply related to the geometry of the array field and the timing profile of the shower. Let us describe how these quantities are usually estimated and present some results.

---

[10] See MAGIC telescope for γ-rays, placed in La Palma in the Canaries: this is actually the biggest γ-ray telescope in the world!

4.4.3.1 The energy of the shower

As regards the energy measurement, detectors usually have the capability to measure only charged particles energy above a certain threshold, and also they are usually located at different heights from ground. This fact allows them to detect also different shower ages s, see Eq.(3.23), and older showers will have a smaller fraction of electrons contributing to the signal. So the electronic size N_e and energy measurement are intrinsically linked. One can argue whether the photons are relevant in determining the total EM size: in practice, high energy photons are revealed by Compton scatterings and pair productions in the detector, and in some detectors the probability to have a conversion of $\gamma \to e$ by means of one of these processes is very low, such that one often is more concerned about the electronic size estimate.
We have already said that the transverse development of the electromagnetic counterpart of the showers, namely the particle density as a function of the distance r to the shower axis, can be well described by the Molière radius R_M, see Eq.(3.20). An accurate parametrization was actually developed by Nishimura, Kamata and Greisen:

$$\frac{\mathrm{d}N_e}{r\,\mathrm{d}r\,\mathrm{d}\phi} = N_e(x)\,\frac{C(s)}{2\pi r_M}\left(\frac{r}{R_M}\right)^{s-2}\left(1+\frac{r}{R_M}\right)^{s-4.5} \tag{4.9}$$

$$\text{with}\quad \left[\frac{\mathrm{d}N_e}{r\,\mathrm{d}r\,\mathrm{d}\phi}\right] = \frac{\#\,\text{particles}}{\mathrm{m}^2}\,,$$

and this is called NKG parametrization. The $C(s)$ factor is a nomalization constant dependent on the shower age, and $N_e(x)$ is simply the total number of secondaries. In particular, recalling the definitions of shower age and Molière radius,

$$s \equiv \frac{3x}{x+2x_{\max}} \qquad \text{and} \qquad R_M \equiv \frac{E_s}{E_0}\,\mathrm{x}_0\,.$$

Notice the units of the Molière radius: in the NKG parametrization it is obviously expressed in [m], while our definition implies [g m^2]. This is a consequence of the usual procedure of dividing by the material density, and both forms of the Molière radius can be encountered in literature. In air, the Molière radius increases with decreasing air density in the atmosphere, and typical values are: $R_M \simeq 80$ m at sea level; $R_M \simeq 200$ m at the position of the shower maximum, which is usually at few km high.

In practice, s and $N_e(x)$ are free parameters which we don't know a priori. What can be done to obtain informations about them? Surely our detectors can measure the transverse profile, and also the number of particles as it develops over time, so these are the starting point. The procedure is fundamentally *iterative*: we start with an estimate of the shower core position and of the direction from the timing profile, namely from the hitting order of the shower towards the interested detectors of the array (see Ex.(4.2) for a simple example). Then fits of these guesses are performed by using the NGK function, which is the major model. Being $\mathrm{d}N_e/r\mathrm{d}r\mathrm{d}\phi$ dependent on s and $N_e(x)$, a mean s parameter is usually used, guessed from data themselves or from MC simulations adapted to the detector altitude and array layout. Once s is also fixed, the shower size can be derived from Eq.(4.9), assuming azimuthal symmetry in the plane perpendicular to the shower:

$$N_e = \int_0^{2\pi}\int_0^{+\infty} \frac{\mathrm{d}N_e}{r\,\mathrm{d}r\,\mathrm{d}\phi}\,r\,\mathrm{d}\phi\,\mathrm{d}r = \int_0^{+\infty}\frac{\mathrm{d}N_e}{r\,\mathrm{d}r}\,2\pi r\,\mathrm{d}r\,.$$

Finally the procedure is repeated, till the best fitting hypothesis are found. In particular we stress that what needs to be done is in fact the study of an *all particle spectrum*, which is the general approach when performing indirect measurements. From the shower's size then informations on the primary particle energy E_0 are also obtained, since they are proportional, see e.g. Eq.(3.33).

KASKADE One of the most known experiments that has been operating in the measurements of CRs is the KArlsruhe Shower Core and Array DEtector, built in 1996 and specialized in energies around the knee, namely $10^{14}\,\mathrm{eV} < E < 10^{17}\,\mathrm{eV}$. The experiment was developed by the very same group which gave birth to CORSIKA itself. Fig.(4.18) shows the field array, which was able to measure both electrons and muons in the shower separately. The array counted 252 detector stations, arranged on a square grid of $200 \times 200\,\mathrm{m}^2$ with a spacing of 13 m. The innermost part of the array was equipped with a tracking system too. Fig.(4.19) shows a scheme for one of the components of the array. Each of these independent sensors had the typical size of 240 m and consisted in liquid scintillators, linked to PMTs. Two layers of absorbing material were implied, lead and iron of thickness of few centimeters: the function was obviously to reduce the energy of the going-through particles, and in particular the electronic component was typically completely stopped. A lower layer of scintillators was also present, to detect essentially low energy muons.

Figure 4.18: Photograph of the KASKADE field array, with a definitely not scaled atmospheric shower. Picture taken from the official website, `https://kcdc.ikp.kit.edu/`.

There are of course many other types of such arrays, but KASKADE is one of the most famous and the one which resembles the characteristics we have depicted for a typical toy model of CRs EAS array. Of course, the accuracy of the description and reconstruction of EAS characteristics results from a compromise between the financial (and computational!) budget and the number of sensors distributed over the largest area with the smallest detector spacing. One often needs to save on the sampling rate, namely on the granularity of the array's sensors over the available area. Much broader areas mean of course that larger shower areas can be resolved, and so higher energies can be collected. On the other hand, larger spaces between the sensors will lead to lower energy shower to be essentially neglected.

4.4.3.2 The direction of the shower axis

We are about to see in a simplified exercise how the direction of the shower axis, namely the informations on the zenith angle θ and the azimuth ϕ, can be obtained.

Exercise 4.2. Direction estimate in a simple air shower array

We are working with an array of 4 detectors, covering a geometrical area of $A = 4 \times 10^8\,\mathrm{cm}^2$, sensitive to cosmic rays at energies larger than 4 PeV with an efficiency of 30%. We want to reconstruct the shower direction and impact time, given a set of measured arrival times of

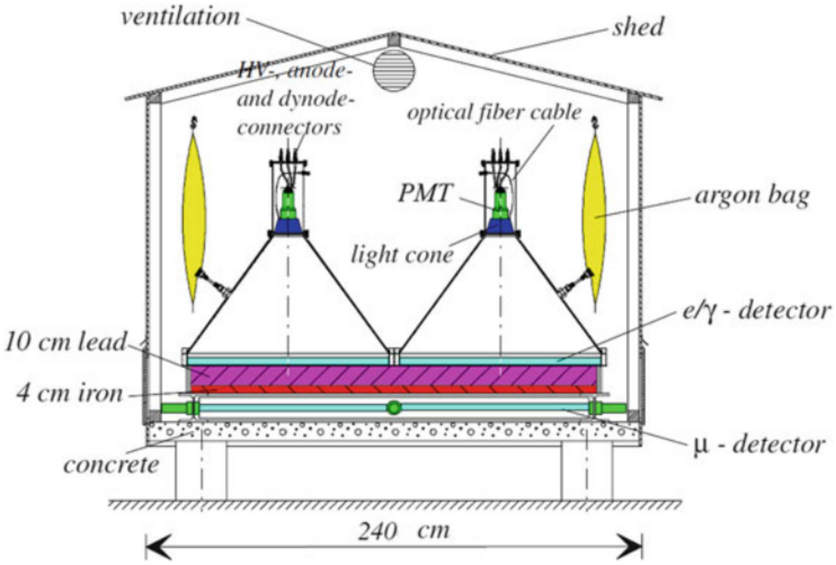

Figure 4.19: Schematic view of one of the 252 sample array detector stations of the KASCADE experiment. Picture taken again from the official website, `https://kcdc.ikp.kit.edu/`.

a shower front at each detector, and estimate the rate of triggered events. When a cosmic ray particle strikes the Earth's atmosphere, it produces an extensive air shower made of billions of secondary particles, which at the sea-level can extend over an area as large as $10\,\text{km}^2$. Consider a simple array of air shower detectors located at the same altitude (z=0), at positions given by the vectors $\vec{x_{\text{det},\,i}}$, with $i = 1, 2, 3, 4$. When the front of an air shower, moving in the direction $(\theta,\ \phi)$, at the speed of light, hits the i-th detector at the time $t_{\text{det},\,i}$, a signal will be generated at each station. We assume that the shower front can be described as a plane, hitting ground at $x = (0,\ 0,\ 0)$ at the time $t = 0$. Note that θ is the zenith angle, i.e. it is measured from the vertical direction.
We shall also assume the following simplifying hypothesis:

- The detector response is instantaneous, that is no delay arises when forming a signal;
- The shower particles are relativistic;
- The array is installed on a flat area;
- The equation of the shower plane at the time t_0 is $\hat{n} \cdot \vec{w} = 0$, being $w_{\text{dec},\,i}$ the projections of the detector coordinates on the shower plane;

Assume also that the array can detect showers from primary particles with energies greater than $E_{\text{min}} = 4$ Pev with efficiency $\epsilon \simeq 30\%$, and also the coordinates and time of arrival are given by:

$$\vec{x_{\text{det},\,1}} = (1,\ 1,\ 0) \qquad t_{\text{det},\,1} = 0\,,$$

$$\vec{x_{\text{det},\,2}} = (-1,\ 1,\ 0) \qquad t_{\text{det},\,2} = 0.707\,,$$

$$\vec{x_{\text{det},\,3}} = (-1,\ -1,\ 0) \qquad t_{\text{det},\,3} = 1.414\,,$$

$$\vec{x_{\text{det},\,4}} = (1,\ -1,\ 0) \qquad t_{\text{det},\,4} = 0.707\,.$$

See Fig.(4.20) for a schematic view of the experiment.

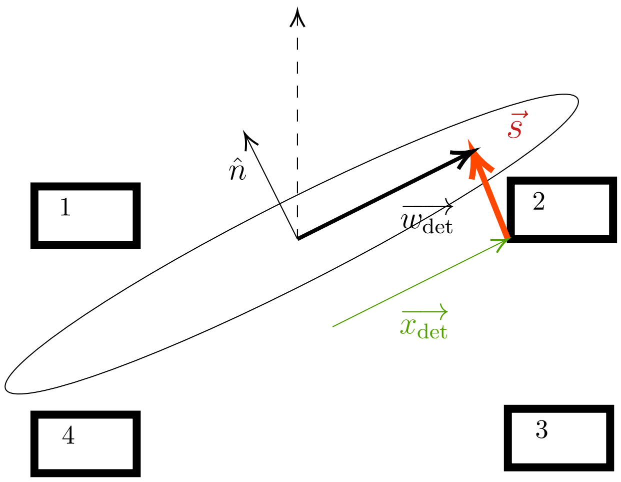

Figure 4.20: Pictorial representation of the simple array studied in the exercise.

1) *What is the shower direction $(\theta,\ \phi)$ at the time t_0?*
Let us first introduce the usual polar coordinates to define the unitary vector $\hat{n}$ orthogonal (and upward directed) to the shower front:

$$\hat{n}\,(\theta,\ \phi) = \begin{pmatrix}\cos\theta\cos\phi\\ \cos\theta\sin\phi\\ \sin\theta\end{pmatrix} \tag{4.10}$$

Let us define $\vec{s}$ as the vector quantifying the distance between the detector and the shower front, with $\vec{s}\cdot\hat{n} = |\vec{s}|$. We can then exploit the fact that, at any time, the position of the shower front which is just above a single detector with respect to the center of coordinates, namely $\vec{x}+\vec{s}$, is given by the propagation velocity c times the time interval $\Delta t = t - t_0$ elapsed from the initial time t_0. Being this velocity parallel to $\hat{n}+\vec{w}$, we can write:

$$\vec{x}+\vec{s} = \Delta t\, c\,(-\hat{n}+\vec{w}) = (t_0 - t)\, c\,(\hat{n}+\vec{w})\ ,$$

where we have inverted the sign of the time interval since the unitary vector $\hat{n}$ is oriented upwards with respect to the ground, and to the velocity. Multiplying both sides for $\hat{n}$ and exploiting the fact that $\hat{n}\cdot\vec{w} = 0$, we get

$$\hat{n}\cdot\vec{x} + \hat{n}\cdot\vec{s} = (t_0 - t)c\,,$$

and this is the generic equation governing the shower front evolution. Now, at the i-th detector, the s_i vector becomes zero when the hit of the shower happens at t_i, namely

$$(t_0 - t)\, c = \vec{x}\cdot\hat{n}\,,$$

$$(t_0 - t_i)\, c = x_i\cos\theta\cos\phi + y_i\cos\theta\sin\phi + z_i\sin\theta\,.$$

This equation, which relates the coordinates $\vec{x} = (x_i,\ y_i,\ z_i)$ with the hitting time t_i, has three unknowns: the angles θ, ϕ and the impact time t_0. But we can in principle exploit three conditions on pairs of detectors. In particular, let's study $(\vec{x_{\mathrm{det},\,1}},\ \vec{x_{\mathrm{det},\,2}})$ and $(\vec{x_{\mathrm{det},\,1}},\ \vec{x_{\mathrm{det},\,4}})$, writing the correspondent form of the above equation:

$$\Delta t_{1,\,2} = \cos\theta\,(\Delta x_{1,\,2}\cos\phi + \Delta y_{1,\,2}\sin\phi) + \Delta z_{1,\,2}\ ,$$

$$\Delta t_{1,\,4} = \cos\theta\,(\Delta x_{1,\,4}\cos\phi + \Delta y_{1,\,4}\sin\phi) + \Delta z_{1,\,4}\ ,$$

and we have taken natural units $c = 1$. Substituting the known values for Δt and Δx given by construction and writing $\Delta t_{1,\,2} = \Delta t_{1,\,4} = 0.707 = \sqrt{2}/2$ we get

$$\frac{\sqrt{2}}{2} = 2\cos\theta\cos\phi \qquad \text{and} \qquad \frac{\sqrt{2}}{2} = 2\cos\theta\sin\phi\,,$$

which can be solved for ϕ by diving the second expression by the first one:

$$\frac{\sin\phi}{\cos\phi} = \tan\phi \overset{!}{=} 1 \qquad \Leftrightarrow \qquad \phi = \frac{\pi}{4},\ \frac{5\pi}{4} = 45°,\ 225°\,.$$

Putting these results into one of the two above equations and solving for θ, one easily finds

$$\frac{\sqrt{2}}{2} \overset{!}{=} 2\cos\theta\left(\pm\frac{\sqrt{2}}{2}\right) \qquad \Rightarrow \qquad \theta = \pm 60°\,,$$

and the negative solution can be discarded, since it would correspond to a shower coming from below the detectors. Let's see whether the degeneracy in the azimuth angle ϕ can be solved by considering the last pair of detectors, i.e. $(\vec{x_{\text{det},\,1}},\ \vec{x_{\text{det},\,3}})$, for which we have $\Delta t_{1,\,3} = 1.414 = \sqrt{2}$ and $\Delta x_{1,\,3} = \Delta y_{1,\,3} = 2$:

$$\Delta t_{1,\,3} = \cos\theta\,(\Delta x_{1,\,3}\cos\phi + \Delta y_{1,\,3}\sin\phi) + \Delta z_{1,\,3}\,,$$

$$\Rightarrow \qquad \sqrt{2} = 2\cos\theta\,\left(\cos\phi + \sin\phi\right)\rvert_{\theta=60°} = \cos\phi + \sin\phi\,.$$

This in particular doesn't solve the degeneracy. It is very important to stress that, for this simple array, the flatness of both the shower front and the array field makes the problem face a lack of informations about the $\hat{z}$ direction, which is fundamental to solve completely for all the unknowns. One may be wondering why, then, arrays such as KASCADE were built in a flat region. The reason is that the shower front itself is not flat, in particular the shape is a sort of **pancake**, namely has a non negligible curvature which helps to resolve $\hat{z}$ displacements. Electrons and positrons are continuously suffering from multiple Coulomb scatterings, which, together with other kinematics effects, create the pancake shape. This is also valid, somehow more mildly, for charged muons, which show a flatter, but still curved, front in the shower. As regards the time t_0 of first impact, we can estimate it simply using one of the two solutions for azimuth angle, $\phi = 45°$, to obtain

$$t_0 = \cos 60°\,(\cos 45° + \sin 45°) = \sqrt{2}/2 = 0.707\,.$$

2) *What is the rate of showers expected to be observed by this array?*
We have already given an expression for the CRs flux, Eq.(4.3), and it was holding from few GeV to TeV region. At higher energies, which are the ones in examination in this exercise, the parametrization is formally analogous but with different values for the K parameter and the spectral index α. We have

$$\Phi\,(E) = 1026\,\left(\frac{E}{1\ \text{GeV}}\right)^{-3.06}\ \text{cm}^{-2}\,\text{s}^{-1}\,\text{sr}^{-1}\,\text{GeV}^{-1}\,,$$

$$\Phi\,(> E) = 2.2\times 10^{-10}\,\left(\frac{E}{1\ \text{PeV}}\right)^{-2.06}\ \text{cm}^{-2}\,\text{s}^{-1}\,\text{sr}^{-1}\,,$$

and this parametrization is valid in the energy range 10^{15} eV $< E < 10^{18}$ eV. The geometrical area seen by the shower front is simply the area A of the detector, which is given, multiplied by the projection factor $\sin\theta$ and by the efficiency ϵ:

$$A_{\text{eff}} = \epsilon\,A_{\text{proj}} \qquad \text{with} \qquad A_{\text{proj}} = A\sin\theta\,. \tag{4.11}$$

The number of particles per unit time shall be given by integration of the differential flux $\Phi(E)$, multiplied by the effective area, over the total solid angle and over energy:

$$\frac{\mathrm{d}N}{\mathrm{d}t} = \int_{4\pi} \int_{E_{\text{min}}}^{+\infty} \epsilon A_{\text{proj}} \Phi(E)\ \mathrm{d}E \mathrm{d}\Omega = 0.262 \times 10^{-2}\,\mathrm{s}^{-1} \simeq 9\,\mathrm{h}^{-1}\ ,$$

where we have used the fact that the parametrization is isotropic, so the only dependence on the angular coordinates is given by A_{proj} and gives

$$\int_{4\pi} A_{\text{proj}}\,\mathrm{d}\Omega = A \int_{4\pi} \sin\theta\,\mathrm{d}\Omega = 2\pi A \int_{-\pi/2}^{\pi/2} \sin^2\theta\,\mathrm{d}\theta = \frac{\pi}{2}\ ,$$

and we have accounted for only downgoing particles. This estimate reveals the possibility to build up a very good statistics, since in practice these kinds of experiments stay operative for several years. The final operations which are usually done with the data collected in a real experiment, then, are the fits to the lateral distribution and shower age. The distinction of the two kinds of front, namely the $e^{\pm}$ and the $\mu^{\pm}$ one, is indeed a very difficult challenge, usually quite impossible to be fulfilled.

Efficiency parameter The efficiency parameter ϵ is very important and accounts for the fact that a lot of uncertainties are unavoidably present in such measurements. In primis, the quantity of detectors per area will affect ϵ; also, not all particles of the shower can be observed in first place, as we have already said regarding neutrons; the atmosphere itself will absorb part of the energy; finally, electronic errors can also be present. Obviously the kind of detector influences, lastly, the efficiency.

With this exercise we can conclude that the direction estimate is not a straightforward task too. As we have seen, the direction of the shower axis, and hence of the primary CR, is obtained in an EAS array measuring the arrival time of the shower front in the intercepted counters: in practice it can be deduced from geometrical considerations by measuring the time delay Δt between different counters. In particular also the shower core can be deduced by this analysis. Then, both the shower core and the direction of the shower axis can be used to complete the subsequent steps of the iterative reconstruction we have already described above.

The experimental situation is complicated by the fact that surface detectors do not observe the number of electrons at shower maximum, but at a fixed depth given by $x_{\text{det}}/\cos\theta$, accounting for the possible zenith angle; a notable exception are the Cherenkov and fluorescence telescopes, which are able to trace the entire shower profile. However, the shower size N_e produced by primaries of a given energy will fluctuate from shower to shower because of differences in the stochastic development of the cascades. We can then finally summarize the sources of **systematic uncertainties** as follows:

- Monte Carlo simulations concerning models of hadronic interactions, Sec.(4.4.1);
- Unpredictable and continuously changing properties of the atmosphere;
- Measures that are performed at different dephts than the x_{max} of showers.

We can get a taste of the impact of these systematic uncertainties by looking at Fig.(4.21), in which the CRs spectrum, built by compilation of the results from a large number of different experiments, is shown. The covered range is around the knee, at $E > 10$ TeV, and a spread of the points is fairly evident at a fixed energy. This spread can only be explained by the large systematic uncertainties, and are mainly due to the conversion from size N_e to energy E_0. The measurements differ one from the other by 15%-25%, and most data sets agree within these systematic uncertainties. Remarkably, the position of the knee at about $E \simeq 4$

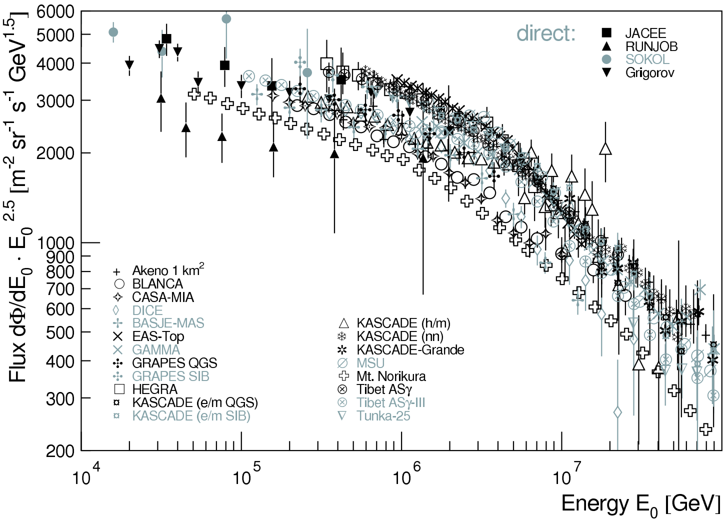

Figure 4.21: All particle spectra in the knee region. Results from direct measurements as well as from air showers experiments. The y coordinate is multiplied by the power of $E^{2.5}$. The knee position is evidently around $E \simeq 4 \times 10^6$ GeV $= 4 \times 10^{15}$ eV. Picture from `https://arxiv.org/pdf/0904.0725.pdf`.

PeV and the hardening of the spectral index is shown by every data sets. Let's recall that, at energies between 10^{16} eV $< E <$ 10^{18} eV, the differential energy flux and the integrated flux can be parametrized by the following relations

$$\Phi\,(E) = 1026\,\left(\frac{E}{1\text{ GeV}}\right)^{-3.06}\quad \text{cm}^{-2}\,\text{s}^{-1}\,\text{sr}^{-1}\,\text{GeV}^{-1}\,,$$

$$\Phi\,(>E) = 2.2\times10^{-10}\,\left(\frac{E}{1\text{ PeV}}\right)^{-2.06}\quad \text{cm}^{-2}\,\text{s}^{-1}\,\text{sr}^{-1}\,,$$

and actually the PeV normalization is more natural for the considered region. Notice that the all particle spectrum of Fig.(4.21) contains no informations about the nuclear mass A of the primaries: this is a completely different challenge.

4.4.3.3 The composition of the shower

We shall start by stating that we are actually far from determining the chemical composition of individual showers, namely the nuclear mass A of the primary of energy E_0. However this is an important quantity, since it could encode some hints on the astrophysical source producing the CR. Actually the nuclear composition of CRs has to be deduced on a statistical basis, and by now we are able to distinguish whether the shower is mostly made by lighter (p, He) or heavier elements (Fe). The procedure involves the estimate of not just the electronic size N_e, but also of the muonic size N_μ and the shower maximum x_{max}. Let us underline that the electronic size N_e (or the weighted sum of electron and muon size, see Eq.(3.30)) gives a measure of the primary energy, while N_μ relates to the primary mass A through the relation Eq.(3.34).

In particular, being N_e and N_μ the actual observables, we need to describe the following relation

$$\begin{pmatrix} N_e \\ N_\mu \end{pmatrix} = \mathcal{M}\begin{pmatrix} E_0 \\ \text{A} \end{pmatrix} \qquad \Rightarrow \qquad \begin{pmatrix} E_0 \\ \text{A} \end{pmatrix} = \mathcal{M}^{-1}\begin{pmatrix} N_e \\ N_\mu \end{pmatrix}\;; \tag{4.12}$$

where $\mathcal{M}$ is the so called *response matrix* or *kernel*, which depends on the detector and needs to be built by MC simulations, comparing each entry of (E_0, A) with the observables values of

(N_e, N_μ). The kernel must be model dependent too and will establish the connection between the searched quantities and the measured ones by inversion of the matrix. The inversion of the kernel is called unfolding, and it is a very challenging task which often introduces a lot of systematic errors, and can be computationally heavy, since the larger number of shower simulated the better shall be the estimate. However, a compromise between computational power availment and needed precision shall be made, and the simplifications introduced in the models together with regularization algorithms again are sources of systematic errors.

The integrating Cherenkov technique provides a way to trace the longitudinal profile of the shower and can give a calorimetric estimate of the shower energy and also the measurement of $x_{\max}$. This quantity is in particular related to the energy E_0, as a function of which it shows a logarithmic increase, and to the composition A via Eq.(3.35). Fig.(4.22) shows $x_{\max}$ as a function of the primary energy E_0, with the loci of light (p) and heavy (Fe) compositions being the adequately labeled straight lines, and these are the outcomes of different hadronic models. The results are indeed spread in between the lines of the two constant uniform compositions simulated. In particular, some features can be noticed:

1) Despite the spread, at energies between 10^{16} eV $< E <$ 10^{17} eV the trend seems to favor a lighter elements composition;
2) At $E \simeq 10^{17}$ eV, the values of $x_{\max}$ are approaching the results of the simulations that use heavy primaries instead, till $E \simeq 4 \times 10^{17}$ eV;
3) Then, above this energy, again the trend is towards the lighter composition, and this trend seems to concern thus the highest energy tail of CRs, which is an important observation as we will see in the following.

Nevertheless, the slopes are quite different from one dataset to the other, the interpretation of these disagreements being quite an unsolved mystery still, and to assess the details of these data different detectors are to be compared, making use of hybrid instruments, as we shall see. Knowing the average depth of the shower maximum for protons $x^p_{\max}$ and iron nuclei $x^{\mathrm{Fe}}_{\max}$ from simulations, the mean mass A is derived with the superposition model of air showers, using Eq.(3.36):

$$x^{\mathrm{Fe}}_{\max} \approx x^p_{\max} - \mathrm{x}_0 \, \log \mathrm{A} \, .$$

The Large High Altitude Air Shower Observatory The Large High Altitude Air Shower Observatory (LHAASO) is a pretty new experiment, operative since 2018 and providing high precision measurements of energy spectrum, composition and anisotropies of CRs in the energy range between 10^{12} eV $< E <$ 10^{17} eV. It is set in China at the altitude from sea level of about 4100 m, which corresponds to $\simeq 600\,\mathrm{g\,cm^{-2}}$ of residual atmospheric depht. Such a height and, in general, high locations of these experiments usually favor the reduction of systematic uncertainties, due to the vicinity to the shower maximum. Fig.(4.23) shows a bird's view of the setup area.

4.5 Ultra High Energy Cosmic Rays (UHECRs)

We have already encountered the Ultra High Energy Cosmic rays when we have discussed about the features which characterize the CRs flux. These are the most energetic counterpart of Cosmic Rays, with energies about $E > 10^{18}$ eV, being around the so called ankle of the spectrum. In this section we will discuss some energy loss mechanisms which are the protagonists of UHECRs propagation, then some techniques and results will be presented.

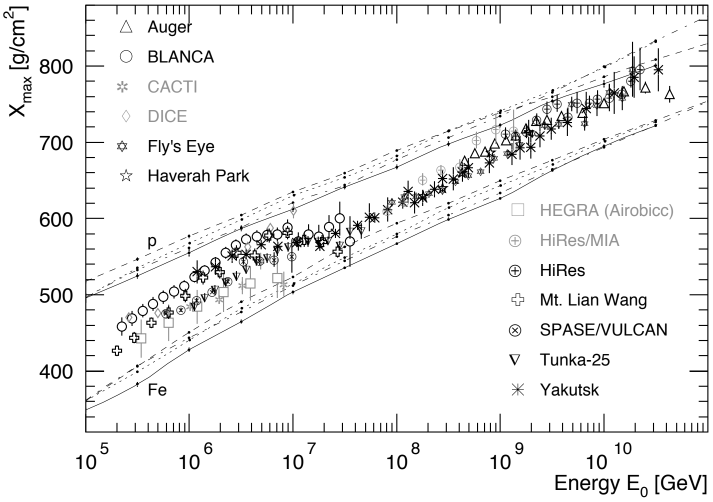

Figure 4.22: Average depth of the shower maximum $x_{\rm max}$ as a function of primary energy, obtained by Auger and other experiments. The lines indicate simulations for proton and iron induced showers using the CORSIKA code with the hadronic interaction model QGSJET, SIBYLL and EPOS, with various upgrades of these same codes. Picture from `https://arxiv.org/pdf/0904.0725.pdf`.

4.5.1 General propagation features

The UHECRs propagation is very interesting for a lot of reasons, and two important ones are the following:

1) The UHECRs Larmor radius $r_{\rm L}$ is so large that their arrival direction should be correlated to the astrophysical source direction in the sky! We shall make a little estimate on the gyroradius of UHECRs protons in Ex.(4.3);

2) The unobserved anisotropies along the galactic plane support the idea that these are of extragalactic origin, see below.

For these reasons a lot of efforts are nowadays devoted to the measure of direction, energy and nuclear mass too of these energetic Cosmic Rays.

Exercise 4.3. UHECRs propagation in the intergalactic magnetic field

The diameter of the Local Group (i.e. the group of galaxies that includes the Milky Way) is about 30 Mpc (where 1 pc= 3.26156 ly). The typical strength of intergalactic magnetic fields is of the order of 10 nG. The Galactic magnetic field measurement is a very complex procedure, which accounts for different indirect estimates, e.g. the Zeeman splitting of $H\alpha$ line, interstellar dust polarization and synchrotron radiation study.

Are cosmic ray protons with an energy of $E = 10^{20}\ eV$ confined within the structures of the Local Group?

Firstly, let us stress that these spectacular energies are encountered in the very tail of the CRs spectra, see Fig.(4.3) and Fig.(4.4), and the so called Ultra High Energy Cosmic Rays are characterised indeed by a very poor statistics and large errors on the measurements. We know that the gyroradius is given by

$$r_{\rm L} = \frac{pc}{ze|\vec{B}|} \simeq \frac{E}{ze|\vec{B}|} = \frac{E}{e|\vec{B}|} \qquad \Rightarrow \qquad r_{\rm L} = 3.3 \times 10^{25}\,{\rm cm} \simeq 10.8\,{\rm Mpc}\,,$$

where we have clearly assumed our particle to be relativistic $E \simeq pc$, and also the fact that $1\,{\rm eV} = 1.6 \times 10^{-19}$ J, $[{\rm G}] = {\rm esu\,cm}^{-2}$, $e = 4.8 \times 10^{-10}\,{\rm esu}$, $1\,{\rm J} = 10^7\,{\rm erg}$. So we can conclude

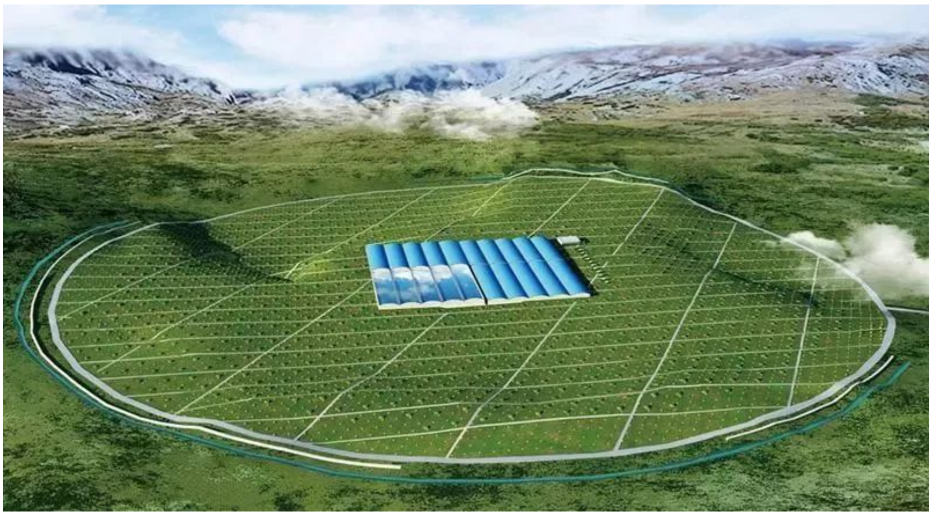

Figure 4.23: Bird's view of LHAASO site. The visible "dots" are the scintillators, which are 4931 stations of surface detectors distant from each other by 15 m, and are employed to measure the electromagnetic component; at the center, some water facilities are used for γ-ray detection; Cherenkov tanks are located underground too for the muonic component; finally the setup is provided with 12 wide field-of-view air Cherenkov telescopes. Picture from the official website `http://english.ihep.cas.cn/lhaaso/`.

that such protons are very hard to be confined in the Local Group. Additionally, the just found value is only a lower bound, since it can even be larger!

GZK cut-off The Greisen-Kuzmin-Zatsepin cut-off predicts a great attenuation of the flux of CRs originating at cosmological distances above a threshold energy $E_{\mathrm{GZK}} = 5 \times 10^{19}$ eV. This would give rise to a spectral distortion, which is referred to as a cut-off. In practice, during propagation, protons would interact with the cosmic microwave background photons, if the proton energy is large enough to achieve the resonant production of the Δ^+ hadron in the center-of-mass system. The two decay channels of the Δ^+ are:

$$p + \gamma_{\mathrm{CMB}} \to \Delta^+ \to p + \pi^0 \qquad p + \gamma_{\mathrm{CMB}} \to \Delta^+ \to n + \pi^+$$

$$(\mathrm{BR}=2/3) \qquad\qquad (\mathrm{BR}=1/3)$$

and we have also written the branching ratios (BR) for the channels. The neutron decays via β^-, i.e. $n \to p + e^- + \bar{\nu}_e$ within the lifetime $\tau_n \simeq \ln 2\tau_{1/2}$ with $\tau_{1/2} = (10.5 \pm 0.2)$ min, and the neutral pion will decay electromagnetically by $\pi^0 \to 2\gamma$, such that in the final state a proton will always be present: this is why we are often referring to the GZK process as a mechanism of energy loss by CRs, since we can imagine that a fraction of the energy of the primary proton is used to recreate a lowered energy final state proton together with other products. The main outcomes of the mechanism, then, are

a) The spectral distortion, due to the fact that the energy of the CR proton above threshold E_{GZK} is reduced;

b) The production of high-energy photons and the so called *cosmogenic neutrinos* from pion decays, which are not to be confused with the cosmic neutrinos. The such produced photons are however usually quite unlikely to be detected, since they are expected to produce e.m. cascades right at their production point.

Exercise 4.4. The Greisen-Zatsepin-Kuzmin process

The GZK (Greisen-Zatsepin-Kuzmin) cut-off is a signature in the Cosmic Ray spectra at high energies due to the interactions of the ultra-relativistic protons with the microwave background.

i) *What is the threshold energy E_{GZK} for the process to happen?*
The threshold is computed in App.(B). We shall do it again completely analogously, but making use of the well known Δ^+ resonance mass $m_\Delta = 1.232\ \text{GeV}/c^2$. The threshold energy is given by the condition of the production of Δ^+ at rest in its COM frame. Starting from the momenta of the particles:

$$p_p = (E_p/c,\ \vec{p_p}) \qquad p_\gamma = (E_\gamma/c,\ \vec{p_\gamma}) \qquad p_\Delta = (m_\Delta c,\ 0)\ ,$$

the invariant mass in the laboratory frame of the initial state is given by

$$\sqrt{s} = \sqrt{(E_p + E_\gamma)^2 - |\vec{p_p} + \vec{p_\gamma}|^2\, c^2} = \sqrt{m_p^2 c^4 + 2\left(E_p E_\gamma - |\vec{p_p}|\,|\vec{p_\gamma}|\, c^2 \cos\theta\right)}\ .$$

This has to be equated as usual to the rest mass of the produced Δ^+, once elevated to the power of two:

$$m_p^2 c^4 + 2\left(E_p E_\gamma - |\vec{p_p}|\,|\vec{p_\gamma}|\, c^2 \cos\theta\right) \overset{!}{=} m_\Delta^2 c^4\ .$$

Taking our proton to be relativistic, namely $\beta \sim 1$ such that $E_p = |\vec{p_p}|\, c$, reminding also that $E_\gamma = |p_\gamma|\, c$ and that the most favorable case is a head-on collision with $\theta = \pi$, we get immediately

$$4E_p E_\gamma = \left(m_\Delta^2 + m_p^2\right) c^4 \qquad \Rightarrow \qquad E_p = E_{\text{GZK}} = \frac{\left(m_\Delta^2 + m_p^2\right) c^4}{4E_\gamma} = \frac{0.16\ \text{GeV}^2}{E_\gamma}\ ,$$

where we have substituted the proton mass $m_p = 938.27\text{MeV}/c^2$. A question now arises naturally: which energy shall we put in E_γ as a representative of the CMB photons? We know that the cosmic microwave background has a nearly perfect black body spectrum (in fact, it is the best black body known in physics!) over about five orders of magnitude, see Fig.(4.24). The maximum peaks at $\lambda \simeq 1.06$ mm, corresponding

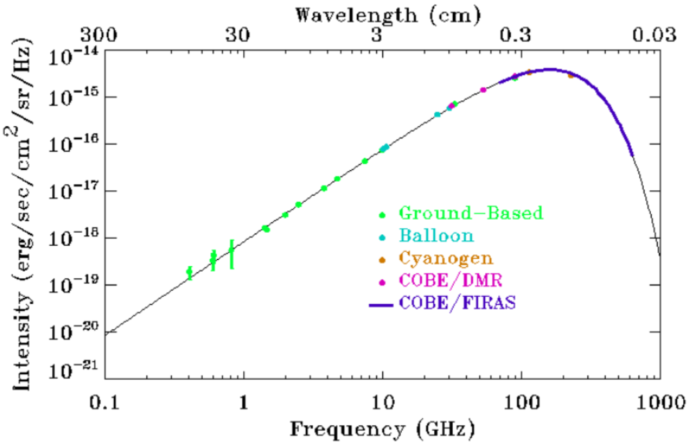

Figure 4.24: Cosmic Microwave Background spectrum, namely the intensity I with $[I] =$ erg s sr Hz cm^2, as a function of frequency in GHz (or wavelength). The CMB follows the expected black body curve over more than 5 orders of magnitude in intensity: the error bars are too small to be seen, even in an enlarged image, and it is impossible to distinguish the observed data from the theoretical curve. Other ground-based and balloon-based results at higher wavelengths are shown. Figure lifted from `https://asd.gsfc.nasa.gov/archive/arcade/cmb_spectrum.html`.

to $\nu \simeq 283$ GHz, in the radio range of the electromagnetic spectrum. The analytical maximization of the BB shape gives a maximum energy such that $E_{\rm max} = f\,kT$, which is the well known result of Wien's displacement law and f is a unit factor, around $f \sim 3$. So a rule of thumb to estimate the representative energy of a CMB photon is to take the high precision measure of the mean CMB temperature, $T_{\rm CMB} = (2.7255 \pm 0.0006)\ K$, and evaluate $kT \simeq 2.34 \times 10^{-4}$ eV, to obtain for the threshold energy $E_{\rm GZK}$

$$E_{\rm GZK} \simeq \frac{1}{f}\,\frac{0.16\ \rm GeV}{2.34 \times 10^{-13}\ \rm GeV}\ \rm GeV \simeq \frac{1}{f}\,6.84 \times 10^{20}\ \rm eV\ ,$$

and this number becomes smaller with high energy photons of the tail of the BB spectrum. In particular, the GZK cut-off is expected to start around $E \simeq 5 \times 10^{19}$ eV, as we have already said before.

ii) *How long is the mean free path of a cosmic UHE proton for this process? Assume a cross section for this reaction equal to $\sigma_{p,\,\gamma} \simeq 250\ \mu b$. Compare such free path to the size of the Milky Way.*
The just provided value of the cross-section is actually a result of a very difficult laboratory measurement using high energy photons and protons at rest. Many parametrizations are given in literature, and this value is appropriate around the threshold value for the production of the Δ^+ resonance at rest. This cross section is expected to encode a lot of details of the signature of different phenomena. Having said this, we can compute the mean free path l_{mfp} of the process

$$l_{mfp} = \frac{1}{n_\gamma \sigma_{p,\,\gamma}} \simeq 9.73 \times 10^{24}\ \rm cm = 3.15\ Mpc\ ,$$

where we have used the fact that 1 μb = 10^{-30} cm and the well known CMB mean photon number density today is given by $n_\gamma = 411\ \rm cm^{-3}$. This size is indeed larger than then the estimated radius of the Milky Way, which is $r_{\rm MW} = 15\,\rm kpc$.

iii) *After the collision, what is the fraction of the total initial energy that is retained by the proton?*
The energy loss y per interaction is relatively small and can be qualitatively estimated considering that, in the final state of the process, a proton and a pion are present, and thus

$$y = \frac{\Delta E_p}{E_p} \simeq \frac{m_\pi}{m_p} = 0.1\ ,$$

so at each process 10% of the energy of the initial proton is lost: at few interactions, le energy of the primary proton is expected to drop below the $E_{\rm GZK}$. With the above quantities, the energy loss length $l_{p,\gamma}$ of a proton in the CMB for this process is

$$l_{p,\gamma} \equiv \frac{1}{< y n \gamma \sigma_{p,\,\gamma} >} = 10^{26}\ \rm cm \simeq 30\ Mpc\ .$$

This size is indeed much larger tha $r_{\rm MW}$, but comparable to the size of our Local Group, namely it is of the order of the distance of the closest galaxy cluster (the Virgo). This important result tells us that all protons originating at distances larger than ~ 30 Mpc from us arrive on Earth with energy necessarily below 5×10^{19} eV, and the eventual detection of CRs protons with energy exceeding this threshold correspond to protons produced in local sources.

iv) *What happens to GZK cut-off when dealing with heavier nuclei than protons?*
For a heavier nucleus with mass A and energy E, the resonant reaction must occur through the interaction of one of the nucleons in the nucleus, which has energy E/A. The threshold energy $E_{\rm GZK}$ for heavier nuclei is consequently higher by a factor A.

Bethe-Heitler or Dip mechanism During the propagation in the CMB, electron-positron pairs can be produced in the following interaction

$$p + \gamma_{\mathrm{CMB}} \to p + e^- + e^+ \, .$$

We have already seen this process in great details in Sec.(4.2.2) and Ex.(4.1), so here we summarize the main results:

$$E_{\mathrm{thr}} = 2 \times 10^{18}\,\mathrm{eV} \qquad \sigma_{BH}^{\mathrm{thr}} \simeq 10^{-4}\,\sigma_{\mathrm{th}} \simeq 0.1\,\mathrm{mb}\,,$$

where the cross section at near-threshold energies is comparable with that of the production of the Δ^+ resonance. For comparison, Compton scattering (which is relevant in many astrophysical processes) has a cross-section that is proportional to σ_{th}. The energy loss per interaction is relatively small, and the fraction of energy loss can be qualitatively estimated as

$$y = \frac{\Delta E_p}{E_p} \simeq \frac{2m_e}{m_p} = 10^{-3}\,,$$

which is smaller by two orders of magnitude with respect to the GZK effect. So the average energy loss lenght shall be about two orders of magnitude larger:

$$l_{p,\gamma} = \frac{1}{< y n_\gamma \sigma_{BH}^{\mathrm{thr}} >} = 9.73 \times 10^{27}\,\mathrm{cm} = 3.15\,\mathrm{Gpc}\,.$$

Fig.(4.25) shows the energy loss of protons in the CMB, with the photoproduction interaction length and the decay length of neutrons. The neutron photoproduction cross section is almost identical to the proton one. You can also spot the fundamental difference between the Δ^+ resonance process and the Bethe-Heitler one.

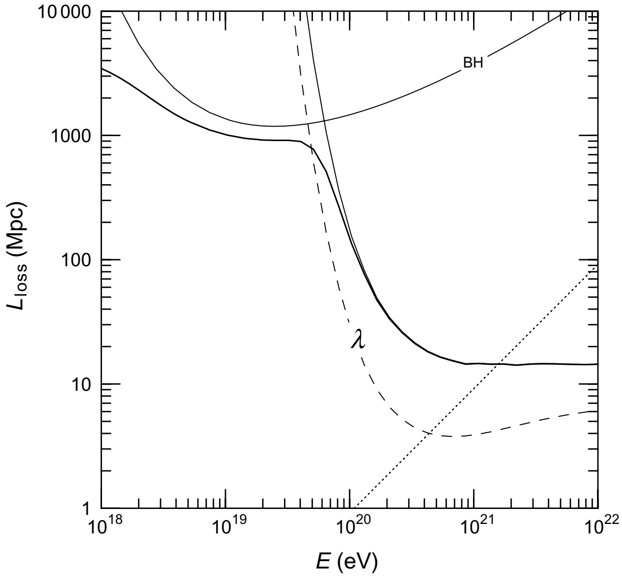

Figure 4.25: Interaction length and energy loss length for protons in the MBR and neutron decay length. The dashed line shows the photoproduction interaction length and thick solid ones are the total energy loss length, the thickest one is for the photopion production; the pair production process is included, labeled as BH, that is Bethe-Heitler. The neutron decay length is plotted with a dotted line.

The adiabatic energy loss The last proton energy loss process accounts for the redshift due to the expansion of the Universe. The current energy loss length due to redshift is the ratio of the velocity of light to the Hubble constant, in fact

$$\frac{1}{E}\frac{\mathrm{d}E}{\mathrm{d}t} = -H_0 \qquad \Rightarrow \qquad l_{\mathrm{exp}} = \frac{c}{H_0} \simeq 1.37\times 10^{26}\,\mathrm{m} \simeq 4300\,\mathrm{Mpc}\,,$$

which is indeed constant with energy. We have clearly used the fact that $H_0 \simeq 70\mathrm{kms}^{-1}\mathrm{Mpc}^{-1}$.

Summarizing, the UHECRs are subject to three important mechanisms of energy loss, and this should be interpreted as a hint that the particles of $E > 10^{19}$ eV are very likely to be products of local sources.

4.5.2 Propagation in Magnetic Fields

Magnetic fields are an important ingredient which has to be taken into account when we want to describe the propagation mechanisms of propagation of (UHE)CRs: they permeate every lenght scale of our Universe. In particular we can summarize their effects in this way:

a) For electrons and positrons, which are lighter with respect to nuclei or even protons, the magnetic fields are responsible for dramatic energy losses, due to deflection of trajectories causing the emission of synchrotron radiation;

b) For protons, synchrotron losses are negligible, except in the strong magnetic fields present close to the sources. Indeed we know that some astrophysical enviroments actually present very strong magnetic fields (magnetars are the most resounding example), and in that case protons and even heavier nuclei shall be deeply affected. On the other hand, usually intergalactic fields are quite weak, and in this other case protons are expected to suffer only from slight deflections of their trajectory.

In particular, we know that the Milky Way itself is permeated by a galactic magnetic field of about $|\vec{B}|\sim \mu$G. The typical Larmor radius r_{L} for a cosmic ray charged particle ze, propagating with an energy E, is given by Eq.(2.14) and normalized to values of interest:

$$\begin{aligned} r_{\mathrm{L}} = \frac{E}{ze|\vec{B}|} &= \left(\frac{10^{20}\,\mathrm{eV}}{4.8\times10^{-10}\,\mathrm{esu}}\,\frac{1}{10^{-6}\,\mathrm{G}}\right) z^{-1} \left(\frac{\mu\mathrm{G}}{|\vec{B}|}\right) \frac{E}{10^{20}\,\mathrm{eV}} = \\ &= \left(\frac{1.6\times10^{8}\,\mathrm{erg}}{4.8\times10^{-10}\,\mathrm{esu}}\,\frac{1}{10^{-6}\,\mathrm{esu\,cm}^2}\right) z^{-1} \left(\frac{\mu\mathrm{G}}{|\vec{B}|}\right) \frac{E}{10^{20}\,\mathrm{eV}} = \\ &= 108\,\mathrm{kpc}\, z^{-1} \left(\frac{\mu\mathrm{G}}{|\vec{B}|}\right) \frac{E}{10^{20}\,\mathrm{eV}}\,, \end{aligned} \tag{4.13}$$

where we have converted into cgs system and $[\mathrm{esu}^2] = \mathrm{erg\,cm}$. It is easy to see that for UHECRs it is much larger than the thickness of the galactic disk. Fig.(4.26) shows the simulated trajectories of 10 CR protons of different energies originating in a fixed position in the galactic plane. The galactic disk lies on the (x, y) plane, and from the left to the right the energies are 10^{18} eV, 10^{19} eV and 10^{20} eV. The main conclusion we can state by simply looking at this figure are

1) At energies below $\underline{10^{18}\ \mathrm{eV}}$ the trajectories are similar to random walks, and it is definitely impossible to keep track of the initial direction, the bending being just too strong;

2) At energies of about $\underline{5 \times 10^{19}\ \text{eV}}$ a cosmic ray proton will be deflected by 1°-5° in the galactic magnetic field, depending upon the direction and length of the trajectory, but anyway the tracking is still difficult due to systematic errors which are comparable to the resolvable deflection angle;

3) At energies above $\underline{10^{20}\ \text{eV}}$ a cosmic ray proton will be less influenced by deflections in magnetic fields, as we can see also from Eq.(4.13). Remarkably, in this case, a galactic source of CRs with that energy would produce a clear **anisotropy** on Earth measurements, which is not observed. Being thus the confinement mechanism in the Galaxy not maintained at the highest energies, the search for extragalactic sources of CRs is motivated.

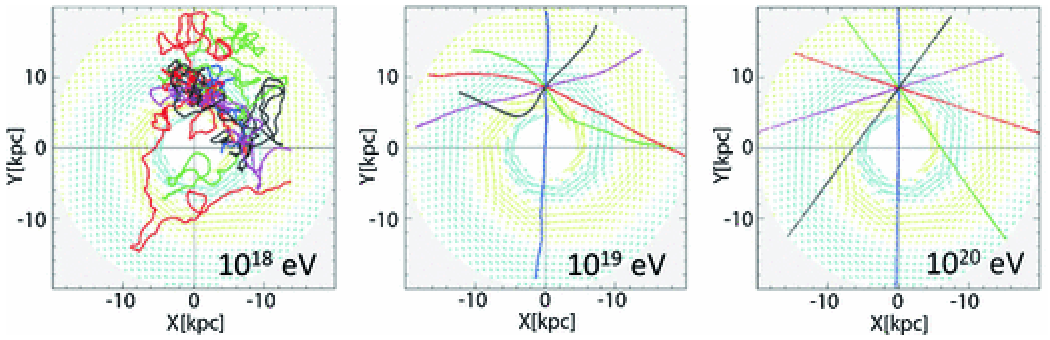

Figure 4.26: Simulated trajectory of charged particles in the galactic magnetic field. Low-energy charged particles are bent by magnetic fields, but those above 10^{20} eV travel along almost straight trajectories with little influence from magnetic fields, thereby retaining the original directional information. Credits to `https://www.semanticscholar.org/paper/On-the-Origin-of-Ultra-High-Energy-Cosmic-rays-(-)-Calvez/40d5c412dd9594ad6c303bbc9759b893ab6100d3`.

What about extragalactic magnetic fields? Magnetic fields beyond the galactic disk are poorly known, and only some upper limits can be imposed by indirect techniques (synchrotron and Faraday rotation) for regions outside galaxy clusters: $|\vec{B}| < 10^{-9}$ G with coherent length of the field of $l_c \sim 1$ Mpc, which corresponds also to the value of the average distance between galaxies. In some galaxy clusters, a very small fraction of the Universe, more precise values can be adopted: $|\vec{B}| \simeq 0.1\ \mu$G-10 μG. However, even such small fields can affect the propagation of UHECRs, even if the energy loss is negligible.

A parametrization can also be given for the the root mean square deflection angle $\theta_{\text{RMS}} =<\theta^2>^{1/2}$ of a particle of energy E moving in a direction perpendicular to a uniform magnetic field B after travelling the distance $d \gg l_c$, which is

$$\theta_{\text{RMS}} \simeq 0.8^\circ\, z \left(\frac{E}{10^{20}\ \text{eV}}\right)^{-1} \left(\frac{d}{10\ \text{Mpc}}\right)^{1/2} \left(\frac{l_c}{1\ \text{Mpc}}\right)^{1/2} \left(\frac{B}{10^{-9}\ \text{G}}\right).$$

At present, no single theory for the generation of magnetic fields in extragalactic space has become widely accepted. Fig.(4.27) shows an analogous work to Fig.(4.26), with extragalactic magnetic fields instead. Notice that here the scale is of Mpc order (perfectly comparable with the mean energy loss lenght $l_{p,\gamma}$ computed in Ex.(4.4)), and also 1 Eev = 10^{18} eV.

While the strong bending prevents us to reconstruct the source direction, it turns out to be useful at least in one aspect: the random walk due to the extragalactic magnetic fields causes an increase in the CRs' propagation path length, and as consenquence also a corresponding *time delay*. More precisely, at the source we could have the effect of an *astrophysical beam*

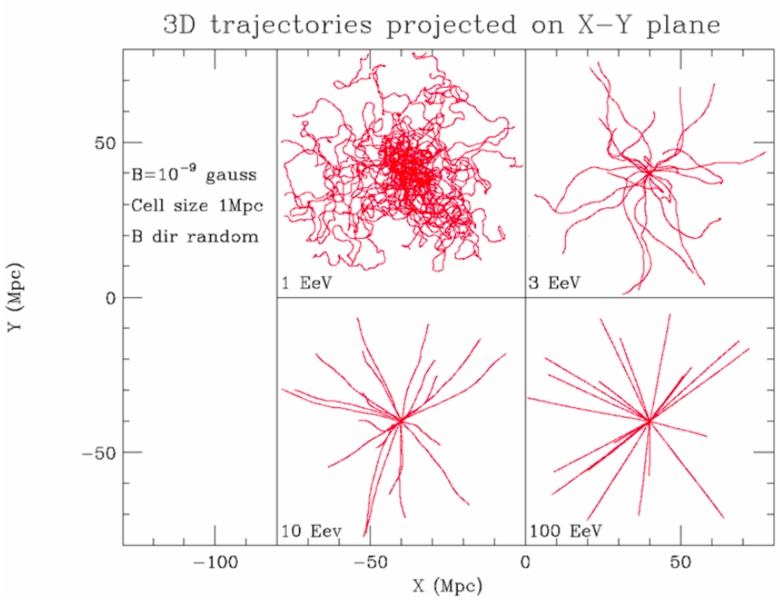

Figure 4.27: Simulated trajectory of charged particles in the extragalactic magnetic field. Analogously to the previous case, those CRs above 100 Eev $= 10^{20}$ eV travel along almost straight trajectories with little influence from magnetic fields, retaining the original directional information. Credits as the other image.

dump because of the interaction of CRs with the enviroment, which produces other particles such as γ or neutrinos. The delays in the time of arrival of CRs with respect to neutral messengers are a precious source of informations, which couldn't probably be collected if we were dealing instead with transient sources (e.g. gamma-ray bursts, solar flares).

4.5.3 Experimental techniques for observing UHECRs

Two detection techniques are principally employed to detect UHECRs. In particular, we can distinguish between

1) *Surface detectors*: this extends the use of EAS arrays to energies above 10^{18} eV. The technique was explained with great details in the Sec.(4.4.2), and the idea is the same: an iterative process allows to guess the direction and then to fit the NKG profile Eq.(4.9), to finally find the best fitting parameters for the shower electronic size N_e^p and age s. Then one can relate these infos to the primary energy E_0 through Eq.(3.30), i.e.

$$E_0 = gE_c \left(N^p_{e,\mathrm{max}} + \frac{E_c^\pi}{gE_c} N^p_\mu \right) ,$$

where we shall recall that g was a numerical correction factor introduced in the Heitler model for e.m. showers, E_c^π was the critical energy at which the mesons starts to be more likely to decay rather than interact, $N_{e,\mathrm{max}}$ is the shower maximum size, N^p_μ is the muon component of the size and E_c was the critical energy for the electromagnetic shower growth;

2) *Fluorescence detectors*: these are similar to Cherenkov detectors, and we shall describe these in more details since in the previous section we have introduced them rather quickly. They essentially exploit the fact that the charged secondary particles in EAS produce ultraviolet light through nitrogen fluorescence.

Fluorescence detectors of UHECRs Nitrogen molecules, excited by a passing shower, emit photons isotropically into several spectral bands between $\lambda \in [300 - 440]$ nm. These decays are characteristically very fast, happening within 10 ns to 50 ns after the excitation. In dry air the color of light produced by lightning is dominated by the emission lines of ionized nitrogen, yielding the primarily blue color observed. The fluorescence yield is 4 photons per electron per meter at ground level pressure: this is very small, but the winning factor is the very high number of $e^{\pm}$ produced in the e.m. shower part.
We also expect that a much larger fraction of UV light is emitted as Cherenkov photons, but this emission is strongly beamed along the shower axis and usually considered as a background to fluorescence detection.

Fluorescence photons reach the telescopes in a direct line from their source, since the emission is *isotropic*. Thus the collected image reflects exactly the development of the e.m. cascade, even if the fluorescence photons would come from aside. In particular, if we track the shower development with a segmented camera, we are, in principle, able to reconstruct perfectly

i) The time of arrival of particles;

ii) The direction of the shower;

iii) The energy E_0 of the shower through the informations on the number of photons recorded (which is a calorimetric measurement), and this can lead to an estimate of $x_{\max}$ too.

We should stress that we have said "in principle": in practice, a number of corrections must be made to account for the scattering and the absorption of the fluorescence light. Also pollution from other sources, such as the Cherenkov component which can be emitted directly, or diffused by the atmosphere into the telescope, must be carefully evaluated and accounted for. A constant monitoring of the atmosphere is indeed needed.

How can we realize this kind of monitoring? We can simply build a segmented camera made by a series of PMTs, which are pointing at slightly different directions in the sky, and are able to record the passing of the fluorescence photons of the shower. Fig.(4.28—Left) shows an example of a 2D camera of such a type. In particular, to obtain a much general possibile orientation of the segmented camera, one should employ an emispherical cover such as the one used in the historical **Fly's Eye** experiment, which was located in Utah and had an arrangement similar to what we can see in Fig.(4.28—Right). The signal shall be constructed by the hit PMTs, and the projection of the shower, namely the hitting area, has the characteristic shape of an ellipse, the fish we have mentioned in Sec.(4.4.2).
Actually, there is another very common concept which slightly modifies the one depicted in Fig.(4.28): large spherical mirrors are used to improve light collection, such that the light is focused on an array of small PMTs, arranged very similarly to what we have described, see Fig.(4.29) for a pictorial view of the idea.

By present, the very best concept of fluorescence detectors is given by the so called *stereo reconstruction*, which implies the use of more than one segmented camera. This arrangement allows to constrain with very high precision the geometry of the shower, since each telescope provides its own shower-detector plane. This is exactly the technique used by the already mentioned Pierre Auger Observatory. Another very appealing and new possibility is given by an arrangement which complements the fluorescence detector with a surface shower detector, such as the ones we have seen in the previous section. These are known as the *hybrid techniques*.

Let us lastly enumerate some pros and cons of the fluorescence detectors in general:

Pro (a) They cover very large effective areas with respect to the surface detectors, being able to observe showers developing even several kms away;

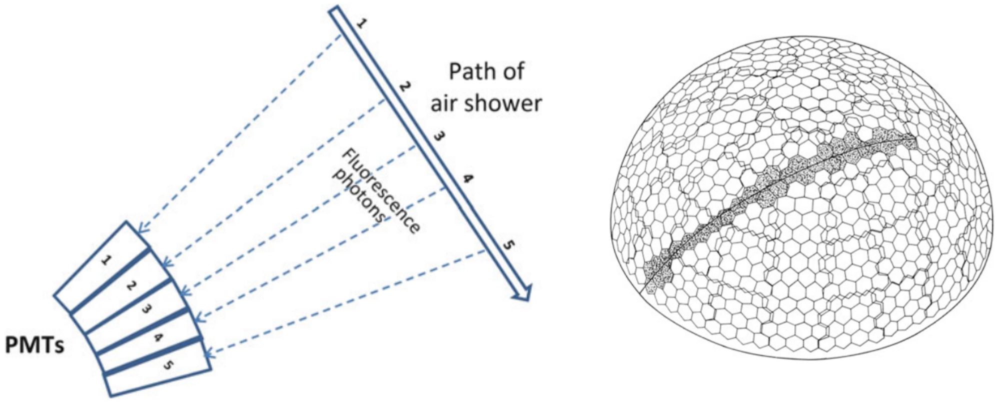

Figure 4.28: Left: A 2D pictorial arrangement of a segmented camera for fluorescence photons detection. Right: The arrangement of the PMTs in the Fly's Eye experiment, which is the natural 3D version of the sketch aside.

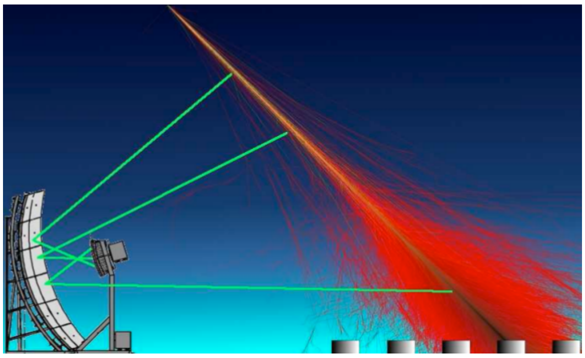

Figure 4.29: Sketch of the detection principles of a fluorescence detector, in the arrangement which comprehends a focusing mirror: the fluorescence light emitted by the air shower is collected on the large spherical mirror and focused onto a camera composed by PMTs, picture from Auger collaboration.

(b) They present the advantage of calorimetric measurement.

Con (a) As have already mentioned, they may only operate in clear, moonless nights. Any spurious source of light would be a problem for the PMTs;

(b) For fluorescence detectors the energy threshold is much higher, $E_{\text{min}} > 10^{18}$ eV, huge showers are needed to produce a relevant signal into them.

4.5.4 Overview on indirect measurements of UHECRs

We have seen what are the techniques implied to measure the UHECRs, namely surface detectors and fluorescence/Cherenkov telescopes. Let us now have a look on some results both from the well known experiments of the past, the ones which were applying a single technique, and the modern, hybrid ones.

4.5.4.1 Single technique detectors

There are several detector installations that were designed to measure cosmic rays at the highest energies. Two of them in particular were the most famous ones, the Akeno Giant Air Shower Array (AGASA) and the HiRes observatory. The first was the largest air-shower array before the advent of the Pierre Auger and Telescope Array detectors (see below) and it took data between 1984 and 2003; the second was essentially an improved version of the pioneering Fly's Eye experiment. On the other hand, their fundamental difference was that AGASA availed scintillation counters, being thus a surface EAS array, while HiRes consisted of two air fluorescence detectors with 360° view in azimuth and a spherical focusing mirror. The spectrum obtained by these two experiments at energies of UHECRs, i.e. $E > 10^{17}$ eV, is shown in Fig.(4.30—Left), together with comparing datasets from Auger. A clear discrepancy is shown: HIres data seem to decrease at energies above $E \simeq 5 \times 10^{19}$ eV, while AGASA's ones increase instead. AGASA dataset appeared to consistently disfavor the hypothesis of the GZK cut-off, which could be a suitable explanation for the HIres decrease instead. Indeed the energy at which the hardening of the spectral index start is precisely the E_{GZK} we have found in Ex.(4.4).

An important aspect which has to be weighted when one wants to interpret such plots is the actual entity of systematic uncertainties. We know that these are always present, but we shall also notice that very often the shown energy spectrum is just enhancing their importance. This is indeed one of these cases: the usual factor E^3 by which the y coordinate is multiplied will increase a lot the differences between the datasets. $\alpha \simeq 3$ is the appropriate spectral index for UHECRs and in the plot the ankle at around $E \simeq 10^{18.5}$ eV is fairly evident thanks to the E^3 factor. On the other hand, since all experiments will present an uncertainty ΔE_0 in the primary estimate, the propagation of errors in the y coordinates shall have higher possible fluctuations. More specifically, with bias of $\Delta E \simeq$ 25%-30%, one obtains

$$y = E^3\,\Phi(E) \qquad \Rightarrow \qquad \Delta y = \left(\frac{\Delta E}{E}\right)^3 \approx 42\%\,,$$

so if we assume that the AGASA points suffer from a 25% systematic overestimation of the energy, all points should be pushed down by 42% along y with respect to the nominal value. This is huge! The appropriate shift of the datasets which allows for agreement is shown in Fig.(4.30—Right).

Despite this observation, at the time these plots were released this discrepancy was a puzzle, and only a part of the scientific community hypothesized the role of systematic uncertainties. To partially solve the mystery, the large hybrid telescopes had to be built up in the next generation of experiments.

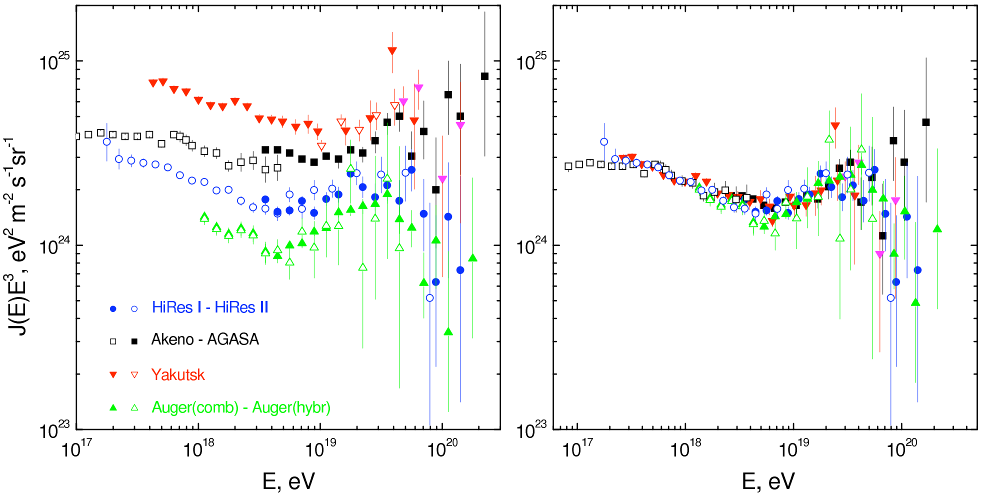

Figure 4.30: Flux of UHECRs as measured with the four detectors that have the largest exposures, namely Yakutsk, AGASA, Auger, and HiRes. The spectrum is multiplied by a power E^3 to enhance the features. Left: cosmic ray spectra as derived by the Collaborations using the calibration of the detectors. Right: cosmic ray spectra after rescaling of the energy scale of the experiments to obtain a common position of the dip. See the review in `https://arxiv.org/pdf/0904.0725.pdf`.

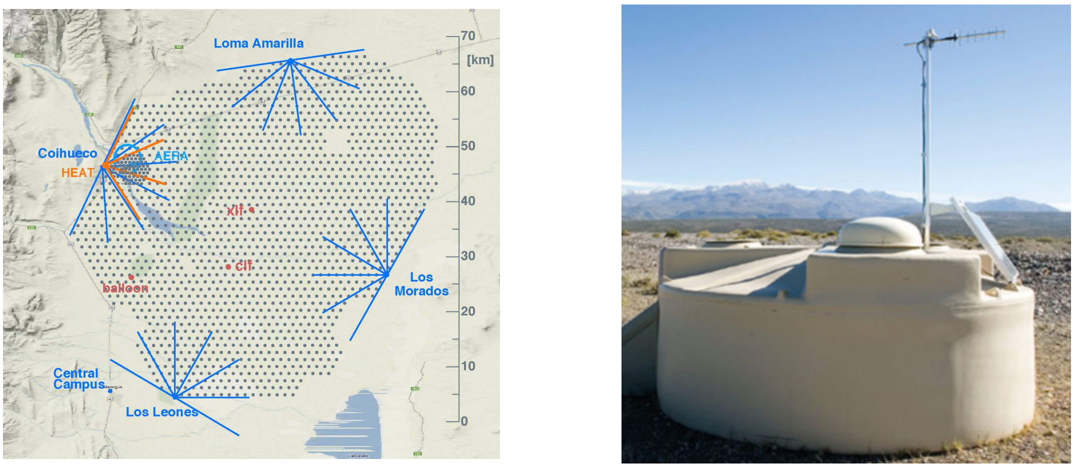

Figure 4.31: Left: The position and azimuthal field of views of the fluorescence detector (FD) eyes surrounding the array is displayed. The dots mark the positions of the 1600 surface detector (SD) tanks. Right: One of the SD water Cherenkov tanks. Picture from `https://www.researchgate.net/publication/277935828_Data_Processing_at_the_Pierre_Auger_Observatory`.

4.5.4.2 Large hybrid observatories

The protagonists are the Pierre Auger Observatory (PAO) and the Telescope Array (TA) Observatory, which are operating respectively in Utah and Argentina, Northern and Southern hemispheres of the Earth. Both are hybrid experiments, in which both fluorescence and surface array detection techniques are used in order to combine and enhance the single detector capabilities and provide an accurate cross-check of systematic uncertainties.

Pierre Auger Observatory (PAO) Fig.(4.31—Left) shows the map of the setup area of PAO. It was completed in 2008, and has been collecting reliable data since 2004. The surface detector (SD) array consists of 1600 water Cherenkov detectors spaced by $\sim$1.5 km on a grid covering a total area of 3000 km^2. Each tank of the SD array, shown in Fig.(4.31—Right) has a 10 m^2 surface and 1.2 m depth of purified water, each equipped with three PMTs to measure the Cherenkov light produced in the water. The SD tanks are sensitive to muons, electrons, positrons, and photons. The fluorescence detector (FD) of the PAO uses the same detection method as HiRes and consists of four eyes, as we can see from the view in Fig.(4.31),

Telescope array (TA) The Telescope Array (TA) Observatory has been collecting data in the high desert in Millard County, Utah, USA, since 2007, observing CRs with energies above 10^{19} eV. It is a hybrid detector, mixing the information from both fluorescence detectors (FD) and surface detectors (SD), as in the case of PAO. Fig.(4.32—Left) shows a typical scintillator implemented in TA. The cosmic rays are observed at three fluorescence sites, see Fig.(4.32—Right), and with 507 SD consisting of 3 m^2 double layer scintillators powered by a solar panel. The three fluorescence light stations allows to reconstruct the shower with the already cited *stereo technique*. Of course the statistics, i.e. the number of showers detected by the SD and FD components, shall be different:

a) FDs have a relatively high energy threshold, so. out of all the showers that effectively hit the setup .only the highest energy ones will leave signals in the fluorescence stations;

b) Surface detectors will collect data for 24h a day, while FDs can observe just under perfect conditions at nights. So the stereo analysis can be applied only to a subset of the detected showers.

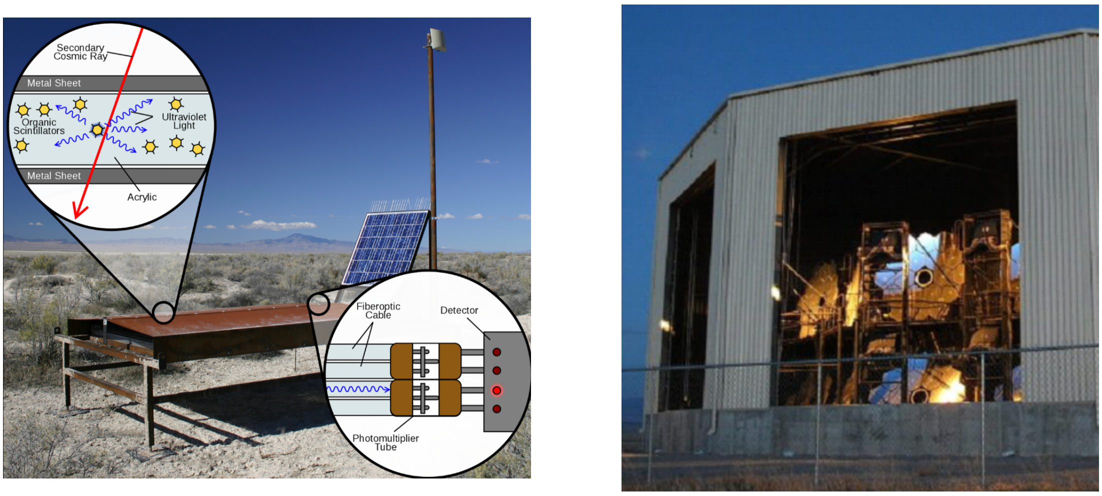

Figure 4.32: Left: Concept of a TA scintillator. Right: The FD concept, which employs a focusing mirror and a camera as usual.

Anyway the hybrid technique is still extremely powerful: through the FDs a much more robust measurement of the primary energy E_0 is obtained, thanks to the calorimetric measurement, while on ground the systematic uncertainties are much larger. Therefore the subsample of events collected with both techniques is extremely precious, allowing to perform relative calibrations of the results from SDs and FDs: essentially you develop some "correction functions" describing the energy measurement from the SDs, to be applied to the larger set where FD's informations lack.

Let's look at some recent results, keeping in mind that the data are continuously updated and we can only catch a glimpse of the recent state of the art. Fig.(4.33—Right) shows the results from PAO, which is the one with the larger statistics indeed, about the UHECRs differential flux. The spectrum is characterized by two clear inflection points corresponding to the second knee around 10^{17} eV and to the ankle near $6\times$ 10^{18} eV. The suppression of the flux above $\simeq 5 \times 10^{19}$ eV is definitely confirmed. Obviously, while the cut-off is evident, its physical reason is still unknown, even though the simple explanation provided by the GZK mechanism is appealing. Actually another acclaimed possible explanation is the fact that the flux suppression at the highest energies could be generated by the photo-disintegration of nuclei and/or the maximum acceleration energy at the CR sources, as we shall see in the following. Fig.(4.33—Left) shows the best fit for the spectral index, performed with the maximum likelihood method leaving the spectral index as a free parameter. Some results from Pierre Auger Observatory are also reported in Fig.(4.34) about the composition of UHECRs, with an analogous analysis to the one in Fig.(4.22). We have already seen that the determination of the charge (or mass) of the incoming primary (UHE)CR is difficult: it deeply relies on the simultaneous determination of the electromagnetic and muonic components of air showers at ground level. The results are also somewhat in contrast with the HiRes ones enumerated in Sec.(4.22): in fact, there is a visible increase towards the lighter contributions in between energies 10^{17} eV $< E <$ $10^{18.5}$ eV, followed by a decrease towards the heavier elements for energies above this range. Clearly, the typical uncertainties and spread of data are consistently smaller. Fig.(4.34—Left) shows the behavior of the width of the $x_{\max}$ distribution, i.e. $\sigma(x_{\max})$.

4.5.5 The UHE cut-off mystery and the ankle

We have seen that HiRes results Fig.(4.30) together with the more refined ones from PAO Fig.(4.33) confirmed the presence of a sharp cut-off in the UHECRs part of the spectrum

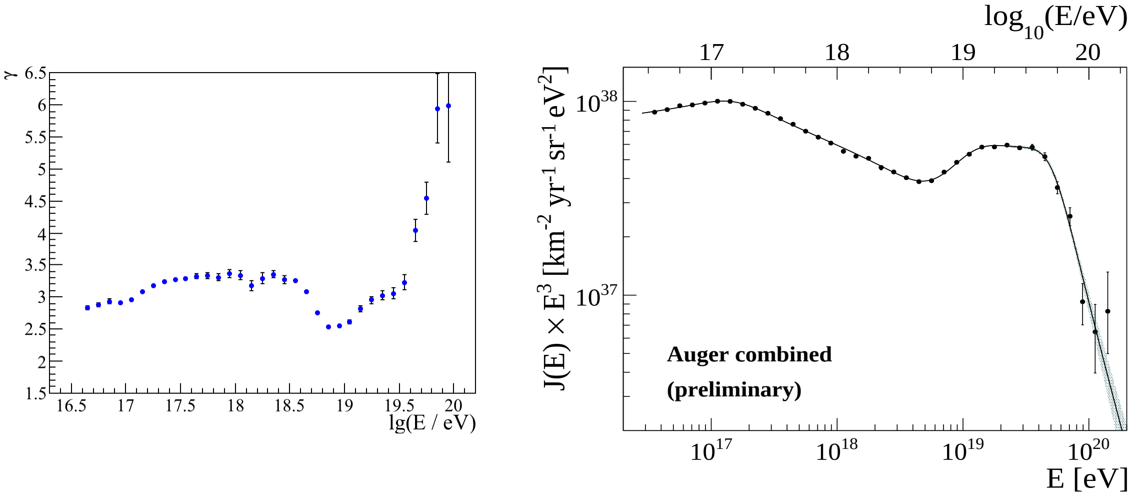

Figure 4.33: Left: Evolution of the spectral index as a function of energy. The spectral indexes are obtained from power law fits to the spectrum. Right: The energy spectrum from the combination of the different measurements, multiplied by the factor E^3. Picture from `https://arxiv.org/pdf/1909.10791.pdf`.

above $E = 5\times10^{19}$ eV. The GZK mechanism predict this as an effect of relativistic kinematic: the energy threshold $E_{\rm GZK}$ for the Δ^+ resonance production is reached and then high energy protons start to lose energy on CMB photons. This kind of process is called *photopion production.* But is it enough to entirely explain the ankle and the cut-off? The answer is of course still a challenge. Actually, considering the entire background photon field, one has to account for the three following processes:

1) CMB interactions: the Bethe-Heitler pair production (Ex.(4.1)) and the photopion production in Δ^+ resonance (Ex.(4.4)). These are the already studied reactions, which can be summarized here:

$$\textbf{GZK} \qquad p+\gamma_{\rm CMB} \to \Delta^+ \to p+\pi^0 \qquad p+\gamma_{\rm CMB} \to \Delta^+ \to n+\pi^+\ ,$$

$$\textbf{BH} \qquad p+\gamma_{\rm CMB} \to p+e^- + e^+\ .$$

These processes are expected to present an energy threshold which shifts to higher values for heavier nuclei, $E_{\rm thr} \to {\rm A}E_{\rm thr}$, since the energy at disposal per nucleon shall be $E \to E/{\rm A}$. So protons travelling through the Universe will be mostly affected by these processes;

2) EBL interactions: photodisintegration of heavier nuclei into lighter ones by interactions with the Extragalactic Background Light (EBL), namely

$$\textbf{EBL} \qquad N+\gamma_{\rm EBL} \to H + \ldots\ ,$$

where N stands for nucleus, and H stands for hadrons. The cross section for photodisintegration is very large, $\sigma_{\rm ph} \simeq 100$ mb, which is much larger than that of the other processes ($\sigma_{\rm GZK} \simeq 250\,\mu$b) and it strongly depends on the atomic number of the nucleus, $\sigma_{\rm ph} = \sigma_{\rm ph}({\rm Z})$, in particular on the nuclear binding energy of the specie. For the most stable isotope, namely ^{56}Fe, the cross section is expected to have a minimum, and even with its smallest value the mean free path $\lambda_{\rm ph}$ for the photodisintegration is barely comparable with the one of GZK mechanism $\lambda_{\rm GZK}$, being $\lambda_{\rm ph} \ll \lambda_{\rm GZK}$ for lighter nuclei. This is actually a kind of important interaction, which has to be taken into account, and which tells us that heavier nuclei are less likely to undergo the GZK

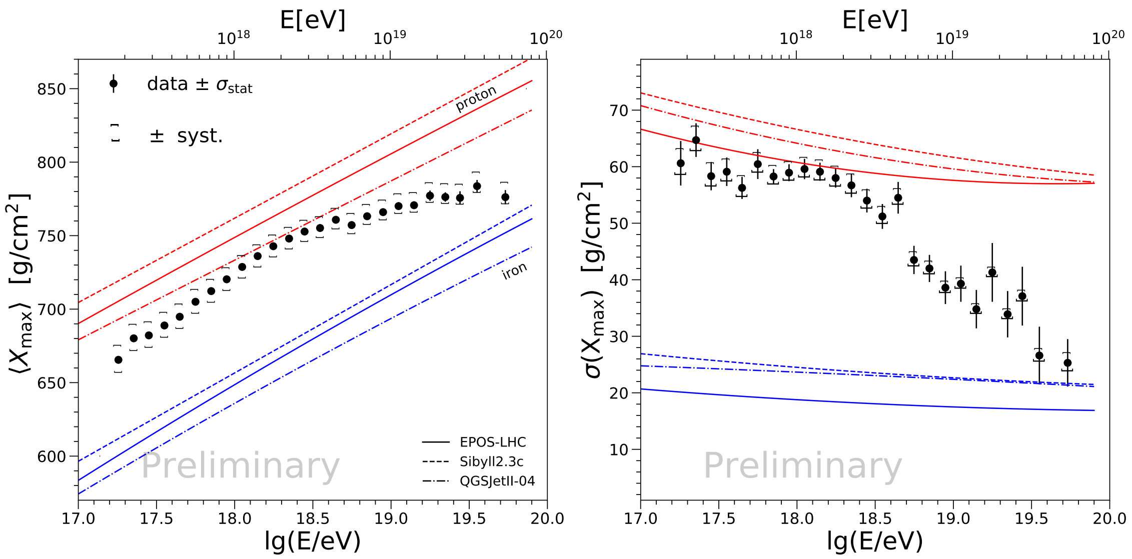

Figure 4.34: The evolution of $x_{\max}$ (left) and $\sigma(x_{\max})$ (right) with energy in comparison with the predictions for proton and iron nuclei of the post-LHC hadronic models EPOS-LHC, Sibyll 2.3c and QGSJetII-04. Picture from `https://arxiv.org/pdf/1909.10791.pdf`.

cut-off. Heavier nuclei could thus undergo each of the three processes, but in practice photodisintegration appears to be more likely in a lot of cases.

The EBL is indeed an important part of the total background photon field, being in fact the most prominent feature of the differential intensity of such a background, second just to CMB. Fig.(4.35) shows the intensity νI_ν as a function of the frequency of the total background of the Universe: EBL is placed in near IR and optical region of the spectrum, and it is believed to be built up by the populations of stars, galaxies, and AGN from cosmological distances, belonging then to all the phases of our thermal history, and being reabsorbed and reprocessed by ISM dust and redshifted by the Hubble flow. This is a very complex background from the point of view of theoretical models, and represents a challenge in our CRs modeling.
As regards the cut-off, then, what can be actually said is that the reason for its appearance **could** be GZK-like CMB interactions, **if** the composition is mostly protonic. So a lot of efforts are being concentrated on the quest of determining the chemical composition of UHECRs, both with the already mentioned techniques and a Multimessenger approach, see below. Otherwise, a reasonable explanation could be just the attainment of the maximum acceleration in the astrophysical sources of these UHECRs, which can be indeed expected, also because of the very active ambient matter of propagation that is the ISM.

Lastly, let us then describe the two possibilities for the explanation of the ankle, which is sometimes referred to as *dip* feature:

a) ***Superposition model***: the depletion is at the intersection of the rise of the extragalactic component and the decline of the galactic one, since the latter shall present a steeper spectrum $E^{-3.5}$ than the extragalactic component E^{-2}-$E^{-2.5}$ which is flatter. This hypothesis does not constrain the lightness of the composition, accounting instead for a mixed one. Fig.(4.36—Left) shows an example of a global data fit with the superposition model, which reveals to be actually quite well suited, but yet not the definitive answer to the problem; Fig.(4.36—Right) shows the evolution of $x_{\max}$ and $\sigma(x_{\max})$ as measured by Auger together with the models for different masses A, and this is transposed in the Left panel in terms of the spectrum;

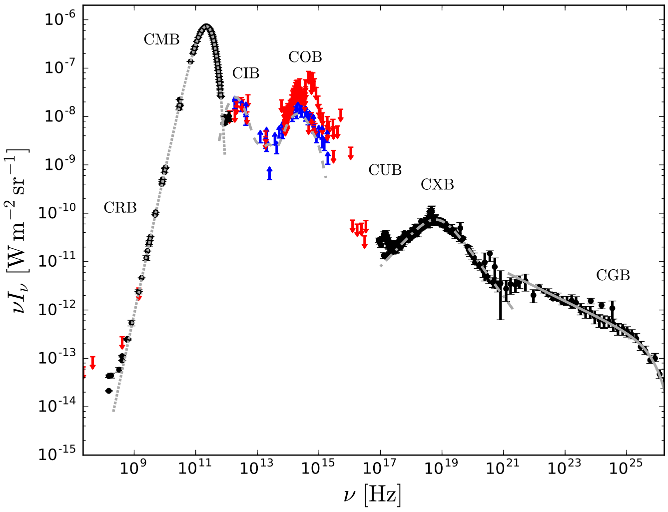

Figure 4.35: Complete cosmic background radiation. Black points with error bars indicate detections, while blue and red arrows indicate lower and upper limits, respectively. The EBL can be seen as the sum os CIB+COB parts. Picture from `https://arxiv.org/pdf/1802.03694.pdf`.

b) ***Dip model***: the depletion is caused by $e^{\pm}$ pair-production by the extragalactic protons with the CMB, i.e. Bethe-Heitler process is the responsible. Actually we have seen that this could explain the data very well at high energies, but with the implication that UHECRs must be mainly protons, which, as we shall see, is not likely the case.

The possible identification of extragalactic sources must exploit informations both on the chemical composition, about which we have seen some results and techniques in Sec.(4.4.3.3), and on the arrival direction distribution of the UHECRs. The latter possibility depends on the type of particle (protons or heavier nuclei) and on extragalactic magnetic fields, and we have discussed this in Sec.(4.5.2). The actual procedure of sources identification is treated in the following section Sec.(4.5.6).

Key informations to distinguish between the two scenarios is provided by the flux of secondary **neutrinos**, which is extremely sensitive to the chemical composition of UHECRs, to which the two hypothesis depend. In fact, the CMB interactions are responsible of a rich production of cosmogenic neutrinos, as we have already said:

$$p + \gamma_{\text{CMB}} \to \pi^+ + n \qquad \text{and}$$

$$\pi^+ \to \mu^+ + \nu_\mu \qquad \mu^+ \to e^+ + \nu_e + \bar{\nu_\mu} \qquad n \to p + e^+ + \bar{\nu_e}\ ,$$

and these are just an example. This production is efficient only in the case of protons, while in the case of heavier nuclei it is significantly suppressed. Thus, a sizeable flux of cosmogenic neutrinos is expected only if UHECRs around 10^{20} eV are protons, i.e. only if CMB interactions are effectively the protagonists (favoring the dip model). This is an aspect of the Multimessenger approach which will be highlighted in the following.

4.5.6 Searching for UHECRs sources

We have seen that there are two models for explaining the ankle in the CRs spectrum at the region of UHECRs. In both of these scenarios the extragalactic sources are indeed the protagonists, whether they produce a heavy or light composition. So the identification of the possible astrophysical extragalactic sources is absolutely a fundamental point and, by present, there are just speculations and no certainties. The right way to treat this issue is to consider both

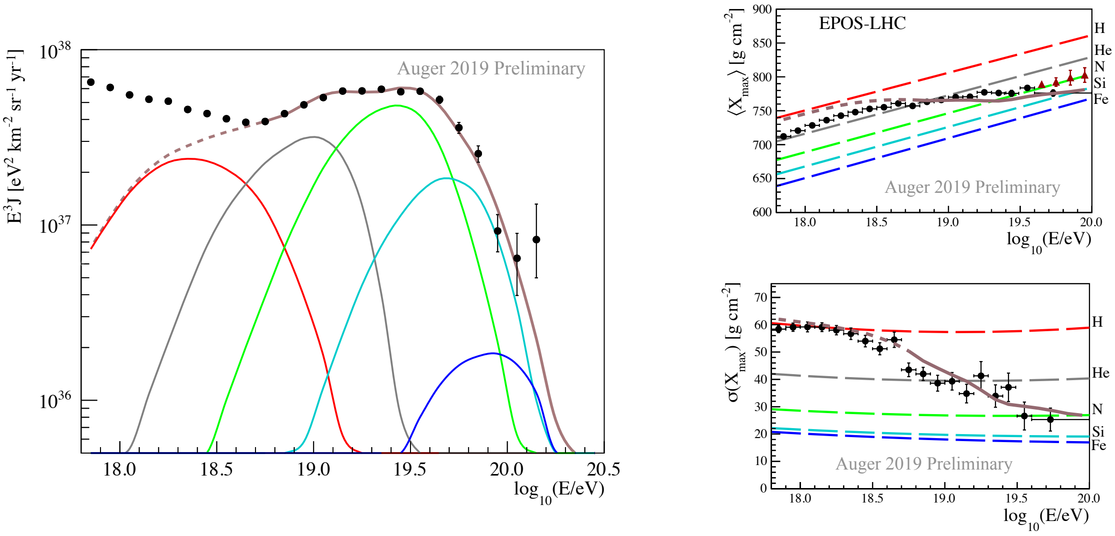

Figure 4.36: Left: The simulated energy spectrum (multiplied by E^3) at the top of the Earth's atmosphere obtained with the best fit parameters: all-particle (brown curve), A = 1(red), $2 \leq A \leq 4$ (grey), $5 \leq A \leq 22$ (green), $23 \leq A \leq 38$ (cyan), $A \geq 39$ (blue). The combined energy spectrum as measured by Auger (Fig.(4.33)—Right) is shown for comparison with the black dots. Right: The first two moments of the $x_{\max}$ distributions as predicted for the model (brown curve) versus pure compositions. The measured mean $x_{\max}$ are shown for comparison as purple triangles. Picture from `https://arxiv.org/pdf/1909.10791.pdf`.

- *the magnetic fields interplay*, since as we have already seen the galactic magnetic fields are about $|\vec{B}|\simeq \mu$G and extragalactic ones $|\vec{B}|\simeq$ nG and are expected to influence the propagation, see Sec.(4.5.2), at least till energies of the order of $E \simeq 100$ EeV $= 10^{20}$ eV;
- *the energy loss lenght* $l_{p,\gamma}$, which was computed in Ex.(4.4) for the Δ^+ resonance and it was found to be $l_{p,\gamma} \approx 30$ Mpc, which is a quite local scale that reveals the very likely extragalactic origin of the vast majority of UHECRs at $E \geq 10^{20}$ eV.

Having said this, we shall guess the need to limit ourselves to the cases in which we have effectively a guess on the direction, i.e. at $E \geq 10^{20}$ eV: anyway, a study of the astrophysical sources at lower energies is still possible, and won't be treated in this section but in the following.

As regards HE investigation, we can trace three different approaches to identify UHECRs sources:

1) Look for excesses into the arrival directions of UHECRs from individual astrophysical objects or regions, for example, the Galactic center, using data from a single experiment. The anisotropies shall be given by the magnetic field interactions, and at least two events from a very strong source are needed to build up their correspondence;
2) Search for statistically significant correlations of CRs arrival directions with catalogs of known astrophysical objects. This is a ***Multimessenger approach***, since the combined astronomical informations and CRs are employed, building a correspondence between the electromagnetic signals of well known sources with the ionizing radiation coming to Earth, that is

$$\text{photons} \quad \leftrightarrow \quad \text{Cosmic Rays}\,;$$

3) Look for anisotropies in the CR arrival direction distribution itself, independently of

any catalogs. These include searches for large scale as well as small scale anisotropies, but as regards the latter ones we have already said that by now no such evidences have been measured, at least in the Galactic plane, and this was one of the main motivations for the hypothesis of UHECRs' extragalactic origin. Large scale anisotropies are then expected, and we are about to see what they results to be.

By now no individual source of UHECRs has been positively identified, but we can review some results of these three techniques to have a taste of the state of the art.
As regards the third technique, the most relevant result is the one by PAO, which is shown in Fig.(4.37—Left). A clear anisotropy in the arrival directions of CRs above $E \geq 8 \times 10^{18}$ eV is present, regardless of the effectiveness of extragalactic magnetic fields, which is attenuated but still present at this energy (see Fig.(4.27)). The anisotropy is **dipolar**, which means that the minimum is located approximately 180°away from the direction of the maximum. This is remarkable, since usually a dipolar anisotropy hides a relative motion between the observer and the source. But what is this relative motion about?

- The Solar System of course revolves around the MW center, but this does not account for such a huge anisotropy. This same argument applies to the CMB-like dipolar anisotropy, which is caused by our relative motion with respect to the cosmic fluid;
- What we call "source" can be actually a composite variety of sources, each one with its own motion with respect to us, and this issue has really to do with the source identification.

As usual, a certain answer to this question is not yet possessed. A very fancy thing to notice is also the position, in equatorial coordinates (see below for a short digression on Astronomical Coordinates), of the anisotropy's bulk: $(\alpha,\ \delta) = (100°,\ -24°)$, while the Galactic center is located at $(\alpha,\ \delta) = (265°,\ -29°)$. Thus, the excess of events points to about 165°away from the direction of the center of the Milky Way, clearly excluding a galactic origin of the excess.

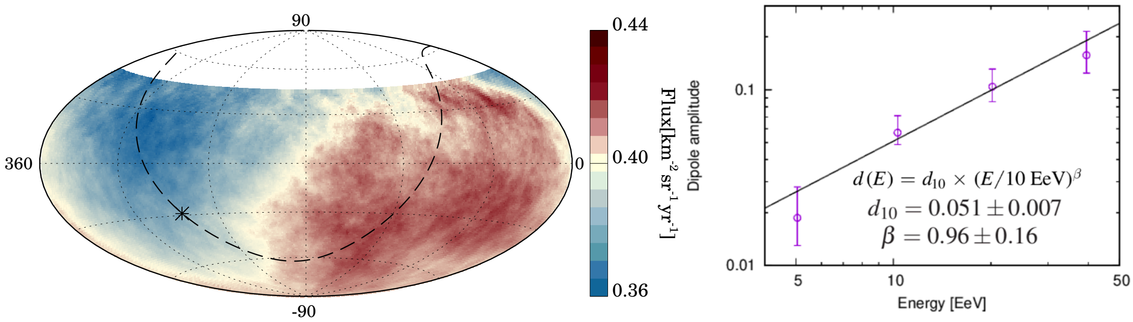

Figure 4.37: Left: The CR flux above 8 EeV, averaged on windows of 45° radius in equatorial coordinates, and this builds the "smoothed out" appearance. The vertical coordinate which goes from -90°to +90°is simply the declination angle α, which is negative at the Southern emisphere as expected. The Galactic plane and the Galactic center are indicated by a dashed line and a star respectively. Right: Energy dependence of the dipolar amplitude measured in four energy bins above 4 EeV. Picture from `https://arxiv.org/pdf/1909.10791.pdf`.

Rayleigh Harmonic Analysis The stardard analysis technique for anisotropies is called *Harmonic Analysis*, which often exploits the Rayleigh formalism. This technique is the general tool exploited in both the third and the first approach for astrophysical sources identification. As an example, let us consider the n events that a particular experimental apparatus has classified as CRs within the energy range $[E,\ E+\Delta E]$. The Rayleigh formalism gives the amplitude A and phase ϕ of the first harmonic, namely the lowest order term in a Fourier-like composition of the events. Calling α_i the i-th right ascension of the event, the following quantities are built

$$s \equiv \frac{2}{n} \sum_{i=1}^{n} \sin(n\alpha_i) \qquad c \equiv \frac{2}{n} \sum_{i=1}^{n} \cos(n\alpha_i) \, ,$$

and if the CR arrival directions are completely random one expects that $< s >=< c >= 0$, which reveals that no preferenced directions is present. In presence of an anisotropy, instead, we shall expect that $< s >\neq 0$ and $< c >\neq 0$, and the amplitude A and the phase ϕ of the first harmonic are given by

$$A = \sqrt{c^2 + s^2} \qquad \text{and} \qquad \tan\phi = \frac{s}{c} \, .$$

In particular, the amplitude A of the CR anisotropy is defined as:

$$A \equiv \frac{I_{\max} - I_{\min}}{I_{\max} + I_{\min}} \qquad \text{with} \quad I = I(E) \, ,$$

and $I_{\max}$, $I_{\min}$ represent the maximum and minimum intensity of cosmic rays from a given direction. We shall stress again that such an harmonic analysis represents a completely standard technique, which can be applied to the third method as well as to the first. Anyway a fundamental difference intervenes between the two: the third approach happens to be more "blind", applying harmonic analysis independently on locating a precise source, with the possibility to study even a large group of relatively weak sources condensed in the galactic plane; the first method is more concerned on individual strong astrophysical sources. Fig.(4.37—Right) shows the behavior of the amplitude A as a function of the energy, to which it is clearly correlated.

Astronomical coordinates

The relative distances of atrophysical objects with respect to Earth appear to be located on a celestial sphere, which is a huge sphere concentric with the Earth. The celestial equator is a projection of the Earth's equator onto the celestial sphere, and the north (south) celestial poles are positioned directly above the north (below the south) pole of our planet. Some common coordinate systems are thus used to identify positions into the celestial sphere.

- *Galactic Coordinates* provides a way of locating objects with respect to our galaxy, since the origin of the system is given by our Sun. The *latitude* b is the angle with respect to the MW plane, while the *longitude* l describes a clockwise angular coordinate in the MW plane as seen from the Galactic North Pole, and it is defined as the angle between the baseline of the center of the Galaxy and the Sun and the line between the star and the Sun. The galactic longitude l is measured in degrees, $l \in [0°, 360°]$; the galactic latitude is measured in degrees too and the interval is $b \in [-90°, +90°]$. Fig.(4.38—Left) shows an illustrative example.
- *Equatorial Coordinates* Equatorial coordinates are essentially determined by the celestial equator and the vernal equinox point. The vernal equinox point is a point on the celestial equator. The sun appears to cross this point from south to north at the beginning of spring. Declination and right ascension define the position of a star on the celestial sphere.
  The *declination* δ is the angle above or below the celestial equator. This angle

is 0° at the celestial equator, +90° at the north celestial pole and −90° at the south celestial pole equivalent to latitude.
The *right ascension* α has zero reference point in the Vernal Equinox Point. The right ascension is 0/24 h at this reference point and increases towards east. Since 360° correspond to 24 hours, 15° right ascension is equal to 1 hour. Fig.(4.38—Right) shows an illustrative example.

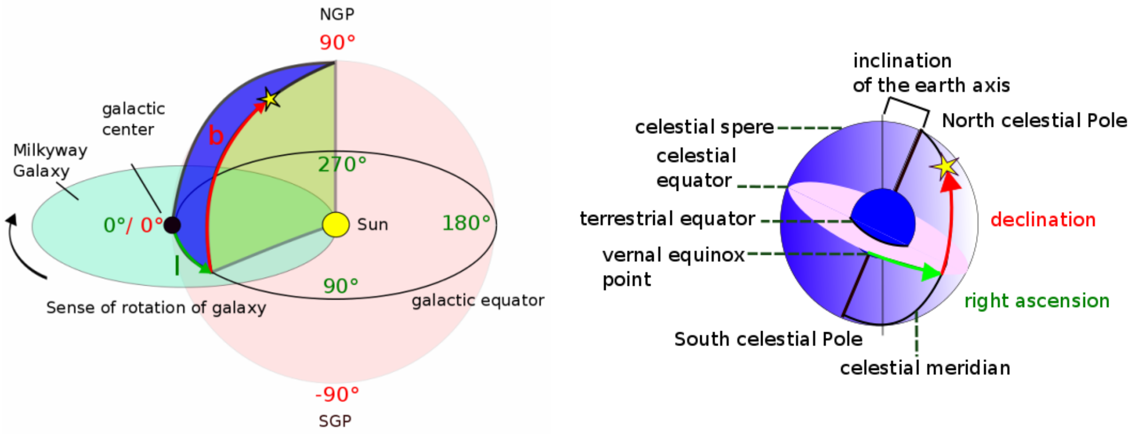

Figure 4.38: Left: Galactic Coordinate System, calling NGP the North Galactic Pole, SGP the South Galactic Pole. The reference is our Sun. Right: Equatorial Coordinate System pictorial representation. The reference is the Earth.

Let us now review some recent results on the correlation of UHECRs with the observed γ-ray flux from the Fermi satellite. This is indeed a Multimessenger approach: we exploit the neutral particles generated by UHECRs interactions during acceleration, i.e. γ-rays, to gain informations about their acceleration sites. In particular, these high enegy photons could be originated by relativistic CRs electrons (*leptonic model*), with a characteristic non thermal distribution, as well as by accelerated protons though decay of secondary neutral mesons π^0 (*hadronic model*). Both steady sources (SN remnants, pulsars, quasars) and explosive ones (GRBs) are natural candidate sources of UHECRs, being identifiable via γ-rays. We shall see in a following subsection Sec.(4.5.7) how the other neutral particles by UHECRs, neutrinos, can be exploited in a Multimessenger approach too.

The Fermi Large Area Telescope (LAT) Skymap Fermi is a satellite detector assessing high energy photons with energies between MeV $< E <$ 100 GeV, which performed the famous complete skymap of the γ-ray intensity shown in Fig.(4.39) in galactic coordinates, and obviously the vertical coordinate shall be the latitude b. The major accumulation of photons intensity is in the central line, representing our Milky Way. This map is of course a superposition of different components:

i) *Diffused radiation*, originating in our Galaxy due to the propagation of CRs in the interstellar medium, dominates the γ-ray sky and is very difficult to model. Anyway, this diffused galactic emission is a foreground for the identification of point sources, and hence affects the determination of their positions and fluxes, so there is the need to somehow model it;

ii) *Galactic and extragalactic individual sources*, appearing as point-like objects, i.e., with angular dimensions much smaller than the resolution of the detectors, over the diffused γ-ray background. Those points in proximity of the plane are galactic objects. It is of course possible to build catalogs of these sources based upon different wavelenght's regimes, and the Fermi LAT collaboration is continuously producing and updating catalogs of these individual sources with location regions, spectral properties, and monthly light curves for each. one It is reasonable to think that these catalogs are very likely to contain also UHECRs sources!

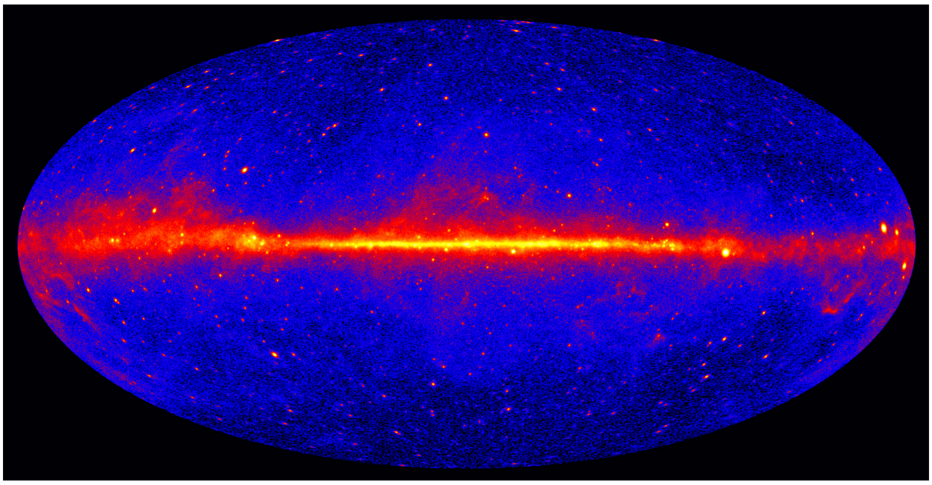

Figure 4.39: The Fermi LAT 5-year image, constructed from front-converting gamma rays with energies greater than 1 GeV. The most prominent feature is the bright band of diffuse glow along the map's center, which marks the central plane of our Milky Way galaxy. From the official site `https://svs.gsfc.nasa.gov/11342`.

In Fig.(4.40), sky models for two distinct populations of extragalactic γ-ray emitters have been created: active galactic nuclei (AGN) and starburst galaxies (SBGs), with the starburst model having been found to fit the data better than the hypothesis of isotropy with a statistical significance of 4σ. Recall that:

- An AGN is a Galaxy which is recognized to host a SuperMassive Black Hole (SMBH) in its center, with a mass of the order of $M_{\text{SMBH}} \simeq 10^6$-$10^{10}$ $\text{M}_{\odot}$. A 1% fraction of all known AGNs is called "ignited" when accretion of mass occurs around the BH, giving rise to powerful relativistic **jets**, which are one of the candidates for accelerating sites of UHECRs;
- A SBG is a region which presents an exceptionally high rate of stars formation, which is deeply correlated with the SN explosion's rate, and we know that SN remnants are another condidate acceleration site for (UHE)CRs.

4.5.7 HE neutrinos in EAS arrays

In the previous section we have seen that measuring neutrinos is an important task which in principle could allow to distinguish a light UHECR composition from a heavy one. This is of course another aspect of a Multimessenger investigation which, as we have just seen, comprehends both the interest of finding an explanation to the ankle feature and of identifying the astrophysical sources of UHECRs by means of the neutral by products of their propagation. Let us notice that we are concentrating on High Energy (HE) neutrinos: the general neutrinos astrophysics shall be treated in another section, here we want to highlight the techniques implied by EAS as PAO.

We have said that a relevant flux of secondary *cosmogenic neutrinos* should be produced in the context of non negligible Δ^+ resonance interactions of light nuclei with the CMB and EBL photons, being instead largely suppressed in the eventuality of heavier nuclei undergoing photodisintegrations. The processes responsible for cosmogenic neutrinos production

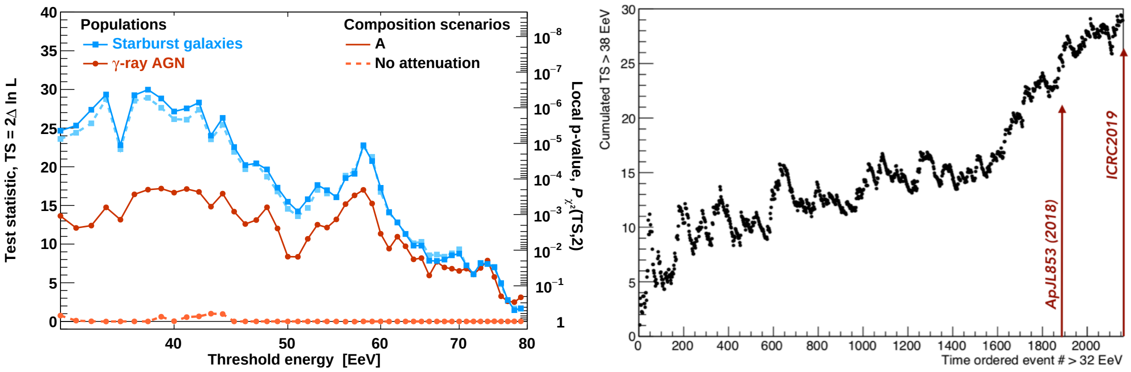

Figure 4.40: Left: Maximum likelihood ratio as a function of energy threshold for the models based on SBGs and AGNs. This ratio is realized as (# correlations in our hypothesis)/(null hypothesis). The results are shown in the attenuation (full line) and no attenuation (dashed line) scenarios. Attenuation is referred to the UHECRs decreasing in intensity due to the energy losses during propagation. The energy dependence is shown for a quite simple reason: the stronger is the magnetic field involved, the better the direction is resolved, so it is an additional test parameter to study if the correlation observed is effectively physically understood (e.g. we do not expect strong correlations at lower energies). Right: Cumulated test statistics for $E_{\rm thr}$= 38 EeV as a function of the time ordered number of events (for the SBG-only model). From the review paper `https://arxiv.org/pdf/1909.10791.pdf`.

will be

$$\beta^- \textbf{ decay} \qquad n \to p + e^- + \bar{\nu}_e$$

$$\pi^\pm \textbf{ decay} \qquad \pi^+ \to \mu^+ + \nu_\mu\,, \qquad \pi^- \to \mu^- + \pi^+$$

$$\mu^\pm \textbf{ decay} \qquad \mu^+ \to e^+ + \nu_e + \bar{\nu}_\mu\,, \qquad \mu^- \to e^- + \bar{\nu}_e + \nu_\mu\,,$$

so in practice only ν_e and ν_μ are expected to be produced. The Δ^+ resonant production with CMB photons produces neutrinos of energies typically 1/20 of the initial proton energy, which has a threshold value of $E_{\rm GZK} \simeq 5 \times 10^{19}$ eV as shown in Ex.(4.4). These are indeed HE neutrinos, with energies above $E_\nu \simeq 1\,\text{EeV} = 10^{18}$ eV.

UHECRs will of course travel for cosmological distances, but the produced neutrinos are expected to not interact neither with CMB and EBL (they are neutral) nor with the Cosmic Neutrino Background, since their interaction cross section is very small. The only phenomenon they should undergo, a part from the obvious adiabatic energy loss, is the *neutrino oscillation*, which allows them to change flavor. In particular, the expected ratio of flavor fluxes in Earth's detectors shall be such that

$$\Phi(\nu_e) \,:\, \Phi(\nu_\mu) \,:\, \Phi(\nu_\tau) = 1 \,:\, 1 \,:\, 1\,,$$

i.e. the τ neutrinos are expected to be detected too. Anyway these fluxes can be very uncertain from the theoretical point of view, essentially for these reasons:

- The composition of CRs is in principle an important unknown;
- The target photons for the interactions is very poorly known: CMB is fairly well understood, but the same cannot be said for EBL, since its redshift evolution is very complex to guess and further complications are introduced by the strong foregrounds the Earth is inevitably permeated with;
- The distribution of sources is, again, unknown, as seen in the previous section: we should investigate on its spectral features (luminosity distribution) and the sources number density too.

What is the exploited idea in EAS arrays to measure neutrinos fluxes in order to extract some useful informations on UHECRs? In practice, such ground based detectors can detect EeV **down-going** neutrinos which, impinging almost horizontally in the Earth's atmosphere, interact and produce a shower. This is in fact the case in which a shower is created in proximity to SD, with a very rich e.m. component, which shall be absorbed completely if the primary particle is instead a less penetrating one (such as a proton), and give rise to much larger scale showers mainly made by muons. The young electromagnetic component is efficiently registered by SD and the ratio $\Phi(\nu)/\Phi_{\text{e.m.}}$ is measured, being sensitive to all flavors.

Additionally, *Earth-skimming* CC interactions by **up-going** τ neutrinos are also exploited. In general, CC interactions can be summarized by the following semileptonic processes:

$$\nu_\mu + N \to \mu + H \qquad \nu_e + N \to e + H \qquad \nu_\tau + N \to \tau + H \ ,$$

and these are represented by the Feynman diagram in Fig.(4.41), in which N and H are the atmospheric interaction target nucleus and the originated hadrons cascade. The fortunate eventualities which this technique needs to exploit are described by this scheme:

1) The ν_l must survive the Earth's absorption, if it is up-going, and interact sufficiently near to the detector. If it is simply a nearly-horizontal particle, as in the previous case, it should again interact deep in the atmosphere to happen nearby the SD;
2) The daughter lepton l must interact or decay in the Earth's atmosphere to give rise to secondaries which arrive at last at the active volume;
3) The final products must have enough energy to trigger the detector and to allow for the track reconstruction.

This is the reason why essentially only the τ flavor is involved in this technique: the CC interaction could in principle produce any flavored lepton, but the e and μ produced will be certainly absorbed by the atmosphere, not being useful for the detector. The ν_τ, instead, is expected to produce a τ lepton, which would very probably give rise to another ν_τ. Being the shortest-living neutrino, this ν_τ would not lose consistent energy and could arrive with enough power to trigger the active volume. This particular event is called *regeneration effect*, referring to the recreation of the ν_τ.
In all cases, since the neutrino cross section grows with energy, PeV and higher energy neutrinos cannot cross the Earth, and their detection is only possible if they interact in close proximity to the detector and produce a cascade.

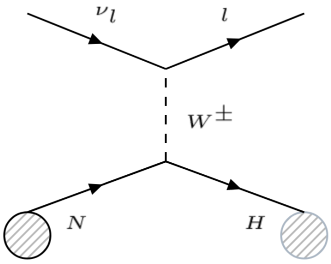

Figure 4.41: Feynman diagram for a general CC process, with a neutrinos of flavor l which gives rise to a lepton l. The nucleon N and the hadronic cascade H are pictorially shown too.

The search for Earth-skimming neutrinos was performed by PAO to identify cosmogenic neutrinos candidates with $E_\nu > 10^{17}$ eV eventually produced in the occurrence of the gravitational wave GW170817. Anyway at the moment no cosmogenic neutrinos has been observed. Fig.(4.42) lastly shows the Earth-skimming technique idea with a pictorial representation.

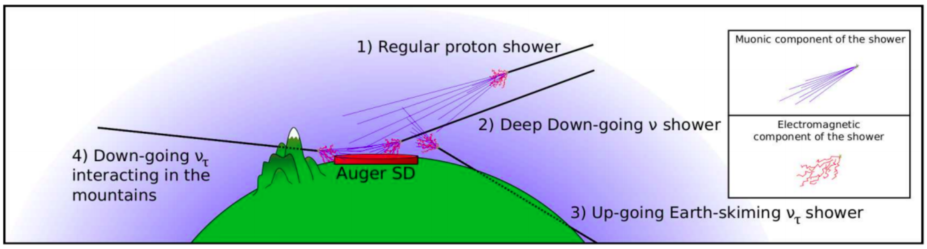

Figure 4.42: Sketch of different inclined showers which can be detected by the Pierre Auger Observatory. (1) An inclined shower induced by a proton interacting high in the atmosphere whose electromagnetic component is absorbed and only the muons reach the detector. Inclined showers presenting significant electromagnetic component at the detector level: (2) a deep down-going ν shower; (3) an Earth-skimming ν_τ shower; (4) and a ν_τ interacting in the mountains. Taken from `https://arxiv.org/pdf/1107.4805.pdf`.

4.6 Cosmic Rays propagation in the Galaxy

Our Galaxy, as seen from aside, can be pictorially traced as in Fig.(4.43): the thickness of the galactic disk is of the order of $h \simeq$ 200-300 pc, and remembering that $1\,\text{pc} \simeq 3.26\,\text{ly}$ with $1\text{ly} \simeq 9.4{\times}10^{15}\text{m}$ one has that $h \simeq 10^3\text{ly}$. The radius of the Milky Way r_{MW} is approximately $r_{\text{MW}} \simeq 15\text{kpc}$, and the total diameter can be estimated by $d_{\text{MW}} = 2r_{\text{MW}} \simeq 2{\times}15\text{kpc} \simeq 10^5\text{ly}$. Modeling it as a cylinder, the total volume is given by

$$V_{\text{MW}} = \pi r_{\text{MW}}^2 \times h = \pi \left(1.5 \times 10^4\right)^2 \, 250\,\text{pc}^3$$

$$\simeq 1.69 \times 10^{11} \left(3.086 \times 10^{16}\,\text{m}\right)^3 \simeq 4.96 \times 10^{60}\,\text{m}^3\,,$$

which is actually at least a order of magnitude smaller than the actual one, computed with the account of the inhomogeneous density of (inter)stellar matter.
Our Solar System is located at the radius of $r_{\text{SS}} \simeq 9\text{kpc} \simeq 2.8 \times 10^4$ ly, and it is far from the galactic bulge, which has a radius of about $r_{\text{bulge}} \simeq 3$ kpc. Stars which are located in the periferic regions are usually metal rich, since the spiral arms are star formation regions, thus those astra are typically young. Stars in the galactic bulge are instead much older and metals poor. A super massive black hole, Sagittarius A*, is known to reside at the galactic center, with a mass of the order of millions of solar masses.
The official NASA site `https://asd.gsfc.nasa.gov/archive/mwmw/mmw_images.html` is very rich of multiwavelenght images of our galaxy, and what is remarkable is their consistent differences as you travel through the regimes of the electromagnetic spectrum. For example,

- At <u>*radio*</u> wavelenghts, a lot of thermal (Bremsstrahlung or blackbody-emitted) radiation connected to the CRs propagation can be seen, and also a non thermal diffused component due to galactic magnetic field's interactions of light CRs particles, such as electronic synchrotron radiation. At the frequency of $\nu_{\text{H}} \simeq 1.4$ GHz, the famous line of atomic hydrogen at $\lambda_{\text{H}} = 21$ cm appears too, as a tracer of the CNM and WNM;

- At <u>*optical*</u> wavelenghts, the images are deeply influenced by dust absorption. The ISM is in fact made by a 1% of dust grains, a component of crystals of carbonaceous or oxygen grains which is responsible for the absorption of the wavelenghts of IR and near IR mostly. Of course also gas clouds can contribute to the absorption, being also easily recognizable by strong emission lines (CO molecule is the main tracer of molecular hydrogen clouds);

- At *γ-rays* wavelenghts the Milky Way appears as in Fig.(4.39), and we have already stressed that the individual points are to be interpreted as individual sources of γ-rays. Of course, we don't expect any star to emit such higher frequencies, and the extragalactic sources appearing outside the plane shall be regarded as AGNs or SBGs. The galactic ones, instead, are mostly Supernova (SN) remnants, and we shall treat them in the following section.

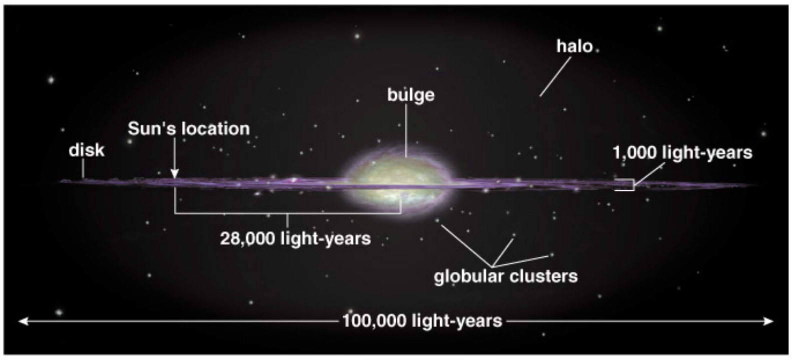

(b)

Figure 4.43: Pictorial view of the Milky Way: typical distances are also sketched, together with the principal structures.

4.6.1 The Galactic Accelerators: SN remnants

A SN remnant is the leftover structure after the star explosion as a Core Collapse SN (CCSN), often referred to Type II SN, which occurs at the end of the fusion process in very massive stars with initial masses of $\mathrm{M} \geq 8\,\mathrm{M}_\odot$. To make a long story extremely short, a nuclear density-like iron core is formed, the infalling material of outer layers is reflected from the nuclear core and a shock wave propagates outwards, heated by neutrino emission from the neutron star. The remnant (which does not comprehend the eventual compact object formed in the process) reveals and develops as a gas bubble, which is characterized typically by a very hot interior and a cold neutral shell. Both of these components are clearly observable in different wavelenghts: the hot interior, heated to $T \simeq 10^6$ K, emits X-rays, while the cold shell has the usual tracer of CO molecule. At the end of their evolution, a SN remnant could possibly have expanded for 30 pc, sweeping up ISM masses of the order of $10^3\,\mathrm{M}_\odot$, till the riding shock wave is exhausted and pressure equilibrium with the enviromental ISM gas is reached. Two famous examples are shown in Fig.(4.44). We can give a simple energy budget for a Type II SN which will be useful in the following. The gravitational energy U released during the core collapse can be easily estimated by

$$U \approx -\frac{GM_c^2}{R_i} + \frac{GM_c^2}{R_f} \approx \frac{GM_c^2}{R_f} \approx 3 \times 10^{53}\,\mathrm{erg}\,,$$

in which we have assumed a collapse of an iron core of $M_c \simeq 1.4\,\mathrm{M}_\odot$ from an initial radius $R_i \simeq 3000$ km to a final radius $R_f \simeq 20\,\mathrm{km} \ll R_i$. Notice that we are using the core mass: the envelope has no time to follow the core collapse, and will be swept away by the explosion, and only a very small fraction of the energy released in the collapse of the core is needed to blow away it. The kinetic energy K of the matter emitted by the SN explosion can be estimated from the mass of the envelope of the pre-collapsing star and the observed velocity of the ejecta: for a typical $M \simeq 10\,\mathrm{M}_\odot$ and $v \simeq 10^3\,\mathrm{km\,s^{-1}}$, one has

$$K \approx \frac{Mv^2}{2} \approx \frac{1.988 \times 10^{34}\,\mathrm{g}\,\left(10^8\,\mathrm{cm\,s^{-1}}\right)^2}{2} \approx 10^{51}\,\mathrm{erg}\,,$$

and we recall that 1 $\mathrm{M}_\odot = 1.988 \times 10^{33}$ g. Finally, the energy radiated away by the SN $E_{\rm rad}$ can be easily estimated considering the typical luminosity of $L \simeq 2 \times 10^8\ \mathrm{L}_\odot$ which is maintained for several months, let's say $\tau = 5$ months. The total energy lost in the form of radiation shall be

$$E_{\rm rad} \approx L \times \tau \approx 2 \times 10^8 \ \left(3.84 \times 10^{33}\ \mathrm{erg\ s^{-1}}\right)\ 5 \left(2.63 \times 10^6\ \mathrm{s}\right) \approx 10^{49}\ \mathrm{erg}\,,$$

where we have used $\mathrm{L}_\odot = 3.84 \times 10^{33}\,\mathrm{erg\ s^{-1}}$ and $1\,\mathrm{months} = 2.63 \times 10^6$ s. From these simple estimates it is clear that

$$U \gg K + E_{\rm rad} \simeq 10^{-2}\,U\,,$$

and then only a small fraction, that is 1%, of the energy released in the collapse is used in the actual explosion. In practice, 99% of the energy must be converted into kinetic energy of massless particles different from the photons, i.e. the neutrinos, and the theoretical relationship between neutrinos and supernovae was experimentally confirmed in 1987 with the LMC SN, whose remnant is in Fig.(4.44—Left).

Figure 4.44: Left: The nearest SN remnant in the Large Magellanic Cloud, namely SN1987A, which exploded in 1987 and constituted the first multimessenger observation of the mankind history. In fact, just prior to the optical counterpart of the explosion, i.e. the sudden brightnening of a source easily visible in the night sky, a bunch of neutrinos were detected at Kamiokande in Japan as a confirmation of the SN models of neutrinosphere and neutrino-driven shock wave. The ten seconds span, within which the detection of 20 neutrinos was performed, corresponds exactly to the modeled time of the transformation of a Fe core into a hot proton-neutron star during the core collapse, and neutrino escaping from the neutrinosphere is indeed predicted to be prior to the lightnening of the explosion. Right: Crab nebula, namely the remnant of the SN SN1054, again a CCSN. In this much older remnant a bubble structure is indeed visible.

Exercise 4.5. Number and Energy Density of Cosmic Rays

We want to estimate the number and energy density of CRs, i.e. $n_{\rm CR}$ and $\rho_{\rm CR}$.
The *number density* corresponds to the number of particles, moving with speed $v \simeq c$, present in a given volume at a given time, and it is measured in $[n_{\rm CR}] = \mathrm{cm}^{-3}$. This quantity can be obtained by dimensional arguments from the integral flux $\Phi\,(> E)$. We have seen that the integral flux of CRs till the knee is parametrized by Eq.(4.4):

$$\Phi\,(> E) = \frac{K'}{\alpha - 1}\left(\frac{E}{1\ \mathrm{GeV}}\right)^{1-\alpha} \qquad \text{with} \qquad [\Phi(> E)] = \frac{\#\ \text{particles}}{\mathrm{cm^2\ sr\ s}}\,,$$

where K' appears an integration constant such that $K' = K \times (1\ \mathrm{GeV})$, with $K \simeq 3$ from Eq.(4.3), and $\alpha \simeq 2.7$. We can reasonably take the minimum energy as $E_0 = 3$ GeV, to leave out of the discussion the solar wind's effects. The number density is then obtained by integrating the integral flux over the solid angle and dividing by the velocity, and for an isotropic flux, such as the one we have parametrized, one has

$$n_{\mathrm{CR}} = \frac{4\pi}{c}\,\Phi(> E_0) = \frac{4\pi}{c}\,\frac{K'}{\alpha - 1}\,\left(\frac{E_0}{1\,\mathrm{GeV}}\right)^{1-\alpha} \simeq 1 \times 10^{-10}\,\mathrm{cm}^{-3}\,,$$

which reveals that one free particle over 10^{10} must be a CRs. This is a small number, and one can remember that the average ISM density is given by $n_{\mathrm{ISM}} \simeq 1\,\mathrm{cm}^{-3}$, which encodes all the matter unbound in stellar enviroments.

The *energy density* of CRs can be obtained by integration of the differential flux given by Eq.(4.1), multiplied by E, over energy and solid angle, and dividing by the velocity $v \simeq c$, which dimensionally gives the right quantity

$$\begin{aligned}
\rho_{\mathrm{CR}} &= \frac{1}{c}\int_{4\pi}\int_{E_0}^{+\infty}\frac{\mathrm{d}^2\phi}{\mathrm{d}E\,\mathrm{d}\Omega}E\,\mathrm{d}E\,\mathrm{d}\Omega = \frac{1}{c}\int_{4\pi}\int_{E_0}^{+\infty}K\left(\frac{E}{1\,\mathrm{GeV}}\right)^{-\alpha}E\,\mathrm{d}E\,\mathrm{d}\Omega = \\
&= \frac{4\pi}{c}\int_{E_0}^{+\infty}K \times (1\,\mathrm{GeV})\left(\frac{E}{1\,\mathrm{GeV}}\right)^{-\alpha+1}\mathrm{dE} = \frac{4\pi}{c}\left[\frac{K \times (1\,\mathrm{GeV})}{\alpha - 2}\,E^{-\alpha+2}\right]\Bigg|_{E_0}^{+\infty} = \\
&= 8.32 \times 10^{-10}\,\mathrm{GeV} = 0.8\,\mathrm{eV\,cm}^{-3}\,,
\end{aligned} \tag{4.14}$$

and we have used a flux of the form of Eq.(4.3). Let us compare ρ_{ISM} with other astrophysical analogous quantities.

i) The **CMB energy density** ρ_{CMB} can be estimated considering that the CMB radiation has a thermal black body spectrum at a temperature of 2.725 K, which corresponds to an energy of $< E_{\mathrm{CMB}} >= 3kT \simeq 7 \times 10^{-4}$ eV, where $k = 8.61 \times 10^{-5}\,\mathrm{eV\,K}^{-1}$ is the Boltzmann constant. Knowing $n_{\mathrm{CMB}} \simeq 411\,\mathrm{cm}^{-3}$, we get

$$\rho_{\mathrm{CMB}} = n_{\mathrm{CMB}}\ < E_{\mathrm{CMB}} > \simeq 0.29\,\mathrm{eV\,cm}^{-3}\,,$$

which is very compatible with our estimate of ρ_{CR}, but there is no link between the two quantities;

ii) The **ISM magnetic field energy density** ρ_{B} can be estimated by the usual formula in CGS system, using the value for the galactic magnetic field intendity $|\vec{B}| \simeq 4\,\mu$G,

$$\rho_{\mathrm{B}} = \frac{|\vec{B}|^2}{8\pi} = \frac{(4 \times 10^{-6})^2}{8\pi} \simeq 6.4 \times 10^{-13}\,\mathrm{erg\,cm}^{-3} = 0.4\,\mathrm{eV\,cm}^{-3}\,,$$

and we have used 1 eV = 1.602×10^{-12} erg. Again, this similarity with ρ_{CR} might suggest a connection between the two;

iii) The **Starlight Density** can be obtained from photometric measurements of the light coming from galactic stars, and the resulting visible photon density is:

$$n_{\gamma,\mathrm{vis}} \simeq 2 \times 10^{-2}\,\mathrm{cm}^{-3} \qquad \Rightarrow \qquad \rho_{\gamma,\mathrm{vis}} = 4 \times 10^{-2}\,\mathrm{eV\,cm}^{-3}\,,$$

assuming 2 eV/photon for the visible light. This is a much smaller value than ρ_{CR}.

We are now able to give at least one reason for which the SN remnants shall be good candidates for acceleration sites of CRs, and further results are in Sec.(4.6.2.4). The reasoning we are going to follow traces back to Zwicky in the 1930's, and is based on the equilibrium between the loss of CRs due to their escape from the galactic volume and the energy provided by supernova shock waves.

In particular, the Galaxy is uniformly filled with the relativistic radiation we detect on Earth:

if we consider the CR sources to be uniformly distributed throughout the Galaxy (which is a very reasonable assumption, since no anisotropies are currently being detected), the total kinetic energy of CRs can be calculated by

$$E_{\rm CR} = \rho_{\rm CR}\, V_{\rm MW} \simeq (1\,{\rm eV\,cm^{-3}})\,(4.96 \times 10^{66}\,{\rm cm^{-3}}) \simeq 7.95 \times 10^{54}\,{\rm erg}\,.$$

If CRs were entirely confined in the galaxy, one should observe an accumulating CRs energy over time, supposedly because of the presence of a new galactic core-collapse supernova explosion. Anyway, another competing mechanism has to be taken into account: the escape of CRs out of the Galaxy with a characteristic escape time (or confinement time) $\tau_{\rm esc}$ should induce a decrease in $\rho_{\rm CR}$. The escape time, as anticipated in Sec.(4.3.3.1), is the average time needed for a CR, trapped by the galactic magnetic field, to reach the galactic boundary. In the following we shall calculate the precise value of $\tau_{\rm esc}$, but for now let us use

$$\tau_{\rm esc} \simeq 10^{7}\,{\rm yr} = 3 \times 10^{14}\,{\rm s}\,.$$

If we assume a steady cosmic rays energy density $\rho_{\rm CR}$, we immediately can estimate the energy loss rate due to the escape of CRs out of the galactic volume:

$$P_{\rm CR} = \frac{\rho_{\rm CR} \times V_{\rm MW}}{\tau_{\rm esc}} = \frac{7.95 \times 10^{54}\,{\rm erg}}{3 \times 10^{14}\,{\rm s}} \simeq 2.65 \times 10^{40}\,{\rm erg\,s^{-1}}\,.$$

Thus, if we want our equilibrium assumption to hold, the power required by the hypothetical cosmic accelerators to replenish the galactic volume shall correspond to this $P_{\rm CR}$. Furthermore, if the supposed accelerators are effectively SNs, one can also notice that the assumption of $\rho_{\rm CR} \sim$ const for a time scale $\tau_{\rm esc}$ is completely reasonable from the astrophysical point of view, since a large variation in the supernova rate $f_{\rm SN}$ in the last, say, billion years is not expected. Of course it is just an assumption: we can't measure anything for billions of years. Anyway, since WWII, when the observations of SNs started with the increasing importance of the newly born cosmology, the expected rate of galactic SNs has been estimated with the result of $f_{\rm SN} \simeq 10^{-9}\,{\rm s^{-1}} = 3\,{\rm century^{-1}}$.

We can conclude that, if SNs are the effective accelerators of CRs, a fraction η of the kinetic energy K transferred by the explosion to the ejected matter should be converted into CR's particle energy. Then

$$P_{\rm SN} = \eta \times f_{\rm SN} \times 10^{51}\,{\rm erg\,s^{-1}}\,,$$

and we can compare these two power rates to obtain the requested equilibrium.

$$P_{\rm CR} \overset{!}{=} P_{\rm SN} \qquad \Leftrightarrow \qquad \eta = \frac{2.65 \times 10^{40}\,{\rm erg\,s^{-1}}}{10^{42}\,{\rm erg\,s^{-1}}} \simeq 1\%\,,$$

which means that the shock waves from supernova explosions are perfectly able to enrich the Galaxy with new accelerated particles and maintain the stationary energy content of CRs. This condition makes the supernova model energetically compatible with the observations. Mechanisms for the particle accelerations in SNs (but also in general) are known and continuously developed: the more classic argument is by Fermi, the so called *magnetic mirror* model, see Sec.(4.6.2), while a more modern one is the *magnetic reconnection.*

4.6.2 The Standard Model of CRs Acceleration

Now that we have seen what are the accelerating sites of CRs in the MW, we can describe what is effectively the acceleration mechanism. This topic will also give some insights on the possible spectral index at the source for Fermi-accelerated CRs, to be compared with the constraints given by the diffusion equation, see Sec.(4.6.3).

The Standard Model for CRs acceleration comprehends different processes, the most classical

arguments being the second and first order Fermi mechanisms, Sec.(4.6.2.1) and Sec.(4.6.2.2), which are indeed a starting point, historically too. We know that CRs are particles whose energies are typically much higher than the thermal energies found in astrophysical environments, so the candidates for acceleration mechanisms should be able to reproduce the fluxes and spectral features we have seen so far. It is clear that what happens in our man-made accelerators can't be even similar to what needs to occur in astrophysical regions: isolated static electric fields cannot be maintained, because the matter is in the state of a plasma, and the ISM has a particularly high conductivity, too.
What has been theoretized is that, for CRs up to the knee, the acceleration is performed in violent processes that produce shock waves and turbulence, whose preferred sites are none other than the SNs. In particular, the bulk of CRs is believed to be accelerated in recursive stochastic mechanisms in which low-energy particles, after a large number of interactions with magnetized clouds and ISM overdensities, will reach high energies, see Sec.(4.6.2.2).

4.6.2.1 Second order Fermi mechanism

The simple idea (1949) of Fermi was based on the Faraday law, which states that a varying B originates an electric field as well by induction, and then in such electric fields charged particles are accelerated:

$$\vec{\nabla} \times \vec{E} = -\frac{\partial \vec{B}}{\partial t} \, .$$

The astrophysical sites should be regions of ISM in which a strongly irregular magnetic field is sustained. Some ISM clouds can indeed reach such conditions, and usually they are also characterized by overdensities $10\rho_{\mathrm{ISM}} \leq \rho \leq 100\rho_{\mathrm{ISM}}$, velocity dispersion $< \sigma_v > \simeq 10 \, \mathrm{km\,s^{-1}}$ and dimensions of the order of $l \simeq 10$ pc.
The acceleration process can be seen as the scattering of the particle by magnetic field irregularities, which can be shown to lead to a net energy gain for the incoming CR particle. In particular, particles interact with each other not through collisions, but by the emission and absorption of collective excitations of the plasma, the *plasma waves*, since the scattering occurs on a length scale much smaller than the mean free path $\lambda = (n\sigma)^{-1}$. The scattering between the particle and the magnetic cloud can be considered as elastic in the reference frame in which the cloud is at rest.

Let us describe Fermi's idea with a simple calculation. We suppose that an incoming CR of mass m enters such a cloud with an angle between the initial direction and the normal to the surface of the mirror called θ_1, while the exiting angle is θ_2. Analogously, let E_1, p_1 be the initial energy and momentum and E_2, p_2 the final ones, see Fig.(4.45). The centre of mass frame of reference shall be that of the cloud moving at velocity v, since the cloud's mass M is such that $M \gg m$. The velocity $\vec{v}$ shall provide us an unidimensional reference axis, $\hat{x}$, along which we perform the boosts. The calculation is in fact simply a game of changing reference frame in relativistic kinematics:

$$\textit{rest frame} \qquad \longleftrightarrow \qquad \textit{comoving frame}$$

$$(\vec{p_1}, E_1, \theta_1) \qquad \longleftrightarrow \qquad (\vec{p_1}', E_1', \theta_1') \, ,$$

i.e. the quantities with superscripts are then referred to the comoving frame. The energy of the particle in this frame is

$$\frac{E_1'}{c} = \gamma \left(\frac{E_1}{c} - \frac{\vec{p_1} \cdot \vec{v}}{c} \right) = \gamma \left(\frac{E_1}{c} - \frac{v}{c} \, p_{1x} \right) \qquad \text{with} \quad p_{1x} = |\vec{p}| \cos\theta_1 \simeq \frac{E_1}{c} \, \cos\theta_1 \, ,$$

and we have assumed our particle to be relativistic, $E_1 \simeq |\vec{p}|c$. Notice also that we are taking a boost from a lab frame in which the particle's velocity is parallel to the cloud's v, i.e. a trailing encounter rather than a head-on (more probable) one. This doesn't mean that we are considering just this possibility: an average mean in angles between $0 < \theta_1 < \pi$ will account for all the cases. Specializing the E' expression for the initial and the final state, one has that in the comoving cloud frame

$$E'_1 = \gamma E_1 \ (1 - \beta \ \cos\theta_1) \ , \qquad E'_2 = \gamma E_2 \ (1 - \beta \ \cos\theta_2) \ .$$

A Lorentz boost back to the rest reference leads to the E_2 expression

$$E_2 = \gamma E'_2 \ \left(1 + \beta \ \cos\theta'_2\right) \ .$$

What we are interested in is actually the difference in energy $\Delta E/E_1$, and to find this we recall that the fundamental assumption of the mechanism is to have a "collisionless" interaction, in which, in the cloud frame, the particle's energy is conserved $E'_1 = E'_2$: it is an elastic scattering, which can be visualized as a particle being simply reflected by an infinite mass mirror. The mirror's velocity remains unmodified, and the particle's p_{1x} momentum is simply flipped. This is why sometimes the Fermi mechanism is said to make use of ***magnetic mirrors*** idea. The relative energy change is given by

$$\frac{\Delta E}{E_1} = \frac{E_2 - E_1}{E_1} = \frac{\gamma E'_2 \ (1 + \beta \ \cos\theta'_2) - E_1}{E_1} = \frac{\gamma E'_1 \ (1 + \beta \ \cos\theta'_2)}{E_1} - 1 =$$

$$\frac{\gamma^2 E_1 \ (1 - \beta \ \cos\theta_1)\,(1 + \beta \ \cos\theta'_2)}{E_1} - 1 = \gamma^2 \ \left(1 - \beta \ \cos\theta_1 + \beta \ \cos\theta'_2 - \beta^2 \ \cos\theta_1 \cos\theta'_2\right) - 1 \ .$$

We now average over the angles. Because of scattering by hydromagnetic waves or irregularities in the magnetic field, it is likely that the particle will exit the cloud with a totally random θ'_2. This means that the probability density function for having the exit angle θ within $[\theta, \ \theta + \mathrm{d}\theta]$ is uniform. In fact, the probability that $\mathrm{d}n(\theta)$ particles exit the cloud with angles in $[\theta, \theta + \mathrm{d}\theta]$ is

$$\mathrm{d}n(\theta) = \frac{\sigma \ 2\pi R \ \sin\theta \mathrm{d}\theta}{\sigma \ 4\pi R^2} = \frac{1}{2} \ \sin\theta \mathrm{d}\theta = -\frac{1}{2} \ \mathrm{d}(\cos\theta) \ ,$$

where we have called σ the number of particles per unit area, which is isotropic since we are in the reference of the cloud. This represents the ratio of the infinitesimal spherical strip (favorable cases) and the total area (the possible cases). The PDF is uniform

$$\frac{\mathrm{d}n(\theta)}{\mathrm{d}(\cos\theta)} = -\frac{1}{2} \qquad \text{with} \qquad \cos\theta \in [1, -1] \ .$$

This is the well known PDF for an isotropic angular distribution, and the first momentum of our variable, $\cos\theta_2$, with respect to it (the average) gives

$$< \cos\theta'_2 >= \int_1^{-1} \cos\theta'_2 \ \frac{\mathrm{d}n(\theta'_2)}{\mathrm{d}(\cos\theta'_2)} \ \mathrm{d}(\cos\theta'_2) = \frac{1}{2} \int_{-1}^{1} \cos\theta'_2 \ \mathrm{d}(\cos\theta'_2) = 0 \ .$$

What remains to treat is the following average

$$\left\langle \frac{\Delta E}{E_1} \right\rangle = \frac{1 - \beta \ < \cos\theta_1 >}{1 - \beta^2} - 1 \ . \tag{4.15}$$

The probability for a relativistic particle to collide at angle θ is proportional to the relative velocity, $n(\theta) \propto c - v \ \cos\theta$, where the particle is taken to be relativistic with velocity $\approx c$. This is reasonable: for a head-on collision with the cloud, $\vec{p_1} \cdot \vec{v} = -p_{1x} v \cos\theta$, the probability

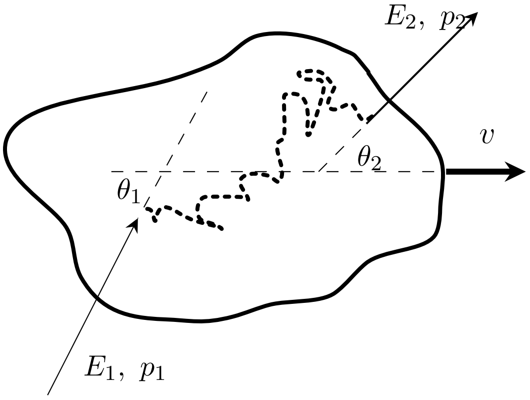

Figure 4.45: Pictorial view of Fermi II order mechanism idea. The cloud velocity is v as in the text, and the twisted line is the hypothetical Markov path of the CR particle.

would have been $n(\theta) \propto c + v\cos\theta_1$. So the PDF is now not anymore uniform, and the first momentum is

$$< \cos\theta_1 >= \frac{\int_{-1}^{1} \cos\theta_1\, n(\theta_1)\, \mathrm{d}(\cos\theta_1)}{\int_{-1}^{1} n(\theta_1)\, \mathrm{d}(\cos\theta_1)} = \frac{\int_{-1}^{1} \cos\theta_1\, (c - v\ \cos\theta_1)\, \mathrm{d}(\cos\theta_1)}{\int_{-1}^{1} (c - v\ \cos\theta_1)\, \mathrm{d}(\cos\theta_1)} =$$

$$= -\frac{v}{2c}\int_{-1}^{1} \cos^2\theta_1\, \mathrm{d}(\cos\theta_1) = -\frac{1}{3}\,\beta\,,$$

and notice that this is an exact result, since the undetermined proportionality factors in the PDF cancel out in the average. If we had started with $\vec{p}\cdot\vec{v_1} = -p_{1x}v\ \cos\theta$, we should have obtained something similar to Eq.(4.15), but with a plus sign in front of $< \cos\theta_1 >$; then, the head-on probability $n(\theta) \propto c + v\cos\theta_1$ average would have given us the same result. Finally, we can plug this result into our relative energy expression to find

$$\left\langle \frac{\Delta E}{E_1} \right\rangle = \frac{1+\beta^2/3}{1-\beta^2} - 1 = \frac{1+\beta^2/3 - 1 + \beta^2}{1-\beta^2} \simeq \frac{4}{3}\,\beta^2\,\left(1+\beta^2\right) \simeq \frac{4}{3}\,\beta^2\,,$$

and we have truncated the result at first order in β, since the cloud is non relativistic. Some different numerical factors can be found in the literature for this rule, however this is the famous result from Fermi, which states that the average increase in energy is of second order in β.

In Fermi's paper of 1949, it was assumed that collisions with interstellar clouds were the main source of energy for the particles. There are however some limits in this picture:

1) The random velocities of interstellar clouds in the Galaxy are very small in comparison with the velocity of light, with $\beta = v/c \lesssim 10^{-4}$. The Fermi second order mechanism shall thus be ***very slow***. In fact, let us suppose that we want this mechanism to accelerate a CR particle from an energy $E_0 \sim$ GeV to $E \sim$ PeV, obtaining a relative gain of $E/E_0 \simeq 10^6$. Let t_{cycle} be the typical timescale for one acceleration cycle, and t the available time for the acceleration process. At each cycle, a gain ΔE is achieved such that

$$\Delta E = \chi E = \frac{4}{3}\,\beta^2\,E \qquad \Rightarrow \qquad E_n = E_0\,\left(1+\chi\right)^n\ ,$$

and E_n is the energy after n cycles. In particular, solving the expression for n and noticing that the number of cycles is nothing but $n = t/t_{\text{cycle}}$, one has

$$n = \frac{t}{t_{\text{cycle}}} \overset{!}{=} \frac{\log(E/E_0)}{\log(1+\chi)} \qquad \Leftrightarrow \qquad t = t_{\text{cycle}}\,\frac{\log(E/E_0)}{\log(1+\chi)}\,.$$

The typical value for the relative gain χ, assuming $v \simeq 30\,\mathrm{km\,s^{-1}}$, is

$$\chi = \frac{4}{3}\,\beta^2 = \frac{4}{3}\,\left(\frac{3\times 10^4\,\mathrm{m\,s^{-1}}}{3\times 10^8\,\mathrm{m\,s^{-1}}}\right)^2 \simeq 1.3\times 10^{-8} \ll 1 \qquad \Rightarrow \qquad \log(1+\chi)\approx\chi\,,$$

and for t_{cycle} we can assume, in the most favorable case, that it should be of the order of the typical lenghtscale of the cloud $l = 10$ pc divided by the light speed:

$$t_{\text{cycle}} = \frac{l}{c} = \frac{3.086\times 10^{17}\ \mathrm{m}}{3\times 10^8\ \mathrm{m\,s^{-1}}} \simeq 10^9\ \mathrm{s} = 32.6\ \mathrm{yr}\,,$$

and we have used 1 pc $= 3.086 \times 10^{16}$ m, and 1 s $= 3.17 \times 10^{-8}$ yr. Finally, the total time required for the acceleration of a CR particle from $E_0 = 1$ GeV to $E = 1$ PeV is given by

$$t = t_{\text{cycle}}\,\frac{\log(E/E_0)}{\chi} = 32.6\ \mathrm{yr}\,\frac{\log(10^6)}{1.3\times 10^{-8}} = 34.7\ \mathrm{Gyr}\,,$$

which is of the same order od magnitude of the age of the universe τ_{hubble}.

2) The ***injection problem***: if the acceleration mechanism has to be effective, the particles must either be injected into the acceleration region with energies greater than that corresponding to the maximum energy loss rate or else the initial acceleration process must be sufficiently rapid to overcome the ionisation energy losses. This is known as the injection problem and is present in all acceleration mechanisms.

3) The ***power law index*** in this model is not explicitly constrained to be $\alpha \approx 2$, as the observations require. An improved version of this theory is indeed needed, and this is called First Order Fermi mechanism.

4.6.2.2 First order Fermi mechanism

Fermi First order mechanism refers to the possibility to find, within a model, a relative energy gain ΔE proportional to a first power of β. It is also called *diffusive shock acceleration* (DSA) process, since, as we shall see, the most rated sites for this process to happen are the regions traversed by strong shock waves, the ones ahead of the supersonic shells of SN remnants being the protagonists.

Let us then imagine a strong shock propagating through a diffused medium with a velocity $-\vec{u_1}$ with respect to the gas rest frame. The matter which traverses the front, in the shock rest frame, shall have velocity $\vec{u_1}$, and the matter which has already been traversed has $\vec{u_2} < \vec{u_1}$ velocity. The shock in fact is expected to convert bulk kinetic energy of the traversing (*upstream*) matter into thermal chaotic energy of the traversed (*downstream*) ISM material, leading to an increase in the temperature T_2. The shock front can be considered as a discontinuity surface with a thickness smaller than the λ_{mfp}: the turbulence makes it essentially untreatable. Rankine-Hugoniot conditions on mass, energy and momentum conservation are the common method to study up(down) stream regions, and in particular the mass conservation reads

$$\rho_1 u_1 = \rho_2 u_2 \qquad \text{and} \qquad \frac{\rho_2}{\rho_1} = \frac{\gamma+1}{\gamma-1}\,,$$

where γ is the adiabatic index, given by the ratio of the specific heat at constant pressure to specific heat at constant volume c_p/c_v. This assumes a simple value for a monoatomic ideal gas: $\gamma = 5/3$. Assuming this approximation to be valid, and calling $\vec{v}$ the velocity of the downstream material in the laboratory frame, one finds

$$u_2 = \frac{1}{4}\,u_1 \qquad \Rightarrow \qquad v \equiv |\vec{v}| = |-\vec{u_1} + \vec{u_2}| = \frac{3}{4}\,u_1\,,$$

and we have used the addition of velocities rule to find v. This v shall now play the role of the cloud velocity we have used in the second order Fermi mechanism, but now the idea is different: rather than having a single source with an alive tangling magnetic field, the accelerated particle is now expected to traverse **several** of these regions, gaining power in each of them with essentially the same collisionless inelastic scatterings. The idea is depicted in Fig.(4.46).

We can always turn our coordinates such that the shock front results in a plane, and the entering and exiting angles with respect to the front's normal are called θ_1 and θ_2 as in Sec.(4.6.2.1). The calculation is again just a matter of changing reference frame, noticing that the upstream and downstream-solidal points of view are perfectly specular. In particular, the downstream region sees an isotropized flow of HE particles coming towards itself due to the inelastic scatterings happening in the other region, and viceversa. Furthermore, the downstream region sees the shock front going away with a velocity $\vec{u_2}$ and the upstream region coming with $\vec{v}$; the upstream region sees the shock and the downstream material with respectively $\vec{u_1}$ and $\vec{v}$.
To study the case in which a CR particle, after having interacted into the upstream region, travel then to the downstream area, we can perform a Lorentz boost along the normal direction, $\hat{x}$, into the downstream-solidal frame

$$\frac{E'}{c} = \gamma \left(\frac{E}{c} - \frac{\vec{p} \cdot \vec{v}}{c} \right) = \frac{E}{c} + \beta \, |\vec{p}| \cos\theta_1 \qquad \text{with} \quad p_x = |\vec{p}| \cos\theta_1 \simeq \frac{E}{c} \, \cos\theta_1 \; ,$$

and we have assumed our particle to be relativistic, $E \simeq |\vec{p}|c$, while $\gamma \simeq 1$ since the shock is assumed to be non-relativistic instead. Notice that, in this case, $\vec{p} \cdot \vec{v} = -p_x v \, \cos\theta_1$: we need to select an appropriate interval in angles to account for head-on collisions from upstream to downstream **only**, i.e. $0 < \theta < \pi/2$ with respect to the normal to the front (different convention than in Fig.(4.46)!). Now, the relative change in energy in this passage is given by

$$\Delta E = E' - E = 1 + v \, |\vec{p}| \cos\theta_1 \qquad \text{and} \qquad \left\langle \frac{\Delta E}{E} \right\rangle = \frac{v}{c} \, \langle \cos\theta_1 \rangle \; .$$

The probability $n(\theta)$ for a relativistic particle to approach the shock front with angles within $[\theta, \theta{+}\mathrm{d}\theta]$ accounts for an isotropized flux and also for a factor $v_{\text{part}} \cos\theta_1$, which is the relative velocity of the HE particle to the downstream gas: $n(\theta_1) \propto v_{\text{part}} \cos\theta_1$. We can then compute the $< \cos\theta_1 >$ with respect to $n(\theta_1)$:

$$< \cos\theta_1 >= \frac{\int_0^1 \cos\theta_1 \, n(\theta_1) \, \mathrm{d}(\cos\theta_1)}{\int_0^1 n(\theta_1) \, \mathrm{d}(\cos\theta_1)} = \frac{\int_0^1 \cos\theta_1 \, (v_{\text{part}} \, \cos\theta_1) \, \mathrm{d}(\cos\theta_1)}{\int_0^1 (v_{\text{part}} \, \cos\theta_1) \, \mathrm{d}(\cos\theta_1)} = \frac{2}{3} \, .$$

The particle's velocity vector is randomised without energy loss by scattering in the downstream region and it then recrosses the shock, and the process can be studied completely analogously since the two regions are specular. The round-trip gain is given by

$$\frac{\Delta E}{E} = \frac{4}{3} \frac{v}{c} = \frac{4}{3} \beta \, ,$$

and this is the original result from Bell (1978), who first proposed such a correction to the Fermi's original idea.

We could also have obtained it by re-using the results from the second order Fermi treatment, with the analogy of performing two reference frame changes, *upstream* $\rightarrow$ *downstream* $\rightarrow$ *upstream*. Since the upstream region is the ISM gas, which is in practice at rest with respect to the front, it shall play the role of the lab frame, and the downstream region is in place of the magnetized cloud comoving system. So one has

$$E_1' = \gamma E_1 \left(1 - \beta \cos\theta_1\right) , \qquad E_2 = \gamma E_2' \left(1 + \beta \cos\theta_2'\right) ,$$

completely analogously, and in this case γ and β are referred to the velocity of the downstream medium in the upstream fluid frame, being then $\beta = 3/4\, u_1$. The fact that here $\vec{p_i} \cdot \vec{v} = p_i v \cos\theta_i$ is not a selection of just trailing collisions: an appropriate integration in angles will give the exact result. In particular, in this case the convention is that of Fig.(4.46)[11]: the adequate intervals for angles describing head-on collision are $\pi/2 < \theta_1 < \pi$ and $0 < \theta_2' < \pi/2$. The resulting mean of the angles within these ranges and with the weight $n(\theta) \propto v_{\text{part}}\, cos\theta$ are

$$< \cos\theta_1 >= \frac{\int_{-1}^{0} \cos^2\theta_1 \, \mathrm{d}(\cos\theta_1)}{\int_{-1}^{0} \cos\theta_1 \, \mathrm{d}(\cos\theta_1)} = -\frac{2}{3} , \qquad < \cos\theta_2' >= \frac{\int_{0}^{1} \cos^2\theta_2' \, \mathrm{d}(\cos\theta_2')}{\int_{0}^{1} \cos\theta_2' \, \mathrm{d}(\cos\theta_2')} = \frac{2}{3} ,$$

and substituting into the expression for the relative energy gain obtained in the previous Sec.(4.6.2.1) one has

$$\frac{\Delta E}{E_1} = \gamma^2 \left(1 - \beta \cos\theta_1 + \beta \cos\theta_2' - \beta^2 \cos\theta_1 \cos\theta_2'\right) - 1 =$$

$$\gamma^2 \left(1 + \frac{4}{3}\beta\right) - 1 \simeq \frac{1 + 4/3\,\beta - 1 + \beta^2}{1 - \beta^2} \simeq \frac{4}{3}\beta ,$$

where we have retained just the first order in β, which is the leading one. We immediately see that this mechanism is much more powerful, being just first order in $\beta = (u_1 - u_2)/c$, and it leads also to a gain which is essentially independent on how the particles are scattered back and forth.

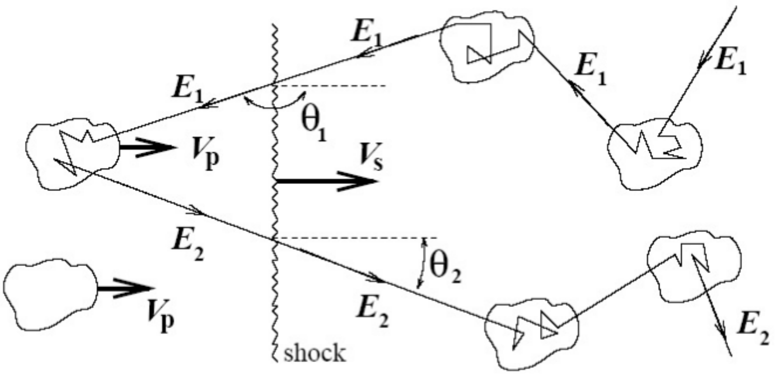

Figure 4.46: Pictorial view of the first order Fermi mechanism idea. Here the front velocity is called V_s and the incoming CR particle's velocity V_p. The entering and exiting angles with respect to the front normal are θ_1 and θ_2. Notice the variation interval for the angles: $\pi/2 < \theta_1 < \pi$ and $0 < \theta_2' < \pi/2$.

---

[11] Maybe it is quite strange to pass from one convention to another. However, one convention was used by the professor ($\vec{p} \cdot \vec{v} = p_x v \cos\theta_1$ with $\pi/2 < \theta_1 < \pi$ for head-on collisions), and the other ($\vec{p} \cdot \vec{v} = p_x v \cos\theta_1$ with $0 < \theta_1 < \pi$ for head-on collisions) was used by M. Longair, "High Energy Astrophysics", and Spurio, "Probes of Multimessenger Astrophysics", the classic textbooks of reference for the course. So it may be useful to be able to distinguish them.

4.6.2.3 The predicted Spectral Index

The most important success of the Standard Model of Acceleration is the capability to reproduce a power law for the differential CRs flux, and in particular the expected spectral index $\alpha \approx 2$ within the framework of the diffusive shock acceleration model. We saw that the relative gain in energy, whatever is the accelerating mechanism, could be parametrized by a χ factor such that

$$\Delta E = \chi E \qquad \Rightarrow \qquad E_n = E_0 \ (1+\chi)^n \ ,$$

and E_n is the energy after n cycles. The number of cycles shall be lower than the maximum $n_{\max}$ given by the ratio between the effectiveness time of the acceleration site (e.g. the expanding lifetime of a SNR, $T_{\rm SN}$, see Sec.(4.6.2.4)) and the typical timescale of one cycle $t_{\rm cycle}$. One can define an escape probability $P_{\rm esc}$, constant over the entire $n_{\max}$ realizations, of a CR's particle to escape, after a collision, the acceleration site and be lost for the successive cycles. The probability P^n that a particle stays confined in the site for n encounters is thus given by

$$P^n = (1-P_{\rm esc})^n \qquad \text{with} \quad n = \frac{\log(E/E_0)}{\log(1+\chi)} \ , \tag{4.16}$$

where we have explicited the number of cycles related to P^n in terms of the initial energy E_0 and the wanted final energy E. The number of particles which, after n cycles, have an energy larger than that (completely generic!) of our target E, shall be proportional to the probability to be confined till at least the n-th cycle, with n being upperly (and strictly) bound by the $k \equiv n_{\rm esc}$ in which the particle escape:

$$N(\geq E) \propto \sum_{m=n}^{m=k-1} \ (1-P_{\rm esc})^m = \sum_{m=n}^{m=k-1} \ P^m = \frac{P^n - P^k}{1-P} \simeq \frac{(1-P_{\rm esc})^n}{P_{\rm esc}} \ ,$$

where we have used the convergence of the geometrical series in P^k ($|P^k| < 1$) and also neglected the term P^k, which is the limit for $k \to \infty$. This should not make sense since $k = n_{\rm esc}$ must be finite, as we have already underlined. However, it is indeed reasonable to assume it to be very large, and the expression is justified. So, in the end, the number of particles $N(\geq E)$ can be written as

$$N(\geq E) = N_0 \ (1-P_{\rm esc})^n = N_0 \ \exp\left\{\log\left[1-P_{\rm esc}\right] \left(\frac{\log(E/E_0)}{\log(1+\chi)}\right)\right\} \ ,$$

where we have introduced N_0, which is the initial number of particles, and also the expression of n in Eq.(4.16). Finally we can make use of the properties of the logarithms to write

$$N(\geq E) = N_0 \left(\frac{E}{E_0}\right)^{-\Gamma} \qquad \text{with} \quad \Gamma \equiv -\frac{\log(1-P_{\rm esc})}{\log(1+\chi)} \simeq \frac{P_{\rm esc}}{\chi} \ ,$$

and expansion of the logarithm is valid for small $P_{\rm esc}$, reading $\log(1-x) \simeq -x$. Again we have obtained a power law spectrum. The correspondent differential quantity is given by differentiation

$$N(E) = N_0 E_0^{\Gamma} \ (-\Gamma) \left(\frac{E}{E_0}\right)^{-\Gamma-1} = K \ \left(\frac{E}{E_0}\right)^{-\Gamma-1} \ ,$$

which is eloquently similar to Eq.(4.3), with α replaced by $\Gamma + 1$. Let us also stress that so far we have not specified any acceleration mechanis, leaving χ undetermined. This result is in fact very general, and holds also for the second order Fermi mechanism, which by the way adds no further constraints on Γ. We are however able to make an estimate on the Γ value by using the result from the first order Fermi mechanism. The escape probability $P_{\rm esc}$ can be given by the ratio between the fluxes $\phi_{\rm esc}$ and $\phi_{\rm coll}$, that are the number of particles per unit time and area to escape and enter the shock front plane. If we call $\rho_{\rm CR}$ the accelerated particles' density, the flux of particles crossing the shock from upstream to downstream is given by

$$\Phi_{\rm coll} = \frac{1}{4\pi}\int_{\Omega(\theta_1)} \rho_{\rm CR}\, \vec{v_{\rm part}}\cdot\hat{n}\,{\rm d}\Omega = \frac{1}{4\pi}\int_0^{2\pi}\int_0^1 c\rho_{\rm CR}\,\cos\theta_1\,{\rm d}\phi\,{\rm d}(\cos\theta_1) = \frac{c\,\rho_{\rm CR}}{4}\,,$$

and we have that for the relativistic particle $v_{\rm part}\approx c$, θ_1 is the incident angle and $\hat{n}$ is the normal to the shock front. On the other hand, $\Phi_{\rm esc}$ is due to the global advection of the downstream fluid away from the shock front with a velocity u_2 with respect to it, so

$$\Phi_{\rm esc} = \rho_{\rm CR}\,u_2 = \frac{1}{4}\,u_1\,\rho_{\rm CR}\,.$$

The escape probability is given by

$$P_{\rm esc} = \frac{\Phi_{\rm esc}}{P_{\rm coll}} = \frac{u_1\,\rho_{\rm CR}}{4}\,\frac{4}{c\,\rho_{\rm CR}} = \frac{u_1}{c}\,.$$

Recalling that, in the case of Fermi first order mechanism, the mean gain per each cycle is $\chi = 4/3\,\beta$, one has

$$\Gamma \simeq \frac{P_{\rm esc}}{\chi} = \frac{u_1}{c}\,\frac{3}{4\,\beta} = \frac{u_1}{c}\,\frac{3c}{4\,(u_1-u_2)} = \frac{3u_1}{4u_1\,(1-1/4)} = 1\,,$$

so eventually we have that the differential CRs flux is constrained by the Fermi first order mechanism to be such that

$$N(E) = K\left(\frac{E}{E_0}\right)^{-\Gamma-1}\Bigg|_{\Gamma=1} = K\left(\frac{E}{E_0}\right)^{-2}\,,$$

completely compatible with our observations. This represents one of the principal results of the diffusive shock acceleration mechanism: it provides a power law spectrum whose index is within the range of the experimental measurements. The power law index of exactly 2 arises for the case of a strong non relativistic shock in an ideal gas and with constant escape probability $P_{\rm esc}$, which was our case study.

4.6.2.4 SN Remnants as Sites for DSA

We have already seen a first reason why the SN remnants shall be good candidates for acceleration sites of CRs. We want now to give at least other two arguments to furtherly sustain this thesis, regarding them now to be sites of the diffusive shock acceleration process. These arguments concern

1) *The efficiency of the acceleration process*
As a summary, we saw that for a typical mass of $M = 10\,{\rm M}_\odot$,

$$U \approx 3\times10^{53}\,{\rm erg}\,,\qquad K\approx 10^{51}\,{\rm erg}\,,\qquad E_{\rm rad}\approx 10^{49}\,{\rm erg}\,:,$$

such that the velocity of the ejected matter, i.e. of the shock front, is

$$|u_1-u_2|\simeq\sqrt{\frac{2K}{M}}\simeq\sqrt{\frac{2\times10^{51}\,{\rm erg}}{10\cdot(1.988\times10^{33})\,{\rm g}}}\simeq 3.2\times10^8\,{\rm cm\,s^{-1}}\quad\Rightarrow\quad\frac{u_1-u_2}{c}\simeq10^{-2}\,,$$

which corresponds to a non relativistic velocity for the shock front but much larger than typical velocities of interstellar materials. More refined models find a range of values which can be riassumed by saying that

$$\chi = \frac{4}{3}\,\beta \simeq 10^{-2} - 10^{-1}\;,$$

and this is just the needed efficiency η of the acceleration process found in Sec.(4.6.1) and required to explain the CRs' acceleration by SN explosions. Let us estimate the total time $T_{\rm SN}$ we expect these sites to be operative in accelerating CRs. In particular, as the shock front expands, it will sweep ISM until a mechanical equilibrium between the expanding gas and the surrounding ISM pressure forces is reached. We have that

$$\rho_{\rm SN} = \frac{m_{\rm eject}}{(4/3)\pi\, R_{\rm SN}^3} = \frac{10\ {\rm M}_\odot}{(4/3)\pi\, R_{\rm SN}^3} \overset{!}{=} \rho_{\rm ISM} = \frac{m_p}{1\ {\rm cm}^3} = 1.6\times 10^{-24}\ {\rm g\ cm}^{-3}$$

$$\Leftrightarrow \quad R_{\rm SN} = \left(\frac{3}{\rho_{\rm ISM}}\frac{10\ {\rm M}_\odot}{4\pi}\right)^{1/3} = \left(\frac{1}{4\pi}\,\frac{6\times 10^{34}\ {\rm g}}{1.6\times 10^{-24}\ {\rm g\ cm}^{-3}}\right)^{1/3} \simeq 1.44{\times}10^{19}{\rm cm} = 5{\rm pc}.$$

The corresponding time to reach this size, assuming that the shell is propagating with uniform velocity $u \equiv |u_1 - u_2|$ all the time (we are neglecting the deceleration) is

$$T_{\rm SN} \simeq \frac{R_{\rm SN}}{u} = \frac{1.44\times 10^{19}\ {\rm cm}}{3.2\times 10^{8}} = 4.4\times 10^{10}\ {\rm s} \simeq 1392\ {\rm yr}\;,$$

and this corresponds to the available time for CRs particles to be accelerated by such a site. Note that this timescale for particle acceleration is $T_{\rm SN} \simeq \mathcal{O}(10^3)$ yr, while the timescale for CRs escaping from our galaxy is $\tau_{\rm esc} \simeq 10^7$ yr, as we will derive in Sec.(4.6.3.1). So a large number of SN explosions, with such a short acceleration time duration with respect to the CR escape time, contributes to filling the Galaxy with high energy particles.
Lastly, a caveat shall be stressed: the fact that protons or heavier nuclei are actually accelerated in the region shock shells is controversial, since most of the detected non thermal radiation, including that in the radio wavelenght region, is almost certainly emitted by electrons losing energy to the strong magnetic fields. A method to discriminate between such sources is indeed needed, as we will see in the following.

2) <u>*The maximum energy*</u>
With simple arguments, it is also possible to derive the maximum energy that a charged particle can reach in the acceleration process due to the diffusive shock mechanism from a supernova explosion. Let us estimate the rate of energy gain $\mathrm{d}E/\mathrm{d}t$ at each acceleration cycle:

$$\frac{\mathrm{d}E}{\mathrm{d}t} \simeq \frac{\chi\, E}{t_{\rm cycle}} \qquad \text{with} \quad t_{\rm cycle} \simeq \frac{\lambda_{\rm cycle}}{u} = \frac{r_{\rm L}}{u} = \frac{E}{{\rm Z}e\,|\vec{B}|\,u}\;.$$

In fact, the time $t_{\rm cycle}$ elapsing between successive "magnetic reflections" in a shock front is given by the typical size of the magnetic field confinement, that is the gyroradius $r_{\rm L}$ of Eq.(2.14), divided by the speed of the shock front u. Combining these informations, one has that the $E_{\rm max}$ attainable during a full lifetime $T_{\rm SN}$ of an acceleration site is

$$E_{\rm max} \simeq \frac{\mathrm{d}E}{\mathrm{d}t}\cdot T_{\rm SN} = \chi\,{\rm Z}e\,|\vec{B}|\,u\cdot T_{\rm SN} = \chi\, ze\,|\vec{B}|\,R_{\rm SN} = \beta\,{\rm Z}e\,|\vec{B}|\,R_{\rm SN}\;,$$

and we have used the fact that $\chi \simeq \beta$, regardless the specific mechanism. Notice also that the rate $\mathrm{d}E/\mathrm{d}t$ is independent on the particle's energy: this is relevant, because the model is not constrained from a particular mechanism of pre acceleration of the charged particles. Inserting typical values one obtains

$$E_{\max} \simeq (10^{-2}) \cdot (4.8 \times 10^{-10}\,\mathrm{statC}) \cdot (4 \times 10^{-6}\,\mathrm{G}) \cdot (1.4 \times 10^{-19}\,\mathrm{cm})\, z \simeq$$

$$\simeq 270\,\mathrm{Z\,erg} = 169\,\mathrm{Z\,TeV}\,.$$

This is remarkable: the SN diffusive shock acceleration is able to explain the fluxes of CRs up to energies of 100 TeV, which is where the knee begins. Also, the maximum attainable energy is linearly proportional to the atomic number Z: a fully ionized heavy nucleus of charge Z could achieve much higher total energy with respect to a proton. Thus, in this model, the knee is explained as a structure resulting from the different maximum energy reached by nuclei with different charge Z, see Fig.(4.47). In practice, we can measure only an *all particle spectrum*, and the general interpolation between the different curves is observed.

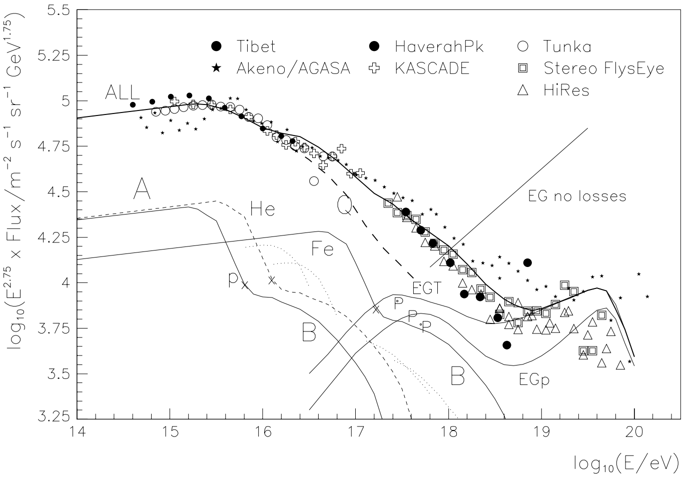

Figure 4.47: The interpretation of the CRs' knee as being due to the correlation between the maximum energy and the nuclear charge Z. The flux of each nuclear species sharply decreases after a given cut-off, which depends on Z. Some compilations of data are also present. From `https://pdfs.semanticscholar.org/ec63/fddc489860cf2972e53447179ace14cbbdcb.pdf?_ga=2.122102155.1040254019.1589645395-2076839075.1588673326.`

4.6.3 The Galactic Diffusion model

The observed spectra of CRs depend on two basic processes: the acceleration in the astrophysical sources (previous Sec.(4.6.2)) and the propagation in the interstellar medium of our Galaxy. In the following sections we want to asses the second aspect.

Upon leaving the source regions, high-energy charged particles diffuse in the random galactic magnetic field, that accounts for their high isotropy and relatively long confinement time. We wish to develop a simple analytic description of CR propagation in the Galaxy, the so called *diffusion equation* formalism, which will provide us a first order analytical estimate of the escape time τ_{esc} as a first useful result (Sec(4.6.3.1)), and then some insights on the spectral properties (Sec.(4.6.3.4)). The ingredients of a good diffusion equation for our CRs shall contain the terms accounting for

- Diffusion through non uniform ISM matter, represented by a scalar diffusion coefficient D;
- Energy loss and gain processes in the ISM;
- Nuclear species fragmentation;

- Radioactive decay of unstable nuclei;
- The input from astrophysical sources, to assure secular equilibrium in CR density.

Of course the result of this treatment is usually an arbitrarily complicated differential equation, which is numerically solvable with a guess on the diffusion coefficient and the source's properties. The guesses are empirically determined from fits to all available data on CRs, and this is a fairly common praxis.

4.6.3.1 The escape time τ_{esc}

We wish to estimate the escape time τ_{esc} of CRs from our Galaxy. We have already seen that the chemical composition of CRs provides informations on the propagation of the CR, see Sec.(4.3.3.1), and we shall adopt here the same distinction: nuclei which are produced by spallation during the ISM propagation are called *light* and subscripted as $\mathcal{L}$, while primary nuclei which are expected to be directly produced by SN are called *heavy*, $\mathcal{M}$, being actually of medium atomic weight. The first are usually Li, Be, B; the latter are C, N, O. The τ_{esc} can be estimated following two methods:

1) Studying the ratio $R_{\mathcal{L},\mathcal{M}}$ between light and medium nuclei;
2) Dating the CR permanence in our Galaxy using radioactive nuclei.

We try to assess the first method with a simple diffusion equation, in which we take into account just the fragmentation and source terms for the nuclear species (neglecting thus decay of unstable isotopes and sources inputs). Notice that we are considering a "diffusion" equation without the typical diffusive term proportional to D: to obtain a first order estimate of τ_{esc}, in fact, it will be sufficient to consider a balance between source and sink terms.

Let's recall that the Solar System abundances of light to medium elements, $R^{\text{SS}}_{\mathcal{L},\mathcal{M}}$, is highly suppressed with respect to the CR's measured one, $R^{\text{CR}}_{\mathcal{L},\mathcal{M}}$:

$$R^{\text{SS}}_{\mathcal{L},\mathcal{M}} \simeq 10^{-5} \qquad \ll \qquad R^{\text{CR}}_{\mathcal{L},\mathcal{M}} \simeq 0.25\,,$$

see also Fig.(4.9), the discrepancy being due to spallation. The production of secondaries by CRs, distributed over the whole galactic volume, depends on the nuclear cross section, the average density of the interstellar material ρ_{ISM} and the distance x traveled between the production and the exit from the Galaxy. The relevant quantity for the production of secondaries is thus

$$\xi \equiv \rho_{\text{ISM}}\, x = \rho_{\text{ISM}}\, c\tau \qquad \text{with} \qquad [\xi] = \text{g cm}^{-2}\,,$$

where we assume a relativistic CR and τ is the typical timescale for the process of interest. The quantity ξ is often called *grammage* or path lenght. We want to find the value of $\xi = \xi_{\text{esc}}$ that reproduces the observed ratio $R_{\text{CR}} \equiv R^{\text{CR}}_{\mathcal{L},\mathcal{M}}$ between the $\mathcal{L}$ and $\mathcal{M}$ abundances. This value shall correspond to the mean amount of interstellar matter traversed by CRs before escaping from the confinement volume. We have already said that the spallation reaction of a $\mathcal{M}$ nucleus producing a $\mathcal{L}$ because of its interaction with ISM protons is

$$\mathcal{M} + p \to \mathcal{L} + \text{anything} \qquad \text{with} \qquad X = \text{C, N, O}\,.$$

This can be quantitatively studied with accelerator data, with high energy protons colliding with a nucleus X at rest. Of course, the cross section should be dependent on the center of mass energy, so it should be the same for the accelerator reaction (with $\mathcal{M}$ at rest) and for the actual ISM one (p is at rest). We are, moreover, assuming the cross section to be approximately independent on the energy, which is not very realistic. If we specialize our case to $Y =$ Be, Li, B, it is possible to extrapolate a probability $P_{\mathcal{M},\mathcal{L}} = 0.28$ from accelerators data of spallation from C, N, O to Be, Li, B, averaged over all the partial cross sections. We want to compute the mean free path for the nuclear interaction process involving light and medium elements, i.e. $\lambda_{\mathcal{L}}$ and $\lambda_{\mathcal{M}}$. The fact that the ISM is essentially made by protons implies that Eq.(2.6) has to be evaluated with A= 1, and then what actually remains to be determined is the nucleus-proton cros sections, which is proportional to the geometrical area of the nuclei, see Eq.(2.8). Predicting an average value of the atomic masses $\mathrm{A}_{\mathcal{L}} = 8.5$ and $\mathrm{A}_{\mathcal{M}} = 14$, we can get

$$\sigma_{\mathcal{L}} \simeq \pi \left(\mathrm{r}_0 \mathrm{A}_{\mathcal{L}}^{1/3}\right)^2 = \pi \left(1.2 \times 10^{-13}\,(8.5)^{1/3}\right)^2\ \mathrm{cm}^2 = 1.884 \times 10^{-25}\,\mathrm{cm}^2 = 188\,\mathrm{mb}\,,$$

$$\sigma_{\mathcal{M}} \simeq \pi \left(\mathrm{r}_0 \mathrm{A}_{\mathcal{M}}^{1/3}\right)^2 = \pi \left(1.2 \times 10^{-13}\,(14)^{1/3}\right)^2\ \mathrm{cm}^2 = 2.628 \times 10^{-25}\,\mathrm{cm}^2 = 263\,\mathrm{mb}\,,$$

and we have used the fact that $\mathrm{r}_0 = 1.2 \times 10^{-13}\,\mathrm{cm}$ and neglected the proton radius in the geometrical cross section. The mean free paths are

$$\lambda'_{\mathcal{L}} = \left.\frac{\omega_a}{\sigma_{\mathcal{L}} \mathcal{N}_a}\right|_{\mathrm{A}=1} = \frac{m_p}{\sigma_{\mathcal{L}}} = \frac{1.66 \times 10^{-24}\,\mathrm{g}}{188 \times 10^{-27}\,\mathrm{cm}^2} \simeq 8.81\,\mathrm{g\,cm}^{-2}\,,$$

$$\lambda'_{\mathcal{M}} = \left.\frac{\omega_a}{\sigma_{\mathcal{M}} \mathcal{N}_a}\right|_{\mathrm{A}=1} = \frac{m_p}{\sigma_{\mathcal{M}}} = \frac{1.66 \times 10^{-24}\,\mathrm{g}}{263 \times 10^{-27}\,\mathrm{cm}^2} \simeq 6.3\,\mathrm{g\,cm}^{-2}\,.$$

We need now to set out a system of differential equations for the number of medium and light nuclei, i.e. $N_{\mathcal{M}}$ and $N_{\mathcal{L}}$, as a function of ξ. The equation that describes the reduction of the number of $\mathcal{M}$ nuclei during their journey is

$$\frac{\mathrm{d}N_{\mathcal{M}}(\xi)}{\mathrm{d}\xi} = -\frac{N_{\mathcal{M}}(\xi)}{\lambda_{\mathcal{M}}}\,, \tag{4.17}$$

in which we recognize the sink term due to nuclear interactions. As regards the $\mathcal{L}$, a source term is needed to describe the possibility of spallation by $\mathcal{M}$ nuclei, and a sink one is similar to that affecting the $\mathcal{M}$ nuclei and accounts for the possibility for a lighter nucleus to disappear by nuclear interaction with $\sigma_{\mathcal{L}}$:

$$\frac{\mathrm{d}N_{\mathcal{L}}(\xi)}{\mathrm{d}\xi} = -\frac{N_{\mathcal{L}}(\xi)}{\lambda_{\mathcal{L}}} + \frac{N_{\mathcal{M}}(\xi)}{\lambda_{\mathcal{M}}}\,P_{\mathcal{M},\mathcal{L}}\,. \tag{4.18}$$

This is a system of ordinary differential equations, and the two needed boundary conditions are $N_{\mathcal{L}}(0) = 0$, $N_{\mathcal{M}}(0) = N^0_{\mathcal{M}}$. The latter is not known a priori, but it is also a dummy parameter: it will disappear at the end when we compare the ratio between elements. The equations are coupled, since the number of $\mathcal{L}$ nuclei in Eq.(4.18) depends on $N_{\mathcal{M}}$. We start from integrating by parts Eq.(4.17):

$$\int_{N^0_{\mathcal{M}}}^{N_{\mathcal{M}}(\xi)} \frac{\mathrm{d}N_{\mathcal{M}}}{N_{\mathcal{M}}} = -\int_0^{\xi} \frac{\mathrm{d}\xi}{\lambda_{\mathcal{M}}} \quad \Leftrightarrow \quad N_{\mathcal{M}}(\xi) = N^0_{\mathcal{M}}\,\exp\left\{-\frac{\xi}{\lambda_{\mathcal{M}}}\right\}\,.$$

This is a pure decay law, as expected. We can substitute this expression for $N_{\mathcal{M}}(\xi)$ into Eq.(4.18), and multiply both sides by $\exp\{\xi/\lambda_{\mathcal{L}}\}$:

$$\frac{\mathrm{d}N_{\mathcal{L}}(\xi)}{\mathrm{d}\xi}\,e^{\xi/\lambda_{\mathcal{L}}} = -\frac{N_{\mathcal{L}}(\xi)}{\lambda_{\mathcal{L}}}\,e^{\xi/\lambda_{\mathcal{L}}} + \frac{N^0_{\mathcal{M}}}{\lambda_{\mathcal{M}}}\,e^{\xi/\lambda_{\mathcal{L}} - \xi/\lambda_{\mathcal{M}}}\,P_{\mathcal{M},\mathcal{L}}$$

$$\Leftrightarrow \quad \frac{\mathrm{d}}{\mathrm{d}\xi}\left[N_{\mathcal{L}}(\xi)\,e^{\xi/\lambda_{\mathcal{L}}}\right] = \frac{N^0_{\mathcal{M}}}{\lambda_{\mathcal{M}}}\,e^{\xi/\lambda_{\mathcal{L}} - \xi/\lambda_{\mathcal{M}}}\,P_{\mathcal{M},\mathcal{L}}\,,$$

and we have simply used the Leibniz rule for the two terms containing $N_{\mathcal{L}}$. As the equation contains exponential functions, the ansatz is of the form

$$N_{\mathcal{L}}(\xi) = c\,\left(e^{-\xi/\lambda_{\mathcal{L}}} - e^{-\xi/\lambda_{\mathcal{M}}}\right)\,,$$

where c is a constant to be determined using the boundary conditions. Substituting this ansatz into the above equation one finds

$$c\,\frac{\mathrm{d}}{\mathrm{d}\xi}\left[\left(e^{-\xi/\lambda_{\mathcal{L}}} - e^{-\xi/\lambda_{\mathcal{M}}}\right)\,e^{\xi/\lambda_{\mathcal{L}}}\right] = c\,\frac{\mathrm{d}}{\mathrm{d}\xi}\left[1 - e^{\xi/\lambda_{\mathcal{L}}-\xi/\lambda_{\mathcal{M}}}\right] =$$

$$= -c\left(\frac{1}{\lambda_{\mathcal{L}}} - \frac{1}{\lambda_{\mathcal{M}}}\right)\,e^{\xi/\lambda_{\mathcal{L}}-\xi/\lambda_{\mathcal{M}}} = c\left(\frac{\lambda_{\mathcal{M}}\lambda_{\mathcal{L}}}{\lambda_{\mathcal{L}}-\lambda_{\mathcal{M}}}\right)^{-1}\,e^{\xi/\lambda_{\mathcal{L}}-\xi/\lambda_{\mathcal{M}}} \overset{!}{=} \frac{N^0_{\mathcal{M}}}{\lambda_{\mathcal{M}}}\,e^{\xi/\lambda_{\mathcal{L}}-\xi/\lambda_{\mathcal{M}}}\,P_{\mathcal{M},\mathcal{L}}$$

$$\Leftrightarrow \quad c = \frac{N^0_{\mathcal{M}}}{\lambda_{\mathcal{M}}}\,P_{\mathcal{M},\mathcal{L}}\left(\frac{\lambda_{\mathcal{M}}\lambda_{\mathcal{L}}}{\lambda_{\mathcal{L}}-\lambda_{\mathcal{M}}}\right) = N^0_{\mathcal{M}}\,P_{\mathcal{M},\mathcal{L}}\left(\frac{\lambda_{\mathcal{L}}}{\lambda_{\mathcal{L}}-\lambda_{\mathcal{M}}}\right)\,,$$

so we can plug this constant into our ansatz, finding finally the solutions for $N_{\mathcal{L}}(\xi)$ and $N_{\mathcal{M}}(\xi)$:

$$N_{\mathcal{M}}(\xi) = N^0_{\mathcal{M}}\,\exp\left\{-\frac{\xi}{\lambda_{\mathcal{M}}}\right\}\,, \tag{4.19}$$

$$N_{\mathcal{L}}(\xi) = N^0_{\mathcal{M}}\,P_{\mathcal{M},\mathcal{L}}\left(\frac{\lambda_{\mathcal{L}}}{\lambda_{\mathcal{L}}-\lambda_{\mathcal{M}}}\right)\left[e^{-\xi/\lambda_{\mathcal{L}}} - e^{-\xi/\lambda_{\mathcal{M}}}\right]\,. \tag{4.20}$$

These two functions Eq.(4.19) and Eq.(4.20) are shown in Fig.(4.48), where it is arbitrarily assumed that $N^0_{\mathcal{M}} = 1$. We can now find the value of $\xi = \xi_{\text{esc}}$ which leads to the right $R_{\mathcal{L},\mathcal{M}} = N_{\mathcal{L}}/N_{\mathcal{M}}$, measured to be $R_{\mathcal{L},\mathcal{M}} = 0.25$. The ratio is given by

$$R_{\mathcal{L},\mathcal{M}} = \frac{N_{\mathcal{L}}}{N_{\mathcal{M}}} = P_{\mathcal{M},\mathcal{L}}\left(\frac{\lambda_{\mathcal{L}}}{\lambda_{\mathcal{L}}-\lambda_{\mathcal{M}}}\right)\left[e^{\xi/\lambda_{\mathcal{M}}-\xi/\lambda_{\mathcal{L}}} - 1\right] \overset{!}{=} 0.25\,,$$

and we can easily isolate ξ to find the right value:

$$\xi_{\text{esc}} = \left(\frac{\lambda_{\mathcal{M}}\lambda_{\mathcal{L}}}{\lambda_{\mathcal{L}}-\lambda_{\mathcal{M}}}\right)\,\log\left[\frac{R_{\mathcal{L},\mathcal{M}}}{P_{\mathcal{M},\mathcal{L}}}\left(\frac{\lambda_{\mathcal{L}}-\lambda_{\mathcal{M}}}{\lambda_{\mathcal{L}}}\right) + 1\right] \simeq 5.012\,\mathrm{g\,cm^{-2}}\,, \tag{4.21}$$

which is highlighted in Fig.(4.48) in red. This quantity is called the average escape length of CRs from our Galaxy. Now we can recall that we have defined $\xi = \rho_{\text{ISM}}\,x = \rho_{\text{ISM}}\,c\tau$, so

$$x_{\text{esc}} = \frac{\xi_{\text{esc}}}{\rho_{\text{ISM}}} = \frac{5\,\mathrm{g\,cm^{-2}}}{1.66\times10^{-24}\,\mathrm{g}} \simeq 10^{25}\,\mathrm{cm} = 3\,\mathrm{Mpc}\,,$$

where we have used an average density for the ISM of $n_{\text{ISM}} \simeq 1\,\mathrm{cm^{-3}}$, or better $\rho_{\text{ISM}} \simeq m_p\,\mathrm{cm^{-3}}$, and of course the conversion $1\,\mathrm{cm} = 3.24\times10^{-19}\,\mathrm{pc}$.

Notably, our Galaxy having a radius of 15 kpc and a thickness of 300 pc, so this result can be explained only if the propagation of cosmic rays resembles that of a random walk: in particular, the vertical thickness is much smaller, and charged particles are trapped in the Galaxy just because of their tangled motions in the MW magnetic field. Correspondingly to such a x_{esc}, finally the **escape time** τ_{esc} can be estimated:

$$\tau_{\text{esc}} = \frac{x_{\text{esc}}}{c} = \frac{10^{25}\,\mathrm{cm}}{3\times10^{10}\,\mathrm{cm\,s^{-1}}} \simeq 3\times10^{14}\,\mathrm{s} = 10^{7}\,\mathrm{yr}\,,$$

as we have previously anticipated. Let us stress that this is just a first order estimate since τ_{esc} is expected to be energy dependent. In particular, since the gyroradius is $r_{\mathrm{L}} = E/(\mathrm{Z}e|\vec{B}|)$, the escape time decreases as the particle energy increases. We shall say something more about the energy dependence of $\tau_{\text{esc}} = \tau_{\text{esc}}(E)$ in the following section Sec.(4.6.3.3).

One can indeed argue that this simple analytic result is in fact dependent on too many assumptions: anyway, a completely independent escape time determination is given by the dating with radioactive nuclei, the cited method 2), and the result is surprisingly compatible.

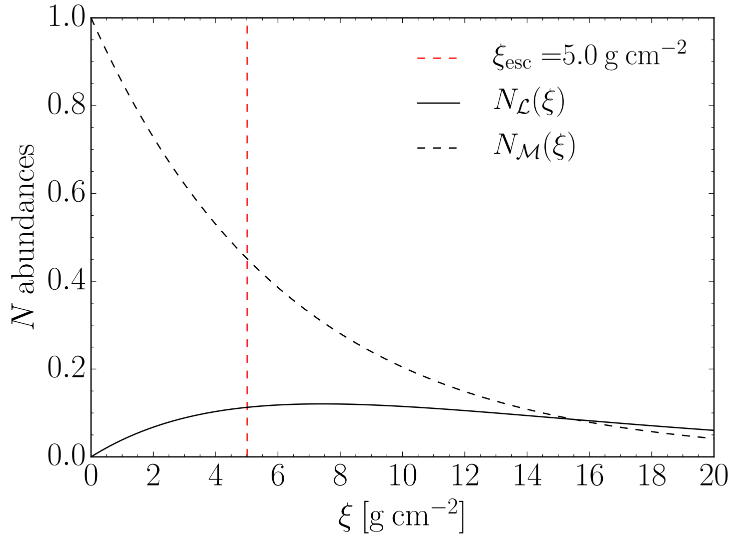

Figure 4.48: Evolution of the number of $\mathcal{M}$ and $\mathcal{L}$ nuclei as a function of the galactic path length ξ. Near the astrophysical accelerators, $\xi = 0$, the $\mathcal{L}$ nuclei are absent. As ξ increases, $N_{\mathcal{L}}$ increases as light nuclei are produced by fragmentation of medium nuclei. The reference value $N^0_{\mathcal{M}}$ is here taken to be $N^0_{\mathcal{M}} = 1$, but it does not influence the ratio $R_{\mathcal{L},\mathcal{M}} = N_{\mathcal{L}}/N_{\mathcal{M}}$. In red the value of $\xi_{\rm esc}$ which leads to the observed $R_{\mathcal{L},\mathcal{M}} = 0.25$.

4.6.3.2 The Diffusion-Loss equation

We are now going to develop a full diffusion-loss equation, which will describe the CRs' journey through the Galaxy, and we will see how this journey is able to modify the CRs' energy spectrum from the sources to the observer.

The observable quantity of interest shall be $\mathcal{N}$, an energy and number density such that $[\mathcal{N}] = \text{GeV}^{-1}\ \text{cm}^{-3}$. Notice that the energy scale is GeV: the solar modulated CRs are too difficult to even be modeled and shall not be considered here. Let us progressively build up all the ingredients we have listed in the introduction of this Section (4.6.3).

1) *Energy losses and gains*

   This term accounts for both loss processes, such as excitation/ionization, Bremsstrahlung, and gains due to acceleration mechanisms. Within the infinitesimal time dt, it can be given by

   $$-\frac{\mathrm{d}E}{\mathrm{d}t} = b(E) \qquad \text{with} \qquad [b(E)] = \text{GeV}^{-1}\ \text{s}^{-1}\,, \tag{4.22}$$

   where $b(E)$ is conventionally positive for energy losses, and negative for energy gains. What we want to obtain is the change in the number and energy density of particles, i.e. we want to express $\mathcal{N}(E)\mathrm{d}E$ variation over time, where $\mathcal{N}(E)\mathrm{d}E$ is of course the number of particles per unit time with an energy within $[E,\ E + \mathrm{d}E]$. To do so, we can consider that the particles present at time t with an energy within $[E,\ E + \mathrm{d}E]$ will have, at time $t + \mathrm{d}t$, an energy within $[E',\ E' + \mathrm{d}E']$ such that

   $$E' = E + b(E)\mathrm{d}t \quad \text{ and } \quad E' + \mathrm{d}E' = (E + \mathrm{d}E)\ + b(E + \mathrm{d}E)\mathrm{d}t\,.$$

   We can combine the two expressions to find

   $$\mathrm{d}E' = -E' + (E + \mathrm{d}E)\ + b(E + \mathrm{d}E)\mathrm{d}t = -b(E)\mathrm{d}t + \mathrm{d}E + b(E + \mathrm{d}E)\mathrm{d}t =$$

   $$= \mathrm{d}E + \frac{\mathrm{d}b(E)}{\mathrm{d}E}\,\mathrm{d}E\mathrm{d}t\,,$$

where in the second row we have performed a Taylor expansion for small dE. The variation of the number of particles per unit time with an energy within $[E,\ E+\mathrm{d}E]$ is given by

$$\mathrm{d}\mathcal{N}(E)\mathrm{d}E = \mathcal{N}(E', t)\mathrm{d}E' - \mathcal{N}(E, t)\mathrm{d}E\,,$$

where the time dependence is emphasized but redundant, since Eq.(4.22) provides essentially a $E = E(t)$ relation. Using the result for dE'

$$\begin{aligned}\mathrm{d}\mathcal{N}(E)\mathrm{d}E &= \mathcal{N}(E', t)\left(\mathrm{d}E + \frac{\mathrm{d}b(E)}{\mathrm{d}E}\,\mathrm{d}E\mathrm{d}t\right) - \mathcal{N}(E, t)\mathrm{d}E = \\ &= \mathcal{N}(E + b(E)\mathrm{d}t, t)\left(\mathrm{d}E + \frac{\mathrm{d}b(E)}{\mathrm{d}E}\,\mathrm{d}E\mathrm{d}t\right) - \mathcal{N}(E, t)\mathrm{d}E = \\ &= \frac{\mathrm{d}\mathcal{N}}{\mathrm{d}E}\,b(E)\mathrm{d}t\mathrm{d}E + \mathcal{N}(E)\frac{\mathrm{d}b(E)}{\mathrm{d}E}\,\mathrm{d}E\mathrm{d}t\,,\end{aligned}$$

and in the second row we have substituted $E' = E + b(E)\mathrm{d}t$, while in the third row a further Taylor expansion for small $b(E)\mathrm{d}t$ has been performed. Finally, the resulting energy losses and gains term is given by applying Leibniz:

$$\frac{\mathrm{d}\mathcal{N}(E)}{\mathrm{d}t} = \frac{\partial}{\partial E}\,\left[b(E)\mathcal{N}(E)\right]\,,$$

and this is the most simple form of our diffusion equation, with just the one derived term.

2) *Sources' injection*
Considering an elementary volume dV in the spatial coordinates, the injection of particles per unit time and energy range can be written as $Q(E,\,\vec{x},\,t)\,\mathrm{d}V$, where $Q(E,\,\vec{x},\,t)$ is the source term. Notice that is has already the right dimensions, so the source term to add into our equation shall be

$$Q(E,\,\vec{x},\,t) \qquad \text{with} \quad [Q(E,\,\vec{x},\,t)] = \mathrm{GeV}^{-1}\,\mathrm{s}^{-1}\,\mathrm{cm}^{-3}\,. \tag{4.23}$$

Obviously the dependence on the $\vec{x}$ coordinates is completely general, and this adds a degree of complexity for the solution of the complete diffusion-loss equation. Usually one builds this term mainly to represent SN remnants and interstellar gas distributions, basing on current HI (21-cm atomic hydrogen emission) and CO (molecular emission used to trace molecular hydrogen) surveys.

3) *Diffusion*
The diffusion term accounts for the exit of particles out of the considered region of space, since at the end the diffusion-loss equation we are building is specialized within the given volume dV. The theory of (advection) diffusion equations leads to the familiar term

$$D\,\nabla^2\mathcal{N}(E, t) \qquad \text{with} \quad [D] = \mathrm{cm}^2\,\mathrm{s}^{-1}\,, \tag{4.24}$$

where D is the mentioned diffusion coefficient and it has the meaning of the typical velocity scale times the typical mean free path for the diffusive process. On the microscopic level, the diffusion of CRs results from particle scatterings on random magnetohydrodynamic waves and discontinuities, which populate the SN shells and HII regions of the ISM. This is important, since these two kinds of region are clearly present in the galactic scale, being also very common. Let us mention, for completeness, that an order of magnitude estimate for the diffusion coefficient D can be determined from dimensional arguments

$$D \sim Lv \sim \frac{L^2}{\tau_{\mathrm{esc}}} = \frac{(300\,\mathrm{pc})^2}{10^7\,\mathrm{yr}} \simeq \frac{(9\times10^{20}\,\mathrm{cm})^2}{3\times10^{14}\,\mathrm{s}} = 3\times10^{27}\,\mathrm{cm}^2\,\mathrm{s}^{-1}\,,$$

and we have assumed that the typical velocity is given by $v \sim L/\tau_{\text{esc}}$. The use of τ_{esc} is justified by the fact that we assume that the dynamics of CRs occurs within the galactic disc, i.e. particles should diffuse to a distance L roughly equal to the thickness of the galactic disc, $L \sim 300\,\text{pc}$. In literature more refined values for D are used, but they agree with this estimate within an order of magnitude.

4) *Nuclear spallation and decay*
To account for nuclei fragmentation and decay, we simply have to add additional terms analogous with the ones seen in Sec.(4.6.3.1), in particular Eq.(4.18). This time a subscript i is needed to label the N different nuclear species. In particular, N diffusion-loss equations are needed to decribe the different species, and each one is coupled to the other by the j-th number and enegy density $\mathcal{N}_j$, which allows the possibility of fragmentation by all the other nuclear species with $\text{Z} > \text{Z}_i$. One has

$$-\frac{\mathcal{N}_i}{\tau_i} + \sum_{j>i}^{N} \frac{\mathcal{N}_j}{\tau_j} P_{j,i}\,, \tag{4.25}$$

where $P_{j,i}$ is the probability of production of i nuclei by spallation of j specie, and τ_i, τ_j are the lifetimes of particles of species i and j. For the spallation process, they correspond to $\tau = \lambda/c$, with λ being the nuclear interaction lenght. The finite lifetime τ_{dec} of unstable elements can also be accounted for by simply assuming that

$$\frac{1}{\tau} = \frac{1}{\tau_{\text{dec}}} + \frac{c}{\lambda}\,,$$

where the smaller between τ_{dec} and λ/c is the dominant term. Of course, when dealing with electrons, positrons, and antiprotons, this nuclear interactions-induced term is not present, and one has to account for the different energy losses with the proper 1) term of Eq.(4.22).

The complete diffusion-loss equation is then built by the all of the terms in Eq.(4.22), Eq.(4.23), Eq.(4.24), Eq.(4.25):

$$\frac{\mathrm{d}\mathcal{N}_i(E)}{\mathrm{d}t} = \frac{\partial}{\partial E}\left[b(E)\mathcal{N}_i(E)\right] + D\,\nabla^2\mathcal{N}_i + Q(E,\,\vec{x},\,t) - \frac{\mathcal{N}_i}{\tau_i} + \sum_{j>i}^{N} \frac{\mathcal{N}_j}{\tau_j} P_{j,i}\,. \tag{4.26}$$

This represents the diffusion-loss equation for the time and spatial evolution of the energy spectrum of the particles. As we have already said, the solution of the most general case is, in principle, extremely difficult, and what is usually done is to solve it with the help of MC simulations. The most famous example is the **GALPROP** code, which was already mentioned in Sec.(4.3.3.3), being frequently used to describe antiprotons diffusion. It is very remarkable: with detailed matter density maps of MW, it provides predictions not only on secondaries' spectrum ($e^{\pm}$ or $\bar{p}$) at the sources, but also on synchrotron radiation effects via galactic magnetic fields modeling and finally on γ-rays emissions too.

4.6.3.3 The Leaky Box Model

Being very complex to treat, the diffusion-loss equation can be on the other hand greatly simplified with a series of assumptions called *the leaky box model*. Summarizing, we assume

a) the injection of particles in the *box*, the galactic volume, is uniform $Q = Q(E)$;

b) the volume $\mathrm{d}V$ is uniformly filled with matter and radiation fields, such that $\nabla^2\mathcal{N} \simeq \mathcal{N}/L^2$;

c) the escape time τ_{esc} depends on the particle energy, charge, and mass number, but it does not depend on the spatial coordinates, $\tau_{\text{esc}} = \tau_{\text{esc}}(E)$.

Under these assumptions, the diffusion term, which is the most problematic in the full diffusion-loss equation, is approximated by a simple leakage term:

$$D\,\nabla^2\mathcal{N} \to -\mathcal{N}/\tau_{\text{esc}}\,,$$

and the diffusion-loss equation Eq.(4.26) reduces to

$$\frac{\mathrm{d}\mathcal{N}_i(E)}{\mathrm{d}t} = \frac{\partial}{\partial E}\left[b(E)\mathcal{N}_i(E)\right] - \frac{\mathcal{N}_i}{\tau_{\text{esc}}(E)} + Q(E) - \frac{\mathcal{N}_i}{\tau_i} + \sum_{j>i}^{N}\frac{\mathcal{N}_j}{\tau_j}\,P_{j,i}\,. \tag{4.27}$$

The general problem is thus translated into a system of coupled transport equations for all isotopes involved in the process of nuclear fragmentation, analogously to what we have seen in Sec.(4.6.3.1) for the $\mathcal{L}$ production from $\mathcal{M}$ nuclei. Also in this model the same caveat of the previous section holds: the complexities of propagation of CRs, and in particular, of electrons and positrons, can be treated only through full MC simulations e.g. via GALPROP. The usual method used by any standard code is that of dividing the galaxy into a spatial grid, either in two dimensions with cylindrical symmetry in the Galaxy or in a full three dimensions, and solve with standard PDEs numerical methods.

Escape time energy dependence Let's say something more about the energy dependence of the escape time τ_{esc} of CRs, to justify the third leaky box model assumption, which seems to assume a different result with respect to the (constant) first order estimate in Sec.(4.6.3.1). An energy dependence of the CR escape time can be deduced from

i) the study of the emission of γ-rays, which reflects the density of hadronic and leptonic CRs (the projectile) and the density of gas and photons in the propagation enviroment (the target);

ii) the measurement of the secondary-to-primary ratios of stable nuclei. The reference ratio is usually that between boron and carbon (B/C), because B is entirely secondary, mainly produced by C, N, O, but also Be/Li can be used.

Both observables are compatible with an empirical dependence of the path length ξ on the particle rigidity R:

$$\xi_{\text{esc}} = \xi_0\left(\frac{R}{R_0}\right)^{-\delta} \qquad \text{with} \quad 0.3 < \delta < 0.6\,,$$

and in general δ, ξ_0 and R_0 are parameters that must be derived from theoretical models or fitting experimental data. The dependence on R is reasonable: particles with low rigidity are expected to suffer a larger deflection during the motion in a magnetic field, recall Eq.(4.7). Such a ξ parameterization leads to

$$\tau_{\text{esc}} = \frac{\xi_{\text{esc}}}{c\,\rho_{\text{ISM}}} \qquad \Rightarrow \qquad \tau_{\text{esc}} = \tau_0\left(\frac{R}{R_0}\right)^{-\delta} = \tau_0\left(\frac{E}{E_0}\right)^{-\delta}\,,$$

and we have clearly assumed that $R = R(E)$ with $E \simeq pc$ for high energies. A notable effect on the leaky box equation is that the escape process dominates at high energy over fragmentation, since τ_{esc} starts to become smaller than τ_i. We shall also stress the fact that the fit parameters ξ_0, E_0 and R_0 are in principle dependent on nuclear species. However, the differences are very likely to be not appreciable, since other uncertainties, such as nuclear interactions' models, are much larger.

4.6.3.4 The Spectrum at the Sources

We finally address the question about the consequences of the propagation of CRs through the ISM on the spectrum of protons (and heavier nuclei) at the sources. The case of electrons and positrons is a special one, and has to be treated separately because of their large energy and spatially-dependent energy losses. The consequences of the propagation, described by Eq.(4.26) or simply by Eq.(4.27), translate into a constraint for the spectral index of the CR energy spectrum near acceleration sites.

We consider *primary protons* $N = N_p$ in a steady-state $\mathrm{d}N_p/\mathrm{d}t$, neglecting the fragmentation processes ($P_{j,i} = 0$). For primary protons and nuclei, the energy loss processes are negligible, and $b(E) \simeq 0$. Lastly, let us consider stable nuclei, such that $\tau_p = \lambda_p/c$. The interaction lenght of protons λ'_p in g cm^{-2} in the ISM can be easily estimated as in Sec.(4.6.3.1), using Eq.(2.6) and the geometrical proton-proton cross section $\sigma_{pp} \simeq \pi \mathrm{r}_0^2 = 45\,\mathrm{mb}$:

$$\lambda'_p = \left.\frac{\omega_a}{\sigma_{pp}\mathcal{N}_a}\right|_{A=1} = \frac{m_p}{\sigma_{pp}} = \frac{1.66 \times 10^{-24}\,\mathrm{g}}{45 \times 10^{-27}\,\mathrm{cm}^2} \simeq 36.9\,\mathrm{g\,cm}^{-2}\,,$$

and clearly $\lambda_p = \lambda'_p/\rho_{\mathrm{ISM}}$. With the above assumptions, the leaky box equation becomes

$$\frac{\mathrm{d}\mathcal{N}_p(E)}{\mathrm{d}t} = 0 \overset{!}{=} -\frac{\mathcal{N}_p}{\tau_{\mathrm{esc}}(E)} + Q(E) - \frac{\mathcal{N}_p\, c}{\lambda_p} \tag{4.28}$$

$$\Leftrightarrow \qquad \mathcal{N}_p\left[\frac{1}{\tau_{\mathrm{esc}}(E)} + \frac{c}{\lambda_p}\right] = \mathcal{N}_p\left[\frac{\lambda_p + c\tau_{\mathrm{esc}}}{\tau_{\mathrm{esc}}\lambda_p}\right] = \mathcal{N}_p\left[\frac{1 + c\tau_{\mathrm{esc}}/\lambda_p}{\tau_{\mathrm{esc}}}\right] = Q_p(E)\,,$$

and finally, substituting for $\lambda'_p = \lambda_p\,\rho_{\mathrm{ISM}}$:

$$\mathcal{N}_p(E) = \frac{Q_p(E)\,\tau_{\mathrm{esc}}(E)}{1 + c\,\rho_{\mathrm{ISM}}\,\tau_{\mathrm{esc}}(E)/\lambda'_p} \simeq Q_p(E)\,\tau_{\mathrm{esc}}(E)\,. \tag{4.29}$$

We were then able to find an analytic solution, with good approximations for protons. One can now notice that $c\,\rho_{\mathrm{ISM}}\,\tau_{\mathrm{esc}} = \xi_{\mathrm{esc}}(E)$, which in the previous section was found to be of the order of $\xi_{\mathrm{esc}} \simeq 5\,\mathrm{g\,cm}^{-2}$, see Eq.(4.21). The term $\xi_{\mathrm{esc}}/\lambda'_p$ can then be neglected in the denominator, justifying the second equality.

The observable $\mathcal{N}_p$ can reproduce the primary CR spectrum, observed at Earth, when multiplied by $c/4\pi$, this can be easily seen by dimensional analysis, remembering $[\mathcal{N}_p] = \mathrm{GeV}^{-1}\,\mathrm{cm}^{-3}$. Hence this is the wanted quantity

$$\mathcal{N}_p\,\frac{c}{4\pi} \equiv \Phi(E) \qquad \text{with} \qquad [\Phi(E)] = \mathrm{GeV}^{-1}\,\mathrm{cm}^{-2}\,\mathrm{s}^{-1}\,\mathrm{sr}^{-1}\,.$$

Finally we see that the differential CRs spectrum is

$$\Phi(E) = \frac{c}{4\pi}\,\mathcal{N}_p = \frac{c}{4\pi}\,Q_p(E)\,\tau_{\mathrm{esc}}(E) = \frac{c}{4\pi}\,Q_p(E)\,\tau_0\left(\frac{E}{E_0}\right)^{-\delta} \propto Q_p(E)\,E^{-\delta}\,.$$

Since we have seen that the observed CRs spectrum is given by $\Phi(E) \propto E^{-\alpha}$, we can isolate the injection term

$$Q_p(E) \propto \frac{\Phi(E)}{E^{-\delta}} = E^{-\alpha+\delta}\,.$$

A numerical estimate on the power-law exponent for this injection term can be obtained by recalling that up to the knee energies, $E \simeq 10^{15}$ eV, the spectral index α was around $\alpha \simeq 2.7$, see Eq.(4.3). By taking for $\delta = 0.6$ from a famous compilation of data, we get that

$$Q_p(E) \propto E^{-2.1}\,,$$

which is a very important prediction for the energy spectrum of CRs at the sources: it constrains models of CR sources to reproduce this energy dependence, with a spectral index -2.

We notice lastly that Eq.(4.29) can give informations concerning the energy spectrum of *heavier nuclei.* Up till now, in fact, our calculations have been specialized to the proton case, but for stable nuclei, in general, the acceleration processes provide (almost) the same energy dependence $Q(E)$ at the sources. However, a fundamental difference resides in the nuclear cross-section σ_{Ap} of a nucleus of atomic mass A colliding with an ISM proton. This cross section is increased by $\mathrm{A}^{2/3}$, and this in practice means that the interaction lenght λ'_A is reduced by the same quantity. The orders of magnitude are the ones found in Sec.(4.6.3.1), and are of a few $\mathrm{g\,cm^{-2}}$. For the most heavy specie, ^{56}Fe, one finds

$$\sigma_{\mathrm{Fe}p} \simeq \pi\left(\mathrm{r_0 A^{1/3}}\right)^2 = \pi\left(1.2\times10^{-13}(56)^{1/3}\right)^2\ \mathrm{cm}^2 = 6.621\times10^{-25}\ \mathrm{cm}^2 = 662\ \mathrm{mb}\ ,$$

$$\lambda'_{\mathrm{Fe}p} = \left.\frac{\omega_a}{\sigma_{\mathrm{Fe}p}\mathcal{N}_a}\right|_{\mathrm{A}=1} = \frac{56\ \mathrm{m}_p}{\sigma_{\mathrm{Fe}p}} = \frac{1.66\times10^{-24}\ \mathrm{g}}{662\times10^{-27}\ \mathrm{cm}^2} \simeq 2.51\ \mathrm{g\,cm}^2\ ,$$

and the effect of interactions in the denominator of Eq.(4.29) cannot be neglected.

5

The Multimessenger Astroparticle Physics

5.1 Photons: γ-rays

We have noted, in Sec.(4.6.2.4), that usually the observed radiation is not an actual fingerprint of CRs' acceleration sites, since electrons and positrons could have been the responsible for such a production, due to the strong galactic magnetic fields. The only way to gain informations about the acceleration sites is by observing the neutral particles (γ-rays and neutrinos) generated by their interactions during acceleration. In fact, the γ-rays are the easiest messengers that we can observe and study, and this section shall be devoted to them. We actually had already a taste on how the sky looks in γ-rays by looking at the Fermi skymap in Fig.(4.39): these messengers are indeed the strongest and the most interacting ones, and we expect that their travels must also be affected by a lot of absorptions.

5.1.1 The Spectral Energy Distribution

A first approach on the γ-rays' sky must start from the classical tool, the Spectral Energy Distribution (SED), which is a quantity allowing the energy emitted by the source in a given region of the electromagnetic spectrum to be represented in a unified way. The *spectral flux density* is given by

$$F(\nu) \qquad \text{with} \quad [F(\nu)] = \mathrm{erg\,cm^{-2}\,s^{-1}\,Hz^{-1}}\ ,$$

a macroscopic quantity which describes the rate at which energy is transferred by electromagnetic radiation per unit surface area and at a given frequency ν. This quantity is usually employed when dealing with continuous radiation, and what can be measured by a detector with cross-sectional area A is the energy per time [erg/s], which is consequently divided by A and the sensitivity frequency interval (adequately selected by a filter) $\Delta\nu$ to obtain $F(\nu)$. This is slightly different from what is the common praxis for HE γ-rays. In particular, when dealing with high energy photons, only individual photons are detected by effective active surfaces of $\mathrm{A}(E_\gamma) = \mathrm{A_{geom}} \cdot \epsilon$, with ϵ being the intrinsic efficiency we have already encountered in Ex.(4.2). As these detectors measure the number of incoming photons in a given energy interval $\Delta n_\gamma/\Delta E_\gamma$ and in a given exposure time T, the quantity equivalent to the spectral flux density corresponds to

$$E_\gamma \frac{\mathrm{d}N_\gamma}{\mathrm{d}E_\gamma} = E_\gamma \frac{1}{\mathrm{A}(E_\gamma)\,T} \frac{\Delta n_\gamma}{\Delta E_\gamma} \qquad \text{with} \quad N_\gamma = \frac{n_\gamma}{\mathrm{A}(E_\gamma)\,T}\ , \tag{5.1}$$

and notice that this has the right dimensions, since an interval in frequency gives the corresponding interval in energy, once multiplied by the Planck constant h.

The amount of power radiated through a given area in the given frequency interval $\Delta\nu = \nu_2 - \nu_1$ or energy $\Delta E = E_2 - E_1$ in the form of electromagnetic radiation or individual photons, respectively, is the ***flux density***

$$J(\nu) = \int_{\nu_1}^{\nu_2} F(\nu)\,\mathrm{d}\nu \qquad \text{with} \qquad [J(\nu)] = \mathrm{erg\,cm^{-2}\,s^{-1}}\,,$$

$$J(E_\gamma) = \int_{E_1}^{E_2} E_\gamma\,\frac{\mathrm{d}N_\gamma}{\mathrm{d}E_\gamma}\,\mathrm{d}E_\gamma \qquad \text{with} \qquad [J(E_\gamma)] = \mathrm{erg\,cm^{-2}\,s^{-1}}\,.$$

In most cases, the $F(\nu)$ and the $\mathrm{d}N_\gamma/\mathrm{d}E_\gamma$ distributions can be represented by power law functions, at least within a limited range of frequency or energy. In this case, the flux density in the considered frequency/energy range is given by

$$J(\nu) \propto \nu\,F(\nu)\,, \qquad J(E_\gamma) = E_\gamma^2\,\frac{\mathrm{d}N_\gamma}{\mathrm{d}E_\gamma}\,.$$

Finally, the Spectral Energy Distribution (SED) is a plot of the flux density $J(\nu)$ versus frequency and/or $J(E_\gamma)$ versus energy of the radiation. It is a very useful tool, and in some cases the detected emission from a source starts in the radio frequency and ends in the TeV γ-rays. In this case, the SED for the source includes both measurement methods, and it can be plotted as a function of either frequency ν or energy $E_\gamma = h\nu$.

5.1.2 The Hadronic Model

We refer to models of CRs' sources as *hadronic models*, and the radiation produced by these kinds of sources is the proper one emitted by CR particles. We expect that a part of the CRs flux which comes from an acceleration site will interact with a target to give rise to some secondaries. In particular, high energy photons are expected to be produced, as well as neutrinos. The possibilities for the target are the following:

i) The jet of CRs particles itself, though it is not very probable;

ii) Protons and nuclei in ISM matter in (extra)galactic enviroments with an average cross-section $\sigma_{pp} \simeq$ 40-50 mb. This is described by

$$p + p \to \pi^\pm,\ \pi^0,\ K^\pm,\ K^0,\ p,\ n...$$

and because of the similarity with the process of production of secondary hadrons in a fixed-target accelerator experiment, this process is usually referred to as the ***astrophysical beam dump*** mechanism;

iii) Low energy ambient photons, possibly the ones produced by the $e^\pm$ co-accelerating with the CRs. The surrounding regions of astrophysical sources (take as a characteristic example an accretion disk aroun a BH, or AGN's relativistic jets) are usually influenced by strong magnetic fields, which give rise to synchrotron radiation. The process comes with an average cross-section $\sigma_{p\gamma} \simeq 0.250$ mb, and is described by

$$p + \gamma \to \Delta^+ \to \pi^0 + p\,, \qquad p + \gamma \to \Delta^+ \to \pi^+ + n\,,$$

which are very similar to the GZK effect into CMB photons, and are called ***photopion productions***, see App.(B). The cross-section for this process is indeed $\sigma_{p\gamma} \ll \sigma_{pp}$, but in some cases the photopion production becomes very important: this is because in some astrophysical enviroments the density of low energy ambient photons is very high.

In all cases, the final states to which these processes lead are characterized by pions, which undergo the known decay channels Eq.(3.26):

$$\pi^0 \to \gamma + \gamma\,, \qquad \pi^+ \to \mu^+ + \nu_\mu\,, \qquad \pi^- \to \mu^- + \bar{\nu}_\mu\,.$$

The energy escaping from the source is therefore shared among CRs, γ-rays and neutrinos produced by the decay of π^0 and $\pi^\pm$. This is essentially the reason why the candidate neutrino sources are in general also γ-ray sources. Of course, high energy photons can be produced also by another kind of sources' model, namely *leptonic models*, see Sec.(5.1.3).

Exercise 5.1. Energy spectrum of γ-rays from π^0 decay

We want to study the energy spectrum $\mathrm{d}N_\gamma/\mathrm{d}E_\gamma$ (and the SED) of the γ-rays produced by the π^0 decay

$$\pi^0 \to \gamma + \gamma\,.$$

The PDF of the emission of $\mathrm{d}N_\gamma$ decay products with energy within $[E_\gamma, E_\gamma + \mathrm{d}E_\gamma]$ can be obtained by a change of reference frame, from the laboratory to the COM frame of the products. In this system, in fact, the products are emitted isotropically (π^0 is a spinless particle!), and the PDF for having an emission angle $\theta^* \in [\theta^*, \theta^* + \mathrm{d}\theta^*]$ is uniform. Analogously to what we did in Sec.(4.6.2.1), we have

$$\mathrm{d}N_\gamma(\theta^*) = \frac{1}{2}\,\sin\theta^*\mathrm{d}\theta^* = -\frac{1}{2}\,\mathrm{d}(\cos\theta^*) \qquad \Rightarrow \qquad \frac{\mathrm{d}N_\gamma(\theta^*)}{\mathrm{d}(\cos\theta^*)} = \frac{1}{2}\,,$$

and we have taken the angular interval to vary over $\pi < \theta^* < 0$, that is $-1 < \cos\theta^* < 1$. Performing now a boost from the COM frame to the lab frame, the energy E_γ in the rest frame is related to the COM frame one E^*_γ by

$$\frac{E_\gamma}{c} = \gamma\left(\frac{E^*_\gamma}{c} + \frac{\vec{p_\gamma}^* \cdot \vec{v}}{c}\right) = \gamma\left(\frac{E^*_\gamma}{c} + \frac{|\vec{p_\gamma}^*||\vec{v}|\cos\theta^*}{c}\right) \qquad \Rightarrow \qquad E_\gamma = \gamma E^*_\gamma\,(1 + \beta\,\cos\theta^*)\,,$$

and we have used $E^*_\gamma = |\vec{p_\gamma}^*|c$. The Lorentz factor γ and β are given by

$$\gamma = \frac{E_\pi}{m_\pi c^2}\,, \qquad \beta = \frac{|\vec{v}|}{c}\,, \qquad \Rightarrow \qquad \gamma\beta = \sqrt{\gamma^2 - 1}\,.$$

In the COM frame, each photon shall have an energy $E^*_\gamma = E^*_\pi/2 = m_\pi c^2/2 = 67.5$ MeV, and we have used $m_{\pi^0} = 135\,\mathrm{MeV}/c^2$. Finally, one finds the energy of the photons in the lab frame, which depends on the emission angle θ^*

$$E_\gamma = \gamma\frac{m_\pi c^2}{2}\,(1 + \beta\,\cos\theta^*) \qquad \text{with} \qquad E^\pm_\gamma = \gamma\frac{m_\pi c^2}{2}\,(1 \pm \beta) = \frac{E_\pi}{2}\,(1 \pm \beta)\,,$$

where we have called $E^\pm_\gamma$ the maximum and minimum values for the lab frame photons' energy. For very high energy pions, $\beta \to 1$ and $E^-_\gamma = 0$ while $E^+_\gamma = E_\pi$. We can take the differential of expression of the Lorentz boost to find:

$$\frac{\mathrm{d}E_\gamma}{\mathrm{d}(\cos\theta^*)} = \gamma\beta|\vec{p_\gamma}^*| = \gamma\beta\,E^*_\gamma = \sqrt{\gamma^2 - 1}\,E^*_\gamma = \frac{m_\pi c^2}{2}\,\sqrt{\gamma^2 - 1}\,.$$

Finally, the energy spectrum $\mathrm{d}N_\gamma/\mathrm{d}E_\gamma$ can be obtained by dividing the isotropic angular distribution by the expression of $\mathrm{d}E_\gamma/\mathrm{d}(\cos\theta^*)$:

$$\frac{\mathrm{d}N_\gamma}{\mathrm{d}E_\gamma} = \frac{\mathrm{d}N_\gamma(\theta^*)}{\mathrm{d}(\cos\theta^*)}\,\frac{\mathrm{d}(\cos\theta^*)}{\mathrm{d}E_\gamma} = \frac{1}{2\gamma\beta|\vec{p_\gamma}^*|} = \frac{1}{m_\pi c^2\,\sqrt{\gamma^2 - 1}} = \frac{1}{\sqrt{E^2_\pi - m^2_\pi c^4}}\,, \tag{5.2}$$

and this is remarkably constant for a given pion energy, thus the probability of emitting a photon of energy E_γ is constant over the range $[E_\gamma^-,\ E_\gamma^+]$. One can also show that, in a logarithmic plot in which one represents $\log(\mathrm{d}N_\gamma/\mathrm{d}E_\gamma)$ as a function of $\log(E_\gamma)$, the medium point $\log(E_\gamma^{\rm mid})$ of the interval in which the quantity is constant is such that

$$\log\left(E_\gamma^{\rm mid}\right) = \frac{1}{2}\left[\log\left(E_\gamma^+\right) + \log\left(E_\gamma^-\right)\right] = \log\left(E_\gamma^+ E_\gamma^-\right)^{1/2} =$$

$$= \log\left[\gamma^2 \frac{E_\pi^{*2}}{4}\left(1-\beta^2\right)\right]^{1/2} = \log\left(\frac{E_\pi^*}{2}\right),$$

so in a logarithmic plot the medium point lies exactly at $E_\pi^*/2 = 67.5$ MeV. In Fig.(5.1) we report the energy spectrum $\mathrm{d}N_\gamma/\mathrm{d}E_\gamma$ and the SED for γ-rays produced by π^0 decay, with a monoenergetic family assumption. Of course the monochromatic assumption is not realistic: one needs to take into account the fact that there is a power spectrum of π^0 at the source. The resulting profile shall then have a shape which is shown in Fig.(5.2): two energy breaks are present, with a large characteristic plateaux too. The low energy break is due to the pion rest mass, because the minimum energy is fixed by the pion mass; the high energy break is due to the spectrum of parent protons. This profile is well recognized as the **pion bump**, and is a clear signature for the process $\pi^0 \to 2\gamma$ in the spectrum of SN remnants as well as in AGN.

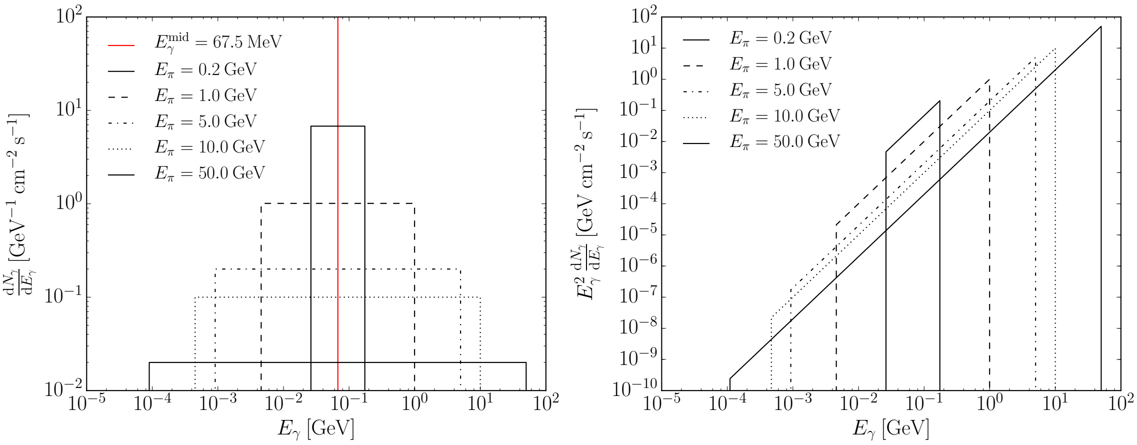

Figure 5.1: Left: The energy spectrum $\mathrm{d}N_\gamma/\mathrm{d}E_\gamma$ for γ-rays produced by π^0 decay, computed for different pion energies E_π. The spectrum is uniform at fixed pion energy, and the range enlarges with larger energies. Right: The SED for the process, each for a uniform family of monoenergetic pions.

NB on the pion bump feature When we are dealing with SN remnants the energy breaks are usually not very much boosted, since the SN is not moving strongly with respect to Earth. On the contrary, in the case of an AGN (jets in particular), these values are indeed depending on γ, being not absolute but highly influenced by the enviroment Lorentz factor with respect to us. So what is actually typical is the plateaux, rather than the two cuts. However we are not very often that lucky to observe such a clear signature in the spectrum of extra galactic objects, since these are very complex enviroments in which many other interactions take place: the spectra are thus usually distorted by the other radiative processes. Therefore, in the end, only SN remnants reveal such a signature, together with galactic enviroments which are defined to be *optically thin*, namely such that photons produced in the pion decay are not likely to undergo further interactions, with a small optical thickness. A lot of effort is being put in the quest for the identification of the pion bump signature in SN remnant,

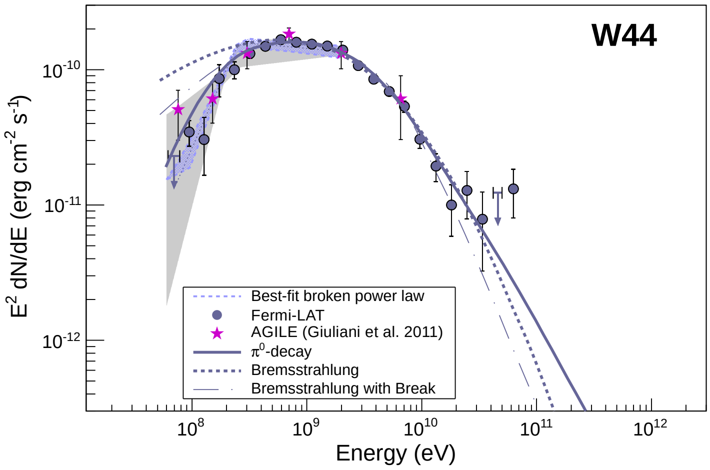

Figure 5.2: From the article `https://arxiv.org/abs/1302.3307v1`. Gamma ray spectra of W44, a SN remnant, as measured with the Fermi-LAT. Color-shaded areas bound by dashed lines denote the best fit smooth broken power law from 60 MeV to 2 GeV, gray-shaded bands show systematic errors due mainly to imperfect modeling of the galactic diffuse emission. Solid lines denote the best-fit $\pi^0 \to 2\gamma$ spectra, dashed(-dotted) lines denote the best-fit bremsstrahlung spectra.

since it can be regarded as a strong evidence of hadronic production of γ-rays, and the work cited in Fig.(5.2) was the first successful one.

5.1.2.1 Estimate of γ-ray flux

Let us make a rule of thumb estimate of the luminosity of γ-rays associated with SNs in our galaxy. The observation of γ-rays from SNRs is in fact the most promising method of addressing the quest for the origin of CRs, through the measurement of the π^0 decay, which reveals the presence of accelerated hadrons interacting with the surrounding material or radiation fields. This signature in SN remnant could then be indeed regarded as a further argument rating SNs as acceleration sites.
We have estimated, in Eq.(4.14), that the average energy density of CRs $\rho_{\rm CR}$ above an energy threshold of $E > 3$ Gev was such that

$$\rho_{\rm CR}\,(> 3\ {\rm GeV}) \simeq 1\ {\rm eV\ cm^{-3}}\ .$$

Let us assume that the energy density of CRs energetic enough to produce secondary mesons, and thus γ-rays, corresponds to 10% of this value, leading to

$$\rho_{{\rm CR}\to\gamma} \simeq 0.1\ {\rm eV\ cm^{-3}}\ ,$$

which is not a very brutal assumption. The power which is associated to this energy fraction is given by

$$P_{{\rm CR}\to\gamma} = \frac{\rho_{{\rm CR}\to\gamma}\cdot V_{\rm MW}}{\tau_{\rm esc}} \simeq 0.3\times 10^{40}\ {\rm erg\ s^{-1}}\ ,$$

and it is given by the sum of all cosmic accelerators that occurred in our Galaxy in the last $\tau_{\rm esc} \approx 10^7$ yr. If this power is effectively to be provided by SN remnants, then, given the rate of SN explosions (namely one per $t_{\rm SN} = 100$ yr), the number of such accelerators $N_{\rm acc}$ is

$$N_{\rm acc} = \frac{\tau_{\rm esc}}{t_{\rm SN}} \approx 10^5\ .$$

The power $p_{{\rm CR}\to\gamma}$ emitted as CRs by one individual explosion is

$$p_{{\rm CR}\to\gamma} = \frac{P_{{\rm CR}\to\gamma}}{N_{\rm acc}} \simeq 3\times 10^{34}\ {\rm erg\ s^{-1}}\ .$$

To obtain a γ-ray luminosity from this estimate we need to guess what is the efficiency $\epsilon_{\mathrm{CR}\to\gamma}$ in the energy transfer from CR particles to secondaries by *pp* interactions, since this is the main channel to produce π^0, because of the fact that the density of gas in ISM is much higher than the photon field one. A reasonable guess for this unknown fraction could be $\epsilon_{\mathrm{CR}\to\gamma} = 0.1$, so finally the power emitted by one source in the form of γ-rays is

$$L_\gamma = \frac{1}{3}\,\epsilon_{\mathrm{CR}\to\gamma} \times p_{\mathrm{CR}\to\gamma} \simeq 1 \times 10^{33}\,\mathrm{erg\,s^{-1}}\,,$$

and the factor 1/3 comes from the fact that $pp \to \pi^\pm$, π^0,so only that fraction of secondary particles in the hadronic shower are actually neutral mesons. If we consider a SNR at distance $D = 1\,\mathrm{kpc} = 3 \times 10^{21}$ cm, the flux of energy arriving on Earth as γ-rays is

$$\frac{L_\gamma}{4\pi D^2} \simeq 0.9 \times 10^{-11}\,\mathrm{erg\,s^{-1}\,cm^{-2}}\,.$$

Since, for a Fermi-like mechanism at sources, we expect an energy spectrum of the E^{-2}-type, and in the hadronic mechanism of γ-ray production the energy spectrum of secondary particles reasonably follows that of the parent CRs[1], we shall identify the arriving number of γ-rays at Earth with the integrated energy density $E_\gamma^2 \mathrm{d}N_\gamma/\mathrm{d}E_\gamma$ for our hypothetic source. Therefore, our estimated spectral energy distribution for a galactic SNR is

$$J(E_\gamma) = E_\gamma^2\,\frac{\mathrm{d}N_\gamma}{\mathrm{d}E_\gamma} = \frac{L_\gamma}{4\pi D^2} = 1.4 \times 10^{-11}\,\mathrm{TeV\,s^{-1}\,cm^{-2}}\,,$$

where we have used the fact that 1 erg = 1.6 TeV.
The tunable parameters in this simple estimate are indeed $\epsilon_{\mathrm{CR}\to\gamma}$ and ρ_{CR}, since we have assumed them, and they will make the difference in the description of different enviroments, being dependent on the density of the target. We have already cited the code GALPROP, providing detailed models of distributions of gas densities throughout our galaxy.

We can conclude by saying that the number of such accelerators in the Galaxy that can be detected is not large. As SNRs can efficiently accelerate CRs for 10^3 years at most, namely in their earliest phases in which the shock front speed is sufficient, the γ-rays are produced within a limited time interval. Taking into account the frequency $1/t_{\mathrm{SN}}$, there could be an order of tens of SNRs able to produce γ-rays in the whole Galaxy detectable in our epoch.

5.1.3 The Leptonic Model

The discovery of a convincing case of a hadronic accelerator through the identification of γ-rays produced by π^0 decays is extremely difficult due to the additional γ-ray production mechanisms by leptons, in the framework of what we call *leptonic model*. In such an alternative scenario photons are produced by several mechanisms, all involving electrons, which are easily accelerated in the presence of astrophysical magnetic fields, and are expected to assume a continuous distribution of energies.

a) **Inverse Compton Scattering**, in which ultra-relativistic electrons scatter low energy photons so that the photons gain energy at the expense of the kinetic energy of the electrons. This is the mechanism responsible for the production of *high energy photons*, and is important in regions where accelerated electrons coexist with a high energy density of soft photons.

b) **Synchrotron radiation**, which provides the enrichment of astrophysical enviroments with *low energy photons*, which can be useful to enhance the Inverse Compton (IC)

---

[1] This is the result of a famous argument which is called *Feynman scaling*.

process. In the enviroments of SNR we have strong magnetic fields, approximately a factor of 10 higher than the mean galactic one. Indeed synchrotron radiation is experimentally very important, providing low energy photons from radio up to even X-rays (from the hot outer shell of SNR).

This model accounting for IC and Synchrotron radiation as a pool of low energy photons is called ***Synchrotron Self Compton*** (SSC): an increase in the IC also increases the number density of target photons, in a kind of equilibrium. Within this equilibrium, we can assume that the ratio between the rates of energy loss of an UR electron by synchrotron and inverse Compton radiation is constant:

$$\frac{(\mathrm{d}E/\mathrm{d}t)_{\mathrm{IC}}}{(\mathrm{d}E/\mathrm{d}t)_{\mathrm{syn}}} = \mathrm{cost}\ .$$

In Fig.(5.3) one can see the typical shape of a SED expected from high-energy electrons moving in a magnetic field. The resulting SED has the two following structures:

1) The first is produced by the synchrotron emission, producing a very characteristic shape, which presents two cuts. The first is in correspondence of the self-absorption frequency, the so called *Synchrotron Self Absorption* (SSC), defining the transition from a source optically thick or thin for the radiation. The drop at large frequencies is due to some cut-off in the energy distribution of parent electrons instead.
2) The second structure is due to the IC scattering of the same electrons with the produced radiation field. Actually, if those high energy photons are produced uniquely by synchrotron radiation target photons, we talk about SSC, but there can be also external photons fields (and in this case we talk about **external compton**), such as CMB or from accretion processes in nearby astrophysical sources (very popular in extra galactic enviroments). In the case of consistent external compton of course this feature shall be extended towards higher energies, while on the other hand in SSC this profile exhibits the same behavior as the SED induced by synchrotron radiation, damped by some factor. At high energies, where no high-energy synchrotron photons are present, the spectrum is dumped.

In Fig.(5.3) the hadronic model for π^0 decay is also shown, and indeed what can be expected to be detected in reality is a mixture of features from both leptonic and hadronic models.

What we are most likely to observe is the *low energy feature* of synchrotron radiation. This can be due to either a beam of accelerated electrons or all the secondaries associated with proton interactions. As an example, whenever we have $\pi^0 \rightarrow 2\gamma$ in the optically thick regime (which is the case for extragalactic objects like BHs), the two photons will give rise to electromagnetic cascades in the ambient medium, and thus to a certain number of electrons and positrons able to produce synchrotron radiation.

Thus the low energy feature is indeed common in both leptonic and hadronic scenarios, and what actually makes the difference in distinguishing them should then be the *high energy feature*, which in a purely hadronic scenario can be explained by

i) π^0 decay;
ii) Bethe-Heitler $p + \gamma \rightarrow p + e^+ + e^-$, giving rise to X-ray;
iii) Synchrotron radiation by p, $\mu^\pm$ produced by decay of mesons.

From the experimental point of view it is thus very difficult to discriminate the two different scenarios relying just on these electromagnetic informations, and the search for evidence of pion bump decay in SNR becomes extremely important. By now we have only two cases in which this feature was confidently detected.

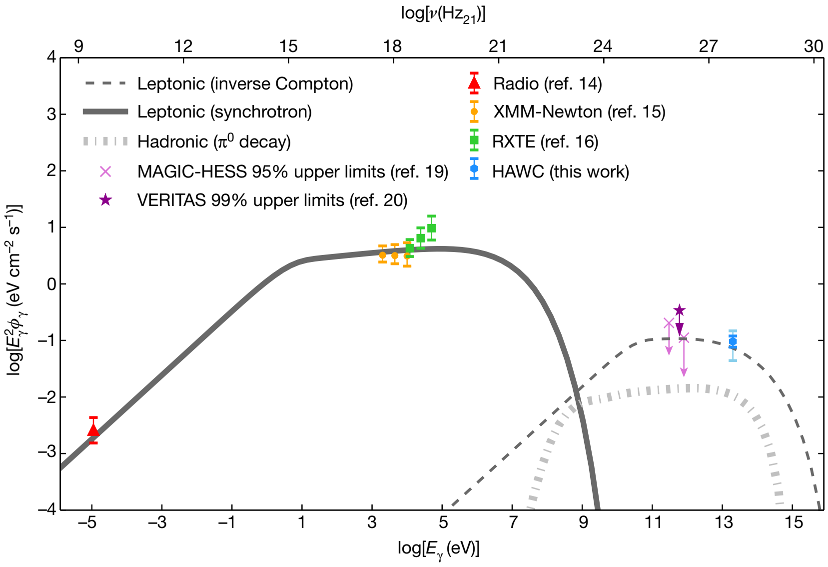

Figure 5.3: Broadband spectral energy distribution of the eastern emission region. The data include radio, soft X-ray, hard X-ray. The multiwavelength spectrum produced by electrons assumes a single electron population following a power-law spectrum with an exponential cutoff. The electrons produce radio to X-ray photons through synchrotron emission in a magnetic field (thick solid line) and teraelectronvolt γ-rays through inverse Compton scattering of the CMB (thin dashed line). The dash-dotted line represents the radiation produced by protons, assuming that 10% of the jet kinetic energy converts into protons. Figure lifted from `https://www.researchgate.net/publication/328049887_Very-high-energy_particle_acceleration_powered_by_the_jets_of_the_microquasar_SS_433`.

5.1.3.1 The Synchrotron Radiation feature

The shape of this SED depends actually on many aspects, since we have a lot of free parameters: the height and the position of the structures change very much depending on the specific properties of the astrophysical enviroments. Let us concentrate on the synchrotron radiation low energy feature. We know that the energy spectra of cosmic ray electrons can be approximated by power-law distributions, and we shall assume such a distribution of electron energies

$$\frac{\mathrm{d}N}{\mathrm{d}E} = K\, E^{-\alpha_e}\ .$$

It turns out that the spectral energy distribution $J(\nu)$ due to synchrotron radiation, in a given magnetic field B, by these electrons is such that

$$J(\nu) = (\text{constant})\, K\, B^{(\alpha_e+1)/2}\, \nu^{-(\alpha_e-1)/2}\ ,$$

and we can recognize that the frequency dependence reflects the spectral index of the primary electrons. We can also see that indeed this has a very typical power-law spectrum, which was highlighted in the Fig.(5.3).

The dependence on B and ν is clear: by increasing B, the synchrotron feature increases too, decreasing with decreasing energy of primary electrons though. This shall also reflect changes in the IC feature, since the two are strongly correlated: with an intense magnetic fiels we should obtain less IC, since intuitively the electrons will lose a lot of energy via synchrotron and they will be less energetic as a pool for IC. And, of course, less IC is expected also for lower primary energies of electrons.

Summarizing, if we have multiwavelenght measurements we can then provide also strong constraints on the intensity of the magnetic field and the properties of the parent electrons.

Of course we need these measurements to be even simultaneous, to avoid to compare differences due to temporal variations of enviroments.

If one even wants to introduce protons in the framework of hadronic models to study the differences in the SED, the situation becomes much more complicated, as other free parameters rise up. An example is the Lorentz boost factor, which is important in characterizing the UR family of electrons in extragalactic objects (jets in AGN). More precisely, the free parameters in toto result to be 8 or more. This is actually a very active atroparticle physics field, both from experimental and theoretical point of view.

5.1.4 The Extragalactic sources for UHECRs

We are finally able to address the issue we have anticipated in Sec.(4.5.6), namely the quest on CRs sources, from a Multimessenger point of view.
From the *galactic point of view*, we said that SNR are the most rated accelerators, being able to provide a maximum energy $E_{\max} \approx 300$ Z TeV (but more refined calculation expect even lower maximum). Anyway the question was still open on whether they are actually the wanted acceleration sites, and from the analysis of the pion decay feature, which was indeed recognized in two SNR, we are now in the position to confirm that they are our wanted sites. The pion bump is however an indirect evidence, which has to do with the modeling of the very complicated SED, so to some degree we are still deepening the issue in the current state of art. The other two open questions are the following:

1) What is the maximum energy of CRs? Experimentally we do observe photons emitted by SNR, possibly by IC, with $E^{\gamma}_{\max} \approx 10$ TeV, and the correspondent energy in protons is still an issue.
2) Can PeV energies be reached in SNR in CRs? Models cannot actually explain the PeV energies, which corresponds to the region of the knee, where the extragalactic sources are believed to come into the game.

So let us now turn into the quest for *extragalactic sources* of UHECRs. The maximum obtainable energy, for a particle in a magnetic field B and scale L, can be estimated with a simple argument, which can be applied to any enviroment, since it accounts only for Faraday's law. In fact, magnetic fields are almost omnipresent in astrophysical objects, and their space/time variations imply the existence of transient electric fields such that

$$\vec{\nabla} \times \vec{E} = -\frac{1}{c}\frac{\partial \vec{B}}{\partial t} ,$$

supplying a consequent amount of energy to charged particles. If U is the speed of the shock, this equation can be rewritten to order of magnitude as

$$\frac{E}{L} \sim \frac{B}{L/U} \qquad \Leftrightarrow \qquad E \approx BU ,$$

so the energy of a particle of charge ze accelerated by the induced electric field is then

$$E_{\max} \simeq \int ze\, E\, \mathrm{d}x \sim ze\, BU\, L .$$

Hence, to order of magnitude, for the parameters adopted for young supernova remnants, $B = 10^{-4}$ T, $U = 10^4\ \mathrm{km\,s^{-1}}$ and $t \simeq 10^3$ yr, we recover roughly $E_{\max} \approx 10^{14}$ eV, which confirms what we have found for SNR.

This argument can be expanded for other acceleration sites and sources, with a fundamental condition to be fulfilled: the size L shall be at least of the order of the Larmor radius r_L (Eq.(2.14)), otherwise confinement is not possible. This translates in a link between the necessary magnetic field, dimension of the site and energy of the accelerated particle, namely the acceleration should occur with a necessary combination of scale L and magnetic field B: if the scale is small, the magnetic field must be huge, and vice versa. More precisely, we can write

$$\frac{E}{1\,\text{EeV}} \simeq \beta\,\text{z}\left(\frac{B}{\mu\text{G}}\right)\left(\frac{L}{1\,\text{kpc}}\right) \qquad \text{with} \qquad \beta = U/c\,,$$

and this is often called the **Hillas criterion**, taking the name from the scientist which gave name also to the plot in Fig.(5.4). Such a diagram allows to identify the possible accelerators which can reach 10^{20} eV, based on the Hillas criterion alone, neglecting in fact energy losses and assuming $\beta \simeq 1$. More refined models shall surely take into account these aspects too. You can see that candidate sources are definitely the most extreme astrophysical enviroments (GRBs or jets), while galactic enviroments such as SNRs are very unlikely to be able to reach the maximum energy.

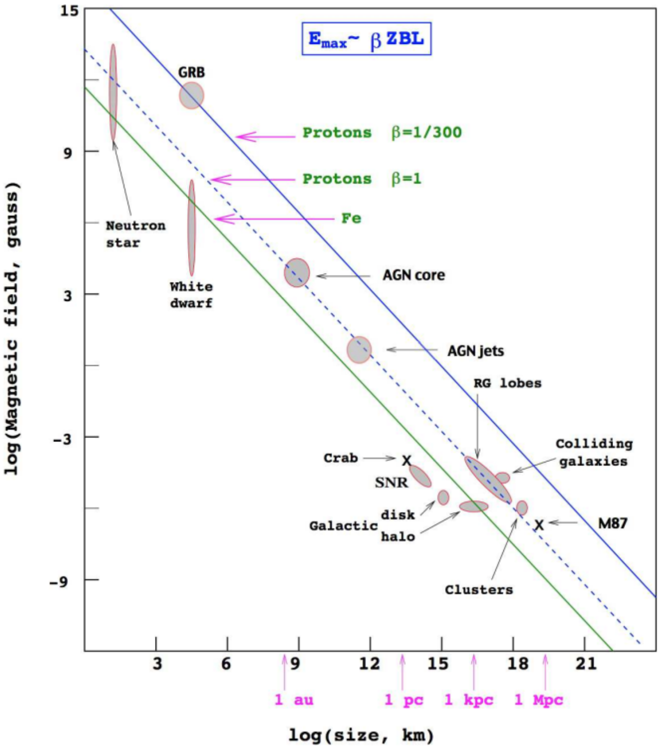

Figure 5.4: Hillas plot for candidate acceleration sites, relating their size and magnetic field strength. To accelerate a given particle species above 100 EeV=10^{2}0 eV objects must lie above the corresponding lines. Taken from `https://www.researchgate.net/publication/50229839_Ultrahigh_Energy_Cosmic_Rays`.

NB on Neutron Stars Neutron Stars are expected to be the leftover of explosions of stars with moderate mass, and because of conservation of angular momentum and magnetic flux during the collapse, such objects reach very intense magnetic fields. They are in equilibrium since the degeneracy neutron pressure balances the gravitational self attraction. Pulsars (see Fig.(5.5—Left)) are a particular type of neutron stars, which are fastly rotating and produce a lighthouse effect that is quite easy for us to detect. The relativistic "jets" emitted at opposite poles are explained by a still to be developed qualitative picture, which is connected to the existence of a rotating magnetic dipole, inclined with a given angle with respect to the rotation axis. The very fast rotation is essentially due to conservation of angular momentum, and the strong magnetic fields make them a suitable candidate as CRs acceleration sites, at least up to the knee or even beyond. We can often see them within SNR nebulas, a famous example being the Crab Pulsar which is shown in Fig.(5.5—Right).

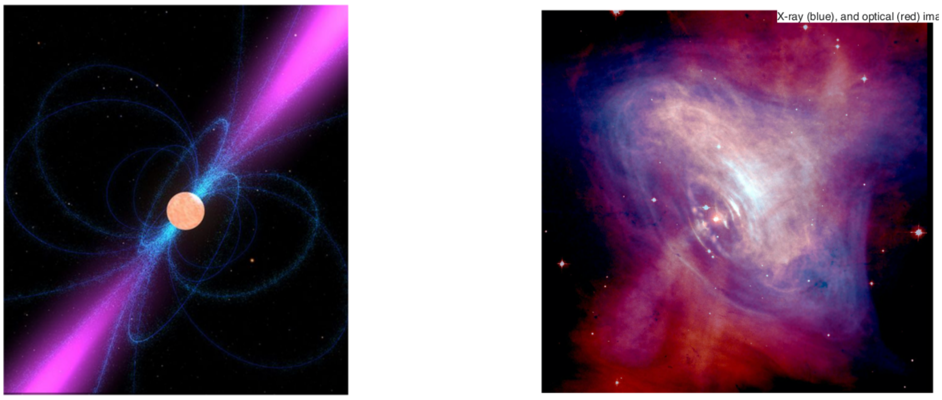

Figure 5.5: Left: A pictorial view of a pulsar, with the lighthouse effect in rotation with respect to a principal axis. Right: Crab nebula, namely the remnant of the SN SN1054, with the visible structure of the omonymous pulsar within.

5.1.5 The High Energy Photons (HE)

By now, the highest energy photon which have been detected have energy around $E_\gamma = 100$ TeV. A distinction between energy ranges of photons is usually employed, and accounts for three cathegories:

1) $E_\gamma \geq 0.5$ MeV is the regime of proper γ-rays;
2) $E_\gamma \geq 100$ MeV is the regime of high energy (HE) photons;
3) $E_\gamma \geq 100$ GeV is the regime of very high energy (VHE) photons.

For each of them the detection techniques are of course different, since photons from these cathegories will have very different ways of interacting with matter, and the study of these relies on the multiwavelenght astrophysical studies, as well as multimessenger approaches (with the study of neutrinos, CRs and GWs toghether). We will also discover that the γ-rays study is deeply linked with the search for physics beyond the Standard Model too, e.g. quest for dark matter or phenomena like invariance violation, oscillations of photons into axions, ecc. Finally, the most alive and critical question mark which is linked to this study is of course the quest for CRs sources, as we have already mentioned several times.
In this section we will talk about the first two cathegories, while the last one will be the object of the following section Sec.(5.1.6).

Let us start by considering that high energy $e^\pm$ are to be connected with powerful accelerators, namely astrophysical objects, and their radiation shall be (for the vast majority) **non thermal**, that is due to synchrotron or IC, since it is expected to be originated by an acceleration mechanism. We will focus on the HE domain, which is ideal to address the quest for CRs sources, since CRs are indeed expected to interact at these sources and give rise to such a radiation, as we saw in the leptonic and hadronic framework[2]. As we saw from the kinematics of π^0 decay, Ex.(5.1), the SED reaches a maximum at energies about $E^*_\pi = 67$ MeV, and this suggests us the reason why HE γ-ray astronomy focuses on $E_\gamma \geq 100$ MeV to search for CRs interaction signatures directly. This is also enforced by the fact that all

---

[2] Of course the whole electromagnetic spectrum is important, but our focus will be on HE.

our Universe is satisfactorily transparent to those photons, which means we have a chance to collect a lot of informations even if we are essentially neglecting all the other parts of the spectrum.

We want now to perform a rush through the history of experimental setups and results in HE γ-ray astronomy, following also a fundamental intuition, given by the already cited Feynman scaling: if the spectrum of photons is always resembling that of the parents (protons or leptons), then we shall expect similar properties too, such as a power-law flux, which at $E_\gamma \simeq$ MeV is still strong enough to be assessed with *direct measurements*, by small sized satellites out of the atmosphere. This is exactly what happened starting from the '60. The following lists fundamental steps in the γ-ray astronomy before the advent of FermiLAT:

i) *Orbiting Solar Observatory III*: the start of γ-ray astronomy was marked by OSOIII, an american satellite launched in 1967, which found γ-rays with $E_\gamma \geq 50$ MeV from all directions in the sky, a great success;

ii) *Small Astronomy Satellite*: SAS confirmed the result from OSOIII, and also found evidences for an isotropic, possibly extragalactic, component, with different properties (direction and energy) than the diffused γ-ray emission of our galaxy;

iii) *Celestial Observation Satellite-B*: at the end of the '70 COS-B was launched, discovering the first extragalactic source named 3C273, which was a Quasar. This result suggested that diffused γ-ray emission could be due to unresolved many different sources, namely the instrument was not sensitive enough to resolve single sources, e.g. Seyfert Galaxies, Blazars and Quasars.

iv) *Energetic Gamma Ray Telescope*: EGRET was a fundamental breakthrough with respect to its predecessors, since it was built to provide a larger statistics, cover huge portions of the sky and better resolution. The energy sensitivity range was about $20\,\text{MeV} < E_\gamma < 30\,\text{GeV}$, with an instrument granting 1 odg greater sensitivity with respect to before. In this energy range photons interact mainly via pair production, so a **pair converter instrument** was needed, with a tracking device (to rebuild the trajectory) and a calorimeter (to measure the energy) too. The concept of EGRET is shown in Fig.(5.6). We shall remember that this experiment was carried by a satellite, so it was not meant to deal with EAS, however a satellite orbiting around the Earth will collect CRs too, and a veto was needed to separate these signals, which in this case are the background to the wanted ones. Finally also the ToF of the pair could be measured by EGRET with great details. These general characteristics indeed resemble what we have described in Sec.(4.3.1) for a toy detector for CRs.
Fig.(5.7) shows the wonderful results of the experiment, which were summarized in the *third EGRET catalogue*, containing all point sources in γ-rays, for a total of 271 objects. A characteristic of the γ-ray sky is that it is highly variable, therefore not all sources were seen at all times. The summarized conclusions were the following:

  - *Extragalactic*: nearly all point sources of γ-rays were BLAZARs, which can be seen up to redshift z=2; nor Seyfert or SBGs were identified; only two examples of radio galaxies were found, M87 and Centaurus A; a lot of diffused radiation was recorded, which is a clear sign of γ-ray radiation different from the MW galaxy's one.

  - *Galactic*: Pulsars, pulsar wind nebulas, SN remnants and binary systems were catalogued as possible point sources. See below for an explanation of these objects. Of course, as regards SNs, the condition of the presence of one of such powerful accelerator is not sufficient to grant the γ-ray production, in fact CRs in this case

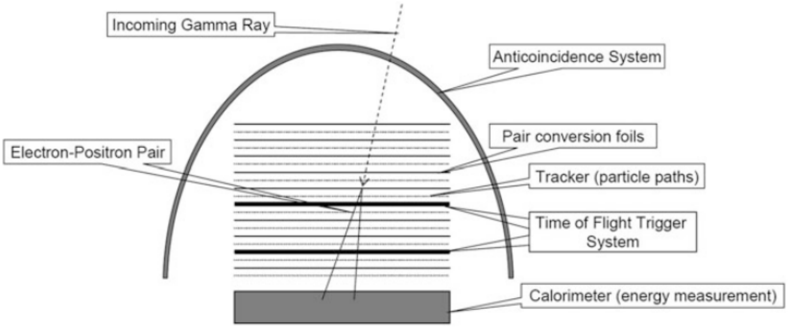

Figure 5.6: Schematic diagram of a telescope which use the conversion of a γ-ray into a $e^{\pm}$ pair (pair-conversion telescope), reproducing the features of the EGRET experiment. The pair conversion was performed by 28 thin sheets of high-Z material, in order to increase the cross section, called foils. Then the direction of $e^{\pm}$ pairs had to be reconstructed too, because it provides informations about the direction of the primary γ-ray: the tracking device consisted of 36 wire grid **spark chambers**, which is a gas based detector deeply used in these first phases of astroparticle history. However, gas based detectors in space has the fundamental limitation that they needed to be continuously refilled due to inevitable losses. The calorimeter at the end of the path plays the role of the destructive instrument, and it was made by 36 NaI crystals read out by 16 PMTs, since the pair was expected to produce an electromagnetic shower in it. The ToF measurement was finally provided by the triggering of two scintillator detectors (which are fast!). The Fermi-LAT is similar, with an improved tracker device which avoids the use of a Time of Flight trigger system.

are certainly accelerated but γ-rays are not necessarily seen too. To be able to see them, a target material is needed, such as dense gas clouds, where the interactions can take place and produce γs.

Active Galactic Nuclei (AGN)

All the cited possibly unresolved sources go under the general terminology of Active Galactic Nuclei (AGNs), and we are going to clarify some classifications of these objects, though this topic is composite and much more extended. Of course, for this characterization, we are going to exploit multiwavelenght, rather than only γ-rays, informations. First of all, we have already hinted at the fact that AGNs are connected by SMBHs, but it's important to realize that not all galaxies hosting a SMBH are active, our Milky Way being a clear example[a].

An AGN is an object containing a *SMBH*, an *accretion disk* around it and two *relativistic jets* propagating orthogonally to the disk' plane, see Fig.(5.8) for an esplicative picture. The way an AGN looks like to us will depend of course on the orientation of the accretion disk with respect to the observer, and this will actually influence also the evidence for two or just one relativistic jet.

a) The ***accretion disk*** is due to diffused material in orbital, quasi keplerian, motion around the BH. It emits X-rays and UV thermal radiation. The accretion mechanism is now a well known energy production process, since the infalling material convert huge amounts of gravitational energy to thermal. Because of conservation of angular momentum, the possibilty to orbit in the disk geometry is realized, and the quasi-circular motion in smaller and smaller orbits is given by the viscous forces in the fluid. The vast majority of the expected luminosity from these objects is coming from the innermost parts of the accretion disk,

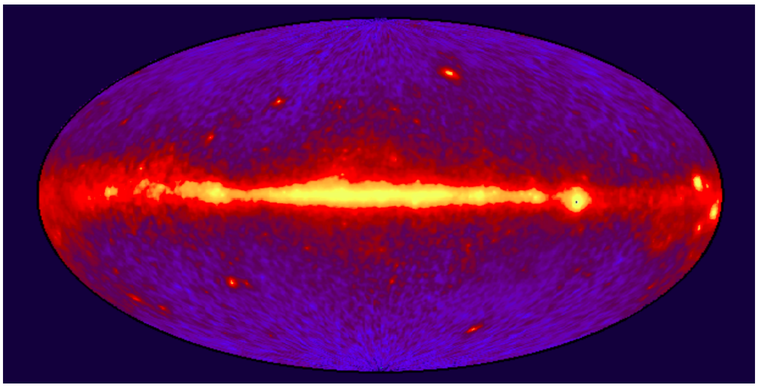

Figure 5.7: Full sky map produced by EGRET's survey above 100 MeV in galactic coordinates, throughout all the experiment's exposure time. A lot of diffused radiation is associated with CRs propagation in the galaxy, that is a lot of π^0 decay's signature. Of course a point source is identified as an excess of photon counts above the diffused emission. Also some extragalactic objects can be seen, to be identified with multiwavelenght observations (indeed different mechanisms are representative of different regions of the spectrum, and e.g. synchrotron radiation can be hardly seen in γ-rays but is usually observed in the radio). Many of the bright sources away from the galactic plane are blazars, while in the galactic plane, the brightest sources were identified as pulsars.

where gas is extremely hot.

b) An opaque ***torus*** is also present, made by gas and dust, namely graphite or carbonaceous grains. The torus surrounds the central part, absorbing and re-emitting radiation at lower frequencies, namely converting UV and X-rays to IR and optical light.

c) The two ***relativistic jets*** project themselves up to several hundreds of kpc away from the nucleus. A lot of question marks are still open about these jets. The more rated opinion is that they are related to streams of relativistic particles, but of course their relation to the accreted material is unknown, and finally also their own production mechanism is still an intriguing issue. Qualitatively, it is thought that, due to the extreme hotness of the innermost orbiting gas, infalling material starts to evaporate, being conveyed by radiation pressure to enrich jets, following the strong magnetic fields' lines. Ionized material in this region is also responsible for variable magnetic fields, accelerating, in the end, to relativistic velocities such materials.

Let us point out also what are the main differences between an ordinary galaxy and an active one.

- The *luminosity* is mostly provided by the innermost part of the accretion disk, while in ordinary galaxies this is not true, and it is coming from stars;
- The *electromagnetic emission* peaks in the radio, while for normal galaxies the maximum is at the optical region;
- The *light distribution* is very concentrated in a single luminous point, i.e. the nucleus, while an inactive galaxy provides diffused stellar light emission.

Active galaxies can be then distinguished by some characteristic properties:

i) **QUASARs**: the name stands for Quasi Stellar objects, which are very luminous with $1\,\mathrm{L_{MW}} < L < 10^5\,\mathrm{L_{MW}}$, tending also to be far away.

ii) **BLAZARs**: they are connected with elliptical galaxies, and their peculiarity is a very bright nucleus. They can have very significant brightness over less than a day timescales.

iii) **Seyfert Galaxies**: those are spiral galaxies, with a very bright nucleus too, with lower luminosities usually, $0.1\,\mathrm{L_{MW}} < L < 10\,\mathrm{L_{MW}}$. Their typical variability is around a month.

iv) **Radio Galaxies**: those are elliptical galaxies with very distinctive and extended jets, emitting synchrotron radiation which manifests strongly in radio. Their luminosity is about $0.1\,\mathrm{L_{MW}} < L < 10\,\mathrm{L_{MW}}$.

Some examples with different filters are shown in Fig.(5.9), Fig.(5.10) and Fig.(5.11).

The different images give also an idea on the appearance of these objects with respect to the observer, in particular in Fig.(5.11) the AGN is seen from aside, but this is not always the case. Let us account for the different orientations of the accretion disk in the following examples:

ex1. *Edge on accretion disk*: in this case the accretion disk is edge on with respect to the observer, and the hot innermost region is hidden from him since it is obscured by the torus. On the other hand the two jets can be clearly seen, and in some cases also the lobes are evident, see Fig.(5.11).

ex2. *Tilted accretion disk*: in this case the observer sees it at an angle, and it is possible to see both the BB radiation from the innermost regions and the synchrotron radiation from the jets. If the result is very luminous it is associated with a QUASAR, otherwise it is a radio galaxy. This suggests that there is a more refined classification of these objects, depending on the amount of energy produced.

ex3. *Face on accretion disk*: in this case one of the jets is pointing towards us, and the other one is hidden behind. Because of the Lorentz boost factor γ, we shall observe much increased luminosity and a faster variability[b], resulting into a BLAZAR.

---

[a] Our Sagittarius A* is indeed supermassive, with $M \simeq 10^6\,\mathrm{M_\odot}$.

[b] In general the variability is associated with instabilities of the accretion disk itself, but it is still a issue to be developed.

Pulsar Wind Nebula A Pulsar Wind Nebula are believed to be associated with young pulsars, born after a SN explosion. They usually create relativistic winds of particles which, in the very early stages of SN life, interact with the relatively dense ejected material. The outcome of this interaction is called Pulsar Wind Nebula, and an example is the Crab Nebula with the Crab pulsar in it, as already mentioned. It is also possible that, in some later stages, the SN remnant shells are not enough dense to provide sufficient target material to produce γ-rays.

Stellar binaries Binary systems are very often found in astrophysical environments. They are believed to be always a combination of a very compact object, either a stellar mass BH or a neutron star, and a massive companion star. Accretion occurs also around this lower scale compact object, providing a source for electromagnetic radiation (electrons) and probably also high energy hadrons, since accretion is a mechanism of particle acceleration through the very strong electromagnetic fields produced in the vicinity of the compact object. This can also be the scenario for the production of jets, and in this case we have a very similar structure to an AGN. These systems are called *Microquasars*, and so far we have identified

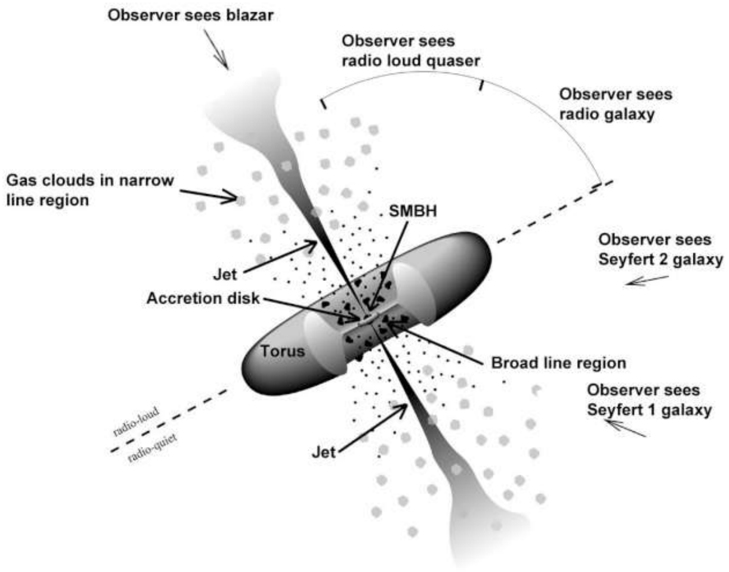

Figure 5.8: This is the quite popular picture illustrating the Unified Model for AGNs, clarifying some mentioned structures. Taken from `https://fermi.gsfc.nasa.gov/science/eteu/agn/`.

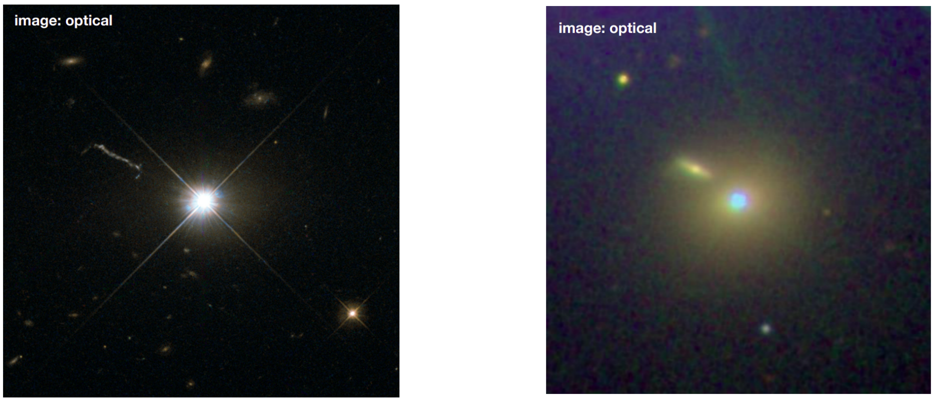

Figure 5.9: Left: A view of the first extragalactic object discovered γ-rays astronomy, the already cited 3C273, which is a quasar. The image is optical, and we can see the extremely bright nucleus. Right: A blazar, called Markarian 421. The hosting elliptical galaxy is fairly evident, and it is almost outshined by the bright nucleus.

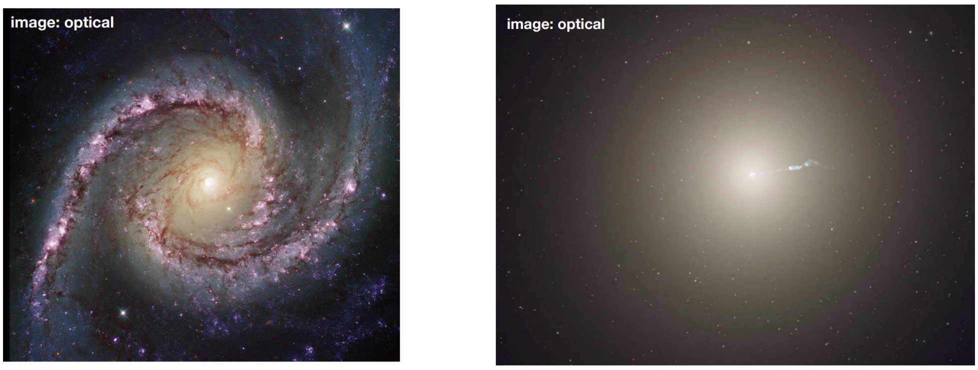

Figure 5.10: Left: A view of a Seyfert galaxy, more precisely NGC 1566, and the spiral arms are evident. In this case the nucleus does not outshine the total figure. Right: an example of a radio galaxy, M87, which in this case can be labeled as a *weak radio galaxy*, to be distinguished by the strong ones like Cygnus A. A glimpse of the jet can be catched too.

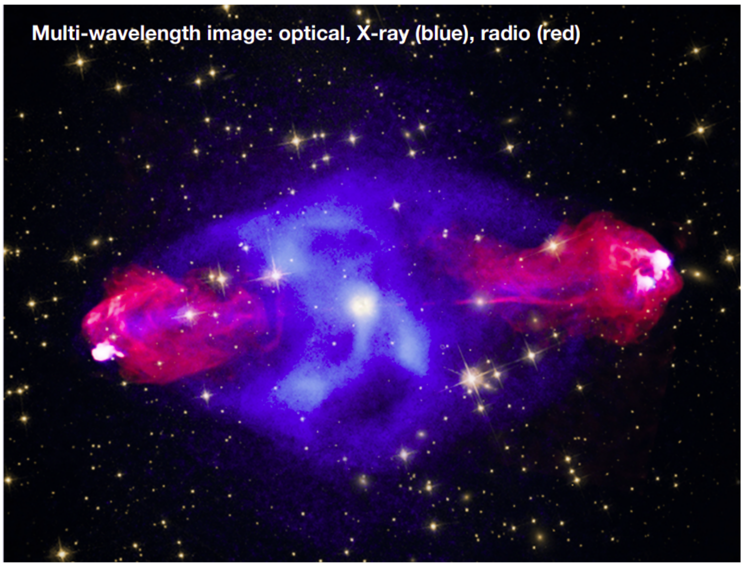

Figure 5.11: This is the famous example of Cygnus A, *a strong radio galaxy*. The image is a combination of optical, X-ray and radio filters, and the radio lobes can be also distinguished.

(as sources of γ-rays above 100 MeV) only two of such objects[3] these are galactic X-ray binary systems exhibiting relativistic radio jets observable in the radio band.

Gamma Ray Bursts (GRBs) Gamma ray bursts are another very important possible extragalactic acceleration site, as we have already mentioned several times. GRBs are extremely intense and fast shots of gamma radiation. They last from fractions of a second to a few seconds, often followed by "afterglows" orders of magnitude less energetic than the primary emission. They are believed to be mostly hard X-ray phenomena, however we have observed few examples of bursts with $E \simeq \mathcal{O}(100\,\text{GeV})$. They can be classified into

- *Short GRBs*, lasting typically $\Delta t < 2$ s and $< \Delta t > \approx 0.3$ s. They have been associated to the coalescence of pairs of massive objects, NS-NS or NS-BH. The system loses energy due to gravitational radiation, and thus spirals closer and closer until tidal forces disintegrate it providing an enormous quantity of energy before the merger. This class were poorly known till few years ago, it has been recently proved by the simultaneous observation of gravitational waves and gamma rays in a NS-NS merger, a great success of the Multimessenger approach.
- *Long GRBs*, lasting typically $\Delta t > 2$ s up to 10 s. This class is believed to be associated to a supernova from a very high mass progenitor, a "hypernova". The connection between large mass supernovae (from the explosion of hypergiants, stars with $M = 100$-$300\,\mathrm{M}_\odot$) and long GRBs is proven by the observation of events coincident both in time and space.

5.1.6 The Very High Energy Photons (VHE)

We are now going to describe the last cathegory of γ-rays, called Very High Energy Photons (VHE), which is the range covered by the cited FermiLAT.

The reason why we want to address such a region in the electromagnetic spectrum is the following: within these energies we might find alternative (to π^0 decay) fingerprints of interactions of hadrons. In fact at $E > 100$ TeV the contribution from leptonic processes to γ-rays is expected to be very small, because of the following reasons:

---

[3] They are called LS I+61 303 and LS 5039.

i) Sychrotron losses typically prevents the acceleration of electrons to energies beyond $E > 100$ TeV, and this is a fact that we can confirm also in accelerators.

ii) Inverse Compton, at those energies, is expected to have a much smaller cross section than at lower energies. We are in the so called Klein-Nishina regime in this case.

Let us first review the most important experimental results from the last and most advanced step of γ-ray astronomy history.

5.1.6.1 The Fermi Mission

In the previous section Sec.(5.1.5) we have depicted the fundamental steps of the γ-ray astronomy before FermiLAT. Let us now finally talk about the real star of the show. We have already encountered the Fermi Large Area Telescope (LAT) when we described its spectacular skymap published in occasion of 5th year anniversary of the FERMI mission, in Sec.(4.5.6). Now we want to understand better the concept of this revolutionary mission.

Fermi reflected the need to furtherly improve the performances (sensitivity, statistics, angular resolution) of EGRET by using refined techniques within essentially the same concept. It is a satellite hosting two types of detectors: **LAT**, a superior advancement of EGRET able to detect from 20 MeV to $E_\gamma > 300\,\mathrm{GeV}$, and the **Gamma Ray Burst Monitor (GBM)**, sensitive to X and γ-rays with energies $8\,\mathrm{keV} < E_\gamma < 30\,\mathrm{MeV}$. FermiLAT has the dimensions of $1.8 \times 1.8 \times 0.72\,\mathrm{m}^3$, and the concept of EGRET is significantly refined. The LAT is again a pair-conversion telescope with a precision tracker section followed by a calorimeter, see Fig.(5.12) for a pictorial scheme. By looking again at the Fermi full sky map in Fig.(4.39), one can see the effects of having much more resolution and improved statistics. Individual sources were in fact identified more efficiently, thanks to the dedicated monitor allowing to scan the location and the time of occurrence of GRBs events. Also a wealth of informa-

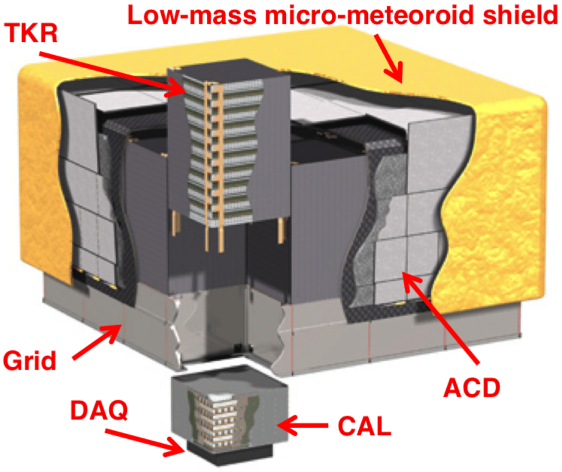

Figure 5.12: The LAT scheme. The upper part is the tracker, the lower part the calorimeter and the surrounding region (in yellow) the veto to CRs. The tracking section of the LAT has 36 layers of silicon strip detectors to record the tracks of charged particles. Unlike EGRET, the LAT basically triggers on all the charged particles crossing the active volume, with no built-in hardware trigger for photon selection that can induce inefficiencies. This drastic change is due to the use of silicon detectors, which allow for precise tracking with essentially no detector-induced dead-time, and are designed to last much longer than gas-based detectors. They allow to get rid entirely of ToF system. Beneath the tracker is a calorimeter comprising an 8-layer array of CsI (cesium-iodine) crystals to determine the pair energy. The effective collecting area is $\sim 6500\,\mathrm{cm}^2$ at 1 GeV with a very wide field-of-view (~ 2 sr), much wider than EGRET.

tions concerning the physics of BLAZARs was provided, and finally the Fermi mission was the protagonist of the two famous multimessenger detections of GRB 170817A (GWs and γ-rays) and TXS 05606+056 (neutrinos and γ-rays). As regards the quest for the π^0 decay signature in SN remnants, Fermi discovered the already cited two famous examples, IC 443 and W44, and the latter is reported in Fig.(5.2). The diffused radiation permeating the MW and reflecting the matter distribution in the galaxy was again scanned and recorded: CRs interactions' targets in fact are essentially dense gas clouds, present all over the universe. A predicted neutrino flux emerged too, reflecting the products of charged mesons' decays, see Fig.(5.13).

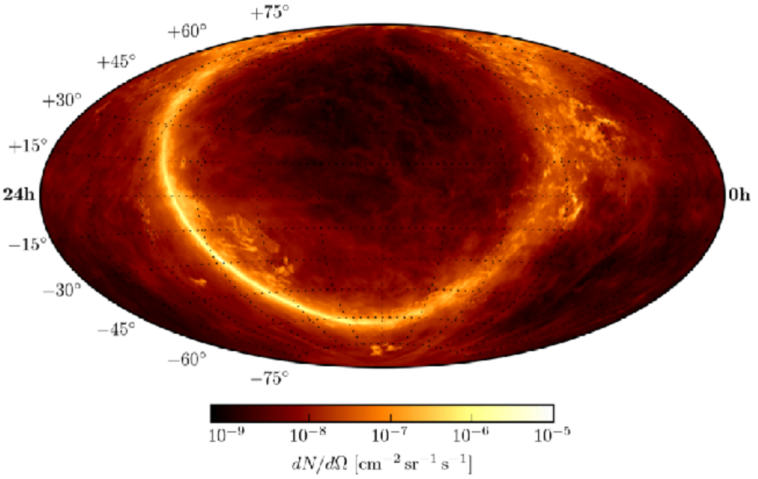

Figure 5.13: Neutrino flux per unit of solid angle, shown as a function of direction in equatorial coordinates. This flux can be associated to the photons detected by Fermi. Taken from `https://www.researchgate.net/publication/329083374_Joint_Constraints_on_Galactic_Diffuse_Neutrino_Emission_from_the_ANTARES_and_IceCube_Neutrino_Telescopes/figures?lo=1`.

The specific scientific results from Fermi are very broad and a complete overview is quite impossible. In Fig.(5.14) one can see an example of a multiwavelenght campaign to build the SED of Markarian 421, a famous blazar shown also in Fig.(5.9). It is characterized by the inevitable variability in time of the fluxes, and this is the reason why the ranges are that wide. The peak position, as well as its height, is expected to reveal informations about the electrons originating the synchrotron emission (which is indeed the responsible for this feature, as we have already said in Sec.(5.1.3)) and the intensity of the magnetic fields in the source. On the other hand, the high energy part can be attributed to either IC or γ-ray emission mechanism by hadronic interactions (see Sec.(5.1.2)), and the distinction between these two scenarios is the main goal for the quest for CRs sources. An example of modeling of the SED of Mrk421 is given in Fig.(5.15).

After ten years of observation, the Fermi mission released several *catalogues* of objects, with a total amount of 5100 individual sources with a larger than 5σ significance, which is a factor 20 higher than the previous EGRET collection. For each of those sources the catalogues provide localizations, fluxes and spectral properties, and for some of those it is also possible to have a multiwavelenght counterpart, thus to associate with certainty the sources of γ-rays. It is of course an easier task in the extragalactic enviroment, where the density of such objcets is much lower: 3100 objects are in fact identified.

Additionally, another very interesting result concerns the so called **Fermi bubbles**.They are two diffused regions of γ-ray emissions, with harder properties as compared to the typical

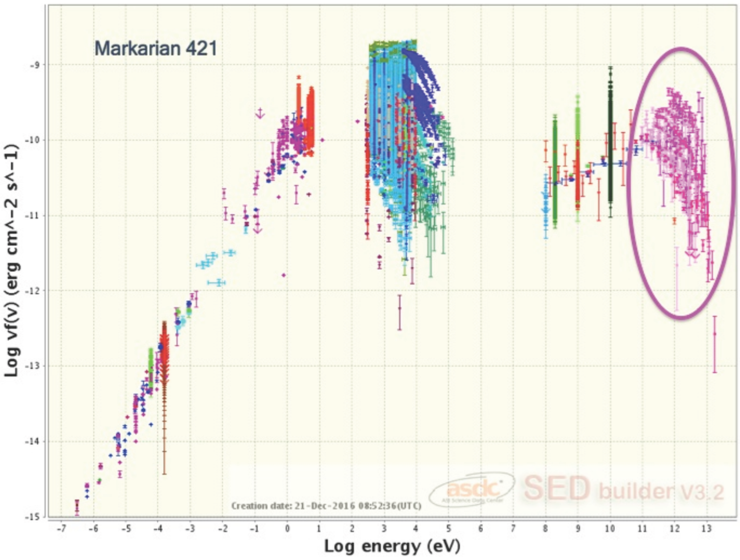

Figure 5.14: The multi-wavelength blazar spectral energy distribution (SED) of Mkn421. The marked VHE gamma-ray points are provided by the Brazilian Science Data Center (BSDC) database. The plot is made collecting data from a dozen catalogues spanning more than 30 years, collected by over 10 different instruments. Taken from `https://www.mdpi.com/2075-4434/5/4/90`.

emission in the rest of the galactic disk, see Fig.(5.16). The origin of these bubbles is still mysterious, but they are likely to be connected with the release of amounts of energy from SgA*. Possibly, the MW in the past went through the mechanism which enpowers jets in AGNs, and the bubbles can be the leftover of these jets, however this is quite qualitative.

5.1.6.2 The challenges in VHE astronomy

There were some obstacles to the establishing the field of VHE γ-ray astronomy, some of those dictated by physics itself and others by the scientific enviroments which was led by accelerators, and financial resources were indeed invested on that new and successful field primarily. Let us summarize the physical challenges:

1) The atmosphere is not transparent to γ-rays, so their detection implies observing the secondaries produced in EAS.

2) The Universe too is not trasparent to γ-rays, in fact photons with VHE will encounter diffused background radiation offering a target for CRs (as we have said talking about cosmogenic neutrinos in Sec.(4.5.6)) and γ-rays. The most important components are EBL and CMB, and we can expect that such processes can happen

$$\gamma + \gamma_\epsilon \to e^+ + e^- \ ,$$

with a probability depending on the cross section $\sigma_{E_\gamma,\epsilon}$ for pair production (Bethe-Heitler) and also on the distance our photons have to propagate through (notice that we have called γ_ϵ the generic target photon). In fact it is reasonable to expect that the longer the path traversed the higher shall be the probability of interaction. The cross section can be parametrized in terms of the energy of the source photon and of the target photon as

$$\sigma_{E_\gamma,\epsilon} \simeq 1.25 \times 10^{-25} \left(1 - \xi^2\right) \text{ cm}^2 \qquad \text{with} \qquad \xi \equiv \sqrt{1 - \frac{(m_e c^2)^2}{E_\gamma - \epsilon}} \ .$$

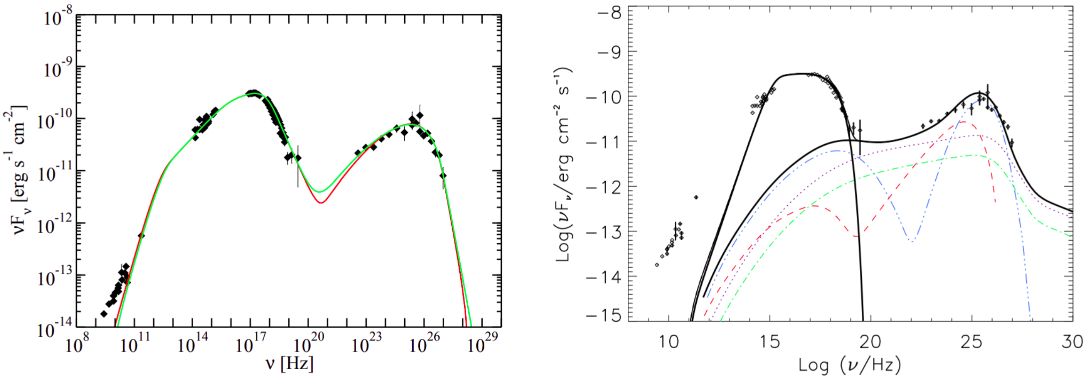

Figure 5.15: Left: SED of Mrk 421 with two Synchrotron Self Compton model fits obtained with different minimum variability timescales: t_{var} =1 day (red curve) and t_{var} =1 hour (green curve). Right: Hadronic model fit components: π^0 cascade cascade (black dotted line), $\pi^\pm$ cascade (green dashed-dotted line), μ-synchrotron and cascade (blue dashed-triple-dotted line), proton synchrotron and cascade (red dashed line). The black thick solid line is the sum of all emission components (which also includes the synchrotron emission of the primary electrons at optical/X-ray frequencies). Figures both from `https://arxiv.org/pdf/1106.1348.pdf`

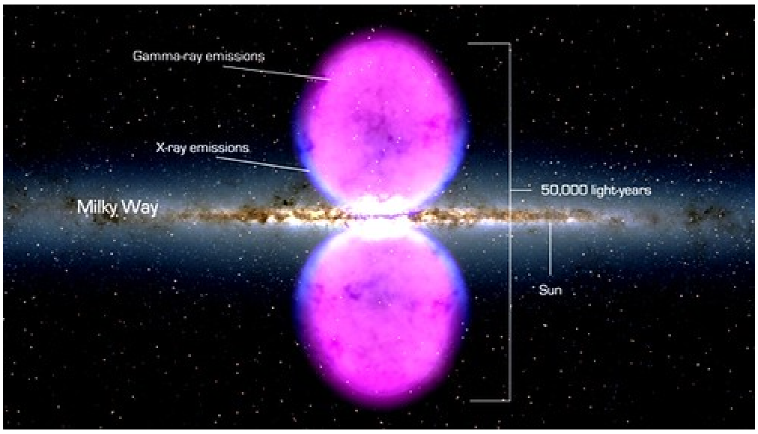

Figure 5.16: View of Fermi Bubbles, with the MW seen in the optical while the bubbles are in X-rays. From the official site `https://www.nasa.gov/mission_pages/GLAST/news/new-structure.html`.

This cross section $\sigma_{E_\gamma,\epsilon}$ is at maximum when

$$\epsilon = 2\,\frac{(m_e c^2)^2}{E_\gamma} \simeq \frac{520\ \text{GeV}}{E_\gamma}\ \text{eV}\,,$$

and the threshold for this process to happen is about a factor 2 lower than this value. If we take for example $E_\gamma = 400$ TeV, the maximum corresponds to a photon in the CMB frequency range, and varying E_γ one can reach values ranging from CMB to EBL ones.
However, while the CMB is very well characterized, the EBL is not, as we have already said. In particular its changes with redshift are very difficult to model, the reason being due to lots of foreground as well as galactic backgrounds which prevent us from measuring EBL in certain frequency regions. The models of EBL usually have to assume a certain energy density and a particular development of galaxies' evolution, more precisely $L(z)$ and $\rho(z)$, respectively luminosity and energy density as a function of redshift. Such model provides us the **optical depht** $\tau_{\gamma\gamma}(E_\gamma, z)$ for the interaction process as a function of the energy E_γ and redshift z, such that the intensity $I(E_\gamma, z)$

that we observe at Earth will be

$$I(E_\gamma, z) = I_0 \, \exp\{-\tau_{\gamma\gamma}(E_\gamma, z)\} \, ,$$

where I_0 is plainly the flux at the source. This an extremely important challenge, since the optical depht becomes relevant already at the energies of TeV, and this translates into the fact that TeV photons can reach Earth only if emitted by sufficiently nearby sources, the maximum distance γ-rays can travel being consequently limited.

5.1.6.3 The experimental techniques for VHE

We know that such photons have to be detected indirectly, after an interaction in the Earth atmosphere giving rise to an electromagnetic shower. There can be two different approaches:

a) *EAS arrays*: we can detect leftover particles at $\sim$ 10 km from sea level in the same way surface arrays for CRs work. This methos provides a snapshot of the shower in the moment in which it reaches ground.

b) *Cherenkov Detectors*: we exploit the production of Cherenkov photons as the shower develops to instrument mirrors able to collect these photons and project them into cameras. This method essentially uses the entire atmosphere as a calorimeter.

They are very different: while EAS arrays will be able to catch only the tail of the shower as it reaches ground, Cherenkov detectors will record photons produced by the shower during its all development, of course with the caveat that they must be pointing almost perfectly towards the primary. Let us also stress the fact that both these methodologies will *inevitably* collect data from CRs too, which actually are much more common than γ-rays. Let us list the fundamental differences:

- **Direction** EAS arrays will detect photons from all directions, while Cherenkov telescopes cannot, having a very small field of view (typically 3-5 degrees).
- **Operativity** EAS arrays could possibly operate 24h a day, while Cherenkov telescopes need special favorable conditions (see Sec.(4.4.2)).
- **Resolution** EAS arrays have poor angular and energy resolutions. In fact, the poor energy resolution is due to the fact that they record just the leftover of the shower, sometimes also very far away from the core and definitely very often far from the depht of the shower maximum, even if located in high mountains. On the other hand the angular resolution is not quite good since EAS arrays estimate the direction of the shower on the basis of the arrival of electrons (and leftover particles in general) at Earth, which have usually very low momentum and for which scatterings are important. Cherenkov telescopes' resolutions, instead, are much better, since the angular one is enhanced by the presence of more mirrors and the energy one is improved by the fact that all the shower development is traced.
- **Rejection** EAS arrays have very poor background rejection power, namely it is very difficult to discriminate showers originated by CRs by the ones from γ-rays. Of course this aspect can be cured if one has at disposal dedicated muons detectors underground, which record muons as leftover particles and provide informations on muonic size. Cherenkov telescopes on the other hand have a good background rejection power, as we shall see. Of course a certain amount of residual background is expected to persist also in Cherenkov telescopes, due to the fact that everything (like starlight of scattered light in the atmosphere) is essentially recorded by them.

The On-Off technique The On-Off technique was developed to handle the residual background, and it is important also for neutrino astrophysics. It is deeply used in astronomy whenever there is an irreducible background from CRs. This background is expected to be diffused and uniform, even if differences can arise because of different paths in the atmosphere or other factors, which can anyway be corrected. We can consider a fixed declination and a band in the sky, the width of which corresponds to the field of view. Imagine that there is a source in this band: if we can observe it at the same declination and right ascension value, we won't record any longer γ-rays produced by an astrophysical object, but we can expect that the background shall be the same in nearby cells of right ascension. We call the cell in which the source is located as the ON cell, while the nearby ones are called OFF ones, since we do not expect them to contain other astrophysical sources. From the ON cell we should collect both signal and background, while from OFF ones we should detect background only. Therefore, by observing the sky in the nearby directions, we can measure the background which can be afterwards subtracted to the ON cell signal.

The first attempts to collect γ-rays from EAS failed, and the Cherenkov based technique, which started from 1934, was the first to have success. In fact, in between the '30s and the '50s, Cherenkov telescopes were applied just to imaging the EAS in the atmosphere, and the very first attempt with γ-rays traces back to the '50s. The primitive idea was to use a garbage can with a small mirror coupled to a PMT, see Fig.(5.17—Left). Anyway this didn't lead to success, due to the very low efficiency in detecting γ-rays.

The breakthrough came only after the installation of a large mirror, installed in Arizona, the Whipple Air Cherenkov telescope, with a diameter of 10 m. This very large mirror was coupled to a camera, which in its first implementation consisted only on a single PMT, and indeed in this configuration the experiment didn't succeed in detecting γ-rays. However, later on the single PMT camera was replaced by 37 PMTs, each of those recording signals independently, making Whipple the first **imaging air Cherenkov telescope** with a segmented camera. Two factors led, eventually, to the success: the usage of the very large mirror, to enhance the collection area, and the segmented camera, since it allowed the signal-to-background rejection. See Fig.(5.17—Right) for reference on the appearance of Whipple. The great success occurred in 1989, with the discovery of a very clear excess of events from the direction of the Crab Nebula, which nowadays is the strongest steady source of γ-rays. Since this great event, many financial resources were concentrated in developing other, equally successful, instruments.

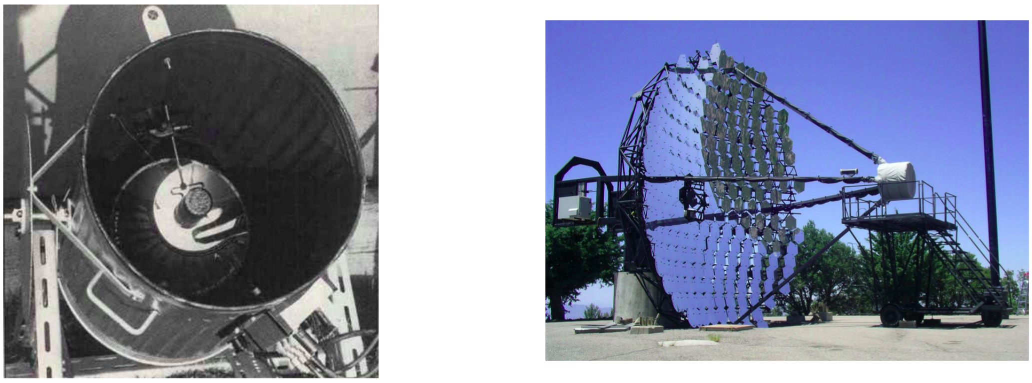

Figure 5.17: Left: The first design of an air Cherenkov counter in a garbage can, used by B. Galbraith and J. V. Jelley in 1953. Right: Photo of the Whipple 10 m large telescope at Mount Hopkins. Figure from `https://arxiv.org/pdf/1207.6003.pdf`.

Gamma-Hadron separation in Cherenkov telescopes In Fig.(5.18—Left) we can see a collection of few events from the first MAGIC telescope, which is an imaging Cherenkov instrument operating even nowadays. This is an illustration of how different events look like in a segmented camera. The Gamma-Hadron separation is a technique which exploits the differences expected in a shower initiated by a γ-ray with respect to one initiated by a hadron. The hadronic shower can be analytically described by the superposition model, Sec.(3.3.4), and shall be built up from a hadronic component as well as an electromagnetic one. Consequently, a hadronic shower will look very *fuzzy*, since the distribution of particles along the trajectory of the primary is much broader in the transversal scale with respect to an electromagnetic shower. Also it shall be much more irregular, with clusters of particles associated to e.m. subshowers. Conversely, an electromagnetic shower will produce a very compact and slim image, an ellipse as projected on a plane, as we can see from Fig.(5.19). Moreover, a γ-ray initiated shower will contain a very low fraction of muons, due to photo-production processes (see Ex.(3.3)). Background from CRs can thus be identified if we search for muon beams and irregular images. This idea is then realized by the performing of a fit of the profile, such as in Fig.(5.18—Right), with an ellipse of course, and the characterization of the ellipse's parameters in terms of width, lenght, size (proportional to the energy), tilt angle (specifying the geometry of the orientation of the telescope's camera).

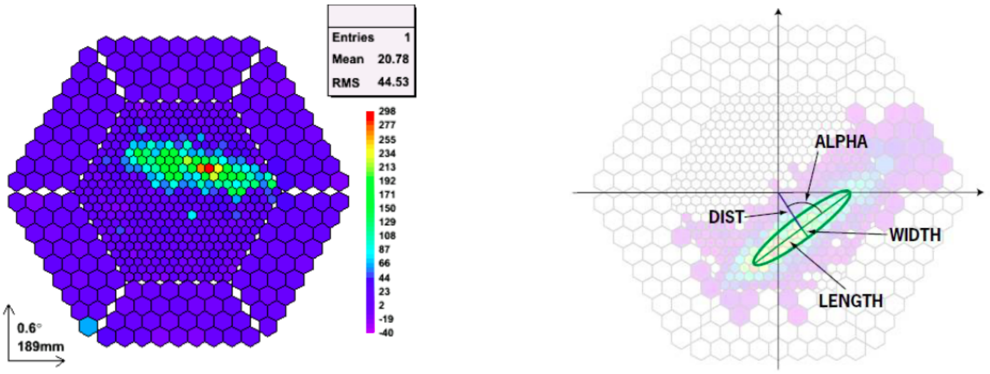

Figure 5.18: Left: A view of a detection in a segmented camera, this in particular is from a component of MAGIC in LaPalma. This image represents a geometrical projection of the shower into a detector. Right: A visualization of the *fish*.

5.1.6.4 The modern Cherenkov telescopes: results

The number of sources which are nowadays known is being recorded in the TeVCat[4], the catalogue of objects at VHE energies. In Fig.(5.20) we can see the latest update of the catalogue, with different source types. The total gives ~ 200 sources, which is not actually impressive if compared with the Fermi catalogue. This is not due to the sensitivity, since actually the imaging Cherenkov telescopes are actually more sensitive, having a larger collection area and being able to distinguish individual photons with much less count eccess. However the Universe is much more opaque at TeV energies, so the sky results to be less populated. Anyway, because of the superior sensitivity of Cherenkov telescopes, a more detailed characterization of the properties of the sources is allowed, both in terms of spectral properties and variability. This can be also appreciated in Fig.(5.14), in which the light purple region is the TeV one, and appears clearly very refined with respect to the bluish (Fermi range) region. Also these SEDs can be typically resolved within just a day, while usually a point in Fermi range is averaged over several days of detection.

---

[4] See the official site `http://tevcat.uchicago.edu/`

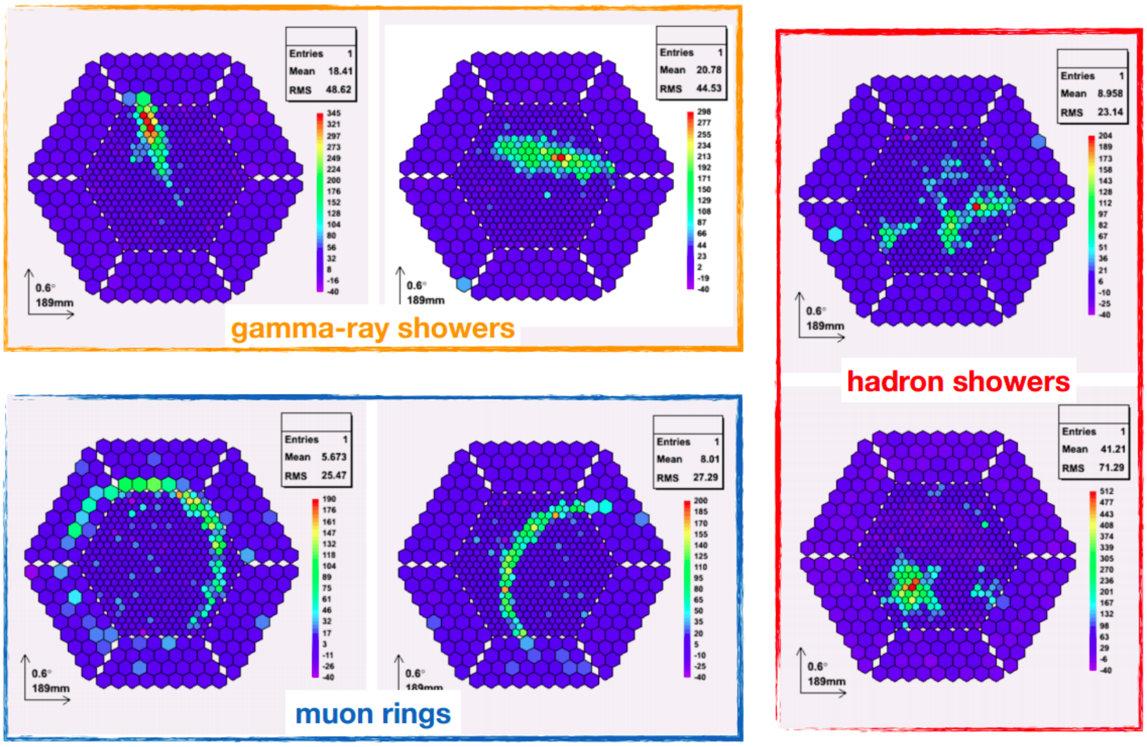

Figure 5.19: A few snapshots of a detection from the first MAGIC telescope, with different profiles of the ellipses. The major intensity is concentrated in the center, and the ellipses are very slim and regular in the cases of γ-ray showers, being irregular and fuzzy for hadronic showers. Muons on the other hand produce very characteristic Cherenkov rings.

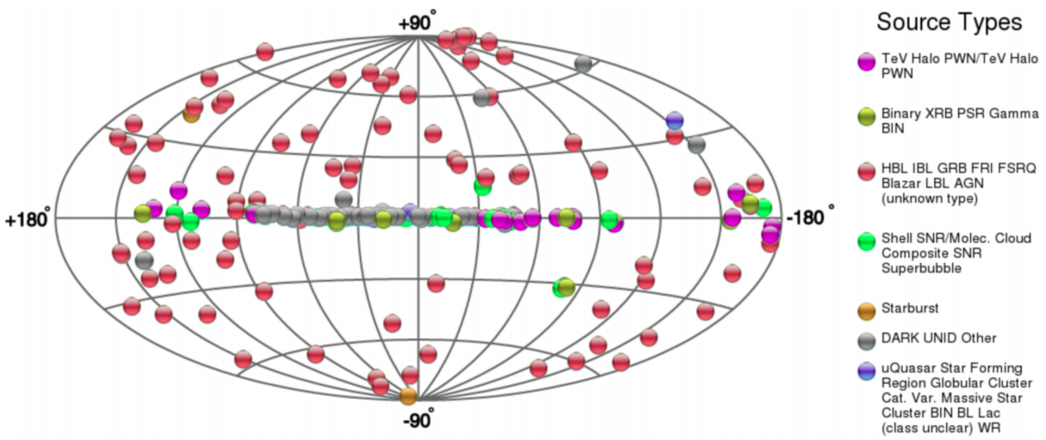

Figure 5.20: Skymap of the TeVCat sources, in galactic coordinates and different colors. The majority of the extragalactic objects are indeed AGNs, more precisely BLAZARs, while the grey dots are still unidentified and don't have a multiwavelenght counterpart, and they are expectably concentrated in the galactic plane. Apart from the mulitude of grey dots, other galactic objects are pulsars, binaries, SN remnants, pulsar wind nebulas ecc. From `http://tevcat.uchicago.edu/`.

Three different installations are operating nowadays, and we are going to describe them in what follows.

The High Energy Stereoscopic System (HESS) The High Energy Stereoscopic System (HESS) Observatory is located in Namibia, in the Southern Emisphere. The initial four HESS telescopes (Phase I, completed in 2004) are arranged in the form of a square having a side length of 120 m, to provide multiple stereoscopic views of air showers. Each telescope of Phase I has a diameter of 13 m, with a total mirror area of 108 m^2 per telescope. See Fig.(5.21).

The Very Energetic Radiation Imaging Telescope Array System (VERITAS) The Very Energetic Radiation Imaging Telescope Array System (VERITAS) is in operation at the Fred Lawrence Whipple Observatory in southern Arizona, USA, which is the same location of the original Whipple Cherenkov telescope. It is an array of four 12 m optical reflectors with similar characteristics as HESS-Phase I. See Fig.(5.22).

The Major Atmospheric Gamma-ray Imaging Cherenkov (MAGIC) The Major Atmospheric Gamma-ray Imaging Cherenkov (MAGIC) originally consisted of a single, very large reflector (236 m^2) installed on the Canary island of La Palma, with a 3.5 degrees high-resolution camera composed of 576 ultra-sensitive PMTs. This first telescope has been fully operational since 2004. In 2009, a second telescope of essentially the same characteristics was added, and now the configuration looks pretty much like in Fig.(5.23). This is the instrument which has the lowest energy threshold above all, around ~ 25 GeV.

Figure 5.21: The HESS telescopes in Namibia. From `http://www.mpi-hd.mpg.de/hfm/HESS/`.

Figure 5.22: The four IACT array VERITAS at Mt. Hopkins, Arizona. From `http://veritas.sao.arizona.edu/`.

Remember that the larger is the mirror the better shall be the energy resolution, and indeed these new instruments represent a development with respect to the predecessor Whipple in this front. Also is remarkable the fact that nowadays the tendency is to make use of more than one mirror, to build up a much more complete *stereo observation* which allows a precise reconstruction of the direction of incidence and height of the shower maximum. Additionally, stereo observations improve the angular resolution and the background rejection power.

Figure 5.23: The two large telescopes of the MAGIC observatory. From `https://magic.mpp.mpg.de/`

Furthermore, the different locations of these instruments determine the regions of the sky which can be scanned, and an idea of these regions can be acquired by looking at Fig.(5.24). An instrument located in the Southern Emisphere is well suited for observing the galactic plane, while in the Northern Emisphere extragalactic sources are better observed.

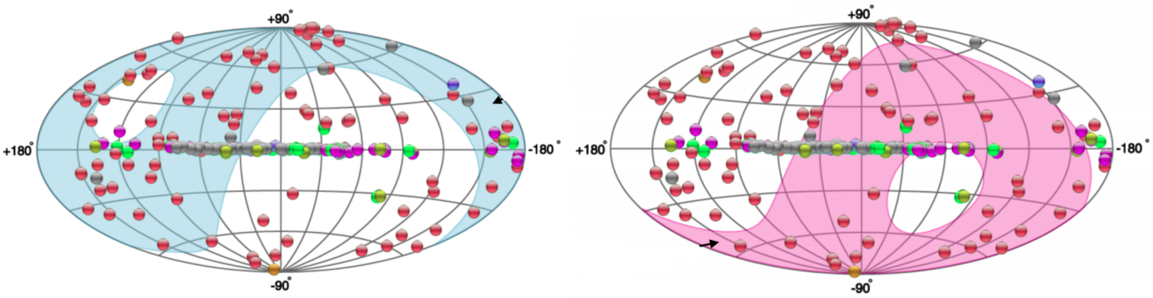

Figure 5.24: Left: Covering regions in the sky by the Cherenkov telescopes VERITAS and MAGIC, in the Northern Emisphere, in galactic coordinates. Right: Covering regions in the sky by the Cherenkov telescope HESS, in the Southern Emisphere, in galactic coordinate.

There is also a catalogue of sources which have been compiled by collecting data over many years, and HESS produced a **survey** of the galactic plane with the characterization of different point sources in various longitudes along the plane. There is also a wealth of results in the characterization of extragalactic objects, thanks to the very strong sensitivity of Cherenkov telescopes. They can actually trace variabilities over also minutes timescales, and BLAZARs can manifest indeed very strong variability, thus these instruments are perfectly suited for them. An example can be seen in Fig.(5.25).

Lastly, a very recent (2019) discovery had a great impact in the scientific community: TeV emission from GRBs were finally detected[5]! The event was called **GRB 190114C** and detected by MAGIC in January 2019, demonstrating the fact that GRBs are *not* exclusively X-ray's phenomena. In Fig.(5.26) we can see a compilation of the SED's data in different regimes.

---

[5] See the interview at `https://www.appec.org/news/very-first-measurements-of-grbs-from-ground-a-breakthrough-`

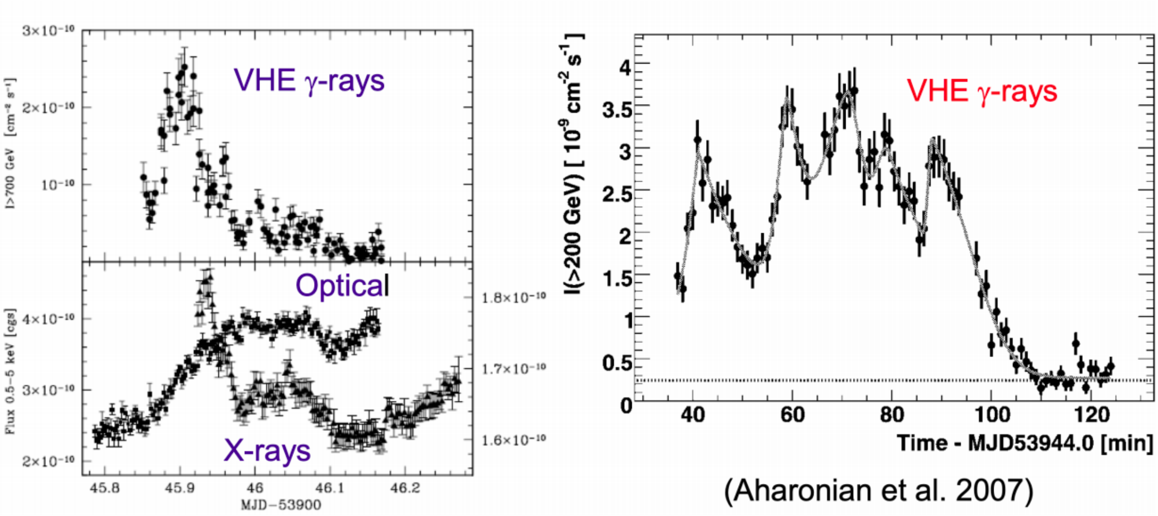

(Aharonian et al. 2007)

Figure 5.25: A demonstration of the variability of a BLAZAR at VHE. The high precision of the resolved variability is remarkable, and notice the timescale of minutes in the right plot.

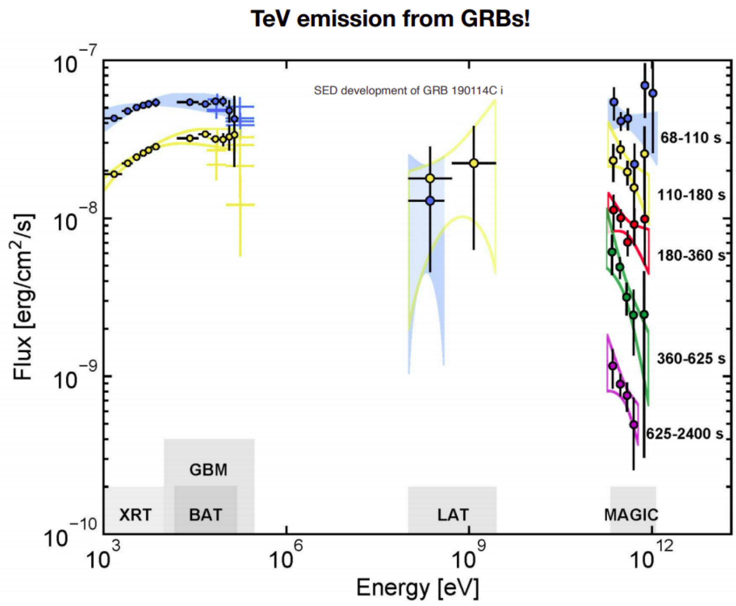

Figure 5.26: SED development of GRB 190114C in time measured by Swift XRT/BAT, Fermi GBM/LAT and by MAGIC. The MAGIC measurement is split into 5 consecutive periods of time. For the first 2 time bins also the data from the mentioned satellites are shown. The small numbers indicate the intervals in delay with respect to the reference time recorded in X-rays, since the TeV energies were detected only after a repointing alerted by GMB satellite X-ray mission. We can also easily compare the contribution of different bands to the flux: the VHE band constitutes over the half of the energy budget, integrated over the remaining other bands, and this is very remarkable, because it means that since the last year we were missing over the half of the energetics of GRBs.

Of course a lot of new efforts and resources are being implied to develop furtherly these kinds of instruments, and in particular a project is the **Cherenkov Telescope Array (CTA)**. This collaboration, ventured by all the three HESS, MAGIC, VERITAS, will increase the number of telescopes with different sizes, from a few very large 20 m diameter class telescopes to a large number of modest area (10–30 m^2) reflectors. The research objectives shall be devoted to both a significant improvement of the flux sensitivities in the standard 0.1–10 TeV energy interval and an expansion of the energy domain of arrays in both directions, down to 10 GeV and well beyond 10 TeV.

5.1.6.5 The modern EAS arrays: results

Also the method of EAS arrays for the investigation of γ-rays was developed with some famous and successful setups. In particular, the feasibility of the measurement at ground level of showers initiated by a γ-ray has been successfully demonstrated by the Milagro and ARGO Collaborations.

MILAGRO The Milagro detector consisted of a large central water reservoir (60×80 m^2), which operated between 2000 and 2008 in New Mexico, at an altitude of 2630 m. The reservoir was covered with a light-tight barrier, and instrumented with PMTs. In 2004, an array of 175 small tanks was added, irregularly spread over an area of 200×200 m^2 around the central reservoir. The strong TeV sources Crab Nebula and Markarian 421 were observed, as well as three extended sources in the galactic plane. See Fig.(5.27).

The High-Altitude Water Cherenkov Observatory (HAWC) The High-Altitude Water Cherenkov Observatory (HAWC) is located at an altitude of 4100 m close to Sierra Negra, Mexico. The observatory was completed in 2015 and it consists of an array of 300 water Cherenkov detectors, which is a fundamental difference with respect to MILAGRO, which was built upon a single large swimming pool. Lots of tanks in fact grant a better segmentation. Each Cherenkov detector has dimensions of 7.3 m diameter and 4.5 m depth, each viewed by 4 upward-facing PMTs. HAWC monitors the Northern sky (instantaneous field-of-view of $\sim$2 sr) and makes coincident observations with other wide field-of-view observatories. A better gamma-hadron separation is achieved by looking at the sizes and the spread of charged particles along the entire instrumented array. Of course this kind of separation technique is not as refined as the one for Cherenkov telescopes, however it is indeed successful. See Fig.(5.28).

Figure 5.27: Milagro EAS array bird's view. From `https://www.nature.com/articles/news.2008.1258`.

Remember that the higher the setup is located, the better the energy resolution, since the experiment gets closer to the shower maximum, thus HAWC effectively represents a great

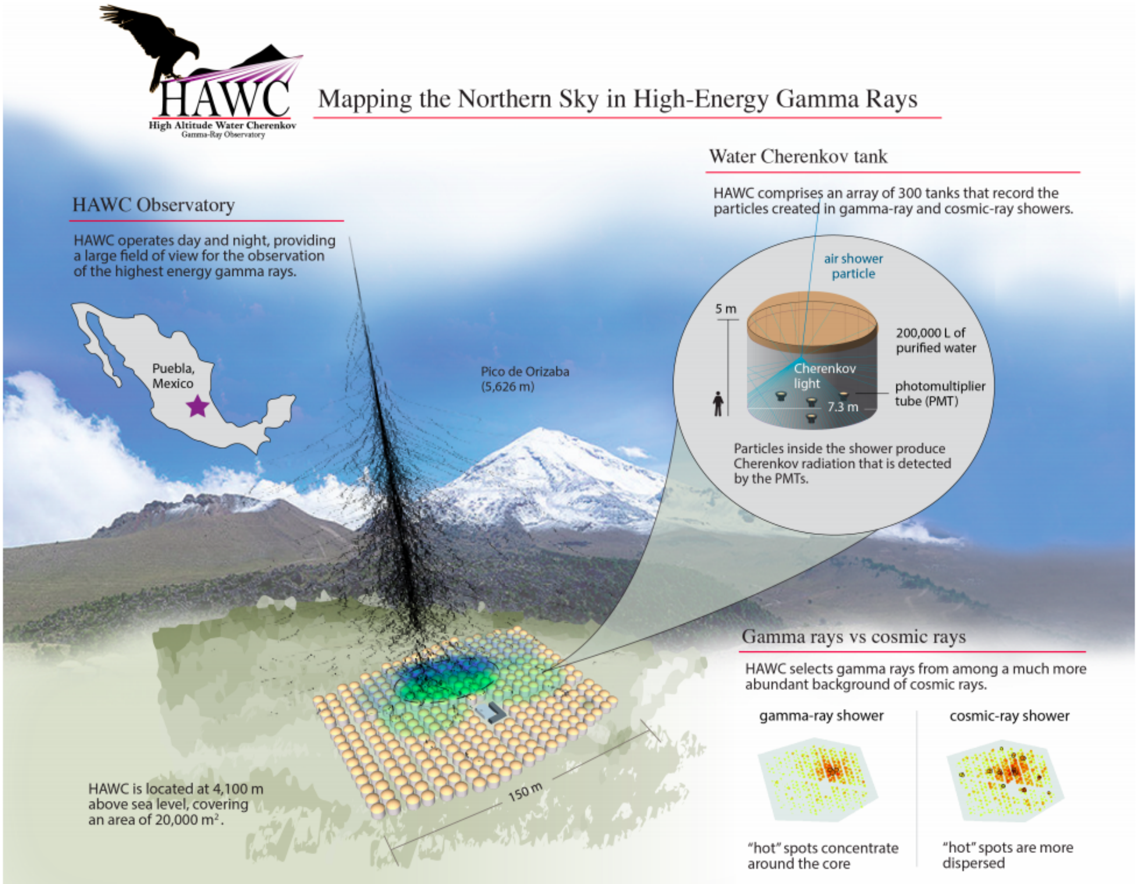

Figure 5.28: HAWC experiment detailed scheme, from the official site.

improvement with respect to the predecessor MILAGRO. Lastly, few results from the HAWK collaboration are shown in Fig.(5.29).

5.2 High Energy Neutrinos

Neutrino astronomy shares with γ-ray astronomy the objective of understanding the sources and mechanisms of CR acceleration, but due to their much larger interaction cross-section, γ-rays are easier to detect than neutrinos. The existence of CR sources, furthermore, seems to guarantee the existence of high-energy neutrino sources, and in this section we will investigate on them.

There are actually a lot of reasons to concentrate on High Energy (HE) neutrinos. Firstly, while low energy ones are object of deep and alive research programs for SNs studies (see below the famous case of SN 1987 A), HE counterparts are strictly connected to the CRs quest. What in fact is expected is that CRs can interact right at their accelerating source to give rise to neutral particles, in this case HE neutrinos, and these consequently shall propagate through the ISM towards us with an undeflected trajectory. We have seen that also γ-rays are produced and can be detected, however photons are characterized by the fundamental difficulty of discerning their leptonic and hadronic origin, while neutrinos cannot be produced in the framework of leptonic models. This is the reason why neutrinos are usually considered as *smoking guns* for the presence of hadronic interactions at the source, which can possibly explain the CRs we observe at Earth as their proper parents. Furthermore, neutrinos are weakly interacting particles, meaning that the interactions they undergo during their propagation are very different from the γ-rays ones, with a substantially *larger mean free path*, see Fig.(5.30).

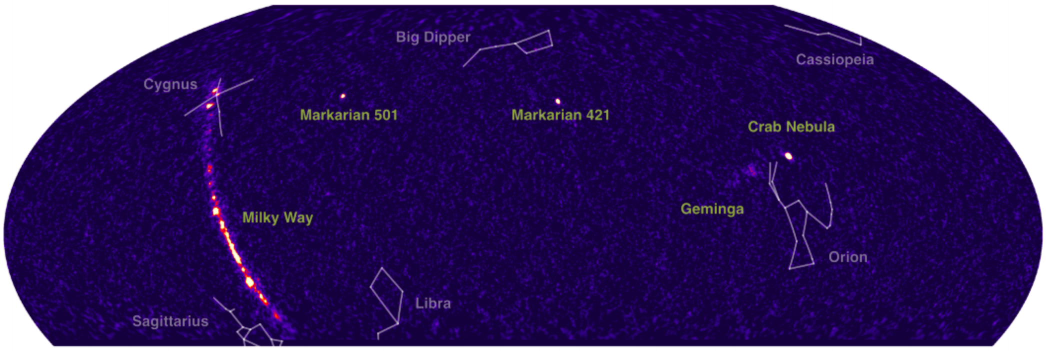

Figure 5.29: HAWC experiment results in terms of sources identification, in the Northern Emisphere, thus regarding just the most extreme parts of the MW. Now the equatorial coordinates are employed, and the survey regards energies above 50 TeV.

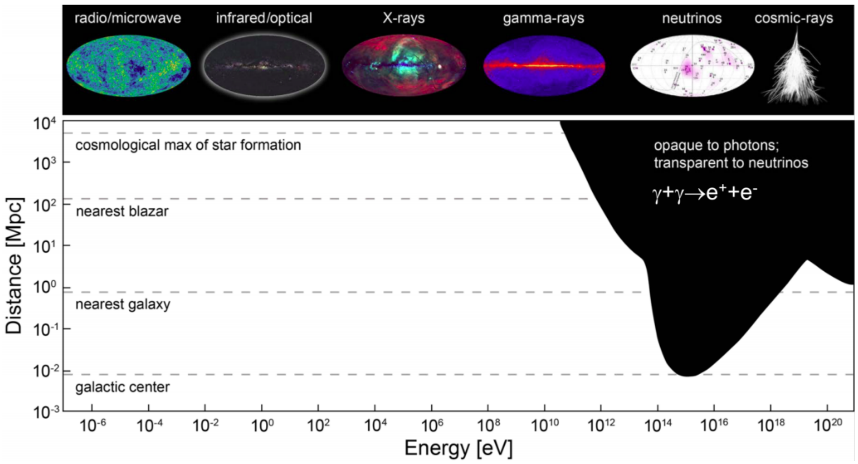

Figure 5.30: Maximum energy distances covered in different regions of the electromagnetic spectrum. The black region is representing the fact that the higher is the energy E_γ the lower shall be the coverable path lenght prior to an interacting process, like Bethe-Heitler's one. At TeV energies, e.g., the galactic center is hardly reached. On the other hand this is not true for neutrinos. Figure from `https://cerncourier.com/a/sn1987a-heralds-the-start-of-neutrino-astronomy/`.

The SN 1987 A The SN 1987 A was the first and so far the only detection of neutrinos coming from a SN explosion in the LMC, 1987. Actually it was the first multimessenger detection in mankind's history, concerning the coincidence between neutrinos and photons. The detection was performed bt three different instruments, Kamiokande, IMB and Baksan. Neutrinos were observed prior to the photons' detection, the reason being the propagation of neutrinos, which is much less affected by the absorbing matter surrounding the SN. In Fig.(5.31) a display of the ToA of different events is shown. A lot of efforts are being devoted to develop a *SN warning system*, in order to anticipate and promptly record outbursts of neutrinos and eventually alert the community for the observation of the electromagnetic counterpart. Of course one needs to know the direction of incoming, and it is very difficult because neutrinos with low energies do not preserve well informations on their original direction, being often of secondary origin. Those neutrinos, in fact, are expected to be created by nuclear processes in the very end phases of the SN explosion, and thus to have a mean energy which is usually relatively low. However simultaneous observations by more than one instrument can help to identify the arrival direction.

Fig.(5.32) shows the SED, as a function of the energy, of three different messengers sum-

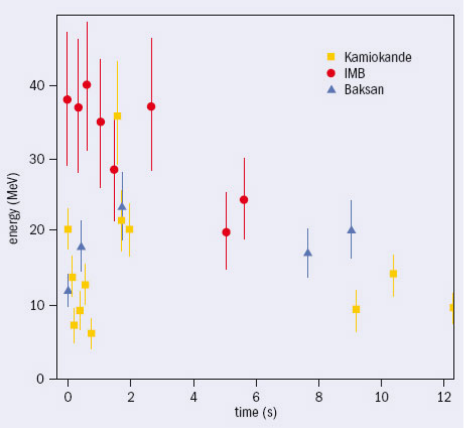

Figure 5.31: Display of the energy as a function of the ToAs of different events, each represented by a single point, referred to the labeled detectors. The order is ∼ 10 MeV, so they are relatively low energy neutrinos. Figure from `https://cerncourier.com/a/sn1987a-heralds-the-start-of-neutrino-astronomy/`.

marized: the Isotropic Gamma-ray Background (IGB), the Isotropic Neutrino Background (INB) and CRs. The first is referred to the diffused component FermiLAT is registering, apart from individual objects, which has a galactic and an extragalactic component (due to CRs interactions with MW matter and unresolved individual extragalactic sources, respectively). The latter is the CRs' spectrum above the knee, as measured by Auger and Telescope Array. Remarkably, these three fluxes are of the same order of magnitude and roughly the same range, at least up to the ankle. This suggests an intimate connection between these messengers!

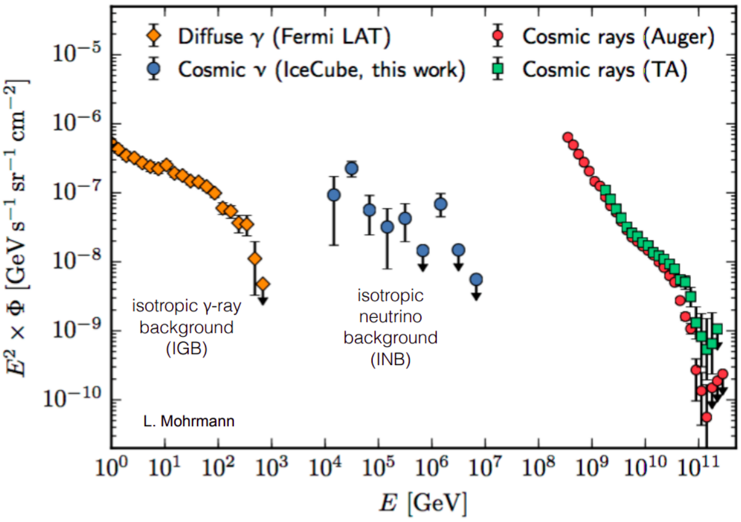

Figure 5.32: The SED, as a function of the energy, of three different messengers summarized: the Isotropic Gamma-ray Background (IGB), the Isotropic Neutrino Background (INB) and CRs.

5.2.1 Neutrinos production mechanisms

Let us now treat the main production mechanisms of neutrinos in astrophysical sources, assuming that they are produced by interactions of CRs. In particular we are interested in their fluxes and spectral properties.

1) *p-p interactions* in CRs production sites surrounded by ISM gas clouds. A clear example is what happens in the case of SN remnants. The interesting reactions were

already treated in Sec.(4.5.5) when we were talking about cosmogenic neutrinos, which originate from

$$p + p \to \pi^0,\ \pi^\pm,\ ... \qquad \text{and}$$

$$\pi^+ \to \mu^+ + \nu_\mu \qquad\qquad \mu^+ \to e^+ + \nu_e + \bar{\nu}_\mu\ ,$$

$$\pi^- \to \mu^- + \bar{\nu}_\mu \qquad\qquad \mu^- \to e^- + \bar{\nu}_e + \nu_\mu\ ,$$

so large quantities of ν_e, $\bar{\nu}_e$, ν_μ and $\bar{\nu}_\mu$ are produced.

2) *p-γ interactions* in CRs sites surrounded by intense photon fields, for example around BLAZARs, but also GRBs sites are believed to share this scenario. The interesting interaction is essentially the Δ^+ resonance of Ex.(4.4):

$$p + \gamma \to \Delta^+$$

$$\text{with} \qquad \Delta^+ \to \pi^0 + p \qquad\qquad \text{or} \qquad\qquad \Delta^+ \to n + \pi^+\ ,$$

and in this framework we shall not expect the production of $\bar{\nu}_e$.

Let us now see what can be deduced regarding fluxes and spectra of HE neutrinos. Given that we can observe a lot of sources of γ-rays with FermiLAT, we can highlight a relation between the spectral properties of γs with that of **muon** neutrinos at sources. Details concerning the specific astrophysical enviroment shall be fundamental, because they reprocess particles, and in particular secondaries such as γ-rays from π^0 decay are quite likely not to traverse the source undisturbed, giving rise to secondary cascades and feeding extra target photons. This is a hint to the fact that hadronic interactions in a specific astrophysical enviroment are usually quite complicated, and the relation between γ-ray spectrum and neutrinos one is not trivial, depending heavily on the thickness of the wanted source.

In general, reprocessing mechanisms such as the one said before are actually occuring, and the spectrum of γ-rays results to be usually *softer* than that of primaries and neutrinos. However, the total energy can be somehow related with a rescaling, such that

$$\int_{E_\gamma^{\min}}^{E_\gamma^{\max}} E_\gamma \frac{\mathrm{dN}_\gamma}{\mathrm{d}E_\gamma}\,\mathrm{d}E_\gamma = K \int_{E_\nu^{\min}}^{E_\nu^{\max}} \frac{\mathrm{dN}_\nu}{\mathrm{d}E_\nu}\,\mathrm{d}E_\nu\ ,$$

with K as a rescaling factor. So if one starts, for example, with a photon distribution like $\mathrm{dN}_\gamma/\mathrm{d}E_\gamma = \mathrm{A}_\gamma E_\gamma^{-\alpha}$ one can easily solve the above relation for $\mathrm{dN}_\nu/\mathrm{d}E_\nu$. This procedure is called *calorimetric estimate*, since we are comparing two energy budgets.

1) On average, in **pp interactions**, one can expect that three pions, π^0 and $\pi^\pm$, are produced at each interaction, each of them carrying a democratic fraction of the primary proton energy, namely $E_p/3$, as shown in the scheme below, where N, M and L are integers assuring the charge conservation. Consequently, one should expect the following relations, regarding the maximum energies, to hold

$$E_\gamma^{\max} = \frac{E_\pi^{\max}}{2} = \frac{E_p^{\max}}{6}\ , \qquad E_\nu^{\max} = \frac{E_\pi^{\max}}{4} = \frac{E_p^{\max}}{12}\ ,$$

and, integrating over all the parent protons, one should expect these scalings to hold, in a very simplicistic scenario. In particular we have thus related the maximum energies of the parent protons to that of gamma rays and muon neutrinos, and we can use these relations in the integrals of the calorimetric estimate. Ultimately, the maximum energies expected shall reflect the maximum ones of the CRs particles.

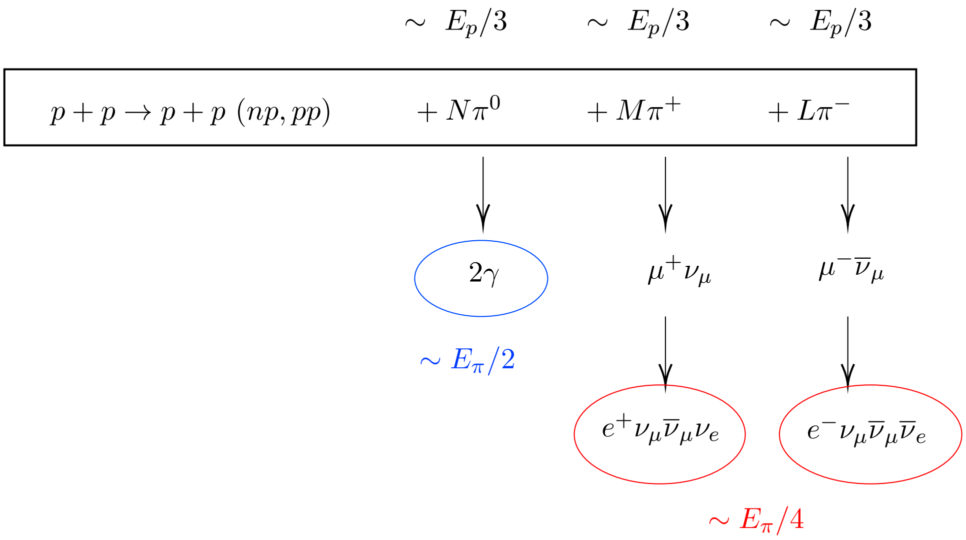

What about the minimum energy? It shall be given by the threshold for the pp reaction to happen, namely by (see App.(B)):

$$E_p^{\min} = \Gamma \, \frac{(2m_p + m_\pi)^2 - 2m_p^2}{2m_p} \simeq \Gamma \times 1.23 \text{ GeV} \qquad \text{with} \qquad \Gamma \equiv \frac{1}{\delta_j \, (1 - \beta \cos\theta)} \, ,$$

and δ is the Doppler boosting factor of the radiation in the jet, θ is the angle between the jet's axis an the line of sight, $\beta = v/c$ is the bulk velocity of the plasma in units of the speed of light. The Γ plays the role of the Lorentz factor of the accelerator relative to the observer, because typically we are observing astrophysical sources at Earth and the processes are happening in a boosted frame. This is true in particular when we are dealing with jets, since the energy budget is computed in the COM frame but all the energetics has to be corrected with the Lorentz factor, which is not simply the relativistic one but accounts also for the beaming angle δ_j, different in every specific BLAZAR.

2) On average, in **pγ interactions**, one can expect that at each interaction the two photons carry $E_\pi/2$ energy, and since each charged pion give four particles at the end every neutrino will carry $E_\pi/4$. We can also find that the average fraction of the proton energy which is transferred to the pion is $< x_{p\to\pi} > \simeq 0.2$, so at the end we get

$$E_\gamma^{\max} = \frac{E_p^{\max} < x_{p\to\pi} >}{2} \, , \qquad E_\nu^{\max} = \frac{E_p^{\max} < x_{p\to\pi} >}{4} \, .$$

So we have characterized the maximum energy expected from neutrinos in the photo-productions too. Of course these are just qualitative frameworks, just to have a rule of thumb.

Let us summarize with a specific example, namely we consider a TeV BLAZAR with an observed spectrum such that $\mathrm{dN}_\gamma/\mathrm{d}E_\gamma = \mathrm{A}_\gamma E_\gamma^{-\alpha}$, and with A_γ as a normalization factor. The predicted associated neutrinos fluxes are the following, for pp and γp interactions respectively[6]:

$$\frac{\mathrm{d}N_\nu}{\mathrm{d}E_\nu} E_\nu^2 \simeq 2 \times 10^{-12} \text{ TeV cm}^{-2}\,\text{s}^{-1} \times \left(\frac{A_\gamma}{3.2 \times 10^{-11} \text{ TeV cm}^{-2}\,\text{s}^{-1}} \right) \left(\frac{10}{\Gamma} \right)^{\alpha - 2} \left(\frac{2.8 - 2}{\alpha - 2} \right) \, ,$$

$$\frac{\mathrm{d}N_\nu}{\mathrm{d}E_\nu} E_\nu^2 \simeq 4 \times 10^{-13} \text{TeV cm}^{-2}\text{s}^{-1} \times \left(\frac{A_\gamma}{3.2 \times 10^{-11} \text{ TeV cm}^{-2}\,\text{s}^{-1}} \right) \left(\frac{10}{\Gamma} \right)^{2\alpha - 4} \left(\frac{2.8 - 2}{\alpha - 2} \right) \left(\frac{E_\gamma^{\text{target}}}{1 \text{ MeV}} \right) .$$

---

[6] The derivations are reported in the research article `https://arxiv.org/abs/astro-ph/0502449v3`.

So we can conclude that we can obtain a parametrization of the spectra of neutrinos, which shall be inevitably model dependent.

5.2.2 Neutrinos interactions and cross section

The other challenge and aim is to detect a **number of events** in an experimental setup (which we will describe in the following) and to count them, namely to have an estimate on

$$\frac{\mathrm{d}N_\nu}{\mathrm{d}t} = \int \mathrm{d}E_\nu \, A_\nu^{\mathrm{eff}} \, \frac{\mathrm{d}N_\nu}{\mathrm{d}E_\nu} \, ,$$

where A_ν^{eff} is the neutrino effective area of the detector comprising the neutrino interaction probability and the lepton detection efficiency after analysis cuts. To have an idea of the scales, one can see in Fig.(5.33) that we are usally around $A_\nu^{\mathrm{eff}} \sim \mathrm{m}^2$, and also one can see that this factor is energy-dependent, due to the increase with the energy of a) the neutrino cross section; b) the muon range and its light yield per unit path lenght.

Let us understand better the concept of the effective area. In Fermi, or more generally in a *γ-ray telescope*, we have usually a cubic active volume of the order of $\mathcal{O}(\mathrm{m}^3)$. The number N_γ of events shall be given by the following integral

$$N_\gamma = \int_{E_{\mathrm{min}}}^{E_{\mathrm{max}}} \frac{\mathrm{d}n_\gamma}{\mathrm{d}E \, \mathrm{d}A} \, A_{\mathrm{eff}} \, \mathrm{d}E \qquad \text{with} \quad [n_\gamma] = \# \, ,$$

where the integral is extended to the range to which Fermi is sensitive, namely $E_{\mathrm{min}} = 10$ MeV and $E_{\mathrm{max}} = 300$ GeV. Notice also that we are using n_γ, consistently with the notation in Eq.(5.1). The effective area can be described by a geometrical factor and an efficiency one, analogously to what we have encountered in Ex.(4.2), Eq.(4.11):

$$A_{\mathrm{eff}} = \epsilon \, A_{\mathrm{geo}} \qquad \text{with} \quad A_{\mathrm{geo}}, \epsilon = A_{\mathrm{geo}}(E), \, \epsilon(E) \, ,$$

and we have explicited the energy dependence of both factors. The geometrical factor is actually the projection of the active area along the direction of the incoming particle, and it shall be $\mathcal{O}(\mathrm{m}^2)$ in the case of FermiLAT.

Applying the same reasoning to a *neutrino telescope*, we know that neutrinos can be detected in an active volume only after they underwent an interaction, e.g. the muonic charged current process (ν_μ-CC) described in Eq.(2.10) and Fig.(4.41):

$$\nu_\mu + N \to \mu + H \, ,$$

in which N and H are the interaction target nucleus and the originated hadrons cascade. Muons in particular are very convenient, since they can propagate several kms with energies $E_\nu \approx 100$ GeV, so we can actually instrument very large volumes to detect the products of such process. These neutrinos will propagate straight in the active volume and emit Cherenkov radiation, which we can also trace to deduce the direction of propagation. With $E_\nu \geq 10$ GeV, the muon will be produced almost collinearly with the neutrino, within few degrees (still much better than the case of neutrinos from SNs, for which the direction is hardly kept undisturbed), and the higher the neutrino energy the smaller this uncertainty gets.

The typical dimensions of the active volumes for neutrino telescopes should then be $\mathcal{O}(\mathrm{km}^3)$, differently from γ-rays ones. However, A_{eff}^ν for neutrino telescopes shall not consequently be of the order of km^2, since we need to take into account for the probability $P_{\nu\to\mu}$ for the conversion, via ν_μ-CC channel, to occur, and this probability is actually very small. It can be calculated as:

$$P_{\nu\to\mu} \approx \sigma_{\nu,\mathrm{CC}}\, n_{\mathrm{target}}\, R_\mu \ ,$$

namely the cross section for the process, $\sigma_{\nu,\mathrm{CC}}$, multiplied by the number density of the target, n_{target}, and the muon range R_μ, that is the average path after which the muon has lost all its energy. At the end, the effective area A_ν shall be given by

$$A^\nu_{\mathrm{eff}} = A_\mu\, P_{\nu\to\mu} \approx \mathcal{O}(\mathrm{m}^2) \ ,$$

since $\sigma_{\nu,\mathrm{CC}}$ accounts for a factor $\sim \mathcal{O}(10^{-6})$, reducing the effective area, and we have called A_μ the effective area given simply by the geometrical factor and the efficiency of the detector in observing the ν_μ-CC channel.

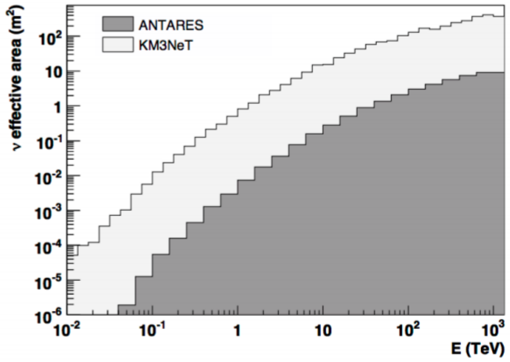

Figure 5.33: Effective area A^{eff}_ν as a function of energy in the two most important HE neutrino detectors. The order of magnitude is about m^2.

The neutrino-nucleon cross section We have talked about the CC process, which is useful in many contexts, but of course neutrinos can interact with the nucleons in the target through many other mechanisms, and a more precise study of the cross section is due. An example of neutrino-nucleon cross section was already given in Fig.(2.8), but we can see it also in Fig.(5.34), where the red peaked line is referring to the so called ***Glashow resonance***, which corresponds to the process in which

$$\bar{\nu}_e + e^- \to W^- \qquad \text{and} \qquad W^- \to \text{hadrons},\ \bar{\nu}_e,\ ...$$

This originates only with an antielectron neutrino interacting with an electron in matter, and produces the W^- boson at the specific energy of $E_{\mathrm{GR}} = 6.3$ PeV. This a very important feature, because it can be used for calibrations, but also for the distinction of pp and pγ interactions, given the fact that the GR resonance concerns just $\bar{\nu}_e$ (which cannot be produced in photo-hadronic interactions). The other two channels, νN CC and νN NC, are the usual charged current and neutral current curves respectively, which lay at slightly different levels.

Neutrino oscillation An important phenomenon which concerns the interaction of neutrinos in matter, and in particular at the sources, is the ***neutrino oscillation***, in which the physics of flavor is involved. Neutrinos with different flavors can in fact be produced by different processes, like the ones we have listed in the previous section Sec.(5.2.1), and we don't expect τ neutrinos in astrophysical enviroments (differently from accelerators' physics). However, neutrinos have the property to change their flavor during their propagation through matter, and we shall expect to detect different flavors from the original ones, in particular

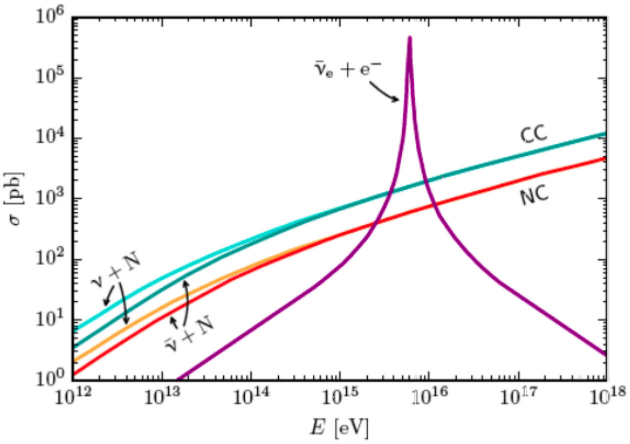

Figure 5.34: The cross section of neutrino-nucleon and antineutrino-nucleon interaction along with the $\bar{\nu}_e\ e^-$ one, responsible for the Glashow Resonance, are shown here. The CS of the latter is very large compared to interaction with nucleons at energy around 6.3 PeV. Figure from `https://arxiv.org/pdf/1808.01272.pdf`.

also the τ flavor shall be present[7].

Let us suppose that all the three neutrinos are massive, and have three different masses eigenstates called $|\nu_1\rangle$, $|\nu_2\rangle$ and $|\nu_3\rangle$. These three mass eigenstates, furthermore, shall not coincide with the flavor eigenstates, $|\nu_e\rangle$, $|\nu_\mu\rangle$ and $|\nu_\tau\rangle$, which are defined by the interaction. The mass eigenstates, conversely, are determined by the propagation effects. These eigenstates are connected by a unitary transformation U, such that the flavor ones can be expressed as superpositions of mass $|\nu_i\rangle$:

$$|\nu_\alpha\rangle = \sum_j U^*_{\alpha\, j}\ |\nu_j\rangle \qquad \text{with} \quad \alpha = e, \tau, \mu\,.$$

The unitary matrix is called the *Pontecorvo-Maki-Nakagawa-Sakata* matrix, or simplt PMNS matrix, and depends on three mixing angles θ_i and on the phase parameter δ, such that $U = U(\delta, \theta_{12}, \theta_{13}, \theta_{23})$. The temporal evolution in vacuum is dictated by mass eigenstates through the Shroedinger equation:

$$|\nu_j(t)\rangle = e^{-iE_j}\, |\nu_j(t=0)\rangle\ .$$

So each individual mass eigenstate will evolve in this way, and since the mass are hypothesized to be different they will consequently evolve differently. Thus we can expect different mixtures of these states, to give peculiar flavor eigenstates results. If we say that the initial flavor is α. the probability to get a flavor β after a certain time t shall be given by

$$P_{\nu_\alpha \to \nu_\beta} = \left| \langle \nu_\beta |\, e^{-iE_j t}\, |\nu_\alpha\rangle \right|^2 = \sum_j U^*_{\alpha j}\, U_{\beta j}\, U_{\alpha k}\, U^*_{\beta k}\, e^{-i(E_j - E_k)t}\ .$$

With the UR assumption, the energy of the neutrino, with $c = 1$, is given by

$$E_j = \sqrt{p_j^2 + m^2} \simeq E + \frac{m_j^2}{2E}\ ,$$

---

[7] Here we shall treat the simplicistic case of "vacuum oscillation", since in this approximation the distinction between Majorana and Dirac neutrinos is not relevant, but this is no longer true for matter oscillations, which applies e.g. at the Sun's center.

and with $t = L$ in natural units, where L is the lenght the neutrino have propagated through, one finds

$$-i(E_j - E_k)t \simeq -i\Delta m^2_{jk}\,\frac{L}{2E} \qquad \text{with} \quad \Delta m^2_{jk} \equiv m^2_j - m^2_k\,.$$

At the end, the probability $P_{\nu_\alpha \to \nu_\beta}$ accounts for an oscillatory factor which reads

$$\sin^2\left(\frac{\Delta m^2_{jk}\,L}{4E}\right) \approx 1.267\,\frac{\Delta m^2_{jk}}{\mathrm{eV}^2}\,\frac{L}{\mathrm{km}}\,\frac{\mathrm{GeV}}{E}\,.$$

The dependence on the squared mass difference, namely Δm^2_{jk}, is dictated by the physics of the propagation, and several experiments are devoted to determine it with high precision. The dependences on E and L are instead dictated by the astrophysics, and also the combined parameter L/E is very relevant in nuclear physics. However in astrophysics L/E is almost fixed, since L is usually huge, and we observe the average effects.

We can conclude that the flavor we expect at Earth for neutrinos depends on the production mechanism, being fully determined by the input energy spectrum and flavor composition of the neutrinos. We shall then distinguish three scenarios:

a) Pion decay: in this scenario we assume the neutrinos to be produced with the decays of the charged mesons, as listed in Sec.(5.2.1). In this case we easily see that

$$\textbf{SOURCE} \qquad \nu_e : \nu_\mu : \nu_\tau = 1 : 2 : 0\,,$$

at the source. This shall translate, at Earth, into equally shared fractions of different flavors, namely

$$\textbf{EARTH} \qquad \nu_e : \nu_\mu : \nu_\tau = 1 : 1 : 1\,.$$

b) Muon damped: in this case extremely high magnetic fields are required, and muons are expected to lose so much energy that the contribution from the muon decays can be neglected. The resulting ratios are

$$\textbf{SOURCE} \qquad \nu_e : \nu_\mu : \nu_\tau = 0 : 1 : 0 \qquad \textbf{EARTH} \qquad 0.19 : 0.3 : 0.38\,.$$

c) Neutron beam: within this framework, neutrinos are produced by neutron β-decays, giving rise to different ratios

$$\textbf{SOURCE} \qquad \nu_e : \nu_\mu : \nu_\tau = 1 : 0 : 0 \qquad \textbf{EARTH} \qquad 0.55 : 0.19 : 0.26\,.$$

Exercise 5.2. High Energy Neutrinos from the TeV Blazar 1ES 1959+650

In May 2002 the Blazar 1ES 1959+650 was observed in a flaring state in TeV γ-rays by HEGRA and Whipple γ-ray telescopes and in X-rays by the RXTE satellite. In June the X-ray observations showed a gradual decline, Whipple however observed another TeV flare. This was a so called "orphan flare" (i.e. visible in γ-rays but not in X-rays). Explaining such flares in leptonic models is not straightforward: a correlation in expected between the two bands being the IC-component measured in γ-rays seeded by the synchrotron radiation measured in X-rays. The event therefore suggested an hadronic nature of the γ-rays coming from 1ES 1959+650. If that would be the case, we could expect also neutrinos coming from that object. Several models were proposed to explain that occurrence, among others where the authors use analytic calculations to derive an approximate relation between the γ-ray and neutrino fluxes from a TeV emitting blazar. They estimate that, under favourable conditions, a few neutrino events could have been observed by the AMANDA neutrino telescope (a predecessor of IceCube) from that source at the time of the 2002 flare. Indeed neutrinos were recorded by AMANDA, however at a significance below 5σ. Recently another 1ES 1959+650 flaring episode in TeV γ-rays was reported by the VERITAS telescopes.

Estimate the number of neutrino events that could be observed by IceCube during a 90 days γ*-ray flare, for proton-proton and proton-photon interactions, assuming a Lorentz factor of* $\Gamma = 10$ *and including the neutrino oscillation effect. Also you should use the IceCube neutrino effective area from the research article* `https://icecube.wisc.edu/science/data/PS-IC86-2011` *(notice the dependence on the source declination).*

5.2.3 A "guaranteed" source of UHE νs

There is a strong indication that the UHE neutrinos should exist, however there is still a degree of uncertainty. The favorable argument is essentially the one presented when we were dealing with cosmogenic neutrinos: since the CRs spectrum extends to energies beyond 10^{18} eV, these UHECRs are believed to be accelerated in extragalactic sources, as said in Sec.(4.5.6). This means that they have to propagate over very large distances, being subject to interactions with photon fields background: this leads to the so called GZK cut-off in the CRs spectrum, as well as the production of neutrinos after the Δ^+ resonance. The properties of those UHE νs are model dependent, and not linked to the details of the specific mechanisms at work at sources, since their production happens during the propagation itself.

Of course this is just an interpretation, since there are still some uncertainties.

i) *The redshift evolution* of sources of UHECRs is uncertain. By redshift evolution we mean the number density and luminosity distributions as a function of redshift, $\rho = \rho(z)$ and $L = L(z)$, which are dependent on cosmological models.

ii) *The maximum energy* in the CRs spectrum, since at the highest energies the spectrum is subject to relevant statistical fluctuations due to very low flux.

iii) *The chemical composition* in the UHECRs fluxes. For these energies we have said that we can have, on a statistical basis, a hint to whether they have lighter or heavier compositions, see Sec.(4.4.3.3), but the details are not yet fully addressed. In fact, according to Sec.(4.5.5),

  - If they are *protons* we predict the highest UHE νs fluxes, because the Δ^+ resonance production is dominant.
  - If they are *heavier nuclei* then the photodisintegration dominates, and we expect less UHE νs.

  All of these aspects became clear only recently, because they account for a multimessenger analysis of photons and CRs, more precisely the awareness of a connection between CRs and neutrinos came out only in 1963. Nowadays we believe that there is a tendency towards heavier nuclei, which is a pessimistic view in terms of neutrino fluxes. Also we know that IceCube detect neutrinos with relatively low energies, and the sensitivity of Ice Cube is such that we exclude the optimistic view of lighter composition.

A famous prediction, which is called **Waxman-Bahcall upperbound**, motivated the establishment of neutrino astronomy in the first years of pioneering studies of the field, and it traces its roots in 1998. The starting point is the observation of UHECRs, and it regards the neutrinos produced directly at the astrophysical sources, and not during their propagation to Earth. It accounts for the following assumptions:

1) CRs are protons, accelerated at sources with a power-law spectrum with a spectral index equal to 2, motivated by the Fermi mechanism.

2) All such protons undergo proton-photon interactions producing neutrons, neutrinos and γ-rays, e.g. an example of a so called neutron-beam.

3) Sources are thin with respect to the nuclear interactions of those neutrons, namely CRs interact once, producing neutrons which are able to escape and decay, giving rise to the CRs we observe.

4) The luminosity evolution of far away sources is not different from any known flux that we observe.

Based upon these assumptions an upper bound was derived, stating that the neutrino fluxes shall be such that

$$E_\nu^2\,\Phi(\nu) \leq 2\times10^{-8}\,\mathrm{GeV\,cm^{-2}\,sr^{-1}\,s^{-1}} \qquad \text{with} \quad 10^3\,\mathrm{GeV} \leq E_\nu \leq 10^{10}\,\mathrm{GeV}\,.$$

The authors at that time actually speculated about a possibility that this bound works also for the case of pp interaction as responsible for the undelying mechanism at sources. There have been several refinements of this prediction, accounting for new experimental limits and showing that this bound can be significantly lower, however this has been considered the essential benchmark for long time. This means that neutrino instruments shall reach this sensitivity at least.

5.2.4 Towards HE νs astronomy: an historical overview

Now we want to make an excursus through the history of neutrino astronomy, with a first glance on the fluxes at our disposal, which cover basically all energy ranges. In Fig.(5.35) different predictions, as well as measurements, of neutrino fluxes as a function of energy are reported, over a huge energy range, from μeV to EeV.
The physics of neutrino was started by Wolfgang Pauli, 1930, which predicted its existence by studying the beta decay, and Enrico Fermi developed the theoretical framework of neutrinos. The actual detection happened in 1956, in an experiment by F.Reines and C.Cowan, Project Poltergeist, regarding solar neutrinos. The awareness of different flavors, with the detection of muon neutrinos, came out in 1970, with the first neutrino detection in a bubble chamber at the Zero Gradient Synchrotron. Solar neutrinos were deeply studied in several experiments, and the idea of using large volumes of water to detect cosmic particle outbursts in 1960 by Markov: this was the predecessor of the concept for modern instruments.

The understanding that CRs interactions can produce **atmospheric neutrinos** came after the 1960', and this kind of particles were characterized with great details. They were distinguished into two cathegories:

a) *Conventional neutrinos*, which reflect the usual channels for charged mesons and muons decay, and they are very well characterized, with known spectra. Their spectrum resembles the CRs one, with a slight offset: CRs one's was about 2.7 (see Sec.(4.2.2)), while conventional neutrinos have 3.7, due to the interplay between the interaction and decay of pions.

b) *Prompt neutrinos*, which are associated to the decay of the Charm particles (namely with the charm and bottom quark). These particles are extremely short lived, giving right away rise to neutrinos, however the cross section for this process is not very well known, and experimentally they are not yet measured.

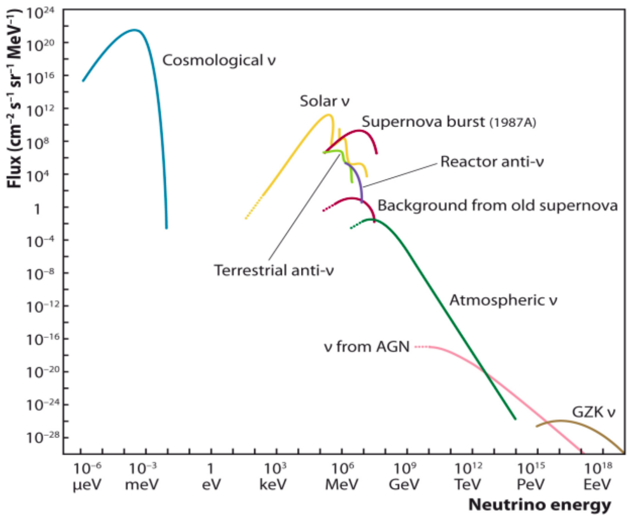

Figure 5.35: Summary plot of predictions for neutrino fluxes at different energies, from μeV to EeV. Cosmological neutrinos are the ones of the so called Cosmic Neutrino Background, and nowadays they are not actually reachable by any instrument. Solar neutrinos are the most common and famous ones, coming from our star, of energies keV to 100 MeV; neutrinos from SN have been detected in the peculiar case of 1987A SN; reactor neutrinos are covering MeV ranges. Atmospheric neutrinos are produced by CRs interaction in the Earth atmosphere, with electronic and muonic flavor, from MeV to 100 TeV. Finally neutrinos from AGNs and GZK (cosmogenic) neutrinos cover the UHE range.

In Fig.(5.36) these two cathegories are pictorially and quantitatively shown.

From Markov idea in 1960 to the first attempt to build such detectors a lot of time passed, simply because of the parallel development of particle physics. After the successful detection of solar neutrinos, an entire new field, connected to neutrino physics, developed, namely the underground detectors progress (IMB, Kamiokande): those first underground laboratories were devoted to the study of proton decay as well as the solar neutrinos. However, being typically sensitive to 10 MeV, these experiments also could measure atmospheric neutrinos, as one can see by looking again at Fig.(5.35). In practice, the atmospheric neutrinos presented themselves as background to those experiments, and between 80'-90' a lot of attempts to measure this background were performed. The, as often happens in science, this unwanted background soon became an important benchmark for particle physics, since nuclear theories of neutrino fluxes from Sun's activity revealed anomalies, more precisely a incongruence between the predicted flux and the measured one, appearing both in the solar neutrinos and in atmospheric ones. This was the road to the discovery of **neutrino oscillations**, for which a Nobel prize was awarded to Takaaki Kajita and Arthur B. McDonald in 2015.

Fig.(5.37) shows a scheme of the installations resembling Markov idea for huge, water supplied, neutrino detectors. In particular underground instruments were first developed to avoid atmospheric background. A cubic km volume provides in fact huge fluxes, as one can see by looking at he IceCube fluxes in units of a year:

- *atmospheric muons*	$7 \times 10^{10}\,\mathrm{yr}^{-1} = 2000\,\mathrm{s}^{-1}$
- *atmospheric neutrinos*	$5 \times 10^{4}\,\mathrm{yr}^{-1} = 1/6\,\mathrm{min}^{-1}$
- *astrophysical*	$\mathcal{O}(10)\,\mathrm{yr}^{-1}$

Muons are then still an unwanted source of background, which has to be avoided by going deeper underground, and the first idea to install a huge instrument in open sea water was launched in 1978, in a project named DUMAND. This project was characterized by features

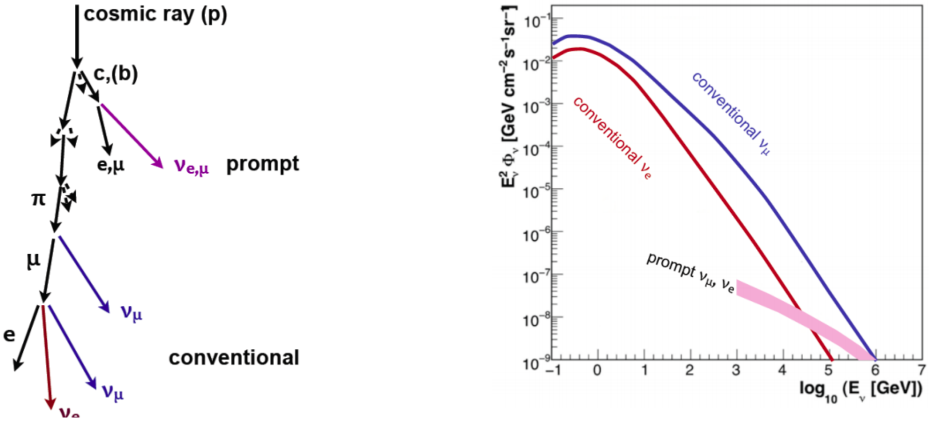

Figure 5.36: Left: Pictorial view of the two components of atmospheric neutrinos, prompt and conventional, see text. Right: Fluxes of the two components at comparison. Prompt neutrinos are expected to reflect the spectral index of CRs more directly, because they don't feel the energy losses of the intermediate mesons, differently from the conventional component. Anyway their fluxes are barely at the level of sensitivity of the current instruments.

which are common also to nowadays instruments (underground, km^3 volume), envised by 22'698 PMTs, which was challenging and costy. In fact it was never realized, but few prototypes were built. DUMAND launched also the idea of the detection of neutrinos by looking for upward moving particles: Cherenkov photons have a strict directionality, so by recording them with PMTs it should be possible to track them and identify the upward moving ones. This is a relevant point, since one can distinguish neutrinos from atmospheric muons. Fig.(5.38) explains this idea: if we have an instrument like Fermi, orbiting around the Earh, CRs can be vetoed in the detector itself, by using an outer layer which, when surpassed, reveals a CR; if the same kind of veto needs to be realized for atmospheric muons in a neutrino telescope, the veto must be applied to the entire atmosphere, namely a shield must cover the Earth revealing if something is able to go through it, but of course this is impossible. A *veto technique is thus impossible* for instruments which use our atmosphere as a target, e.g. neutrino but also Cherenkov γ-ray telescopes at Earth. However, while the latter ones can exploit the different properties of hadronic and electromagnetic showers, for neutrino telescopes it is impossible since they record a single particle going deep underground, which can be either a neutrino or a muon. In a DUMAND-like setting we would have observed just charged particles, since Cherenkov radiation is sensitive to charged particles only, and it would have been typically a muon. This muon could have been originated by primary interaction of CRs or one given by the CC channel of the associated muon neutrino. The distinction of the two cases, in the basis of a single event, would indeed be impossible, but of course downward going particles can be of both types, while upward going must unavoidably be products of CC channel, or even atmospheric neutrinos produced at the other side of the Earth.

The distinction between the last two possibilities is still an unknown. However, they can possibly have different energetics, as one can spot by looking at Fig.(5.35), in which AGN's and atmospheric neutrinos have very different spectra. This is the only information we can exploit to distinguish them, together with the **On-Off** technique exploited in γ-rau telescopes, with the similar reasoning of isotropicity of atmospheric neutrinos vs beamed incoming direction of astrophysical ones. Of course, single events don't tell much about this point, and the statistical basis is due.

A Russian team, which originally worked within the DUMAND project, developed the idea to use Lake Baikal water, which is well known to be exceptionally clear and transparent.

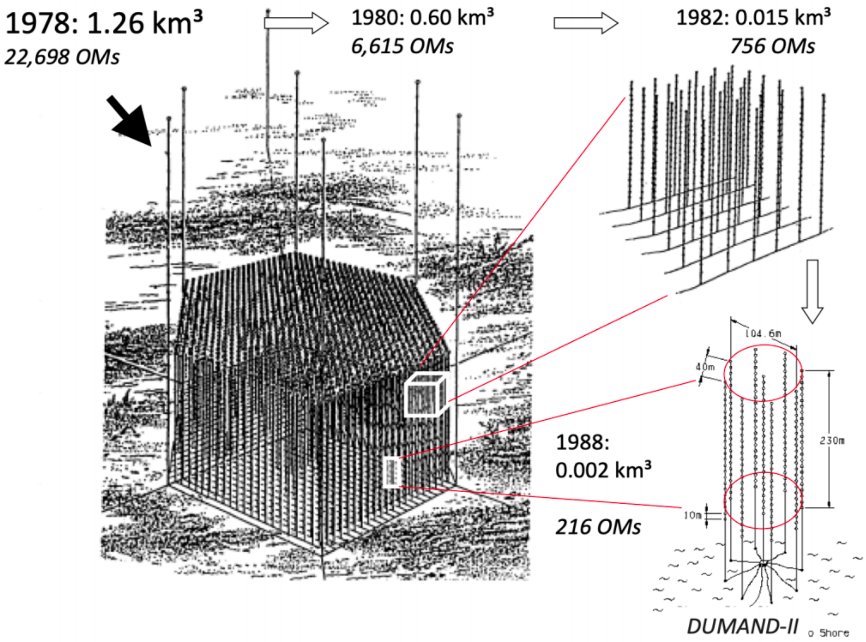

Figure 5.37: The originally conceived DUMAND cubic kilometer detector and the phased downgrading to the 1988 plan for a first generation underwater neutrino telescope DUMAND-II. Photomultipliers were aligned on strings (see the insert in the upper right part) which could be encored at the bottom of sea water and kept vertical by supports.

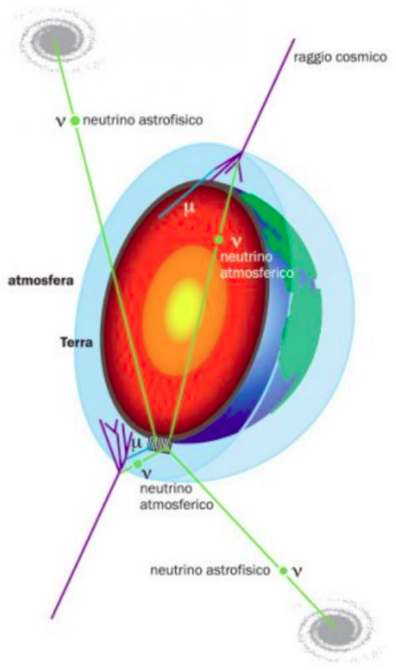

Figure 5.38: A cross sectional view of Earth. Our hypothetic detector is placed at the South Pole, and would record a track which is either upwards or downwards going. The latter ones are correspondent to atmospheric muons or the CC channel product of an astrophysical neutrino, while the first ones are unavoidably due to astrophysical neutrinos which have traversed all the Earth, or atmospheric neutrinos produced at the other side of the Earth.

This Lake is very deep too, with almost ~ 2 km depht, and it has also the advantage that, in winter, it is usually covered by a very thick layer of ice, allowing to walk on the installation. Of course a lot of technical challenges appeared, e.g. the building of PMTs in glass spheres was not well established at the time. Between 1993 and 1994 they were able to deploy strings of such light sensitive detectors, and they could record signals from downwards going muons. The initial success provided a great push, and after a team of Germans the NT200 design was finally developed, as we can see in Fig.(5.39), and the first upward moving track was finally seen in 1996. This was the first milestone of neutrino telescopes.

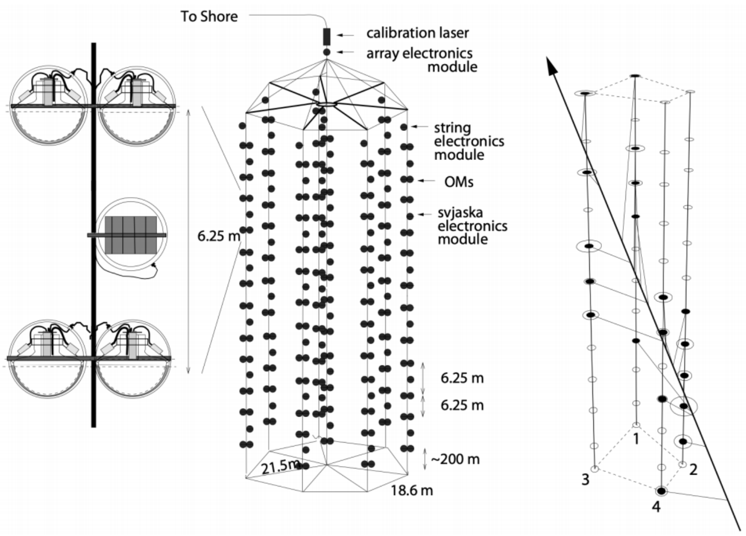

Figure 5.39: Left: The Baikal Neutrino Nelescope NT200. Right: one of the first upward moving muons from a neutrino interaction recorded with the 4-string stage of the detector in 1996. The Cherenkov light from the muon is recorded by 19 channels.

Meanwhile the scientific community was very thrilled, and a conference in 1998 in Venice, led by a Padua professor, initiated a series of very important workshops devoted to neutrino telescopes. A very young professor, Francis Halzen, from Winsconsin University, launched finally the innovative idea to use polar ice for neutrino telescopes. In particular, Antarctica offered an ideal ground: the ice depht is about 3.5 km. The project was called *Dio Volente Detector*, since it

> *"required a number of happy accidents to make it feasable, but if this should come to pass, it may provide the least expensive root to a truly large neutrino telescope. Exploratory studies may begin in South Pole station in the next few years."*

This was very revolutionary, since in the meanwhile Kamiokande (and other such installations) was successfully operating with the Cherenkov radiation technique, but with much smaller volumes. The project formed and a collaboration was built, called **AMANDA, Antartic Muons And Neutrino Detector Array**, which developed exploratory works at the South Pole station. They developed the concept of hot water drilling, that is the technique to drill holes in the ice by pumping hot water, in order to drop a string of PMTs which are consequently covered by Antarctica ice by refilling the hole with cold water back again. AMANDA was not successful since the very beginning, in fact the properties of polar ice, a part from the superficial layers, were fundamentally unknown. The original installation thus installed few sensors at the depth of few hundred meters, and it was found that an exceeding scattering occured, because of consistent air bubbles in the ice. Fig.(5.40) shows the absorption and scattering coefficient models developed in several years and describing the optical properties of polar ice in terms of an absorption and a scattering lenght, as a function of depht and wavelenght. Since the first strings of AMANDA were deployed at very shallow depths, initially the experiment had to face such small scattering lenghts that there was no way to use it as a tracking device. However it was predicted that, by going much deeper, the ice should have been freed of bubbles thanks to the increased pressure, more precisely this should happen $\sim$ 1300 m deep. Resources were collected to reach these depths, and finally AMANDA was enpowered with 677 optical modules in 19 strings of PMTs in glass sphere, installed at about 1500-2000 meters underground. It was in operation up to 2005, and constituted the major step after the predecessors, recording with great precision the fluxes of atmospheric neutrinos up to energy ranges of TeV and paving also the way to the installation of a neutrino telescope in ice. Actually AMANDA did not detect astrophysical neutrinos, a part from the notable case of the BLAZAR in Ex.(5.2) which did not have a sufficient statistical significance.

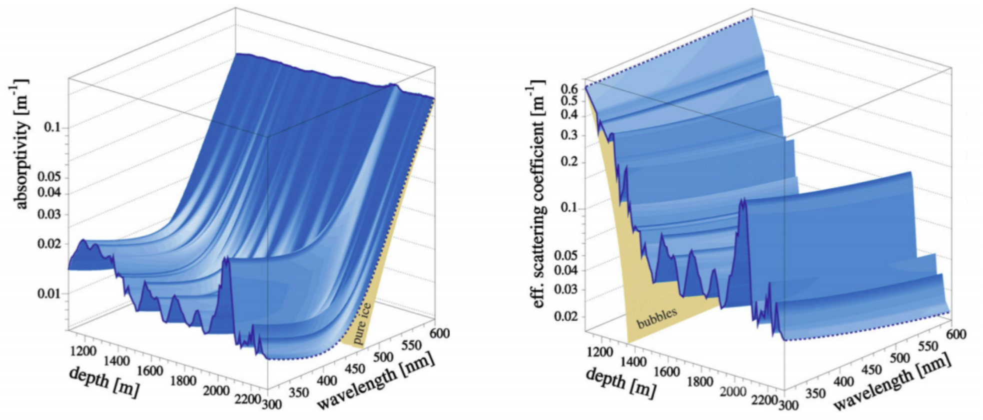

Figure 5.40: Absorption coefficient (left) and scattering coefficient (right) in South Polar ice as functions of depht and wavelenght. Some peaks are evident, and a prominent feature is shown in correspondence of a dust layer due to past volcanic activity: the South Pole's ice encodes all the geological history of our planet. Despite this one dust layer, which is around 2 km, remarkably the polar ice is the most transparent material available in nature. The absorption lenght is about $\sim$ 100 m, that is orders of magnitude more transparent than water, at the price of a certain scattering lenght due to imperfections in the crystal associated with bubbles and dust grains.

Anyway, after the AMANDA success, fundings were collected to realize its heir, a new neutrino telescope in ice. We should also mention that, meanwhile, there was also a project which envisioned to use the Mediterranean sea as a detector, in the line of DUMAND. The project was called **NESTOR**, and relied on the fact that the greek seabed is exceptionally deep, reaching $\sim$ 4000 m. However operations at those depths are very challenging. The prototype of this project was ANTARES, see Fig.(5.41), developed by a French group. This detector is today still in operation, but is going to be dismounted soon for the installation of a cubic chilometer detector in the Mediterranean sea, Sicily.

The real step forward finally happened with **IceCube**. Fig.(5.42) shows the concept of IceCube. It is a CR array for EAS combined with the instruments of a neutrino telescope. Fig.(5.43) shows also a brief pictorial summary on the neutrino astronomy history, till the endpoint of IceCube. As a summary, we can say that neutrino astronomy deployed both lake (Baikal) and sea (Mediterranean) water, as well as polar ice, and there are some differences between these mediums. Water is definitely different from ice in terms of absorption and scattering lenght: it is free of bubbles, so photons propagates almost straightly in it, preserving memory of their direction. On the other hand water is less transparent and photons get absorbed nearby, and this is a fundamental difference with respect to ice. Another

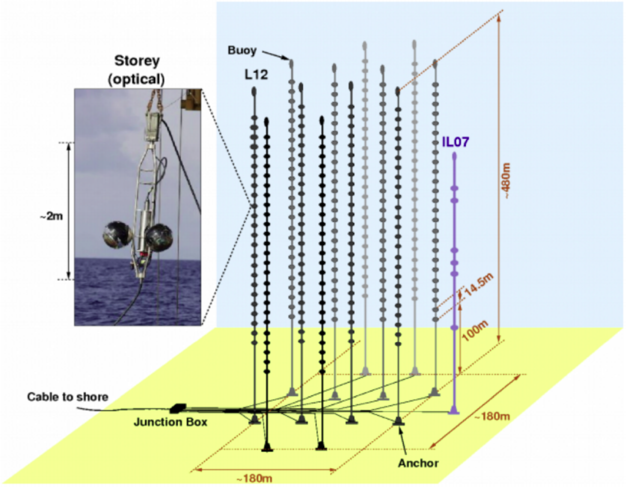

Figure 5.41: Schematic of the ANTARES detector. Indicated are the 12 strings, and the instrumentation line in its 2007 configuration (IL07). Shown as an insert is the photograph of a storey carrying 3 photomultipliers.

different is of course the fact that ice is a "dead enviroment", while sea in populated by lots of biological activities, which emit light as a disturbance, together with the light emitted by the potassium 40!

5.2.5 The IceCube breakthrough

IceCube published finally the first detection of an astrophysical neutrino in 2013, which was indeed a breakthrough, opening definitively the window to neutrino astronomy. Only few years after the discovery of the first neutrino source occurred too in 2017, and a lot of papers were published[8]. Fig.(5.44) shows a simulation of neutrino signature in the ice, which of course is dependent on the flavor of the neutrino, compared to real data. Remarkably, the Double-Bang feature is shown as a simulation, and it is a unique signature for astrophysical neutrinos, since, as we have seen, we actually don't expect τ neutrinos to be produced at sources, and neither in the Earth atmosphere, a part from a neutrino oscillation process, which is negligible at the energies of interest. So neutrino oscillations are important just in the context of propagation from astrophysical sources.

The actual discovery of a cosmic neutrino flux is based on the energetic properties of these events, since they can be distinguished from atmospheric neutrinos because of their different spectrum. Indeed, IceCube successfully measured this spectrum, as shown in Fig.(5.45), between the energies of 10^4 GeV $< E_\nu <$ 10^7 GeV. The energy spectrum is compatible with a power-law with a spectral index of 2.5 between 25 TeV and 3 PeV, which is very different compared with the 3.7 of atmospheric neutrinos. Evidence for a harder spectrum between 200 TeV and 8 PeV is found too, with spectral index 2.1.

Anyway, the direction of incoming neutrinos is still an open question, as is shown in Fig.(5.46), in which the different detections of IceCube are marked. So far, just a successfull identification of a neutrino source was developed, which is the case of the TXS 0506+056 BLAZAR. The search of the sources of neutrinos is a very active field, and one can perform it on a statistical basis using the On-Off technique by γ-ray telescopes: we know that the background from CRs is expected to be isotropic, with differences just due to different propagation lenght

---

[8] See the original paper `https://arxiv.org/abs/1311.5238`.

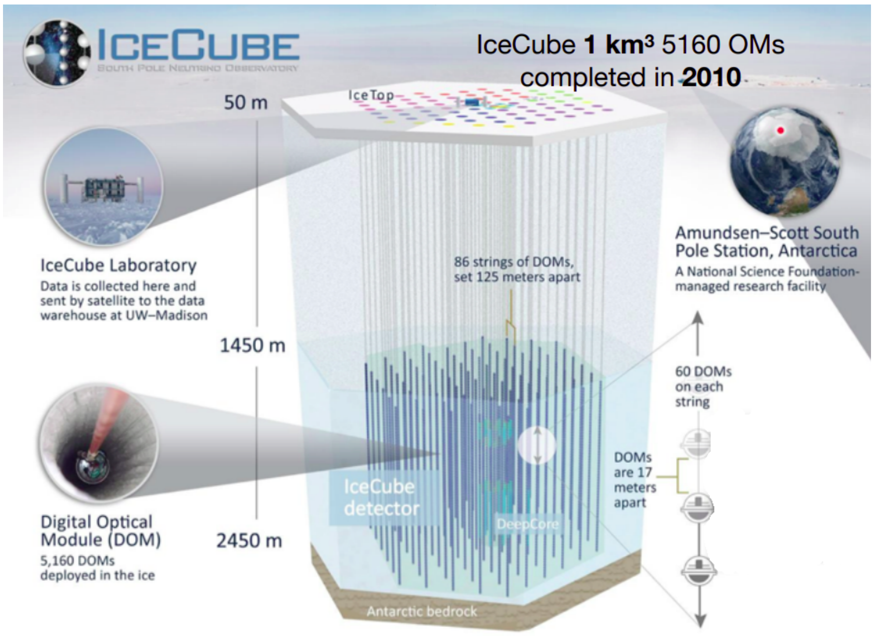

Figure 5.42: Scheme of IceCube concept. Its facility consists of 86 strings, deployed at larger depths than AMANDA, namely around ∼ 1450-2450 m. The deepest part is more instrumented, it is the part devoted to neutrino physics, reaching the depths in which polar ice has the best optical properties. It has also a facility on the top, which is very similar to Auger actually: these are tanks of water which then freezed into ice, watched by two PMTs at a spacing much smaller than Auger, that is about ∼ 100 m in between the tanks and the strings. Summarizing, it has a CR EAS array on the top, detecting energies lower than Auger but with a very similar concept.

in the atmsphere, and if there is a neutrino source it shall be located at a correspondent marked pixel in the skymap. This is done routinely, and a result is shown in Fig.(5.47): the majority of these neutrinos are atmospheric, and the idea is to find spots in which an accumulation of counts is not compatible with the degree of background. However this technique suffers from what in statistics is called the **look elsewhere effect**: if we have many pixels in the sky, and we look for an upward fluctuation in the pixel, the more pixel we look the more probable becomes the spotting of an extremely rare fluctuation in the background. So this identification requires very strong significances, stronger than 5σ, for a clear excess.

There are actually a few spots in the sky which can be identified as sources, since they show upwards fluctuations in the background, as shown in Fig.(5.48). At the moment they are still compatible with background fluctuations, at the statistical level, however it is clear that

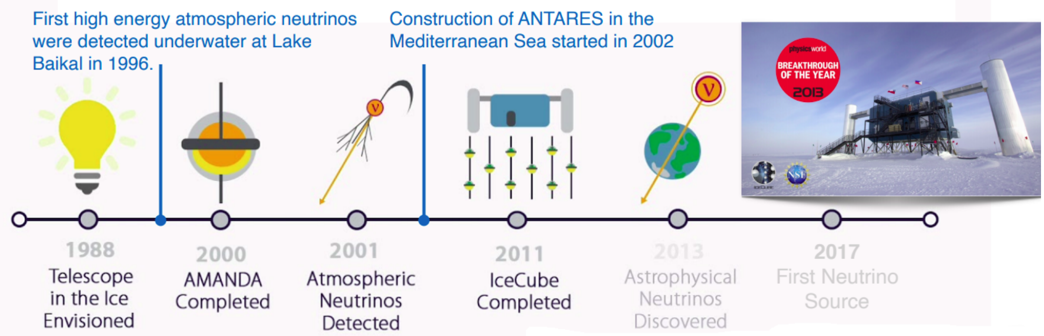

Figure 5.43: Pictorial timeline of neutrino astronomy history.

sources of neutrinos shall in the future come out, as statistics increases. The BLAZAR TXS 0506+056 is recognized too with the On-Off technique, but the real technique which led to its actual identification was different, a *multimessenger* one. The idea is to alert the astronomical community any time a UHE neutrino is recorded such that any other facility, Cherenkov telescopes, FermiLAT ecc. can point at that direction to investigate further. This is called the **IceCube Target Opportunity Program**. In september 2017 the TXS 0506+056 was recorded[9] with very good precision from the direction of a known BLAZAR, establishing the identification of a cosmic hadron accelerator with $>$ PeV energies. The direction was defined with great precision, refined 4h later thanks to CPU consuming codes for simulating the direction over the huge extragalactic volumes. The fact that several facilities followed up, including the MAGIC Cherenkov telescope, produced a very detailed SED, as we can see in Fig.(5.49).

The BLAZAR identification was actually a surprise, since it was an object with a theoretized low ambient radiation field, namely the SED does not show a lot of reprocessed radiation from the nearby clouds to the BLAZAR, such that photohadronic interactions are expected to be suppressed. So this class of sources is expected to be light in neutrinos, as compared to ones which have lot of radiation fields. Of course simplified models in BLAZAR physics are to be refined, and a lot of efforts are being put in this sense.

5.3 Gravitational Waves

In 2017 a great breakthrough for multimessenger astrophysics outbursts: the detection of a GW in coincidence with a γ-ray burst opened the field of GWs as another mean for the multimessenger study of our Universe. Let us summarize the main features of GWs.

The gravitational radiation is the type of messenger which has the *lowest interaction probability*, such that even the weak interactions are much stronger. We can compare the relative strenght of the fundamental forces at a fixed distance (since they depend strongly on it in principle) and test particle by comparing their intensity between two protons placed in very close contact, namely a distance of 10^{-18} m: Tab.(5.1) shows this comparison.

Strong	Electromagnetic	Weak	Gravitational
1	10^{-2}	10^{-7}	10^{-39}

Table 5.1: The table shows the relative intensity of the fundamental interactions, scaled to the strong one.

We know that neutrinos are weakly interacting particles, and this fact makes them very powerful astronomical messengers, since astrophysical sources and enviroments are essentially transparent to them. This argument is true, and even stronger, for GWs: they are the messengers which allow us to explore the most extreme cosmological sources. The capability to reconstruct GWs' arrival direction is yet not comparable to both the standard astronomical methods performed for other messengers and to neutrinos' technique, since nowadays the direction is estimated in IceCube with $< 1°$ precision, in some cases even lower. However the powerful feature of GWs is the fact that the Universe is transparent to them. Another important advantage is that fluxes decrease with the square of the distance for photons and neutrinos, and this is not the case for GWs: their amplitude is inversely proportional to the distance. This reflects in the horizon, namely in the number of reachable objects.

---

[9] See the scientific article `https://arxiv.org/abs/1807.08816`.

What are the differences between neutrinos, γ-rays and GWs in the MM context? Both HE neutrinos and VHE γ-rays require hadron acceleration, if they are to be associated to CRs. This is the scheme of the so called **astrophysical beam dump**, in which an accelerator produces a beam of hadrons (and leptons) and these hadrons interact with a target giving rise to secondary particles. The secondaries are p, $e^{\pm}$, deflected in the magnetic fields, together with a neutral counterpart composed by photons and neutrinos and is directional. This interaction of CRs is necessary to have neutrinos, but in this interaction the nature of the accelerator is not fixed, since the target is the fundamental ingredient. So, by looking at neutrinos and γ-rays, one cannot fix anything about the astrophysical source. GWs, instead, are produced by the *bulk motion* of the progenitor, such that they carry informations on the dynamics of the source internal engine. A multimessenger approach is then needed for a complete understanding of the physics.

GRBs as sources of GWs and νs GRBs, despite being known from '60s, have been better understood only after 2017. We can consider them as sources of joint neutrinos and GWs, and there are two different mechanisms which are believed to power them.

1) *Accretion onto a compact object*, e.g. the merger of a binary system NS-NS, BH-NS or BH-BH. These three examples are expected to emit GWs, and the first two of them shall emit also neutrinos and photons in the merging phase, which is the endpoint of the coalescence. These shall be the cases of Short GRBs production, with $\Delta t \leq 2$ s.

2) *Rapidly rotating NS* which emerge from the collapse of a massive star. In this case, a SN is produced and Long GRBs originate, with $\Delta t \geq 2$ s. In this second case neutrinos and photons are detected while GWs are disfavoured, since the matter collapse is essentially symmetric to good degree, and GWs require a non-spherical acceleration of matter, their radiation being quadrupolar in nature[10].

This is the best example of a golden MM observation, because the case of the coalescence is predicted to give rise to joint messengers, νs and γs, however nowadays no such observation has been performed yet.

5.3.1 Sources of GWs

We have said that GRBs can be candidate sites for GWs emission, and now we want to make a more general summary about the possible sources of gravitational radiation. Tab.(5.2) shows the main features of the possible known sources. The case of SN explosion is also listed, since there is the possibility to have an asymmetric collapse, even though it is usually disfavored, but the most relevant example is given by the compact objects inspiral. Of course also the configuration of two massive stars orbiting each other can be a candidate, with the difference of the strain order of magnitude, which shall be much smaller in this case.

Source	h	f **(Hz)**	**M** ($\mathbf{M_\odot}$)	**R (km)**	**r (Mpc)**
Supernova	10^{-21}	/	1.4	/	10
NS-NS Inspiral	10^{-21}	100	2.8	90	15
MBH-MBH Inspiral	10^{-16}	10^{-4}	10^{7}	10	1000

Table 5.2: The table shows the main features of GWs sources, h being the strain.

---

[10] GWs are expected to create tidal forces between geodesic motions of test particles, squeezing and stretching their configuration with respect to the rest position. This is the principle to be exploited in the GWs detectors.

The first proof of the existence of GWs came from an indirect, well known, observation: the Hulse Taylor binary pulsar, discovered in 1974. This type of source is given by a NS-NS inspiral, one of which is a pulsar. The pulses were essential, since the lighthouse effect rate was measured with great details. The emission of GWs is expected to cause an expense in the energy of the system, which must thus decrease in time. It is possible to predict the emitted power P for a system of objects at a distance D and the reduced mass μ:

$$P = \left(\frac{32}{5}\right) \frac{\omega^6 G \mu^2 \, D}{c^5} \qquad \text{with} \quad \mu \equiv \frac{M_1 M_2}{M_1 + M_2} \, .$$

Hulse and Taylor were able to measure a tiny but steady decrease in the period of the bynary system, and this discovery grant them the Nobel prize in 1993. The rate was given by

$$\frac{\mathrm{d}\tau}{\mathrm{d}t} = -(2.423 \pm 0.0006) \ \times 10^{-12} \, ,$$

and it was in extraordinary agreement with the predicted from GR rate of decrease. The prediction in fact, which takes into account also the non-circular orbit of the system, is of $\mathrm{d}\tau/\mathrm{d}t \simeq 2.4 \times 10^{-12}$, completely compatible with the measured one. The dynamics is pictorially shown in Fig.(5.50). The orbit of PSR 1913+61 has been observed for several tens of years by now, and it shrinks by $\sim$ 3.1 mm/orbit, such that the two stars will merge in $300{\times}10^6$ yr.

5.3.2 Detecting GWs

As already mentioned, the first evidence of the PSR 1913+61 is **indirect**, since it is not a direct measurement of a GW. To detect them directly we need a tangible proof of their tidal effects on the spacetime they propagate through. They are longitudinal waves, so these effects are expected to be present in the directions orthogonal to their propagation one. If one measures the relative entity $\Delta L/L$ of the stretching (squeezing) a feeling of the amplitude of the GW itself, namely the strain h, can be obtained, since the two are proportional: $\Delta L/L \propto h$. The size of this effect shall depend on the source distance r just inversely, such that $h \propto 1/r$.

5.3.2.1 The first GWs detectors

The first idea which was developed to detect GWs concerned *resonant bars*, attempting to monitor the distance between two free falling test masses, but the predicted strain in matter is extremely weak, being of the order of 10^{-22}-10^{-20}. For a detector consisting of a bar with a length of 1 m, this corresponds to a displacement as big as 10^{-20} m or less, which is already 1 billionth of the width of a typical atom. Also a lot of noise sources challenges the first resonant bars.

Actually the first concept of GW detector was the so called **Weber bar**: a large piece of metal characterized by a typical resonance frequency related to its size. If the bar is crossed by a wave with the right frequency, the amplitude of the tidal strains would be naturally amplified, and piezo-electric sensor can record these significant changes in the bar's properties. There were a lot of these GWs antennas developed in the past, two of those are still operating in Italy, AURIGA (Padova) and NAUTILUS (Frascati) in INFN laboratories. Of course the resonance principle has a fundamental drawback: the GW's frequency must be exactly that right one. The greatest challenges for these types of detectors are concerned with the aim to isolate perfectly the test mass from sources of noise, e.g. thermal noise or man activity's vibrations.

Another concept, developed in the Netherlands, was that of **MiniGRAIL spherical detector**, which was essentially a modern forms of the Weber bar, but with spherical geometry, sensitive to all directions and allowed polarization measurements. The sensitivity was pretty good, $\Delta L/L \sim 4 \times 10^{-21}$.

5.3.2.2 Laser interferometers

The technique which allows a broader sensitivity band is based upon *Laser Interferometers*. Large mirrors play the role of test, freely falling masses. These share essentially the Michelson interferometer setup: a laser beam is split into two orthogonal paths, with reflectors (the mirrors) at the end, see Fig.(5.51). Finally the two beams are reunited and are watched by a photo-sensitive device. If the system is at rest the interference fringes are stationary, while the occurence of a gravitational wave will induce a shift in the pattern of the fringes (measurable up to $\sim 10^{-18}$). The sensitivity depends on the length of the arms. To increase it, light travels many times forth and back between the mirrors (Fabry Perot cavity), which provide effective path lengths of $\sim$ 10 km or higher.
Several concepts are developing this technique, GEO was a German predecessor and the next generation of Interferometers is led by LIGO collaboration (Hanford and Livingston, USA), VIRGO (Pisa, Italy). The two LIGO have longer arms ($\sim$ 4 km), being consequently more sensitive than VIRGO ($\sim$ 3 km). The increasing number of such interferometers for GWs has an extremely important impact, since their combined study allows to reconstruct the arrival direction of GWs. Some blind directions are of course present for each of these interferometers, and the presence of the others can often cure this lack of informations.

A lot of efforts are being put to overcome the challenges of noise, both with a constant development of the **suspension** systems and in the optical instrument, since **quantum noise** is intrinsically present whenever a light beam is implied, and usually an increased intensity allows a better performance. However, with the increased intensity of the beams, **radiation pressure** is higher too, and this has been addressed by using huge test masses, with high inertia. This is of course a technological challenge.

5.3.2.3 The first detection: GW 150914

The first actual detection of a GW happened in September 14 of 2014, regarding a merging of a binary BH system of 30-35 $M_\odot$, by LIGO collaboration, and it was called **GW 150914**. After this detection, other two followed named GW 151226 (binary BH with 14-7 $M_\odot$) and GW 170104 (binary BH with 31-19 $M_\odot$), two years later to allow the upgrading of the setup. These are three cases associated by pairs of BHs, and the masses were deduced from the analysis of the waveform (that is the evolution of the strain in time), since it is possible to fit it with Post Newtonian numerical models. The discovery of the latter one was awarded a Nobel prize in 2017. By today there are several tens of these BH-BH produced GWs, and actually the typical masses distributions are being reconstructed thanks to the increasing statistics.

The concept of the detection was based on laser interferometry, as we have described in the previous section. The amplitude and the frequency of the GW is inferred from the fringe shift caused by spacetime deformation of the arms, and a photodiode detector record this interference image to be measured. In particular, it is possible also to reconstruct how this shift evolves with time: if we have a coalescence phenomenon, then the properties of the GWs emitted are expected to evolve with time as the system shrinks. The waveform shall be called **chirping waveform**, because of the acustic counterpart which is increasing in pitch (frequency) and amplitude. The endpoint of the coalescence is called *inspiral*, which happens just prior to the merging of the orbiting objects.

GWs are emitted during the coalescence phase, and at the merging the physical process which happens is the flow of accelerating relativistic matter colliding and originating a sort of *astrophysical beam dump*. So a multimessenger observation can be expected to anticipate the gravitational signal and to be present at the merging end.

5.3.2.4 The multimessenger detection: GW 170817

What joins these first detections together is the fact that they are produced by BH-BH merging, in which the electromagnetic (and weak) counterpart is expected to be completely swallowed by the progenitors. So we are quite unlikely to detect photons and neutrinos from these events, and a multimessenger observation is not possible.

The breakthrough in multimessenger astrophysics concerning GWs occured in 2017, with the detection of gravitational waves from the fusion of two neutron stars in the NGC 4993 galaxy, 130 million light-years away. In this fusion, in fact, is expected also the **electromagnetic radiation** counterpart, in a broad wavelenght spectrum from γ-rays to radio. Locating the source by the gravitational interferometers in an angular area of about 5 degrees enabled to point 70 telescopes operating on the whole e.m. spectrum, and they succeed in detect a GRB. One of these telescopes was indeed FermiLAT, but essentially the entire astronomical community collaborated. The host galaxy was identified almost immediately.

This was the first evidence that **(short) GRBs** can be associated to the merging of two compact objects, since up to that point just their connection with SN explosions was observed. Through this multiwavelenght measurement it was also possible to prove the production of heavy elements up to gold and platinum, providing a major breakthrough also from the point of view of nuclear astrophysics.

This is possibly one of the most productive area of astroparticle physics, after more than two years from this discovery still a wealth of paper are being continuously published. The official press release is very interesting: `https://www.ligo.caltech.edu/page/press-release-gw170817`.

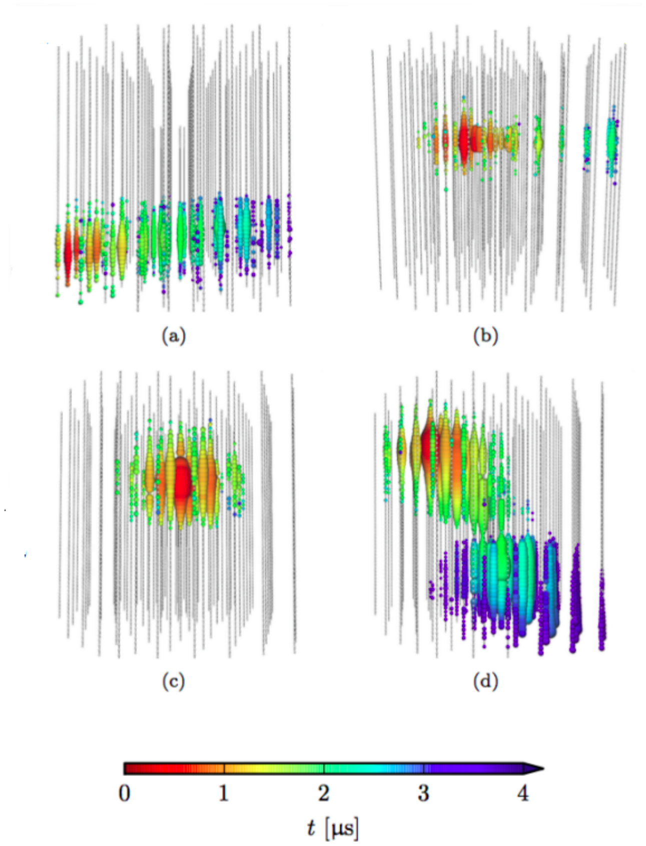

Figure 5.44: A simulation of neutrino signature in the ice, compared to real data. The first line refers to a muon neutrino, and the left upper plot shows data of a through-going track, while the right one the starting track of ν_μ. The muon neutrino here undergoes a CC interaction, producing a muon which preserve the direction of the neutrino quite well. The upper right plot presents also the spherical light emission from the hadronic cascade caused by the fact that the interaction happens inside the detector. In both cases the direction can be reconstructed pretty well, while the energy not as much since just the muon energy can be recorded. The left plot in the second line shows a cascade of the three flavors, ν_μ, ν_τ and ν_e, compared to a simulation in the right of a so called *Double-bang* (or Lollipop) of ν_τ. In fact, all flavors can undergo NC interactions, also ν_e and ν_τ, which propagates in a much shorter track than that of muonic ones. The spherical light distribution is seen again, and the reconstruction of the direction is not so well performed as in the previous case. On the other hand, the energy is reconstructed very well, since these processes happen entirely inside the detector. If extremely high energy τ neutrinos are present, their propagation time is enough to leave a track in the detector, and the Double-Bang signature is produced, namely one can distinguish the cascade at the interaction point and the one at the decay point. The color indicates time, so e.g. in the upper left plot the track develops from the left to the right; the size of the dots is a measure of the number of photons.

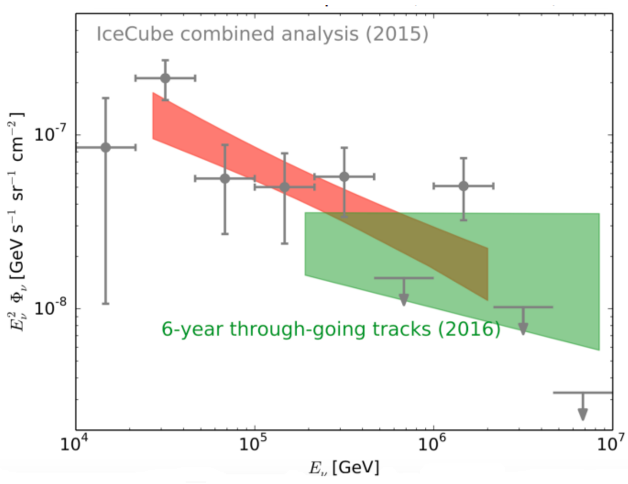

Figure 5.45: Spectrum of cosmic neutrinos measured in a combined analysis of all detection channels. The red bar indicates the best fit with a power-law spectral hypothesis. The gray points display the result for a fit of the neutrino flux in individual energy bands. A new measurement based on 6 years of through-going muons (green bar) that is sensitive at higher energies indicates a harder spectrum above few hundred TeV. Figure from `https://inspirehep.net/literature/1509013`.

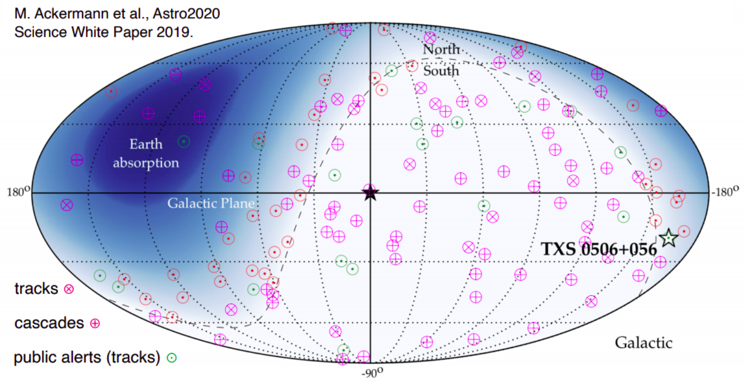

Figure 5.46: Map of the different detections of IceCube, at the uppermost energies, in galactic coordinates. At high energies (few tens TeV) a clear excess of events is observed excluding an atmospheric-only origin. Directions show no obvious accumulation either around individual sources or the Galactic plane.

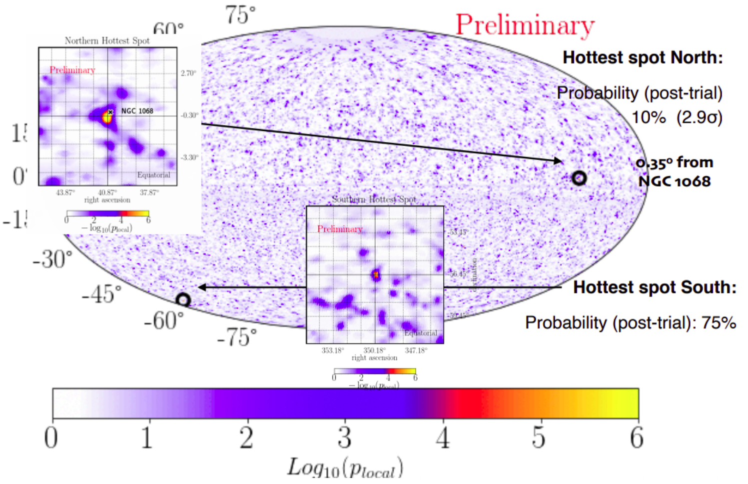

Figure 5.47: Map of neutrinos in IceCube, the majority of those being the atmospheric ones.

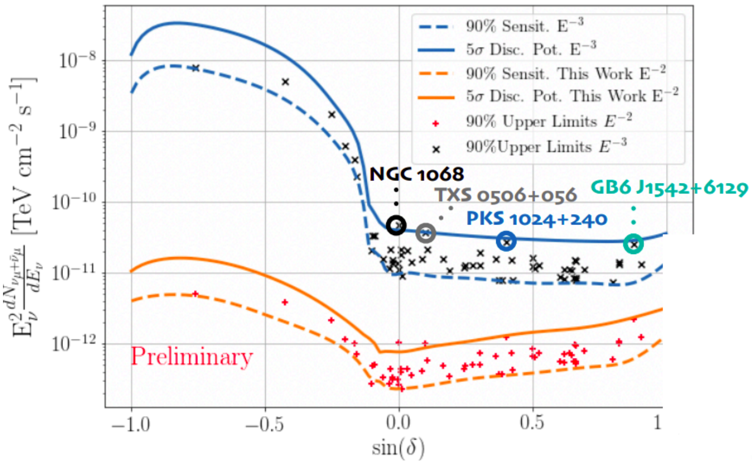

Figure 5.48: Neutrino SED, with the candidate sources highlighted with their name. The BLAZAR TXS 0506+056 is recognized too with the On-Off technique. Figure from `https://arxiv.org/abs/1907.06714`.

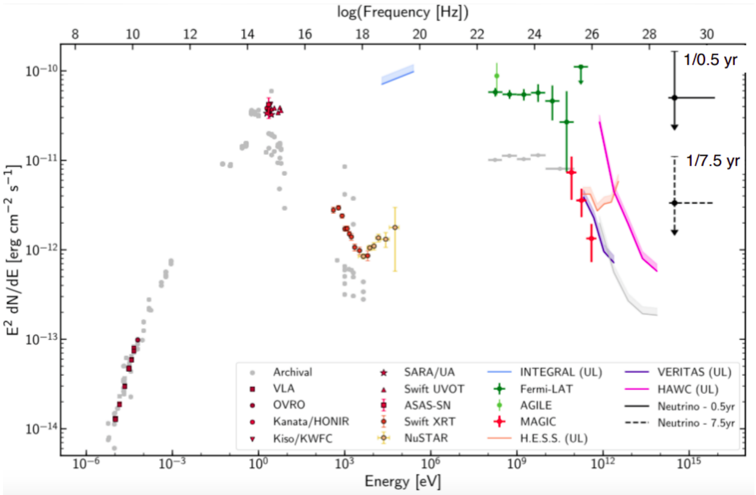

Figure 5.49: SED of the event TXS 0506+056, covering all energy ranges and with combined evidences from a lot of instruments.

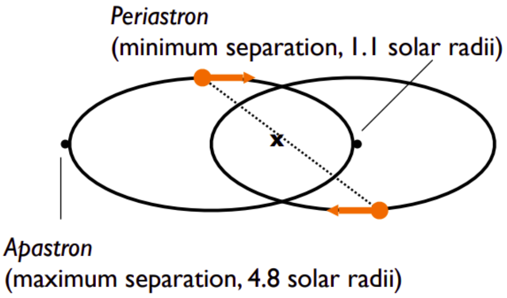

Figure 5.50: Pictorial view of the Hulse-Taylor pulsar system. The pulsar and its companion (both with a mass of ∼1.4 solar masses) follow elliptical orbits around their common center of mass, with an orbital period of 7.75 hours. The period can be measured by radio telescopes at the earth. Several periods can be folded together to form a "template" (average pulse). Note that there are lots of random as well as regular variations among individual pulses, but the templates provide very stable "clocks".

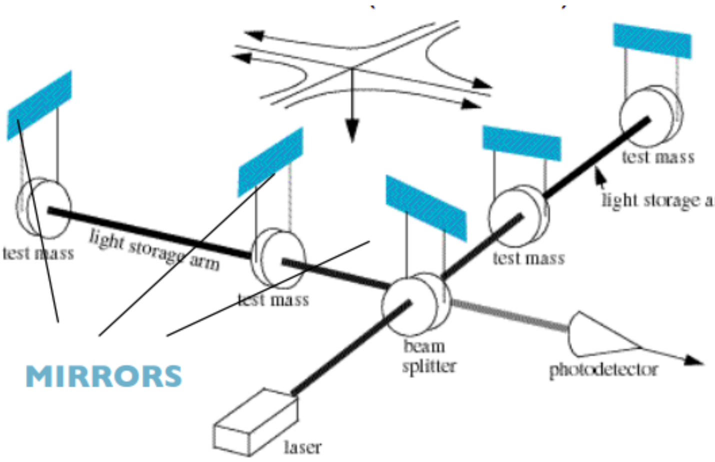

Figure 5.51: Pictorial view of the LIGO scheme: the beam from the laser is split into two orthogonal long arms of km-scale length, L1 and L2, each forming a resonant cavity. A small portion of the light is taken out from each beam to measure the radiation phase. If a change in the length difference L1-L2 occurs, it can be measured as a phase difference in the photo-detector.

Appendix A

Summary and OoM

Symb.	Definition	Value or (usual) units
$m_e c^2$	electron mass $\times$ c^2	$0.510\,998\,9461(31)$ MeV
r_e	classical electron radius $e^2/4\pi\epsilon_0 m_e c^2$	$2.817\,940\,3227(19)$ fm
α	fine structure constant $e^2/4\pi\epsilon_0 \hbar c$	$1/137.035\,999\,139(31)$
N_A	Avogadro's number	$6.022\,140\,857(74)$ $\times 10^{23}$ mol^{-1}
ρ	density	g cm^{-3}
x	mass per unit area	g cm^{-2}
M	incident particle mass	MeV/c^2
E	incident part. energy $\gamma M c^2$	MeV
T	kinetic energy, $(\gamma - 1) M c^2$	MeV
W	energy transfer to an electron in a single collision	MeV
$W_{\max}$	Maximum possible energy transfer to an electron in a single collision	MeV
k	bremsstrahlung photon energy	MeV
z	charge number of incident particle	
Z	atomic number of absorber	
A	atomic mass of absorber	g mol^{-1}
K	$4\pi N_A r_e^2 m_e c^2$ (Coefficient for dE/dx)	$0.307\,075$ MeV mol^{-1} cm^2
I	mean excitation energy	eV (*Nota bene!*)
$\delta(\beta\gamma)$	density effect correction to ionization energy loss	
$\hbar\omega_p$	plasma energy $\sqrt{4\pi N_e r_e^3}\ m_e c^2/\alpha$	$\sqrt{\rho\,\langle Z/A\rangle} \times 28.816$ eV $\hookrightarrow \rho$ in g cm^{-3}
N_e	electron density	(units of r_e)$^{-3}$
w_j	weight fraction of the jth element in a compound or mixt.	
n_j	$\propto$ number of jth kind of atoms in a compound or mixture	
X_0	radiation length	g cm^{-2}
E_c	critical energy for electrons	MeV
$E_{\mu c}$	critical energy for muons	GeV
E_s	scale energy $\sqrt{4\pi/\alpha}\ m_e c^2$	21.2052 MeV
R_M	Molière radius	g cm^{-2}

Figure A.1: Summary of variables fundamental values and order of magnitude used throughout the second chapter. The γ and β parameters have their usual relativistic meaning. Table lifted from `http://pdg.lbl.gov/2019/reviews/rpp2019-rev-passage-particles-matter.pdf`.

Appendix B

Pion production

A brief description of how pions can be produced is here presented. We have already said that, when entering the Earth's atmosphere, CRs collide with nucleons of atmospheric nuclei (mainly oxygen and nitrogen) and produce a cascade of secondary particles. The constitutive process is the following:

$$p + N \to \pi^{\pm},\ \pi^{0},\ K^{\pm},\ K^{0},\ p,\ n\ ...$$

and these products are mainly pions. On the other hand pions can be also produced by interactions of high energy protons with photons, so let's do some simple kinematic considerations to find whether some processes are actually allowed to happen. In particular two classes of reactions are analyzed: hadronic processes and pion photo-productions.

B.1 Pion photo-productions

a) *Photo-production of neutral pion*
The process is described by

$$p + \gamma \to p + \pi^{0}$$

We can write the four momenta of the particles in the initial state as $p_\gamma = (E_\gamma/c,\ \vec{p_\gamma}) = (|\vec{p_\gamma}|\,,\ \vec{p_\gamma})$ and $p_{p,\,\mathrm{in}} = (E_{p,\,\mathrm{in}}/c,\ \vec{p_{\mathrm{in}}}) = \left(\sqrt{m_p^2c^4 + |\vec{p_{\mathrm{in}}}|^2\, c^2}/c,\ \vec{p_{\mathrm{in}}}\right)$. So the invariant mass in the initial state is immediately given by Eq.(1.3):

$$\sqrt{s} = \sqrt{m_p^2c^4 + 2E_{p,\,\mathrm{in}}E_\gamma - 2\,|\vec{p_{\mathrm{in}}}|\,|\vec{p_\gamma}|\,c^2\cos\theta}\ .$$

The threshold energy for the process is the total energy available in the COM frame, where the produced particles are at rest, i.e. $E_{\mathrm{thr}} = E^{*}$, and it is given by the invariant mass calculated in that frame $\sqrt{s}$ to the power of two:

$$\sqrt{s} = \sqrt{m_p^2c^4 + m_\pi^2c^4 + 2m_pm_\pi c^4} = m_pc^2 + m_\pi c^2\ ,$$

$$\Rightarrow \qquad E_{\mathrm{thr}} = \left(\sqrt{s}\right)^2 = m_p^2c^4 + m_\pi^2c^4 + 2m_pm_\pi c^4\ .$$

Let's impose that the energy of the initial state, $E_{\mathrm{in}} = s$ is equal to the threshold energy to find the minimum energy for this process to happen:

$$E_{\mathrm{in}} \overset{!}{=} E_{\mathrm{thr}} \qquad \Leftrightarrow \qquad E_{p,\,\mathrm{in}}E_\gamma - |\vec{p_{\mathrm{in}}}|\,|\vec{p_\gamma}|\,c^2\cos\theta \overset{!}{=} \frac{1}{2}\left[m_\pi^2c^4 + 2m_pm_\pi c^4\right]\ ,$$

and we can divide the RHS by $m_p c^2$, noticing that $E_\gamma = |\vec{p_\gamma}|\, c$, and introducing the γ_p Lorentz factor of the proton:

$$\gamma_p = \frac{E_{p,\,\text{in}}}{m_p c^2} \qquad \text{and} \quad \sqrt{\gamma_p^2 - 1} = \sqrt{\frac{E_{p,\,\text{in}}}{m_p^2 c^4} - 1} = \sqrt{\frac{E_{p,\,\text{in}} - m_p^2 c^4}{m_p^2 c^4}} = \frac{|\vec{p_\text{in}}|\, c}{m_p c^2}\ ;$$

$$\Rightarrow \qquad \gamma_p\, |\vec{p_\gamma}|\, c - \sqrt{\gamma_p^2 - 1}\, |\vec{p_\gamma}|\, c \cos\theta \overset{!}{=} \left[\frac{m_\pi^2 c^2}{2 m_p} + m_\pi c^2\right] .$$

Dividing by c^2 and taking into account a high γ_p and the most favorable case, namely a head on collision $\theta = \pi$, one eventually finds

$$\gamma_p \simeq \frac{1}{2} \frac{m_\pi c}{|\vec{p_\gamma}|} \left(\frac{m_\pi}{2 m_p} + 1\right) ,$$

and in particular the minimum energy E_min is given by:

$$E_\text{min} = \frac{m_p c^2}{2} \frac{m_\pi c^2}{|\vec{p_\gamma}|\, c} \left(\frac{m_\pi}{2 m_p} + 1\right) \simeq 6.79 \times 10^{16} \left(\frac{E_\gamma}{1\,\text{eV}}\right)^{-1} \text{eV}\, ,$$

for $m_{\pi^0} = 134.97\,\text{MeV}/c^2$ and $m_p = 938.27\,\text{MeV}/c^2$, and these kind of energies are indeed assumed by cosmic rays primary particles. Notice also that this threshold is very much higher than the one for the dip mechanism Eq.(4.5), since now there is not the suppressing factor m_e/m_p but instead m_π/m_p. Assuming a CMB photon with an average energy of $T_\text{CMB} = 2.73\,\text{K} = 2.4 \times 10^{-4}$ eV, we get such an estimate:

$$E_\text{min} \simeq 6.79 \times 10^{16} \left(\frac{2.4 \times 10^{-4}\,\text{eV}}{1\,\text{eV}}\right)^{-1} \text{eV} \simeq 2.83 \times 10^{20}\,\text{eV}\, ,$$

but there are many CMB photons with higher energy and the threshold proton energy can be actually lower. The neutral pion will again electromagnetically decay $\pi^0 \to 2\gamma$, and the result is that the produced proton will inevitably have a reduced energy.

b) *Photo-production of charged pion*

As well as neutral pions, the charged mesons can be produced too. Notice that in the previous derivation we have specified only in the end the neutral pion mass. So the results are identical for this process:

$$p + \gamma \to n + \pi^+$$

once we substitute m_p with m_n for the numerical estimate. So:

$$E_\text{min} = \frac{m_n c^2}{2} \frac{m_\pi c^2}{|\vec{p_\gamma}|\, c} \left(\frac{m_\pi}{2 m_n} + 1\right) \simeq 7 \times 10^{16} \left(\frac{E_\gamma}{1\,\text{eV}}\right)^{-1} \text{eV}\, ,$$

for $m_{\pi^+} = 139.6\,\text{MeV}/c^2$ and $m_n = 939.565\,\text{MeV}/c^2$, and again these energies are not that surprising, and very close to the previous result. Also the estimate for the CMB photon made above give a very similar result:

$$E_\text{min} \simeq 7 \times 10^{16} \left(\frac{2.4 \times 10^{-4}\,\text{eV}}{1\,\text{eV}}\right)^{-1} \text{eV} \simeq 2.92 \times 10^{20}\,\text{eV}\, .$$

The neutron produced is expected to decay weakly by β^- process, $n \to p + e^- + \bar{\nu}_e$ within the usual lifetime $\tau_n \simeq \ln 2\, \tau_{1/2}$ with $\tau_{1/2} = (10.5 \pm 0.2)$ min, such that a lower energy proton is again present in the final state.

The photo-meson productions studied here, once one identifies the γ with a CMB photon, often go under the name of **GZK effect**, or GZK cut-off, which is the acronym of the three scientists that have theorized them: Kenneth Greisen, Vadim Kuzmin and Georgiy Zatsepin. The cut-off refers to the fact that, once applied to CMB photons, these processes describe a model of energy loss for UHECRs in the ankle of the spectrum, see Sec.(4.2.2). The effect starts to be significant, together with the dip mechanism (see Ex.(4.1)), at $E \simeq 5 \times 10^{18}$ eV, and might suggest that the proton component of the CR flux drops sharply above the threshold energy $E_{\rm min}$. The latter was calculated in this section with an example of mean energy of $T_{\rm CMB}$, but the treshold is expected to be lower due to the high energetic tail of the CMB planckian spectrum.
The cross-section for these processes, finally, were studied in laboratory and, close to the threshold, is about $\sigma_{\gamma p} \simeq 250\,\mu$barn.

B.2 Hadronic processes

a) *Neutral pion production by proton-proton interaction*

This process is of great interest for hadronic showers, since it represents the principal mechanism of production of π^0 to give rise to the electromagnetic counterpart of the shower:

$$p + p \to p + p + \pi^0$$

Let us study the process with the same kinematic laws as done before. We can write the four momenta of the particles in the initial state as $p_{i,\,\rm in} = (E_i/c,\, \vec{p_i}) = \left(\sqrt{m_p^2c^4 + |\vec{p_i}|^2 c^2}/c,\, \vec{p_i}\right)$. So the invariant mass in the initial state is

$$\sqrt{s} = \sqrt{2m_p^2c^4 + |\vec{p_1}|^2 c^2 + |\vec{p_2}|^2 c^2 + 2E_1E_2 - |\vec{p_1} + \vec{p_2}|^2 c^2} =$$

$$= \sqrt{2m_p^2c^4 + 2E_1E_2 - 2\,|\vec{p_1}|\,|\vec{p_2}|\,c^2\cos\theta}\,.$$

The threshold energy for the process is the total energy available in the COM frame $E_{\rm thr} = E^*$ and is given by

$$E_{\rm thr} = (2m_pc^2 + m_\pi c^2)^2\,,$$

and we can impose the equality again to find the minimum energy $E_{\rm min}$ for the process to happen:

$$E_{\rm in} \overset{!}{=} E_{\rm thr} \qquad \Leftrightarrow \qquad E_1E_2 - |\vec{p_1}|\,|\vec{p_2}|\,c^2\cos\theta \overset{!}{=} \frac{1}{2}\left[m_\pi^2c^4 + 4m_pm_\pi c^4 + 2m_p^2c^4\right]\,.$$

Now we can divide the RHS by $m_p^2c^4$ and introduce the γ_i Lorentz factor of the protons, completely analogously with what we did before:

$$\gamma_1\gamma_2 - \sqrt{\gamma_1^2 - 1}\sqrt{\gamma_2^2 - 1}\cos\theta = \frac{1}{2}\left(\frac{m_\pi^2}{m_p^2} + \frac{4m_\pi}{m_p} + 2\right) = 1 + m_\pi\left(\frac{m_\pi}{2m_p^2} + \frac{2}{m_p}\right)\,.$$

If we assume one proton to be at rest, namely $\vec{p_2} = 0$ and $\gamma_2 = 1$, and always accounting for head on collisions $\theta = \pi$, we obtain

$$\gamma_1 = 1 + m_\pi\left(\frac{m_\pi}{2m_p^2} + \frac{2}{m_p}\right) \simeq 1.2984\,,$$

so the energy of the proton must be $E_{\rm min} = \gamma_1 m_pc^2 = 1221\,\text{MeV}$, and in the laboratory frame this energy translates into:

$$E_{\rm kin} = E_{\rm min} - m_pc^2 = (\gamma_1 - 1)\,m_pc^2 \simeq 280\,\text{MeV}\,.$$

The cross-section of this reaction is also determined by the strong interactions and is about the geometrical cross-section of the proton, $\sigma_{pp} \simeq 4 \times 10^{-6}\ \mathrm{cm}^2$.

b) *Charged pions production by proton-proton interaction* The same kind of study can be done for the following reactions

$$p + p \to p + n + \pi^+ \qquad p + p \to p + p + \pi^+ + \pi^- \ ,$$

finding very similar thresholds.